EVAPORATED THIN-FILM TUNABLE DISTRIBUTED RC-FILTERS

A STUDY OF EVAPORATED THIN-FILM VOLTAGE-CONTROLLED TUNABLE DISTRIBUTED RC-FILTERS

By

PIETER L. SWART
B.Sc.(Eng.), B.Sc.(Eng.)(Hons.), M.Sc.(Eng.)

A Thesis

Submitted to the School of Graduate Studies

in Partial Fulfilment of the Requirements

for the Degree

Doctor of Philosophy

McMaster University

March 1971

DOCTOR OF PHILOSOPHY (1971)
(Electrical Engineering)

McMaster University
Hamilton, Ontario

TITLE: A Study of Evaporated Thin-Film Voltage-Controlled Tunable Distributed RC-Filters

AUTHOR: Pieter L. Swart, B.Sc.(Eng.) (University of Pretoria)
B.Sc.(Eng.)(Hons.) (University of Pretoria)
M.Sc.(Eng.) (University of Pretoria)

SUPERVISOR: Professor C.K. Campbell

NUMBER OF PAGES: 232, xiv

SCOPE AND CONTENTS:

The analysis, construction and performance of a new type of thin-film tunable filter is described.

The construction of the devices is discussed with particular reference to the properties of the evaporated materials. The basic unit is used as both a notch filter and a bandpass amplifier to demonstrate its capabilities. The effects of parasitics in the experimental devices are taken into consideration to account for the experimental results.

ABSTRACT

The analysis, construction and performance of a new type of evaporated thin-film filter is described. It has the capability of frequency tuning by means of a single bias voltage.

The device is basically a uniformly distributed resistance-capacitance network (URC) with a thin semiconductor film incorporated in the structure. The resistive film, insulator and semiconductor films constitute a metal-insulator-semiconductor system (MIS) whose capacitance is bias dependent. The device differs from other proposed tunable thin-film filters in the fact that the capacitance can be altered independently of the distributed resistance.

A theory is developed to account for the effects of MIS-losses and parasitic inductance on the performance of URC-null networks. These parasitic effects manifest themselves in four different ways:

(i) A shift of the null from the position predicted by the ideal theory.

(ii) A change in the notch parameter α for an optimum null.

(iii) A detuning effect in the case of tunable notch filters.

(iv) A reduction in the available tuning range; the so-called "tuning range compression".

Experimental units were made by vacuum evaporation of Nichrome, Y_2O_3, CdS and $A\ell$ onto alumina substrates. An attempt is made to relate the device characteristics to the material properties. In this respect,

the relative dielectric permittivity and thickness of the insulator, the doping density of the semiconductor, the semiconductor-insulator interface states and the bulk states in the semiconductor are found to be the most important parameters.

Filters were built which operated in the frequency range 600 kHz to 6 MHz. The best notch filter has a tuning capability of 30% with a ±15V bias voltage. The notch depth is over 60 dB in most cases. A tunable bandpass amplifier which was constructed, has a centre frequency which can be shifted between 6 MHz and 7 MHz with a ±3.5V bias voltage. The Q of this particular device was measured to be 742.

ACKNOWLEDGEMENTS

The author is indebted to Dr. C.K. Campbell for his helpful advice and encouragement during the course of this work. The author also wishes to express his thanks to Dr. S.S. Haykim and Dr. J. Shewchun, the other members of his Ph.D. Supervisory Committee, for their interest in the investigation.

Many thanks are due to Dr. H.I. Ralph for his advice during the initial stages of the project.

The author is grateful to Mr. V.A.K. Temple for the use of his computer programs for calculations of MIS capacitance and conductance curves. He also benefited from discussions with Mr. R. Clarke and Mr. E. Jones.

This project was financed through a grand-in-aid from the National Research Council of Canada to Dr. C.K. Campbell. The author is also indebted to McMaster University for financial support in the form of a McMaster Assistantship and a University Scholarship. The financial aid received from the Council for Scientific and Industrial Research, Pretoria, is also gratefully acknowledged.

Finally, thanks are due to Mrs. Kathy Paulin for the typing of the thesis.

TABLE OF CONTENTS

Page

CHAPTER 1 - INTRODUCTION 1

1.1 Thin-Film Integrated Circuits 1
1.2 Scope of this Work 3

CHAPTER 2 - REVIEW OF THE METAL-INSULATOR-SEMICONDUCTOR (MIS) THEORY 6

2.1 Introduction 6
2.2 Physics of the MIS-system 7
2.2.1 Ideal MIS Device 7
2.2.2 Non-Ideal MIS Device 19
2.2.2.1 Charges in the Insulator 19
a) Fixed Charges and Metal- Semiconductor Work Function Differences 19
b) Mobile Ions and Traps in the Insulator 20
2.2.2.2 Interface States 22
2.2.2.3 The Small Signal ac Impedance of the MIS-Capacitor 24
(i) Weak Inversion 26
(ii) Strong Inversion 32
(iii) Accumulation 32
(iv) Depletion 34
(v) Time Constant Dispersion 34
(va) A Continuum of Interface States 34
(vb) Random Fluctuations in Surface Potential 35
(vi) Additional Loss Mechanisms Pertaining to Evaporated Thin-Film MIS-Devices 38

CHAPTER 3 - THEORY OF THE UNIFORMLY DISTRIBUTED RC (URC) THIN-FILM FILTER 41

3.1 General 41
3.2 The Uniformly Distributed RC Low-Pass Filter (URC) 41
3.2.1 The Ideal URC Low-Pass Filter 41
3.2.2 The URC Low-Pass Filter in the Presence of Dielectric Loss 47

TABLE OF CONTENTS (cont'd) Page

3.3 The URC Notch Filter 54
3.3.1 The Ideal URC Notch Filter 54
3.3.2 The Influence of Parasitic Inductance 60
3.4 The URC-Bandpass Filter 70
3.4.1 Introduction 70
3.4.2 Ideal URC High Q Bandpass Filter 70
3.4.3 URC Bandpass Network with a Non-Ideal Wideband Amplifier and Distributed Network 74
3.5 Conclusion 78

CHAPTER 4 - THE TUNABLE URC-FILTER 79

4.1 Introduction 79
4.2 Ideal Tuning Characteristics of the Tunable Notch Filter 83
4.3 Effects of MIS-Losses and Parasitic Inductance on the Tunable URC Notch Filter 86
4.4 Conclusion 92

CHAPTER 5 - APPARATUS AND MATERIALS FOR THE FABRICATION OF EVAPORATED THIN-FILM FILTERS 93

5.1 Introduction 93
5.2 The Vacuum Coating Unit 93
5.3 The Thickness Monitor 96
5.4 Measurement of the Substrate Temperature 99
5.5 The Electron Beam Evaporation System 104
5.6 Evaporation Sources and Materials 104
5.6.1 Cadmium Sulfide 104
5.6.2 Yttrium Oxide 105
5.6.3 Silicon Monoxide 106
5.6.4 Silicon Nitride 108
5.6.5 Nichrome 109
5.6.6 Aluminum 110
5.6.7 Gold 111
5.7 Mask Construction 111

CHAPTER 6 - THE VACUUM EVAPORATION OF YTTRIUM OXIDE 114

6.1 Introduction 114
6.2 Techniques of Producing Thin Y_2O_3 Films 114
6.3 Mechanisms of Evaporation 116
6.4 Structural Properties of Electron Beam Evaporated Y_2O_3 Films 119
6.5 Electrical Properties of Y_2O_3 Films Deposited for this Work 119
6.6 Conclusion 123

TABLE OF CONTENTS (cont'd) Page

CHAPTER 7 - THE VACUUM EVAPORATION AND PROPERTIES OF CADMIUM SULFIDE THIN-FILMS 124

7.1 Introduction 125
7.2 Preparation of CdS Thin-Films 125
(a) Single Source 125
(b) Multiple Source Evaporation 130
7.3 Post-Evaporation Treatments 131
(a) Gilles and Van Cakenberghe Recrystallization Process 131
(b) Embedding Technique 132
(c) Organometallic Techniques 133
7.4 Physical and Electrical Properties of Evaporated CdS Films 134
7.5 Hall Mobility and Free Carrier Density Determination in Evaporated Thin-Films of CdS 139
7.5.1 Proposed Experiment for Determining Doping Densities and Transport Properties of Thin Semiconductor Films 140
7.5.2 Calculation of the Relationship Between the Measured Mobility and the Mobility of Electrons in the Film 147
7.5.3 Calculation of μ when μ_h' is known 154
7.5.4 Modulation of Ionized Impurity Scattering by the Field-Effect 155
7.6 Conclusion 161

CHAPTER 8 - MEASURING EQUIPMENT 162

8.1 Introduction 162
8.2 Apparatus for the Measurement of the CV, IV and the Quasi-static CV-Characteristics of MIS Devices 162
(i) Small Signal Capacitance and Conductance Measurements 164
(ii) Current-Voltage Characteristics 168
(iii) Pinhole Blow-out 168
(iv) Quasi-static Capacitance-Voltage Measurements 170
(v) High-Frequency CV-Curves 173
8.3 Transfer-Function and Impedance Measurement of URC-Filters 173

CHAPTER 9 - EXPERIMENTAL ANALYSIS 179

9.1 Introduction 179
9.2 Post-Evaporation Treatment 180
9.3 MIS-Capacitance and -Conductance Measurements 185
9.3.1 Calculation of the Doping Density 191
9.3.2 Instabilities in the Y_2O_3-CdS-System 194

TABLE OF CONTENTS (cont'd) Page

9.4 The Tunable URC-Filter 197

9.4.1 The URC Notch Filter 197

9.4.2 The Influence of Parasitic Losses and Stray Inductance 199

(a) Detuning 199

(b) Tuning Range Compression 201

9.4.3 The Experimental URC Bandpass Filter 204

9.5 Conclusion 209

CHAPTER 10 - CONCLUSIONS AND RECOMMENDATIONS 210

APPENDIX A - CALCULATION OF THE RESISTORS $R_{n,ss}$ AND $R_{p,ss}$ OF THE MIS EQUIVALENT CIRCUIT 215

APPENDIX B - 219

B.1 Electron Beam Pulsing Unit 219

B.2 Electron Beam Rate Controller 219

REFERENCES 222

LIST OF FIGURES

Figure		Page
2.1	Schematic Representation of the Thin-Film MIS-Structure	8
2.2	Energy Band Diagrams of an MIS-Structure under Various Bias Conditions (n-type Semiconductor)	11
2.3	Ideal CV-Curves for an n-type Semiconductor	12
2.4	Energy Band Diagram of n-type MIS Device	14
2.5	Theoretical CV-curve for $A\ell$-Y_2O_3-CdS Capacitor	18
2.6a	Arbitrary Distribution of Charge (ions) in the Insulator of an MIS-Structure	21
2.6b	Drift due to Tunneling from the Accumulation Layer into Traps located inside the Insulator	21
2.7	The Small Signal ac Equivalent Circuit for the MIS-Capacitor in the Depletion-Inversion Regime of Operation	31
2.8	Equivalent Circuit for the MIS-Capacitor in Heavy Inversion	31
2.9	Equivalent Circuit of the MIS-Capacitor in Accumulation	33
2.10	Small Signal ac Equivalent Circuit of the MIS-Capacitor in Depletion	33
2.11	Equivalent Circuit Applicable to a Continuum of Interface States	36
2.12	Equivalent Circuit for a Continuum of Interface States with the Surface in Depletion-Accumulation	36
2.13	Surface State Equivalent Circuit if the Surface is in Weak Inversion	36
2.14	Real Part of the Impedance of a Nichrome-Y_2O_3-CdS MIS Capacitor	40
3.1	Physical Structure and Circuit Symbol of a URC-Network	42
3.2	Incremental Model of the URC Network	44

LIST OF FIGURES (cont'd)

Figure		Page
3.3	A Comparison Between the URC Low-Pass Filter Response and the First and Second Order Butterworth Filters	48
3.4	A Comparison Between the Phase Response of the URC Low-Pass Filter and the First and Second Order Butterworth Filters	49
3.5	Incremental Model of the URC-Network Taking Dielectric Dissipation into Consideration	51
3.6	The Π- and T-Equivalent Circuits of the URC Low-Pass Filter	53
3.7	Phase Angle of Y_2 and Z_b as a Function of Normalized Frequency	55
3.8	The URC-Notch Filter	57
3.9	Theoretical Magnitude and Phase Response of the URC-Notch Filter	61
3.10	The URC-Notch Filter with Parasitic Notch Inductance	63
3.11	Effect of the Notch Inductance Parameter η on the Normalized Notch Frequency x_1 for Various Values of the Dissipation Parameter B.	66
3.12	Effect of the Notch Inductance Parameter η on the Notch Parameter α for Various Values of the Dissipation Parameter B	67
3.13	Predicted Transfer Function Response of an $A\ell$-Y_2O_3-Nichrome Notch Filter for $\eta=0$ and $\eta=5.5\times10^{-3}$ Compared With Experimental Response	69
3.14	The URC-Bandpass Amplifier	71
3.15	Ideal URC Bandpass Amplifier Response for Three Different Values of the Notch Parameter α	75
3.16	URC Bandpass Network with a Non-Ideal Wideband Amplifier and Distributed Network	76
4.1	Pictorial Representation of Tunable URC Distributed Filter	81
4.2	The Ideal High Frequency Capacitance-Voltage Curve	84

LIST OF FIGURES (cont'd)

Figure		Page
4.3	The Voltage Transfer Function of the Ideal URC-Notch Filter Calculated for Three Different Bias Voltages	85
4.4	Calculated Tuning Characteristics of the Tunable URC-Notch Filter in the Presence of MIS-Losses and Notch Inductance. $B(\omega)=B=10^{-2}$; $L_n=32nH$; $R=400\Omega$; $R_n=14.4181\Omega$.	89
4.5	Calculated Tuning Characteristics of the Tunable URC-Notch Filter in the Presence of MIS-Losses and Notch Inductance. $B(\omega)=B=10^{-2}$; $L_n=320nH$; $R=400\Omega$; $R_n=20.2043\Omega$.	90
5.1	Schematic Diagram of the Vacuum System	95
5.2	Photograph of the Interior of the Vacuum Evaporation System	97
5.3	Details of Substrate Temperature Sensor	100
5.4	Calibration Curve for the GB41J1 Thermistor	102
5.5	Comparison between the Temperature of the Front Surface of the Substrate as obtained by the Thermistor and the Temperature of the Heater	103
5.6	Photograph of Two of the Masks	112
6.1	Dielectric Losses in an $A\ell$-Y_2O_3-$A\ell$ Capacitor as a Function of the Post-Evaporation Treatment	120
6.2	Leakage Current in Device #40 after the Bake in Air	120
6.3	Interference Fringes for an $A\ell$-Y_2O_3-$A\ell$ Sandwich	122
7.1	Equilibrium partial Vapour Pressures of Sulfur, Cadmium and Selenium as a Function of Temperature	127
7.2	Resistivity of Evaporated CdS as a Function of the Substrate Temperature	129
7.3	Cross-Sectional View of MISIM-Structure	141
7.4	Top-View of Hall-Field Effect Configuration	141

LIST OF FIGURES (cont'd)

Figure		Page
7.5	Potential Distribution in the Ideal MISIM-Structure	142
7.6	Mid-plane Potential ϕ_o as a Function of Normalized Surface Potential in a Symmetrical MISIM-Structure	148
7.7	Schematic Representation of the Semiconductor in the Hall-Field Effect Sample	150
8.1	Photograph of the Micropositioners and the Vacuum Chamber Assembly	163
8.2	Block Diagram of the Experimental Set-up for Capacitance-Voltage and Current-Voltage Determinations	165
8.3	Switching Network	166
8.4	Switch Positions and Bias Resistors in Switching Network	167
8.5	Block Diagram of CV and GV Measurement System	169
8.6a	Simplified Equivalent Circuit of a Leaky MIS-Device	171
8.6b	Voltage Waveform	171
8.7	Photograph of the Apparatus for the Measurement of the CV, IV and the Quasi-Static CV-Characteristics of MIS-Devices	174
8.8	Open-Circuit Voltage Transfer Function Measurement	175
8.9	Magnitude and Phase Measurement of a Two-Terminal Impedance	176
8.10	Photograph of the Network Analyzer	178
9.1	Cross-Sectional View of a Tunable URC-Filter	181
9.2	Photograph of a Tunable URC-Filter on a 1" x 1" Ceramic Substrate	182
9.3	Leakage Current as a Function of Bias Voltage in a NiCr-Y_2O_3-CdS-$A\ell$ Thin-Film Tunable Filter	184
9.4	Calculated Real Part of the Input Impedance of an Ideal URC Filter as a Function of Frequency	186

Figure		Page
9.5	The Measured Real Part of the Input Impedance of a Nichrome-Y_2O_3-CdS-Aℓ Device as a Function of Frequency	188
9.6	The Measured Capacitance and Conductance of a Nichrome-Y_2O_3-CdS-Aℓ Device	189
9.7	Determination of Doping Density by means of the Depletion Approximation	192
9.8	DC Drift in Sample #51	195
9.9	MIS-Capacitance as a Function of Time Illustrating the Asymmetric Drift Rates in a Nichrome-Y_2O_3-CdS-Aℓ Structure	196
9.10	Tuning Range of #51 URC Tunable Notch Filter	198
9.11	Tuning Range of #54 URC Tunable Notch Filter	198
9.12	Experimental Arrangement for Determining the Voltage Transfer Function of the Tunable URC Notch Filter	200
9.13	Schematic Diagram of the HP Model 1123 High Impedance Probe	200
9.14	Tuning Characteristics of #54 URC Tunable Notch Filter	202
9.15	Tuning Characteristics of #51 URC Tunable Notch Filter	202
9.16	URC Tunable Notch Filter (#56)	203
9.17	Example of Tuning Range Compression	203
9.18	URC Bandpass Amplifier	205
9.19	Phase Shifter and Bias for URC-Network	205
9.20	Comparison between the Experimental and Calculated Response of the URC Bandpass Amplifier	207
9.21	High-Q Tuned Amplifier (#48)	208
9.22	High-Q Tuned Amplifier with Tunable Centre Frequency (#54)	203
B1	Pulsing Unit for the Electron Beam System	220
B2	Block Diagram of the Electron Beam Rate Controller	221

CHAPTER 1

Introduction

1.1 Thin-Film Integrated Circuits

There are currently two main approaches to integrated electronics, namely silicon monolithic and thin-film circuits. Thick-film technology has emerged during the last few years as a third alternative, but for the purpose of this discussion it may be considered to be analogous to the thin-film technique.

A certain hybridization has occurred whereby some components or sub-systems are produced by one process and are interconnected by one or other means with the other components produced by another technique. Thin-film resistors and capacitors usually have superior qualities compared to the ones that are formed by diffusions and oxidations on a single crystal silicon wafer. Bipolar and unipolar active devices, on the other hand, are made most readily by means of the silicon technology. Monolithic operational amplifier chips may for instance be attached to a very accurate thin-film resistor ladder network to form part of an analog to digital converter. The drawback of the hybrid approach is the large number of interconnections that has to be made. This leads to high production cost and a reduction in circuit reliability. Many problems are also encountered in isolating different components in the silicon wafer from each other.

Thin-film resistors and capacitors can be produced to very accurate tolerances on insulating substrates. Control of the circuit parameter values during the deposition and trimming afterwards by means of a laser beam, say, allow for very critical tolerances. Some work has also been done in producing active devices, e.g., insulated-gate field-effect transistors, on the same substrate. Not all the problems regarding these active devices have been solved to date, but recent work in this respect has been very encouraging.

These thin-film components can be produced by vacuum evaporation of metals, insulators and semiconductors in a single pump-down of a vacuum system. This leads to considerable savings in processing time and steps. Because these components are produced on insulating substrates, achieving isolation between different components is virtually no problem. In addition, the substrate itself is not critical: it does not have to be single crystal. Borosilicate glass with a low alkali content and glazed alumina substrates are probably the most widely used as substrate materials.

The compatibility of distributed RC-circuits with thin-film technology gave impetus to the study of thin-film distributed circuits. The distributed RC-network is a multi-layer structure of resistive, insulating and conducting films. In general, both the thickness and width of the resistive and insulating films may be varied along the length of the structure to produce resistance and capacitance per unit length that are functions of position. It is common practice, however, to keep the thickness constant and to vary the width. If the width is

constant, it is called a uniformly distributed resistance-capacitance circuit, or URC circuit in short. If the taper is such that the resistance and capacitance are exponential functions of the distance along the length, it is called exponentially tapered. This is commonly known as the ERC-filter. A considerable effort has gone in recent years into developing sophisticated synthesis techniques for these distributed networks. These are generally quite complicated, because the two-port parameters of distributed circuits involve hyperbolic functions of complex variables. Computer optimization may prove to be a much more powerful tool in getting the desired transfer functions. It is possible that techniques may evolve for connecting an arbitrary number of URC-sections in some optimum fashion in order to achieve the particular network response within a specified error.

The distributed network can lead in some instances to a considerable saving in the number of components and interconnections. The twin-T null-network is a common circuit that can be constructed from six lumped components, namely three resistors and three capacitors. With distributed networks, a null-circuit may be produced by a single URC-section and a lumped resistor.

The apparent importance of thin-film devices and distributed circuits prompted the present investigation.

1.2 Scope of this Work

This thesis describes a thin-film filter whose cut-off frequency may be changed by the application of a dc bias voltage. The device is basically a modified uniformly distributed RC-filter. It differs

from the standard URC-network in that an evaporated semiconductor film is incorporated into the device in order to vary the capacitance. The introduction of the semiconductor into the system leads to a wide variety of problems which are non-existent in the conventional URC-filter. These problems pertain to the properties of evaporated semiconductor films and the insulator-semiconductor interface. An attempt will be made to relate the characteristics of the voltage-controlled tunable URC-filter to the properties of the evaporated materials.

Chapter 2 reviews the theory of the metal-insulator-semiconductor (MIS) structure, and provides the basis for understanding the characteristics of the tunable filter.

Chapter 3 introduces the reader to the URC-network. It is discussed both as a low pass filter, and in the notch and bandpass configurations. The influence of parasitic effects is also treated in this section. The theory is developed for taking parasitic inductance and dielectric loss into consideration. An experiment performed on a low loss Nichrome-Y_2O_3-$A\ell$ notch filter, confirmed the predictions regarding the influence of parasitic inductance.

Chapter 4 treats the tunable notch filter theoretically and also introduces the effects of MIS-losses and parasitic inductance on the filter performance.

A review of the vacuum evaporation of thin-film devices is given in Chapter 5. The subsequent two Chapters, namely 6 and 7, expound further on the properties of electron beam evaporated Y_2O_3 and CdS. The excellent dielectric properties of Y_2O_3 are underlined by measurements of the dielectric losses, leakage currents, and the

relative dielectric permittivity. A new experiment is proposed in Chapter 7 for a better characterization of CdS thin-films. It may yield more reliable data on the doping density and the transport properties of electrons in evaporated films.

In Chapters 8 and 9 the experimental equipment and the performance characteristics of the tunable filters are presented.

CHAPTER 2

Review of the Metal-Insulator-Semiconductor (MIS) Theory

2.1 Introduction

A various number of review articles on the MIS-system exist at the present time[1-4]. All of these are mostly relevant to the Si-SiO_2 system with single crystal Si and usually steam-grown SiO_2. This system is fairly well understood, at least in a phenomenological sense, and great strides have been taken in the technological world in producing stable, well characterized Si-SiO_2 interfaces. These find application in MIS field-effect transistors and MIS varactors for use in parametric amplifiers[6], etc. The situation regarding evaporated thin-film field-effect devices is not as desirable from a practical point of view at the moment. The thin-film MIS-system is inherently much more difficult to understand and problems with drift and instabilities have not all been solved. The properties of evaporated insulators and semiconductors and their interfaces are not well understood and much more research work has to be done.

It is, nevertheless, of tremendous value to investigate the thin-film MIS-system on the hand of the theory for the Si-SiO_2 system. Wherever possible, an attempt will be made to point out the intrinsic differences between the two systems. Only the aspects of the theory which pertain to the rest of the thesis will be considered in the subsequent paragraphs.

2.2 Physics of the MIS-system

2.2.1 Ideal MIS Device

A thin-film MIS-capacitor is shown schematically in Figure 2.1. It consists of (for instance) an evaporated aluminum field plate, an evaporated dielectric (Y_2O_3 in this case), a semiconductor film (CdS) and a thin film of Aluminum on the CdS to form an ohmic contact. Vacuum evaporated CdS-films are invariably n-type and therefore the semiconductor film will be considered to be n-type in the rest of the discussion.

The behaviour of the small-signal MIS capacitance as a function of the field-plate voltage V_g may be described qualitatively as follows:

If the field-plate is made positive with respect to the semiconductor, electrons are accumulated at the semiconductor-insulator interface so that the semiconductor is much like a metal. The small-signal capacitance will approach the "insulator capacitance" C_i. Alternatively, if the applied voltage is made negative, the electrons will be repelled from the interface and a space-charge region of uncompensated donor-ions will be left behind. This depletion-layer or space charge capacitance will effectively be in series with the insulator capacitance and the total MIS-capacitance will be reduced. If the bias voltage is made even more negative, the surface will invert, i.e., a very narrow region of p-type conductivity will form adjacent to the semiconductor-insulator interface. These holes are mainly being generated in the depletion region and are swept to the interface.

The build-up of this inversion-layer is an exponential function of the semiconductor surface voltage. Most of the induced charge in the

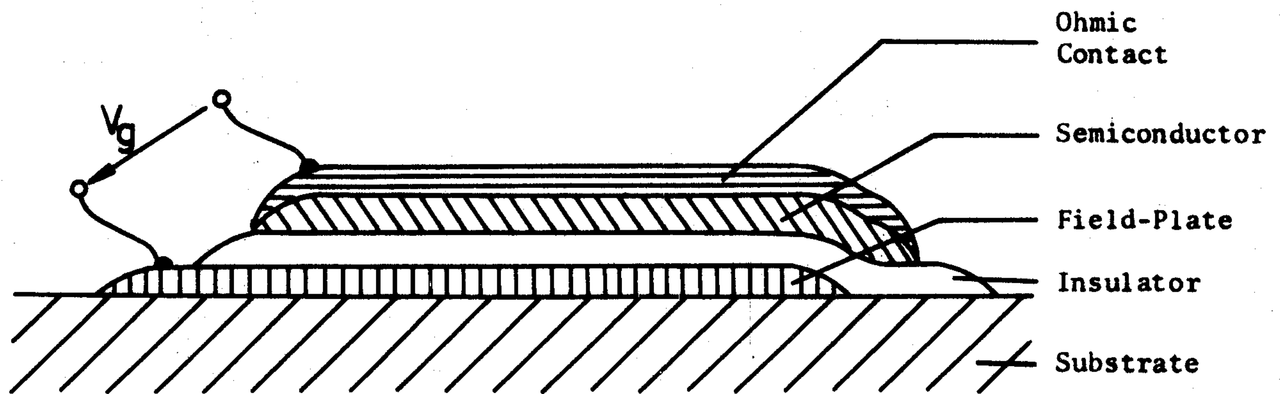

Figure 2.1 Schematic Representation of the Thin-Film MIS-Structure. (Not to scale.)

semiconductor will appear eventually in the inversion layer and the depletion-layer will approach a maximum value. If the measurement frequency is low enough so that the inversion layer has time to respond, the small-signal MIS capacitance will again approach the insulator capacitance. In the accumulation and depletion regimes of operation majority carriers (electrons in the case of an n-type semiconductor) have to respond when a small-signal capacitance measurement is done. The dielectric relaxation time of the semiconductor (defined as $\tau=\varepsilon_s/\sigma$ where ε_s = absolute dielectric permittivity of the semiconductor and σ = bulk conductivity of the semiconductor) determines the frequency dependence in these regions. For 100Ω-cm CdS, this time constant is of the order of 10^{-10} seconds. One would therefore not observe any frequency dependence of capacitance in the accumulation and depletion regimes of operation of the MIS-capacitor at frequencies say less than 100MHz. This statement may not be valid in the presence of interface states.

In the inversion mode of operation the charge transport involves a flow of minority carriers between the bulk and the inversion layer. The time constant associated with this process is determined essentially by the generation-recombination processes in the depletion region. It has been shown[30] that this time constant may be many orders of magnitude larger than the minority carrier lifetime or the dielectric relaxation time. No inversion layer response has been observed in the course of the investigations for this thesis. It will be neglected further on, and only the high frequency response will be considered.

In the discussion so far it has been tacitly assumed that the dc-bias variation is so slow that equilibrium conditions exist between all regions in the semiconductor. If the bias is swept so fast that this condition is violated, the inversion layer will not have time to build up. (The bias is being swept from accumulation to a large negative voltage on the field-plate.) Under these circumstances the depletion layer will become wider and will not reach a constant value that is independent of voltage. The capacitance will therefore be decreasing all the time, similar to the pn-junction capacitance under reverse bias conditions. The same type of CV-curve can also be observed when the oxide is leaky.

The energy band diagrams for the various cases discussed above, namely accumulation, depletion, inversion and deep depletion, are shown schematically in Figure 2.2. The system is assumed to be ideal, i.e., no surface states or insulator charge, and no metal-semiconductor work function difference. The different types of C-V curves are shown schematically in Figure 2.3. These have been calculated for an ideal MIS-structure with the following parameters:

$A = 0.38 \times 0.38\ cm^2$

$t_i = 3200Å$

$\varepsilon_i = 10$

$\varepsilon_s = 10$

$n_i = 2.1 \times 10^{-2}\ cm^{-3}$

$N_d = 2 \times 10^{16}\ cm^{-3}$

$T = 300^oK.$

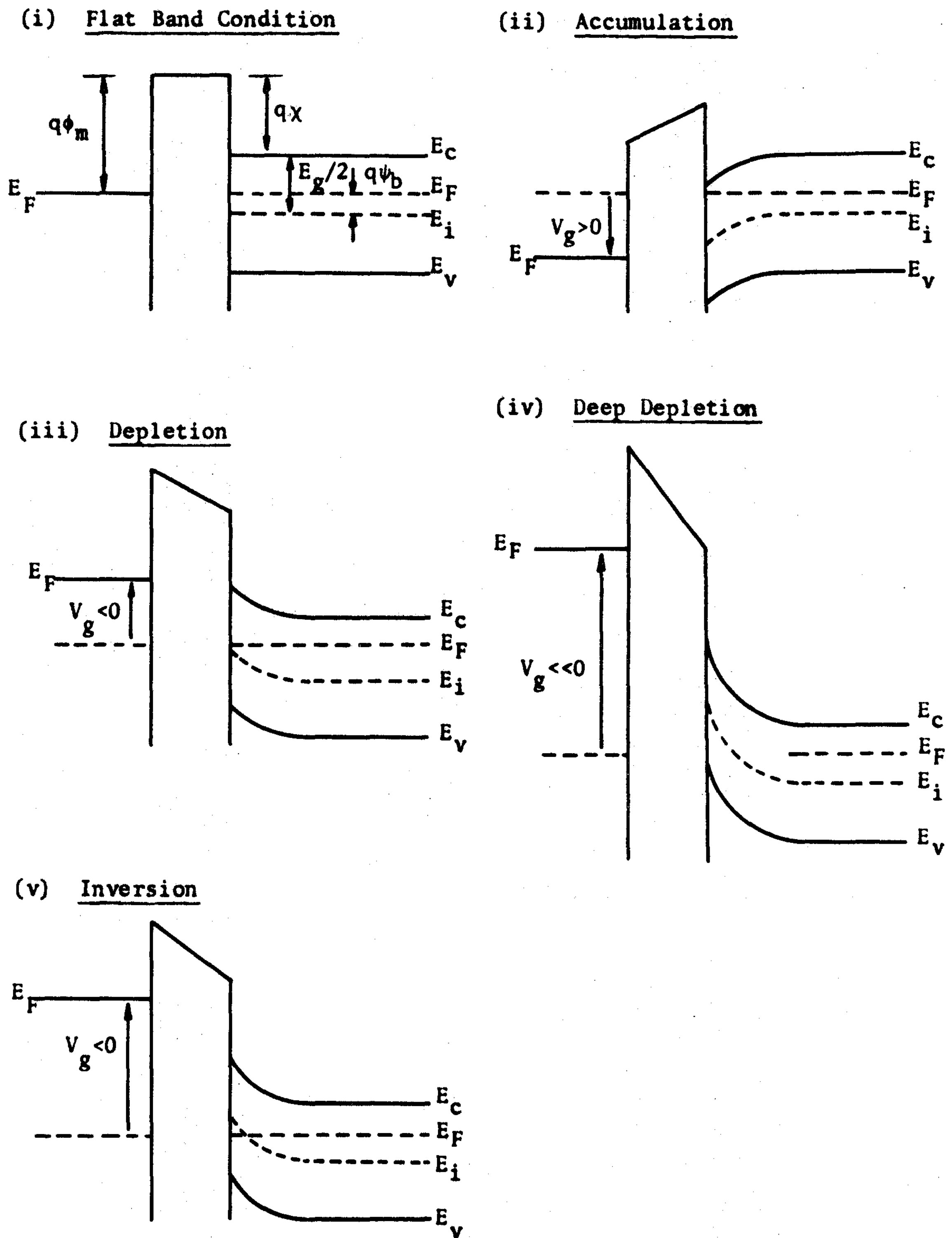

Figure 2.2 Energy Band Diagrams of an MIS-Structure under Various Bias Conditions. (n-type Semiconductor.)

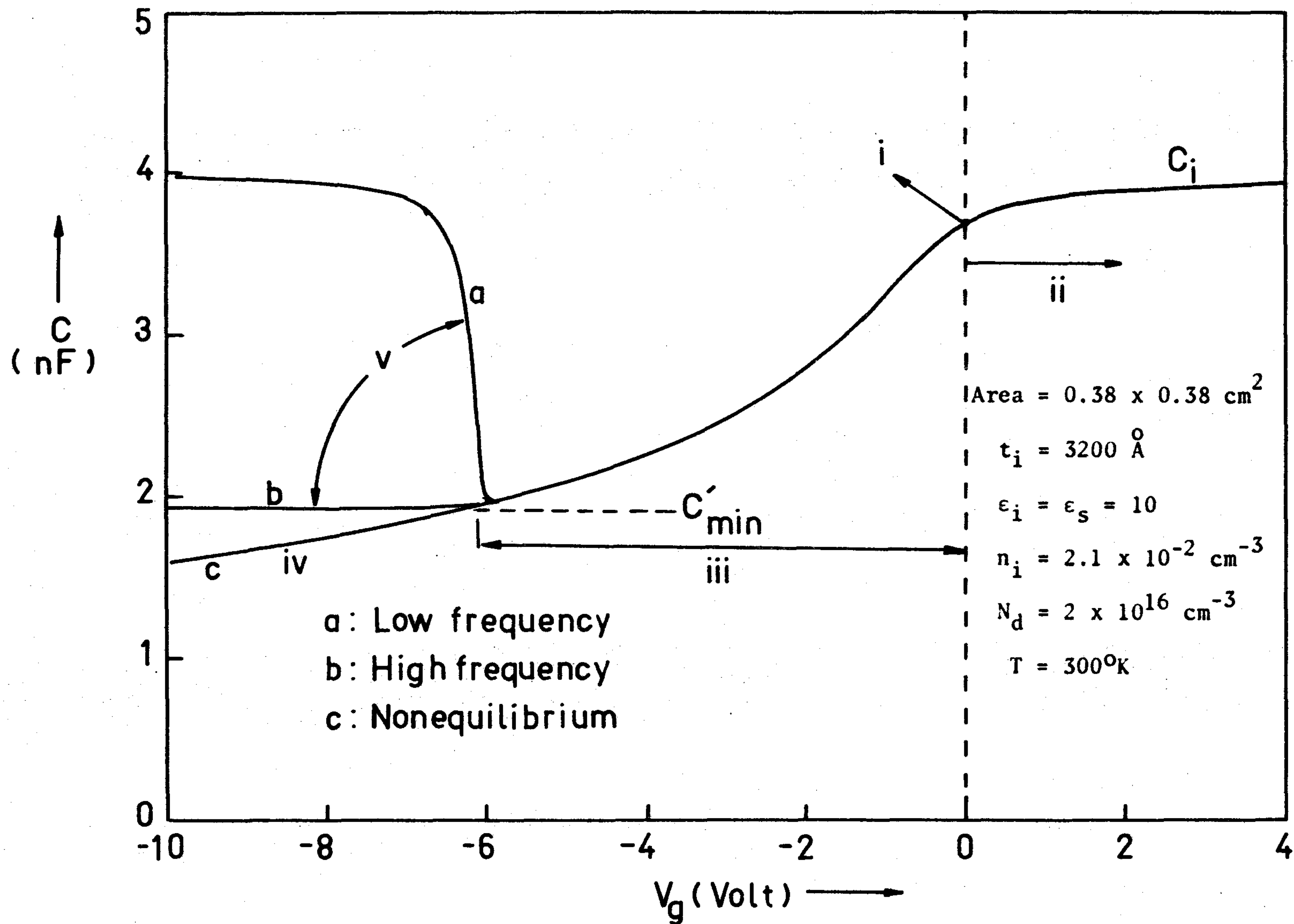

Figure 2.3 Ideal CV-curves for an n-type Semiconductor.

As has been pointed out above, the capacitance of the ideal MIS-capacitor consists of the insulator capacitance and space charge capacitance in series. Assume unit area.

$$C = \frac{C_i \, C_{sc}}{C_i + C_{sc}} \tag{2.1}$$

In order to calculate C for this ideal structure, it will be necessary to obtain an expression for the space charge capacitance C_{sc}.

The potential distribution, space charge and electric field in the semiconductor may be obtained by a solution of Poisson's equation[4]. The potential is defined as zero in the bulk and is measured with respect to the intrinsic Fermi level as shown in Figure 2.4. The surface potential is ψ_s and is positive for an n-type semiconductor in accumulation.

$$\frac{\partial^2 \psi}{\partial x^2} = - \frac{\rho(x)}{\varepsilon_s} \tag{2.2}$$

where ε_s is the absolute dielectric permittivity of the semiconductor and $\rho(x)$ is the total space charge density given by

$$\rho(x) = q(N_d - N_a + p - n) \tag{2.3}$$

where it has been assumed that the donors N_d and acceptors N_a are completely ionized. p and n are the densities of free holes and electrons, respectively. It has also been assumed that $(N_d - N_a)$ is the uniform doping level in the semiconductor. The assumption of a uniform doping density in evaporated CdS films is questionable as will be discussed in Chapter 7.

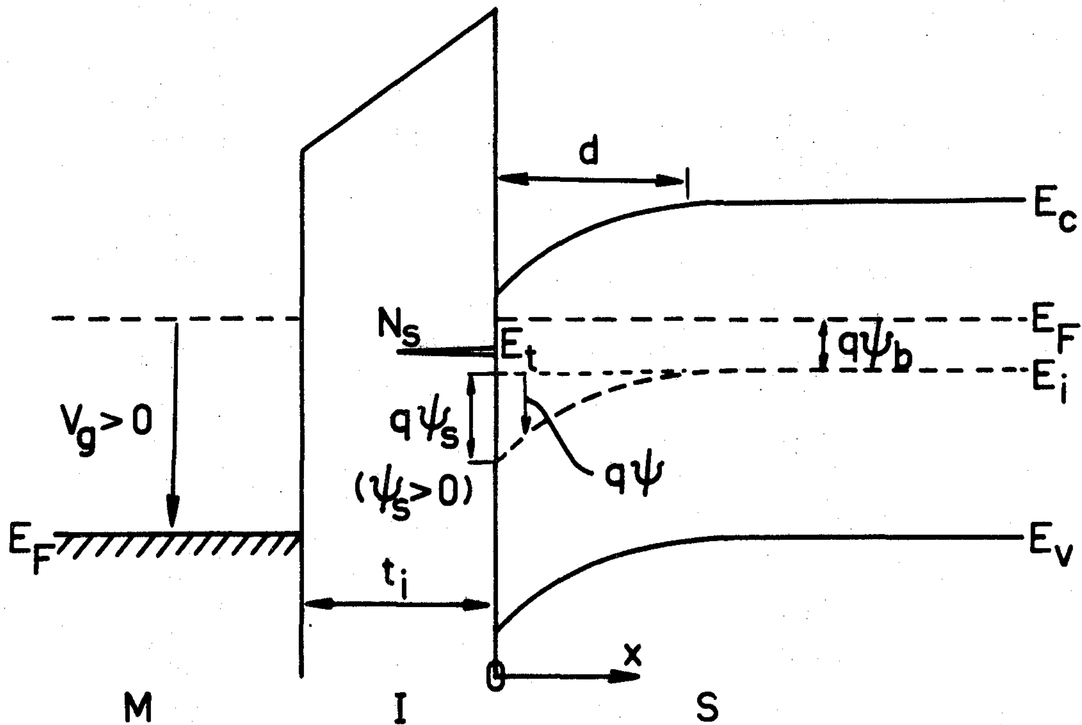

Figure 2.4 Energy Band Diagram of n-type MIS Device. The Field-Plate Potential is such that the Surface is in Accumulation.

$\psi_s > 0$: accumulation

$\psi_s = 0$: Flat band condition

$\psi_b < \psi_s < 0$: Depletion

$\psi_s = \psi_b \pm$ few kT : midgap

$2\psi_b < \psi_s < \psi_b$: weak inversion

$\psi_s < 2\psi_b$: strong inversion

($\psi_b < 0$ for n-type semiconductor)

In thermodynamic equilibrium, and if the semiconductor is non-degenerate, the carrier concentrations are given by

$$n = n_b e^{\frac{q\psi}{kT}} = n_b e^{\phi} \tag{2.4}$$

and

$$p = p_b e^{\frac{-q\psi}{kT}} = p_b e^{-\phi} \tag{2.5}$$

where p_b and n_b are the bulk carrier densities.

In the bulk where $\psi=0$ and $\rho(x)=0$, it follows that $N_d-N_a = n_b-p_b$. Poisson's equation becomes:

$$\frac{\partial^2\phi}{\partial x^2} = \frac{-q^2 n_b}{kT\epsilon_s} \left\{ \frac{p_b}{n_b}(e^{-\phi}-1)-(e^{\phi}-1) \right\} . \tag{2.6}$$

After integrating once, one obtains:

$$\mathcal{E} = -\frac{\partial\psi}{\partial x} = \pm \frac{2kT}{qL_D} \cdot F(\beta\psi, \frac{p_b}{n_b}) \tag{2.7}$$

$$\text{where } L_D = \sqrt{\frac{2kT\epsilon_s}{n_b q^2}} = \text{Debye length} \tag{2.8}$$

and

$$F(\beta\psi, \frac{p_b}{n_b}) = \left\{ \frac{p_b}{n_b}(e^{-\beta\psi} + \beta\psi - 1)+(e^{\beta\psi} - \beta\psi - 1)\right\}^{\frac{1}{2}} \tag{2.9}$$

$$\beta\psi = \frac{q\psi}{kT} = \phi \quad .$$

It has to be pointed out that this solution has been obtained by using the boundary condition $\psi=0$, $\mathcal{E}=0$ for large x, i.e., no space charge in the bulk. This condition will only be satisfied in the case of relatively thick films where the condition $t_s \gg L_D$ is satisfied. t_s is

the thickness of the semiconductor film. If this is not the case, the problem becomes considerably more difficult and closed form solutions are generally not obtainable. We will assume for the rest of the discussion that this condition is satisfied.

The total space charge follows from Gauss' Law:

$$Q_{sc} = \varepsilon_s \mathcal{E}_s = \pm \frac{2\varepsilon_s kT}{qL_D} \cdot F(\beta\psi_s, \frac{p_b}{n_b}) \quad . \tag{2.10}$$

The differential space charge capacitance follows now from this expression for Q_{sc}:

$$C_{sc} = \frac{\partial Q_{sc}}{\partial \psi_s} = \frac{\varepsilon_s}{L_D} \; \frac{\frac{p_b}{n_b}(1-e^{-\beta\psi_s})+(e^{\beta\psi_s}-1)}{F(\beta\psi_s, \frac{p_b}{n_b})} \quad . \tag{2.11}$$

The applied voltage appears partially across the insulator and partially across the semiconductor space charge layer.

$$V_g = V_i + \psi_s \tag{2.12}$$

The voltage drop across the insulator is given by

$$V_i = \frac{Q_{sc}}{C_i} \tag{2.13}$$

$$\therefore \qquad V_g = \frac{Q_{sc}}{C_i} + \psi_s \tag{2.14}$$

$$\frac{\partial V_g}{\partial Q_{sc}} = \frac{1}{C_i} + \frac{1}{C_{sc}} = \frac{1}{C} \tag{2.15}$$

The low frequency curve may be calculated directly from this expression and the expression for C_{sc}. The high frequency curve is of more importance to what follows and therefore we will concentrate on it.

In the depletion regime the potential is given by

$$\psi = \psi_s(1 - \frac{x}{x_d})^2 \tag{2.16}$$

where the surface potential ψ_s is given by

$$\psi_s = \frac{-q(N_d-N_a)x_d^2}{2\varepsilon_s}$$

and $\qquad\qquad\qquad\qquad\qquad\qquad\qquad\qquad\qquad$. (2.17)

$$Q_{sc} = q(N_d-N_a)x_d$$

x_d is the width of the depletion region.

The capacitance in the depletion region[7] may be obtained by using the expressions (2.14), (2.17) for V_g, ψ_s and Q_{sc}. After some algebraic simplifications it turns out to be:

$$C_d = \frac{C_i}{\sqrt{1 + \frac{2C_i^2}{\varepsilon_s q(N_d-N_a)} \cdot V_g}} \tag{2.18}$$

This expression is very useful for getting approximate CV-curves.

As has already been pointed out, the depletion region reaches a maximum width x_m when the surface is strongly inverted. Strong inversion takes place when the surface potential $\psi_s \doteq 2\psi_b$ where ψ_b is defined in Figure 2.4. Using these definitions and expression (2.17), x_m turns out to be: (assume $N_d >> N_a$)

$$x_m = \sqrt{\frac{4\varepsilon_s kT \cdot \ell n(\frac{N_d}{n_i})}{q^2 N_d}} \quad . \tag{2.19}$$

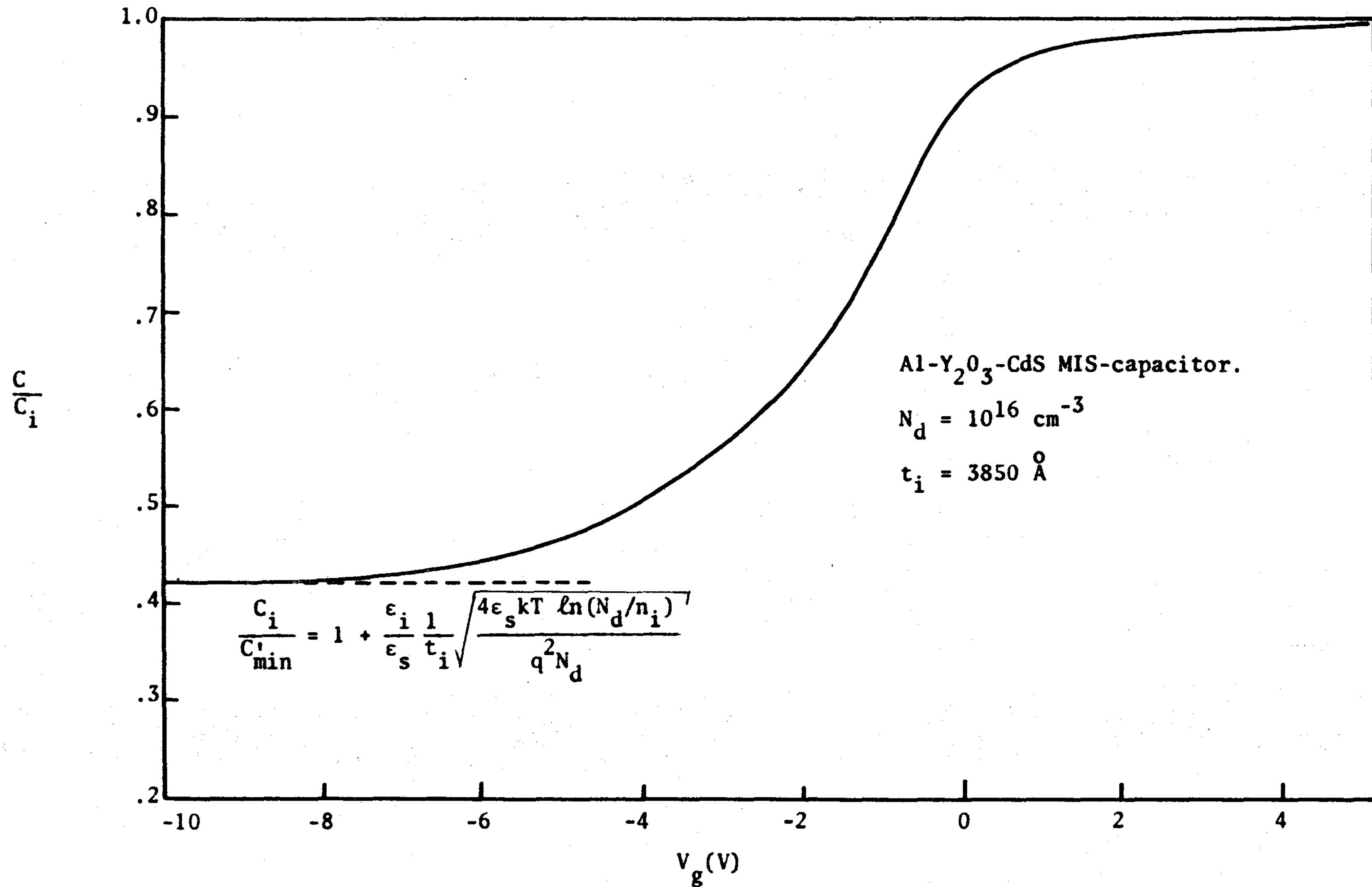

Figure 2.5 Theoretical CV-curve for Al-Y_2O_3-CdS capacitor.
$\phi_{ms} = Q_{ss} = 0$; no surface states.

The high frequency capacitance minimum can therefore be derived as:

$$C'_{min} = \frac{C_i}{1 + \frac{\varepsilon_i}{\varepsilon_s} \cdot \frac{x_m}{t_i}} \qquad (2.20)$$

and

$$\frac{C_i}{C'_{min}} = 1 + \frac{\varepsilon_i}{\varepsilon_s t_i} \sqrt{\frac{4\varepsilon_s kT \cdot \ell n(\frac{N_d}{n_i})}{q^2 N_d}} \qquad (2.21)$$

This expression is very useful for calculating the doping density N_d if the doping density is uniform through the thickness of the film.

2.2.2 Non-Ideal MIS Devices

The foregoing discussion has focussed on the ideal MIS-device in order to get a simple picture of its behaviour. In practice one invariably has to take the intrinsic aberrations of this system into account. The charges in the insulator, states on the insulator-semiconductor-interface, states in the semiconductor bulk, metal-semiconductor work function difference, etc., have to be considered, for they have a pronounced effect on the device. Interface states occuring at the semiconductor-insulator interface have a very pronounced effect on the CV-curves and the impedance of the MIS-capacitor, and they will be discussed in some detail.

2.2.2.1 Charges in the Insulator

a) Fixed Charges and Metal-Semiconductor Work Function Differences

It has been found[8] for Si-SiO_2 devices that fixed charges exist within 200Å or so from the interface. These charge centres are called

fixed because their occupancy can not be changed over wide ranges of temperature and surface potential. This charge will cause a parallel shift of the MIS-curves along the voltage axis. It is customary to lump all effects that cause a parallel shift of the MIS-curve along the V-axis into this fixed charge. Therefore, the metal-semiconductor work function difference $\phi_{ms}=\phi_m-(\chi + \frac{E_g}{2q} - \psi_b)$ is considered to be a part of the fixed charge. There is also some evidence of a fixed positive charge in the case of the evaporated CdS-SiO_2 system[20].

b) <u>Mobile Ions and Traps in the Insulator</u>

Another type of charge in the insulator, namely mobile ions, poses a greater restriction on the feasibility of MIS-devices. Because of the small physical diameter of ions like Na^+ and H^+, and the relative openess of most insulator lattices, an undesirable time-dependent drift may occur in the CV-curves. The field in the insulator is usually of the order of 10^5 to 10^6 V/cm, and drift may occur even at room temperature.

Snow, et al.[9], analyzed an MIS-system with an arbitrary charge distribution in the insulator. They showed that the effective gate voltage will be equal to:

$$V_g - \phi_{ms} + \frac{Q_{fc}}{C_i} + \frac{1}{t_i C_i}\int_0^{t_i} x\rho(x)dx \qquad (2.22)$$

where V_g = field-plate voltage

Q_{fc} = fixed charge near the S-I interface

$\rho(x)$ = charge distribution in the insulator

ϕ_{ms} = metal-semiconductor work function difference.

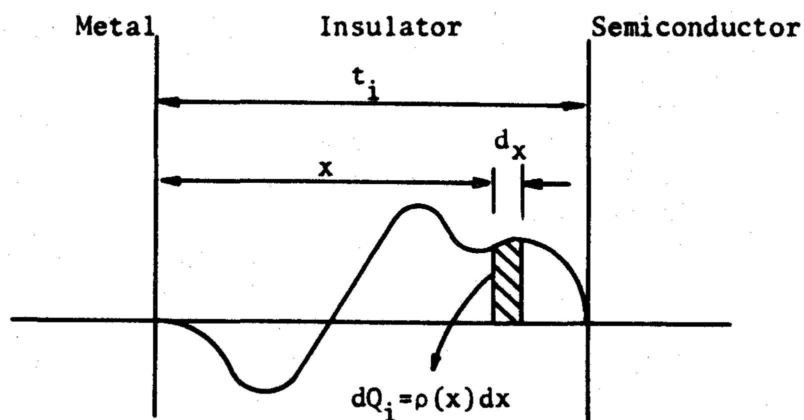

Figure 2.6a Arbitrary Distribution of Charge (ions) in the Insulator of an MIS-Structure.

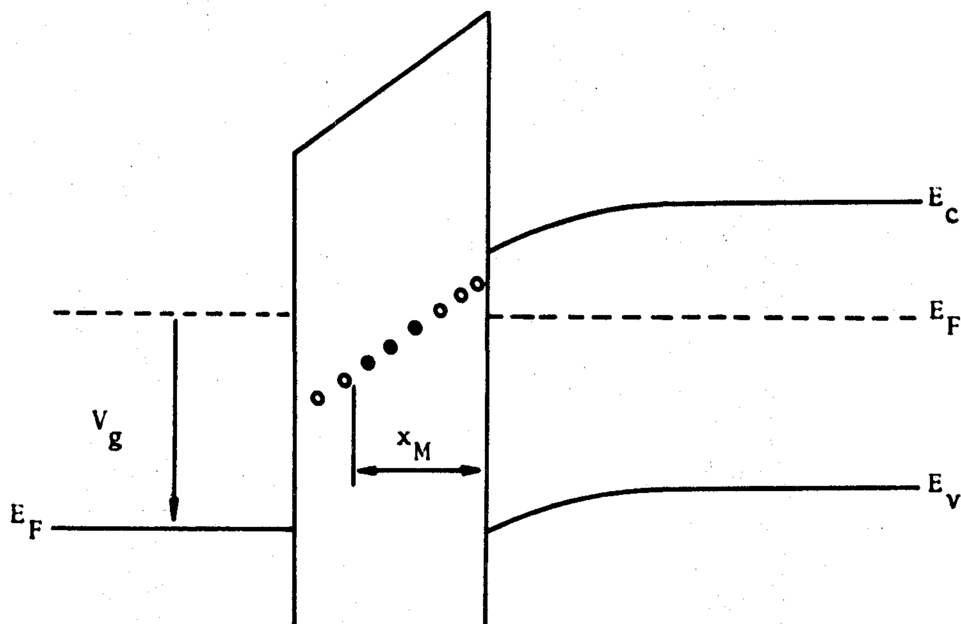

Figure 2.6b Drift due to Tunneling from the Accumulation Layer into Traps located inside the Insulator. x_M is the maximum tunneling depth during the time the measurement is performed.

If the temperature is sufficiently low so that the mobile ions have a negligibly small mobility, equation (2.22) indicates that a parallel shift of the whole CV-curve along the voltage axis will occur. If, however, the ions are moving under the influence of the electric field, a time dependent drift of the capacitance under fixed bias V_g will occur. If the mobile charge is positive and the semiconductor n-type, the capacitance will drift towards larger values if the bias voltage is changed from a negative value to a positive value and then kept constant. It is believed that this is the type of drift that had been observed for the Al-Y_2O_3-CdS-Al MIS-devices investigated for this thesis. This will be discussed in Chapter 9.

In addition to this type of instability, traps inside the insulator may trap some of the carriers at the interfaces. This type of instability has been described by Hofstein[11] and observed experimentally for evaporated insulators by Koelmans and DeGraaff[13]. If this trapping occurs at the S-I interface, it will cause a drift opposite to that observed for positive ions. If, however, trapping of holes occurs at the M-I interface, it will cause a drift in the same direction as for positive ions and it will be difficult to distinguish between the two processes.

2.2.2.2 Interface States

It has been shown theoretically[15,16] that localized states may exist in the vicinity of a semiconductor surface due to the abrupt change in the periodic potential of the bulk. Experimentally[17] it was found that such states do exist and that their density approaches the

density of surface atoms, namely 10^{15} cm^{-2}. It is a very difficult problem to relate the experimental results to the above-mentioned theories due to the rearrangement of the surface atoms as a consequence of their different environment. In the case of a solid-solid interface, e.g., semiconductor-insulator, the problem becomes even more difficult from a fundamental physical point of view. For this reason, relatively simple phenomenological theories have been proposed to explain the experimental results[23].

It has been found experimentally[18,19] that the density of the interface states in the case of Si-SiO_2, and for that matter other I-S combinations, is orders of magnitude lower compared to atomically clean surfaces. Furthermore, it has been discovered that a quasi-continuum of surface states exists in the bandgap of Si at the Si-SiO_2 interface. In addition, the density of these surface states, N_{ss} cm^{-2}-eV^{-1}, depends strongly on the method of preparation of the insulator[2]. With current Si-SiO_2 technology, densities of interface states of less than 10^{10} cm^{-2} - eV^{-1} is possible[2]. For thin-film devices, these range from $10^{13}cm^{-2}$ - eV^{-1} for evaporated SiO_2 on CdS[21], to less than 5 x 10^{10} cm^{-2} - eV^{-1} for a plasma-anodized aluminum-CdSe structure[22].

The characteristics of the interface states are of importance to electronic MIS devices due to the fact that they change the CV-characteristics, introduce ac losses and are a cause of 1/f noise. We will principally be interested in the ac losses which they introduce into the practical MIS device. Therefore, in the following paragraphs we will investigate the small-signal ac impedance of the MIS capacitor semi-quantitatively.

2.2.2.3 The Small Signal ac Impedance of the MIS-Capacitor

Ideally, the MIS capacitor may be represented by a constant capacitor C_i in series with a voltage variable capacitor C_{sc}. This is not so in practice for small ac signals, because frequency and bias dependent losses are being introduced into the system by an imperfect dielectric, interface states, states in the bulk of the semiconductor due to defects, the ohmic contact on the semiconductor, etc. It will be a very complicated problem to calculate all these effects exactly in a practical situation. We therefore chose to explain it semi-quantitatively and will show which effects will dominate in a thin-film MIS-structure.

The problem of calculating the small-signal ac impedance of the MIS structure has been treated by various authors[18,24-32]. Yunovich[27], for instance, discussed the MIS device in the accumulation regime, while Hofstein and Warfield[30] treated it in heavy inversion. We will follow the treatment of Lehovec and Slobodskoy[29] very closely, except where it becomes necessary to extend or to modify it.

Let us consider an n-type semiconductor with a single interface state level E_t with a density of states N_s cm^{-2}. We will neglect leakage current through the insulator, mobile or fixed charges in the insulator and will also assume that the semiconductor thickness >> diffusion length. Assume unit area. All the potentials are defined in Figure 2.4.

Different equivalent circuits pertain to the various modes of surface potential as defined in Figure 2.4. The various cases will be discussed subsequently and the appropriate approximations made pertaining

to each.

It will be assumed that each voltage, charge and current may be defined as a dc part plus a small ac part, i.e., $Y(t)=\bar{Y}+y=\bar{Y}+\tilde{y}$. For this condition, ac voltages and currents are linearly related.

For charge neutrality:

$$Q_m + Q_{ss} + Q_{sc} = 0 \tag{2.23}$$

where Q_m = charge on the field plate

Q_{ss} = surface state charge of the semiconductor

Q_{sc} = space charge associated with an excess or deficit of electrons and holes.

Suppose $Q_m = \bar{Q}_m + \tilde{Q}_m$ where $\bar{}$ refers to the dc part and $\tilde{}$ to the sinusoidally varying ac part. A complex capacitance [C] may then be defined as

$$[C] = \frac{\tilde{Q}_m}{v_g} \tag{2.24}$$

where v_g = applied ac voltage. As has been mentioned before, [C] will be complex due to dispersion effects.

$$v_g = v_i + v_{sc} \tag{2.25}$$

where v_i = ac voltage across the insulator

v_{sc} = ac voltage across the space charge layer in the semiconductor.

From (2.23), (2.24) and (2.25) it follows that

$$\frac{1}{[C]} = \frac{1}{C_i} + \frac{1}{[C_{sc}] + [C_{ss}]} \tag{2.26}$$

where $C_i = \frac{\tilde{Q}_m}{v_i}$ (2.27)

C_i = insulator capacitance (real if there are no dielectric losses)

$$[C_{sc}] = \frac{-\tilde{Q}_{sc}}{v_{sc}} = \text{space charge "Capacitance"} \qquad (2.28)$$

$$[C_{ss}] = \frac{-\tilde{Q}_{ss}}{v_{sc}} = \text{interface state "Capacitance"} \qquad (2.29)$$

From (2.26) it may be seen that the insulator capacitance is in series with the parallel combination of two complex capacitances $[C_{sc}]$ and $[C_{ss}]$.

The real nature of these "capacitances" may be obtained by studying in detail the supply of carriers to them when the surface potential is perturbed by a small ac signal.

(i) Weak Inversion

For this particular case the dc bias is such that $2\psi_b < \psi_s < \psi_b$,

where ψ_b = potential in the bulk of the semiconductor, and

ψ_s = surface potential.

The narrow inversion layer at the surface is connected to the bulk of the semiconductor by a depletion layer where the density of majority carriers is much lower than in the bulk. Charge storage effects may take place in the insulator capacitance, the surface states, the inversion layer and as a depletion charge between the depletion layer and the semiconductor bulk. These charges, namely $\tilde{Q}_{ss}$, $\tilde{Q}_I$ and $\tilde{Q}_D$ are associated with capacitors $[C_{ss}]$, $[C_I]$ and $[C_D]$ respectively. The subscripts I and D refer to the inversion and depletion layer respectively.

There are several sources to supply charge to these capacitances, and a current may be associated with each source. If small signal conditions prevail, i.e., $\frac{qv}{kT} < 1$, the voltages and currents are linearly related and resistances may be associated with these different current components.

The interface state "capacitor" receives its charge from the conduction and valence bands at the surface, and these currents are denoted by $i_{n,ss}$ and $i_{p,ss}$ respectively. The corresponding resistors are $R_{n,ss}$ and $R_{p,ss}$. These may be calculated quite readily if we assume a single level of interface states that obey Shockley-Read statistics.

It is shown in Appendix A that

$$R_{n,ss} = \frac{kT}{q^2} \cdot \frac{1}{c_n \bar{n}_s N_s (1-\bar{f})} \tag{2.30}$$

and

$$R_{p,ss} = \frac{kT}{q^2} \cdot \frac{1}{c_p \bar{p}_s N_s \bar{f}} \tag{2.31}$$

where c_n, c_p = electron and hole capture probabilities

$\bar{n}_s$, $\bar{p}_s$ = free electron and hole concentrations at the interface if the Fermi level is at E_t

$\bar{f}$ = Fermi function for the interface states.

It is also shown in Appendix A that

$$\frac{R_{n,ss}}{R_{p,ss}} = \frac{c_p}{c_n} \cdot \frac{N_v}{N_c} \cdot \exp\left\{-\frac{(E_t - E_v + E_F - E_c)}{kT}\right\} \tag{2.32}$$

But $E_v + E_c \doteq 2E_i$

$$\therefore \qquad \frac{R_{n,ss}}{R_{p,ss}} = \frac{c_p}{c_n} \cdot \frac{N_v}{N_c} \cdot \exp\{-\frac{(E_t - E_i + E_F - E_i)}{kT}\} \qquad (2.33)$$

In the inversion regime $\frac{R_{n,ss}}{R_{p,ss}} >> 1$, so that $R_{p,ss}$ may be considered as a short circuit.

The insulator capacitance C_i is supplied with charge through the displacement current of C_D and by the flow of minority carriers between the bulk and the inversion layer. The minority carrier flow is controlled by three resistances, namely $[R_{p,b}]$, $R_{p,D}$ and $R_{g,D}$.

$[R_{p,b}]$ accounts for the generation-recombination of holes and their flow rate in the bulk semiconductor adjacent to the space charge layer. Garrett[24] and Berz[26] have shown that the dispersion mechanism which is responsible for this resistance, namely diffusion of minority carriers, occurs at frequencies corresponding to the minority carrier lifetime. The impedance may be obtained by solving the continuity equation for holes.

$$\frac{\partial p}{\partial t} = -\frac{p}{\tau_p} + D_p \nabla^2 p \qquad (2.34)$$

Let

$$p = \bar{p} + \tilde{p} = \bar{p} + ae^{j\omega t}$$

$$(2.35)$$

$$\therefore \qquad j\omega\tilde{p} = -\frac{\tilde{p}}{\tau_p} + D_p \frac{\partial^2 \tilde{p}}{\partial x^2}$$

where τ_p = hole lifetime in the bulk. It is customary to assume that the semiconductor thickness $d_s >> L_p$ (diffusion length). This may not always be the case for thin-film semiconductors and the effect of the

back contact should be taken into account. We will assume that $d_s >> L_p$ and obtain the boundary conditions:

$$\tilde{p}\Big|_{x=d} = \tilde{p}_d = \text{hole density at the edge of the depletion region.}$$

$$\tilde{p}\Big|_{x=\infty} = 0 \quad .$$

We may now solve for $\tilde{p}$ and then obtain $[R_{p,b}]$

$$[R_{p,b}] = \frac{(D_p\tau_p)^{1/2}}{\sigma_p(1+j\omega\tau_p)^{1/2}} \tag{2.36}$$

where σ_p = bulk hole conductivity.

If $\omega << \frac{1}{\tau_p}$,

$$[R_{p,b}] = R_{p,b} = \frac{(D_p\tau_p)^{1/2}}{q\mu_p p_b} \quad . \tag{2.37}$$

The second resistor, in series with $[R_{p,b}]$, namely $R_{p,D}$, is associated with the hole current through the depletion region to the semiconductor-insulator interface. $R_{p,D}$ is usually negligible compared to $[R_{p,b}]$ for it is associated with a carrier concentration which is larger than the bulk minority carrier concentration. Hofstein and Warfield[30] have shown that

$$R_{p,D} \doteq \frac{1}{\mu_p q}\int_0^d \frac{n(x)}{n_i^2}\,dx$$

$$= \frac{L_D}{q\mu_p p_b} \tag{2.38}$$

$$\therefore \qquad \frac{R_{p,b}}{R_{p,D}} \doteq \frac{L_p}{L_D} >> 1$$

where $L_p = \sqrt{D_p \tau_p}$ and L_D is the Debye length associated with the donor concentration in the bulk.

The third resistor $R_{g,D}$ which appears in parallel with the previously mentioned two, was introduced by Hofstein and Warfield[30] to account for generation-recombination in the depletion layer. By assuming that $\tau_p = \tau_n = \tau_o$ and that there exists only a single level of traps in the centre of the gap of the semiconductor in the bulk, they managed to prove that

$$R_{g,D} = \frac{\tau_o V_{sc}}{q n_i d} \quad . \tag{2.39}$$

The inversion layer capacitance C_I is supplied by the flow of holes between the inversion layer and the surface states and by the flow of holes from the bulk through the depletion layer.

$R_{n,D}$ is a resistor that accounts for the flow of electrons through the depletion space charge layer. Lehovec and Slobodskoy[29] showed that

$$R_{n,D} = \int_o^d \rho_n dx = \frac{\bar{Q}_I}{n_i^2 q^2 \mu_n} \tag{2.40}$$

where $\bar{Q}_I$ = dc charge in the inversion layer.

The equivalent circuit which is valid for the weak inversion regime is depicted in Figure 2.7. A resistance R_o is included to account for the bulk resistance of the semiconductor and the ohmic contact on the back surface. The resistance due to the ohmic contact may actually dominate in thin-film CdS MIS-devices at high frequencies.

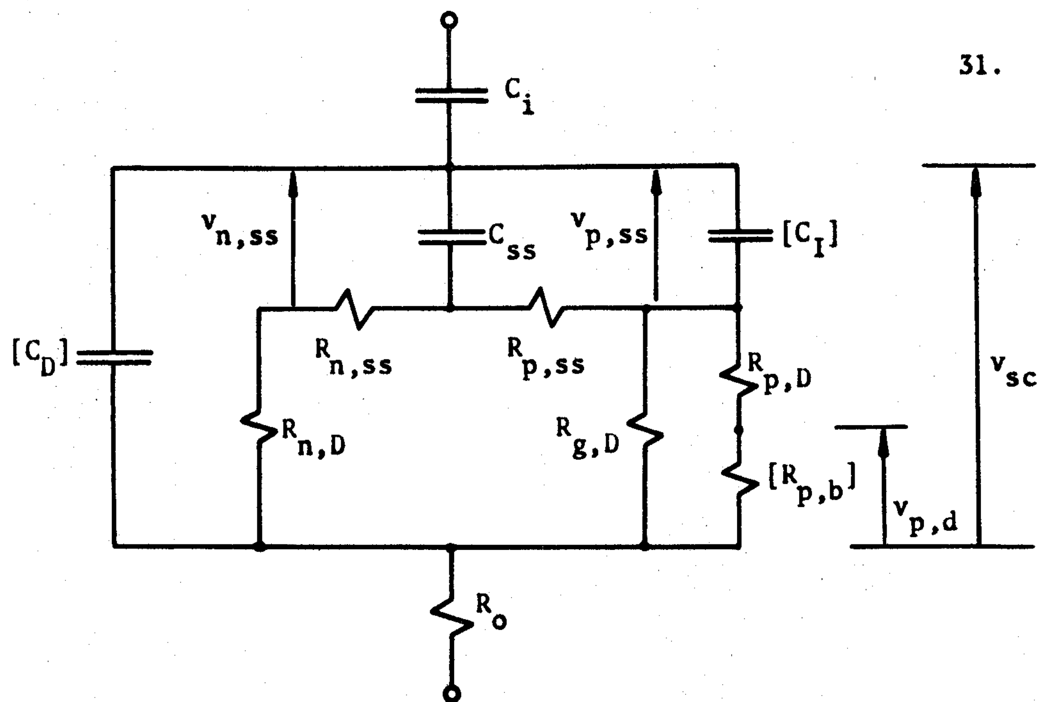

Figure 2.7 The Small Signal ac Equivalent Circuit for the MIS-Capacitor in the Depletion-Inversion Regime of Operation.

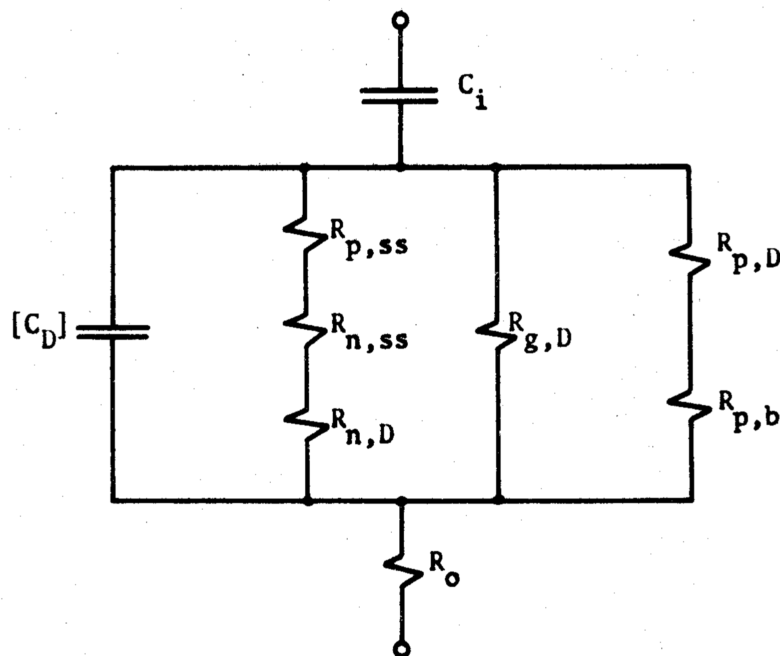

Figure 2.8 Equivalent Circuit for the MIS-Capacitor in Heavy Inversion.

(ii) Strong Inversion

If the surface potential of the semiconductor is such that $\psi_s < 2\psi_b$, it is said to be strongly inverted. Under these circumstances $C_I >> C_{ss}$ and the equivalent circuit simplifies[30] to the one shown in Figure 2.8.

(iii) Accumulation

If $\psi_s > 0$, there is an accumulation of majority carriers in a space-charge layer adjacent to the semiconductor-insulator interface. Since no inversion layer exists for this mode, the inversion capacitance is zero. Charge is stored in the surface states as before, and in the accumulation layer. The last mechanism of charge storage corresponds to a "capacitor" [C_A].

The equivalent circuit valid for accumulation is shown in Figure 2.9.

$R_{n,A}$ accounts for the flow of electrons through the accumulation space charge layer. In the accumulation regime the charge transport in response to the ac signal is a flow of majority carriers. The time constant for this process is the dielectric relaxation time $\tau = \frac{\varepsilon_s}{\sigma_b} << 1$. For this reason, $R_{n,A} << R_o$ and most of the losses will be due to the surface states and the ohmic contact to the semiconductor.

The resistor $R_{p,A}$ accounts for the flow of holes through the accumulation layer. It may be shown that[29]

$$R_{p,A} = \int_o^d \rho_p dx \doteq \frac{\bar{Q}_A}{n_i^2 q^2 \mu_p} \qquad (2.41)$$

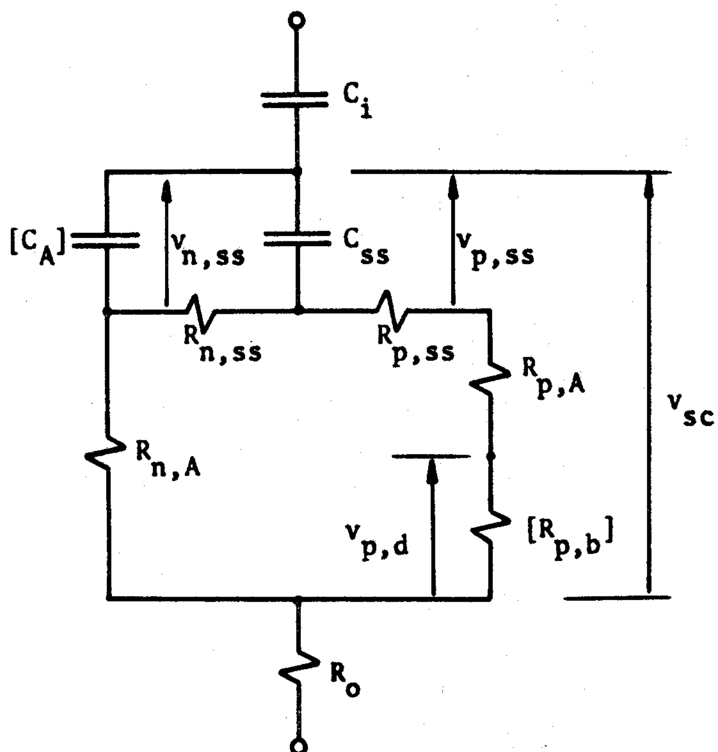

Figure 2.9 Equivalent Circuit of the MIS Capacitor in Accumulation.

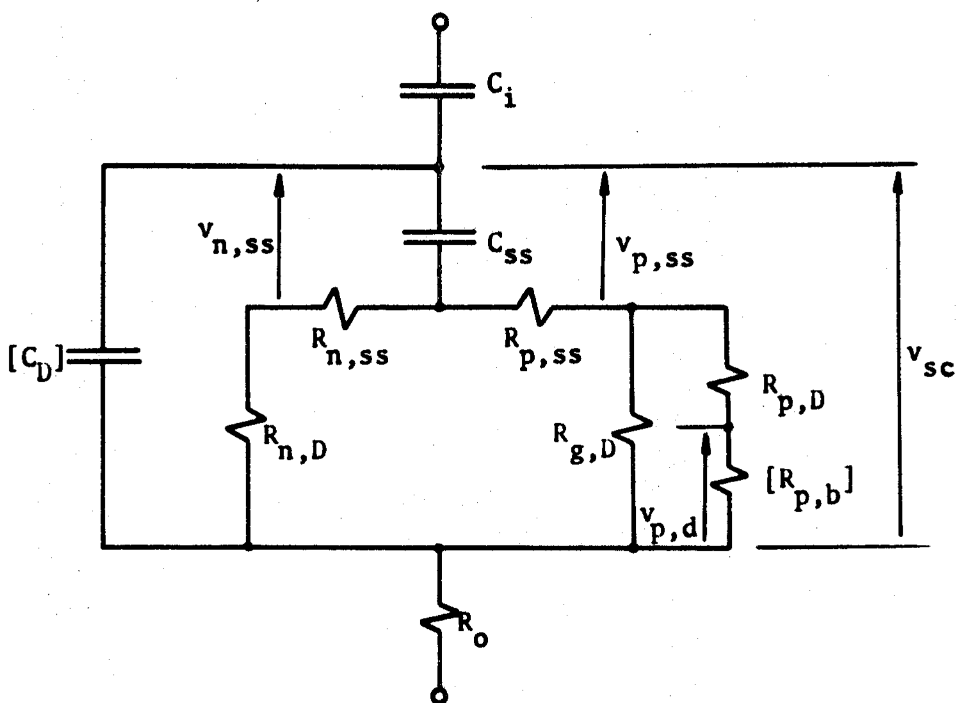

Figure 2.10 Small Signal ac Equivalent Circuit of the MIS Capacitor in Depletion.

where $\bar{Q}_A$ = dc charge in the electron accumulation layer.

(iv) Depletion

If the dc bias is such that $\psi_b < \psi_s < 0$, the majority carrier density in a region close to the S-I interface is less than in the bulk of the semiconductor. In addition, the surface potential is not large enough to allow the creation of an inversion layer. Under these circumstances, the equivalent circuit shown in Figure 2.10 applies.

(v) Time Constant Dispersion

Thus far we have assumed that the impedance due to the interface states may be represented by a simple lumped RC-circuit. This may not be the case in practice due to two effects, namely a distribution of interface states in the bandgap of the semiconductor and local fluctuations in the surface potential along the interface. Because of the fact that both $R_{n,ss}$ and $R_{p,ss}$ depend exponentially on the surface potential, the last mentioned effect may be very important under certain circumstances.

(va) A Continuum of Interface States

It was found experimentally[18,19] that a continuum of interface states exists in the Si-SiO_2 system. It is not unreasonable to expect a similar state of affairs in other insulator-semiconductor systems. A single level of traps in the insulator for instance, will look like a distribution of interface states[13].

The admittance due to the continuum of interface states may be obtained by integrating the expression for Y_{ss} as it pertains to a single interface state level[32]. This is due to the fact that the capture and emission of carriers can occur by states located within a few kT of the Fermi level.

$$Y_{ss} = \int \frac{j\omega q^2}{kT} \cdot \frac{N_{ss}(E)\bar{f}(1-\bar{f})}{1 + \frac{j\omega \bar{f}}{c_n \bar{n}_s}} \, dE \qquad (2.42)$$

where N_{ss} = density of interface states, cm^{-2}-eV^{-1}

E = energy in electron volt.

If one assumes that the density of interface states N_{ss} and the electron capture rate does not vary rapidly with energy, equation (2.42) may be evaluated analytically.

$$Y_{ss} = \frac{qN_{ss}}{2\tau_{n,ss}} \ln(1 + \omega^2 \tau_{n,ss}^2) + j\frac{qN_{ss}}{\tau_{n,ss}} \cdot \tan^{-1}(\omega\tau_{n,ss}) \qquad (2.43)$$

where $\tau_{n,ss} = \frac{1}{c_n \bar{n}_s}$. The distributed RC-network shown in Figure 2.11 applies in the case.

(vb) Random Fluctuations in Surface Potential

An additional dispersion occurs due to random fluctuations in the surface potential as a result of random fluctuations in the surface state density, the insulator thickness and fixed charges in the insulator. Nicollian and Goetzberger[18] found that by assuming a characteristic area A_c over which the surface potential is constant, and by assuming a Poisson distribution for the probability that there are N build-in

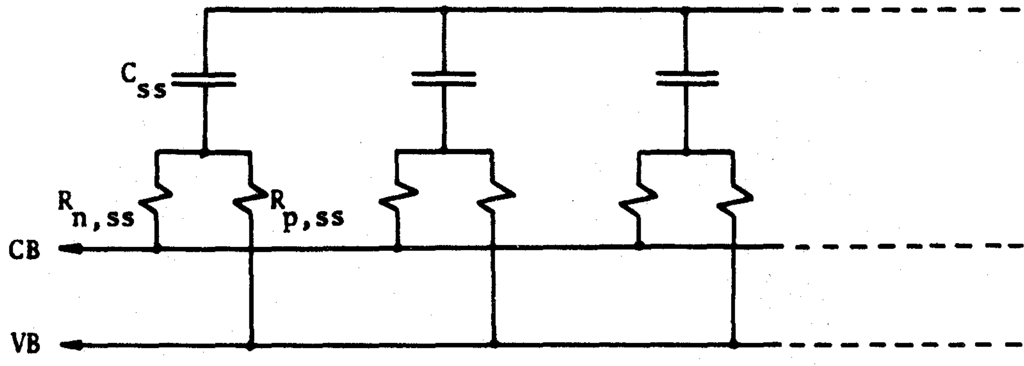

Figure 2.11 Equivalent Circuit Applicable to a Continuum of Interface States.

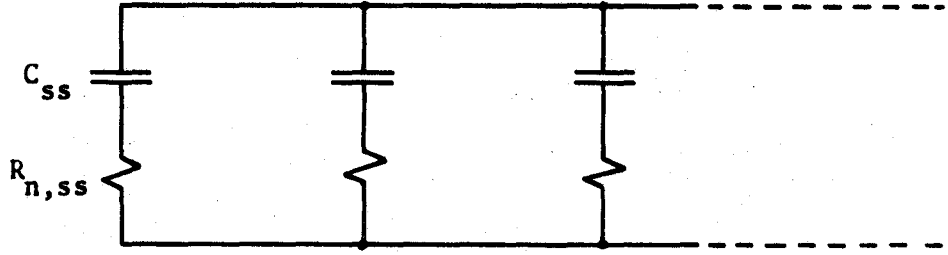

Figure 2.12 Equivalent Circuit for a Continuum of Interface States with the Surface in Depletion-Accumulation.

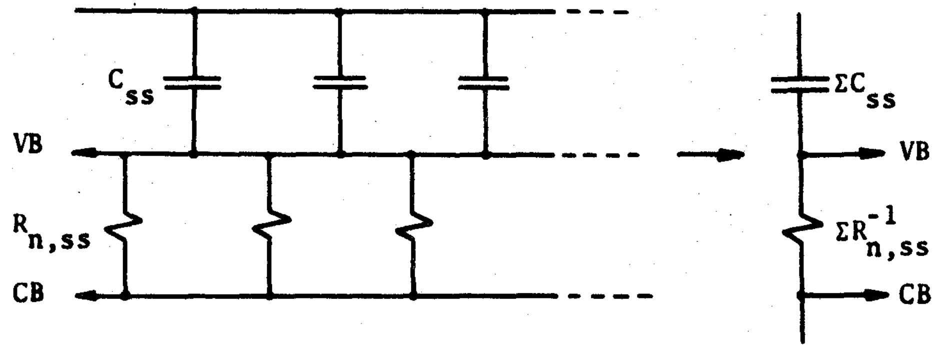

Figure 2.13 Surface State Equivalent Circuit if the Surface is in Weak Inversion.

charges and charged interface states in A_c, they could account for the experimental results.

They obtained the following expressions for the parallel conductance G_p and capacitance C_p due to the interface states:

$$G_p = \frac{\omega q N_{ss}}{2} \{2\Pi(\sigma_s^2+\sigma_b^2)\}^{-\frac{1}{2}} \int_{-\infty}^{\infty} e^{-(z+y)} \ell n(1+e^{2y}) d(\frac{q\psi_s}{kT}) \quad (2.44)$$

$$C_p = qN_{ss} \{2\Pi(\sigma_s^2+\sigma_b^2)\}^{-\frac{1}{2}} \int_{-\infty}^{\infty} e^{-(z+y)} \tan^{-1}(e^y) d(\frac{q\psi_s}{kT}) + C_{sc}(\bar{\psi}_s) \quad (2.45)$$

where

$$\sigma_s = \frac{qW}{kT(WC_i+\varepsilon_s)} \left(\frac{q\bar{Q}}{A_c} \right)^{\frac{1}{2}} \quad (2.46)$$

and

$$\sigma_b = \frac{q^2(\bar{N}_d W)^{\frac{1}{2}}\{1-e^{\frac{-q\bar{\psi}_s}{kT}}\}}{2kT\{WC_i+\varepsilon_s\}} \quad (2.47)$$

$$y = \ell n\left(\frac{\omega}{\bar{v}\sigma_n n_i} \right) - \frac{q(\psi_s-\psi_b)}{kT} \quad (2.48)$$

$$z = \frac{q^2(\psi_s-\bar{\psi}_s)^2}{2k^2T^2(\sigma_s^2+\sigma_b^2)} \quad (2.49)$$

$\bar{N}_d$ = mean ionized donor density

$\bar{Q}$ = mean density of surface charges

$\bar{\psi}_s$ = mean surface potential

W = depletion layer width at the potential ψ_s

A_c = characteristic area.

For accumulation and depletion, $R_{p,ss} >> R_{n,ss}$ and the equivalent circuit may be simplified to the one shown in Figure 2.12.

For weak inversion, $R_{p,ss} << R_{n,ss}$. If the frequency is comparable to $1/\tau_{n,ss}$, there will be no loss associated with $R_{p,ss}$ and it may be put equal to zero. From the equivalent circuit it is clear that the interface state circuit is now characterized by a single time constant at each bias. This has been verified experimentally by Nicollian and Goetzberger[18]. The circuit is shown schematically in Figure 2.13.

(vi) Additional Loss Mechanisms Pertaining to Evaporated Thin-Film MIS-Devices

Nicollian and Goetzberger[18] found experimentally that for steam-grown SiO_2 on single crystal Si the losses introduced by the capture and emission of carriers by interface states are far more important than the losses introduced by traps in the Si space charge layer[31]. Evaporated thin CdS films have a polycrystalline structure with the average size of the crystallites of the order of the thickness of the film, i.e., a few hundred to a few thousand Å. Many traps exist due to the grain boundaries between the crystallites and due to the imperfections in the crystallites themselves. Therefore, it may not be justifiable to assume that the losses introduced by these bulk states are negligible.

Since the nature of these states are unknown and since it is to be expected that their density will depend strongly on the exact conditions during the deposition of the film, their characterization

will be quite difficult in general.

It may therefore be concluded that the equivalent circuit for the MIS-capacitor is quite complicated and calculation of all the components may be impossible for evaporated thin-film devices. Fortunately, it turned out that at the frequencies where the tunable filters were used for this work, the real part of the MIS-impedance stayed very nearly constant. It is suspected that the ohmic contact at the back of the semiconductor is responsible for the introduction of this resistor. At lower frequencies the real part is increasing and that is probably due to the interface and bulk states.

For all practical purposes, the MIS-devices used in this thesis may therefore be considered to have a constant resistor in series with it. One experimental curve of the real part of the MIS-impedance versus frequency is shown in Figure 2.14.

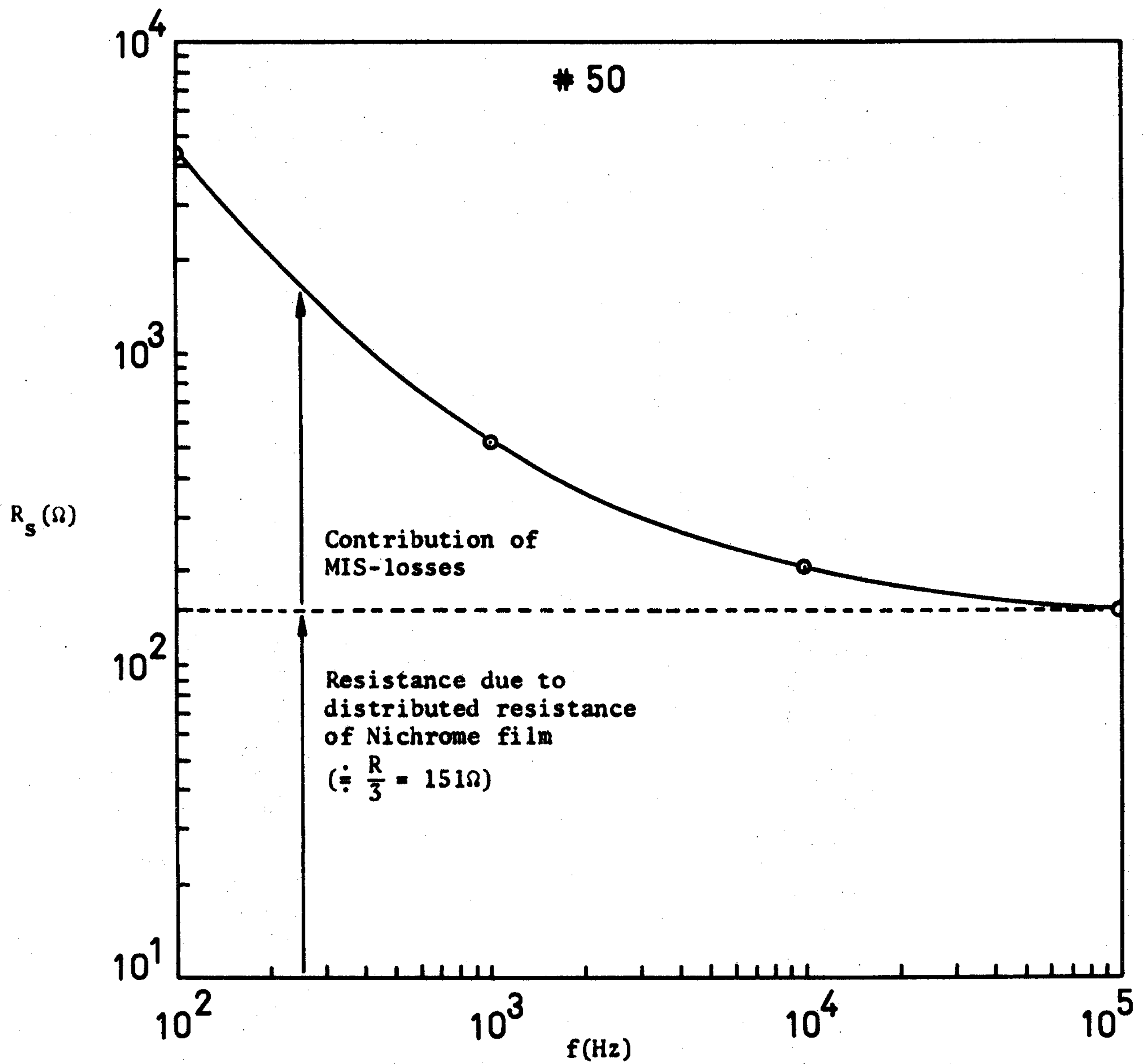

Figure 2.14 Real Part of the Impedance of a Nichrome-Y_2O_3-CdS MIS Capacitor.
$t_i \doteq 4500$ Å.

CHAPTER 3

Theory of the Uniformly Distributed RC(URC) Thin-Film Filter

3.1 General

In order to understand the operation of the thin-film tunable filter, it will be necessary first of all to discuss the uniformly distributed circuit in some detail. No attention will be paid to the exponentially tapered structure, even though it has more desirable properties in many instances. It is felt that the URC-network may serve as the basic building block for many applications. By cascading them in some optimum fashion, characteristics even superior to a single ERC-section may be possible.

First of all, we will discuss the ideal URC filter. Further on the effects of dielectric loss and parasitic inductance will be introduced because of their importance in determining the tuning characteristics of the tunable URC-filter.

The notch filter and high Q bandpass filter will be discussed as possible applications of the simple URC-structure.

3.2 The Uniformly Distributed RC Low-Pass Filter (URC)

3.2.1 The Ideal URC Low-Pass Filter

The URC-filter consists of a highly conducting layer, a dielectric layer and a resistive layer as shown in Figure 3.1. Usually one needs fairly thin dielectric and resistive layers in order to restrict the physical size to reasonable dimensions. Typical figures may be as follows:

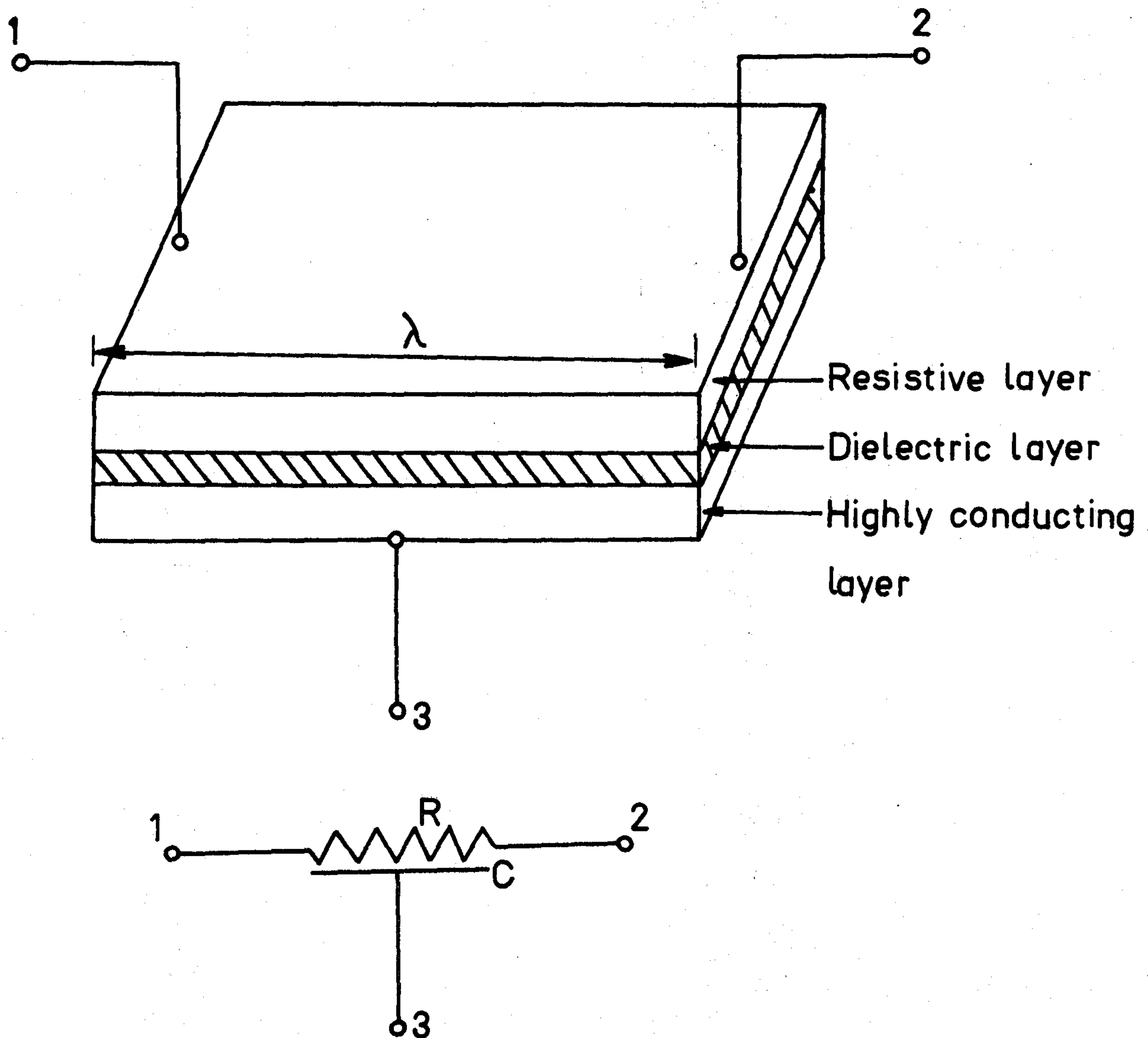

Figure 3.1 Physical Structure and Circuit Symbol of a URC-Network. (Not to Scale.)

3000Å for the dielectric layer

100-200Å for the resistive layer

2000Å for the conducting layer.

The dimensions of the active area may be a few millimeters to a side.

It is obvious from the figures given above that thin-film technology is particularly well suited to making these distributed filters.

Assume the conducting layer has zero resistance and the dielectric layer is lossless. Let r_o and c_o designate the resistance and capacitance per unit length respectively.

An incremental equivalent circuit is shown schematically in Figure 3.2.

Setting up Kirchhoff's voltage and current equations, one obtains:

$$v(t,z) = r_o \cdot \Delta z \cdot i(t,z+\Delta z) + v(t,z+\Delta z) \tag{3.1}$$

$$i(t,z+\Delta z) - i(t,z) = -c_o \cdot \Delta z \cdot \frac{\partial v(t,z)}{\partial t} . \tag{3.2}$$

By allowing $\Delta z \to 0$, and by taking the Laplace transformation on both sides of equation (3.1) and (3.2) one obtains:

$$\frac{dV(s,z)}{dz} = -r_o \cdot I(s,z) \tag{3.3}$$

$$\frac{dI(s,z)}{dz} = -sc_o V(s,z) \tag{3.4}$$

We have assumed the initial conditions to be zero.

Differentiating equation (3.3) and substituting for $\frac{dI(s,z)}{dz}$ from equation (3.4), the following second order differential equation

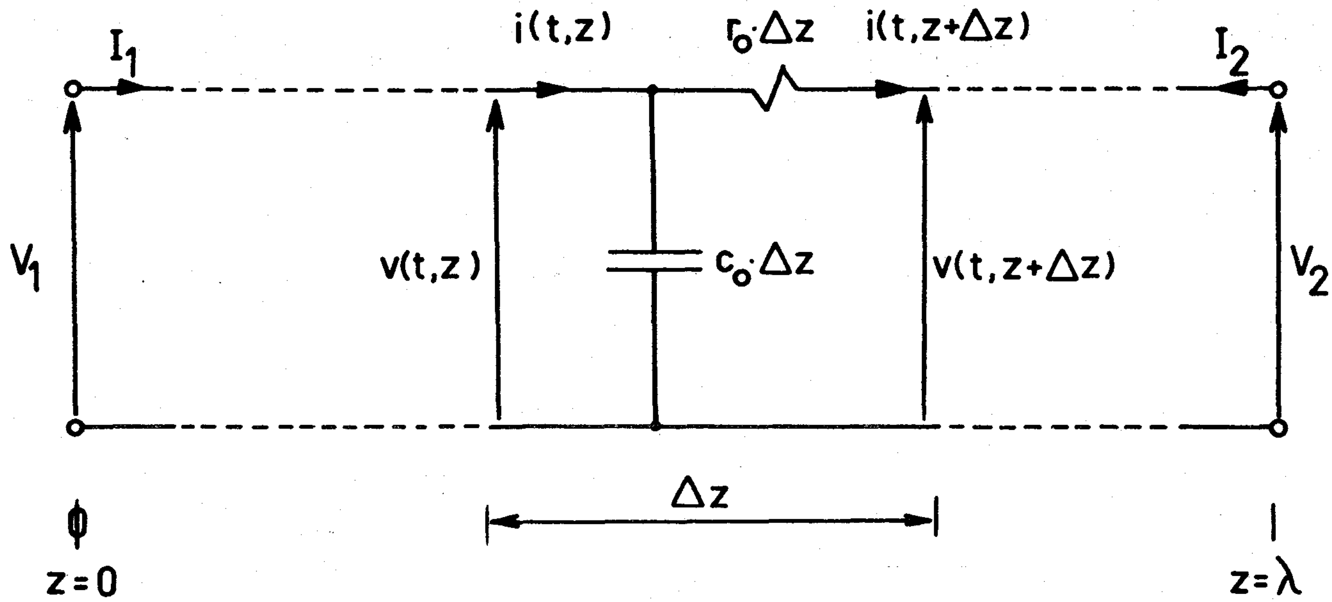

Figure 3.2 Incremental Model of the URC-network

is obtained:

$$\frac{d^2V(s,z)}{dz^2} - sc_o r_o V(s,z) = 0 \quad . \tag{3.5}$$

This differential equation may be solved quite readily:

$$V(s,z) = Ae^{\S z} + Be^{-\S z} \tag{3.6}$$

where

$$\S = \sqrt{sr_o c_o} \quad .$$

An expression for I(s,z) may be obtained from (3.4).

By using the boundary conditions

$$\begin{aligned} V(s,o) &= V_1 \\ V(s,\lambda) &= V_2 \\ I(s,o) &= I_1 \\ I(s,\lambda) &= -I_2 \end{aligned} \tag{3.7}$$

the y-parameters turn out to be:

$$y_{11} = y_{22} = \frac{1}{Z_o} \cdot \coth\gamma \tag{3.8}$$

$$y_{12} = y_{21} = -\frac{1}{Z_o} \cdot \text{cosech}\gamma \tag{3.9}$$

where

$$\gamma = \S\lambda = \sqrt{sc_o r_o \lambda^2} = \sqrt{sRC} \tag{3.10}$$

$$Z_o = \sqrt{\frac{r_o}{sc_o}} = R\sqrt{\frac{1}{sRC}}$$

λ = total length of the structure

$R = r_o\lambda$ = total series resistance

$C = c_o\lambda$ = total capacitance.

The z-parameters may be obtained from the y-parameters by standard means.

$$z_{11} = z_{22} = Z_o \cdot \coth\gamma$$
$$z_{12} = z_{21} = Z_o \cdot \operatorname{cosech}\gamma \tag{3.11}$$

The open-circuit voltage transfer function follows immediately:

$$T = \left.\frac{V_2}{V_1}\right|_{I_2=0} = \frac{1}{\cosh\gamma} \quad . \tag{3.12}$$

By using the product expansion of the hyperbolic cosine function, namely

$$\cosh\gamma = \prod_{n=1}^{\infty} \left\{1 + \frac{4\gamma^2}{(2n-1)^2\Pi^2}\right\}$$

the poles of T may be located.

It may be seen that $1/\cosh\gamma$ is an all-pole function with the poles located on the negative real axis of the s-plane at

$$s = \frac{-(2n-1)^2 \cdot \Pi^2 \omega_o}{4} \qquad n = 1,2,3,\ldots \tag{3.13}$$

where

$$\omega_o = \frac{1}{RC} \quad .$$

Because of the nature of the poles of the transfer function, $|T|$ has an exponential cut-off as a function of frequency.

$$T = \frac{1}{\cosh\gamma} = \frac{1}{\cosh\sqrt{j\omega RC}} = \frac{1}{\cosh\sqrt{jx}}$$

where $x = \omega RC$ = normalized frequency.

$$\text{If } x >> 1, \ \cosh\sqrt{jx} \doteq \frac{e^{\sqrt{jx}}}{2}$$

$$\therefore \qquad T \doteq \frac{2}{e^{\sqrt{jx}}} = 2e^{-\sqrt{jx}} = 2e^{-\sqrt{\frac{x}{2}}} \cdot e^{-j\cdot\sqrt{\frac{x}{2}}} \tag{3.14a}$$

$$\therefore \qquad |T| \doteq 2e^{-\sqrt{\frac{x}{2}}}$$

$$|T| \doteq (6.02 - 6.142\sqrt{x}) \text{ dB.} \tag{3.14b}$$

A plot of $|T|$ (dB) versus $\sqrt{x}$ will therefore approach a straight line for large x.

The magnitude and phase of the URC low-pass filter is compared with the magnitude and phase of first and second order Butterworth filters in Figures 3.3 and 3.4 respectively. The expressions for the Butterworth filters have been normalized so that their 3dB points correspond to the 3dB point of the URC filter which occurs at $x = 2.44$, i.e., $\sqrt{x} = 1.562$. It may be seen from Figure 3.3 that the URC-filter behaves like a first order Butterworth filter for $\sqrt{x} < 2$. Beyond $\sqrt{x}<2$, the transfer function has an exponential cut-off.

Equation (3.14a) also predicts the exponential increase in the phase angle as is shown in Figure 3.4.

3.2.2 The URC Low-Pass Filter in the Presence of Dielectric Loss

It is inevitable that some losses will occur in the dielectric layer between the resistive and conductive layer of the thin-film URC filter. Carson[33], et al., analyzed the effect of dielectric losses on the two-port parameters and the voltage transfer function of the URC-filter. It was found sufficient to introduce an incremental conductance

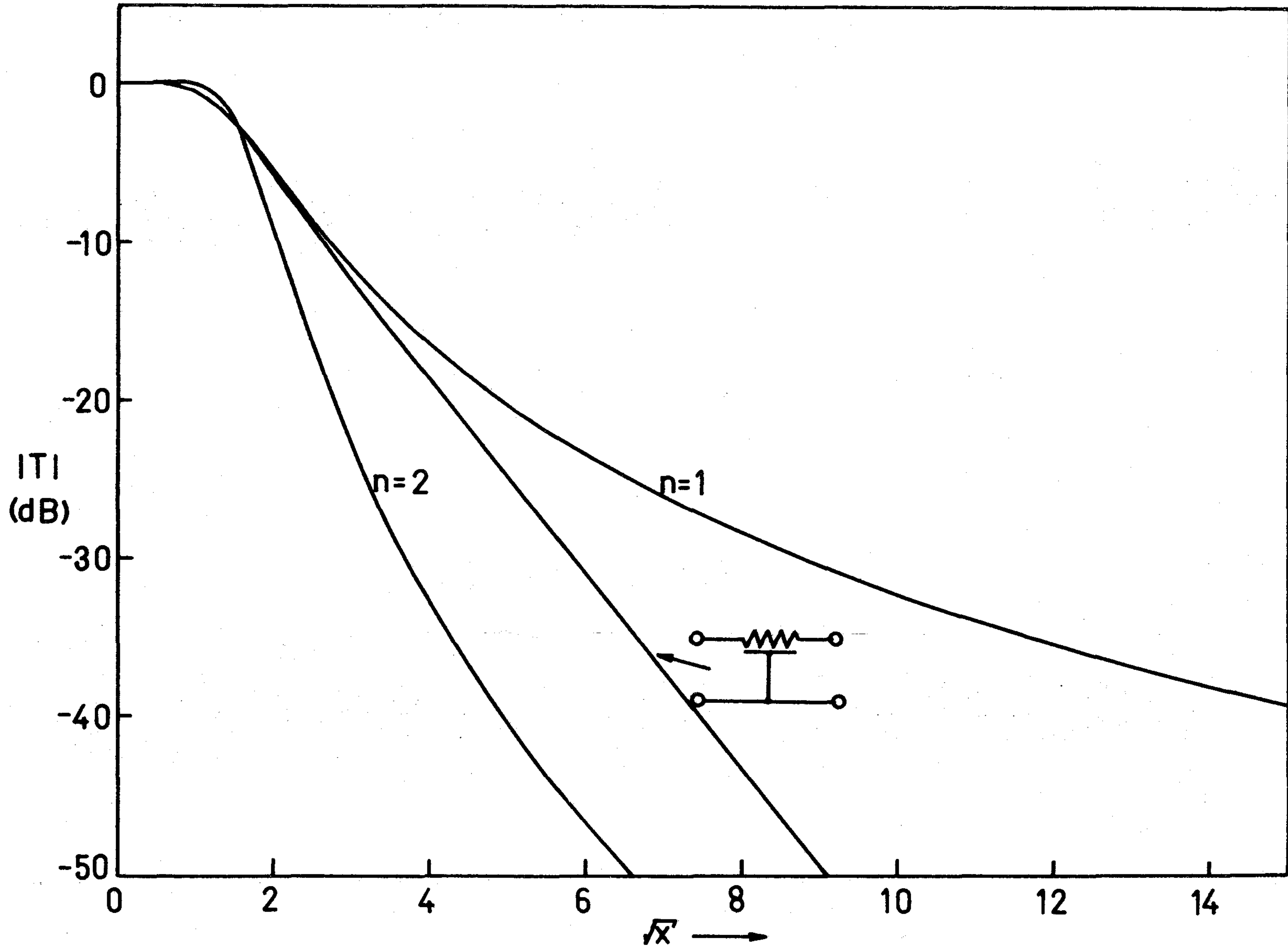

Figure 3.3 A Comparison Between the URC Low-Pass Filter Response and the First and Second Order Butterworth Filters

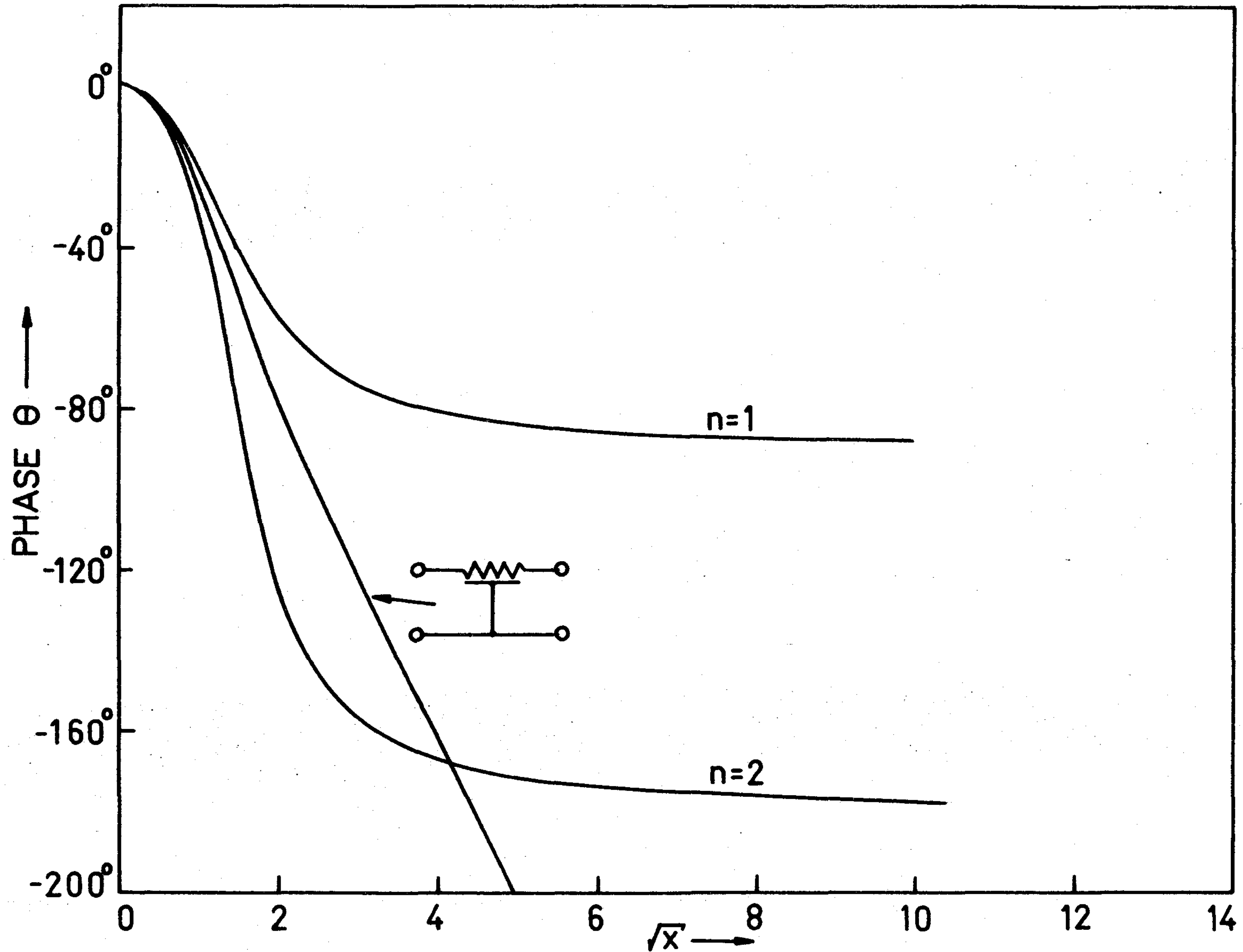

Figure 3.4 A Comparison Between the Phase Response of the URC Low-Pass Filter and the First and Second Order Butterworth Filters

$g_s(\omega)\cdot\Delta z$ in series with the incremental capacitance of Figure 3.2. This is shown schematically in Figure 3.5.

Following exactly the same procedure as in the case of the lossless structure, the voltage and the current equations may be written down:

$$
\begin{aligned}
v(t,z) &= r_o\cdot\Delta z\cdot i(t,z+\Delta z) + v(t,z+\Delta z) \\
i(t,z+\Delta z) - i(t,z) &= -c_o\cdot\Delta z\cdot\frac{\partial v_1(t,z)}{\partial t} \qquad (3.15) \\
v_1(t,z) &= v(t,z) + \frac{i(t,z+\Delta z) - i(t,z)}{g_s\cdot\Delta z}
\end{aligned}
$$

By allowing $\Delta z\to 0$, and by taking the Laplace transformation with initial conditions equal to zero, one obtains:

$$\frac{dV(s,z)}{dz} = -r_o I(s,z) \qquad (3.16)$$

$$\frac{dI(s,z)}{dz} = -sc_o\left\{V(s,z)+\frac{1}{g_s(s)}\cdot\frac{dI(s,z)}{dz}\right\} = \frac{-sc_o\cdot V(s,z)}{1+sc_o/g_s(s)} \quad . \qquad (3.17)$$

Differentiating (3.16) and substituting (3.17) into the result, the following second order differential equation is obtained:

$$\frac{d^2V(s,z)}{dz^2} - \frac{sc_o r_o}{1+sc_o/g_s(s)}\cdot V(s,z) = 0 \quad . \qquad (3.18)$$

A comparison between (3.18) and (3.5) reveals that the differential equations are analogous, except that sr_oc_o has changed to $\dfrac{sr_oc_o}{1+sc_o/g_s(s)}$.

Since the boundary conditions are the same as those given in equation (3.7), the y-parameters, z-parameters and open circuit voltage transfer function may be written down immediately:

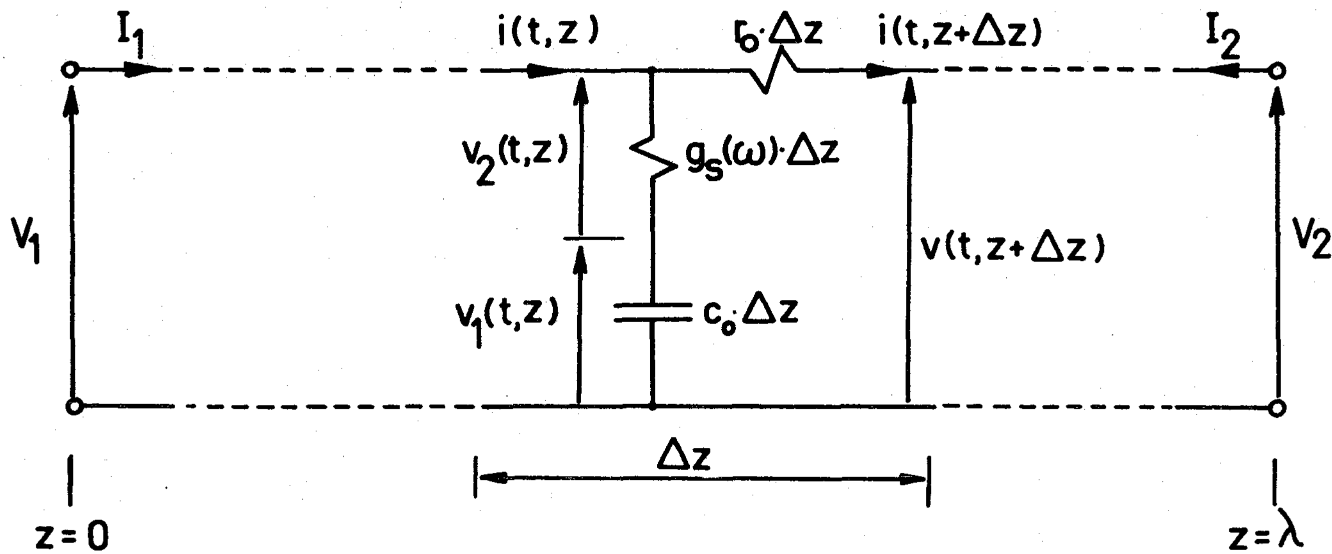

Figure 3.5 Incremental Model of the URC-network taking Dielectric Dissipation into Consideration

$$y_{11} = y_{22} = \frac{1}{Z_o} \cdot \coth\gamma$$

$$y_{12} = y_{21} = \frac{-1}{Z_o} \cdot \text{cosech}\gamma \qquad (3.19)$$

$$z_{11} = z_{22} = Z_o \cdot \coth\gamma$$

$$z_{12} = z_{21} = Z_o \cdot \text{cosech}\gamma \qquad (3.20)$$

$$T = \left.\frac{V_2}{V_1}\right|_{I_2=0} = \frac{1}{\cosh\gamma} \qquad (3.21)$$

where $$\gamma = \sqrt{\frac{sr_oc_o\lambda^2}{1+sc_o/g_s(s)}} = \sqrt{\frac{sRC}{1 + sRCB(s)}} \qquad (3.22)$$

$$B(\omega) = \frac{1}{RG_s(\omega)} \qquad (3.23)$$

$$G_s(\omega) = \int_o^{\lambda} g_s(\omega)\cdot dz = g_s(\omega)\cdot\lambda \qquad (3.24)$$

$$R = r_o\lambda$$

$$C = c_o\lambda$$

$$Z_o = R\sqrt{\frac{1 + sCRB(s)}{sCR}} \qquad (3.25)$$

λ = length of the structure.

The influence of the dielectric loss will be investigated in its influence on the URC-notch filter.

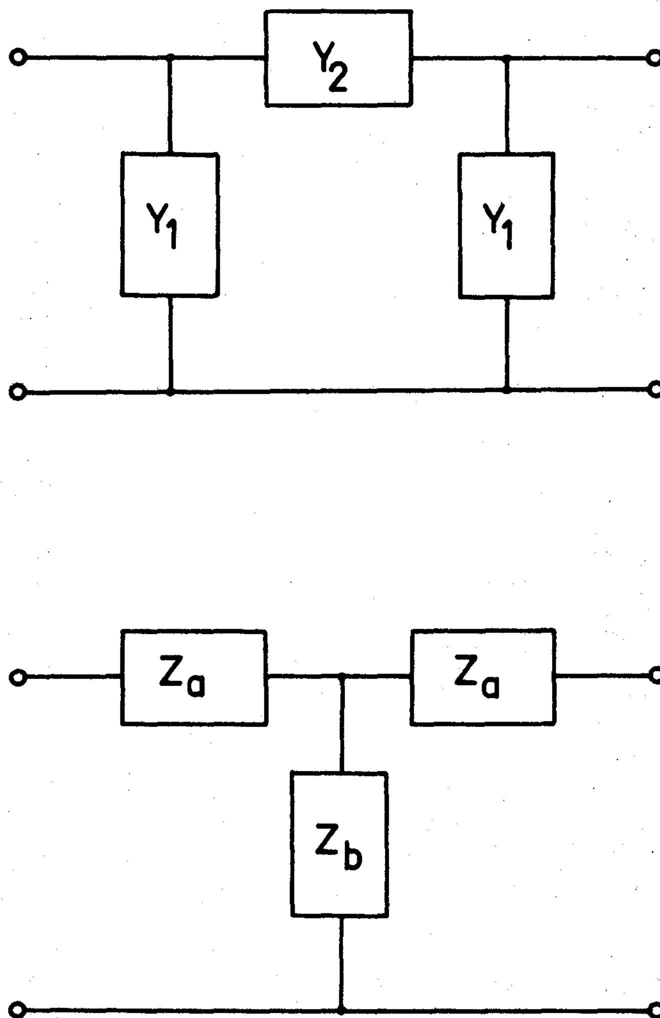

Figure 3.6 The Π- and T-Equivalent Circuits of the URC Low-Pass Filter.

$$Y_2 = -y_{12} = \frac{\sqrt{jx}}{R\sinh\sqrt{jx}}$$

and

$$Z_b = z_{12} = \frac{R}{\sqrt{jx}\cdot\sinh\sqrt{jx}}$$

where $x = \omega RC$.

3.3 The URC Notch Filter

3.3.1 The Ideal URC Notch Filter

Although the open circuit voltage transfer function of the URC low-pass filter is a meromorphic function, it is possible to get zeros on the $j\omega$-axis[35]. This may be achieved by a suitable choice of lumped, passive elements to be used in conjunction with the URC-network.

The type of immittance to be used, may be obtained quite readily if we consider the T- and Π-equivalent circuits of the URC low-pass filter[34].

A zero of transmission will occur when either an admittance $Y_p = -Y_2$ is placed in parallel with Y_2 or an impedance $Z_s = -Z_b$ in series with Z_b.

The nature of these immittances may be obtained by plotting the phase angle of Z_b and Y_2 as indicated in Figure 3.7. The expressions for Y_2 and Z_b follow from Figure 3.6.

$$Y_2 = -y_{12} = \frac{\sqrt{jx}}{R \cdot \sinh\sqrt{jx}} \tag{3.26}$$

and

$$Z_b = z_{12} = \frac{R}{\sqrt{jx} \cdot \sinh\sqrt{jx}} \tag{3.27}$$

where $x = \omega RC$.

If we restrict outselves to positive resistors, capacitors and inductors, the phase angle of Y_2 and Z_b should correspond to negative resistors, capacitors and inductors. It may be seen from Figure 3.7 that the phase angle θ of Z_b lies between -90° and -180° for $0<x<11.19$. This corresponds to a negative resistor in series with a negative inductor. The impedance Z_s is therefore a positive resistor in series

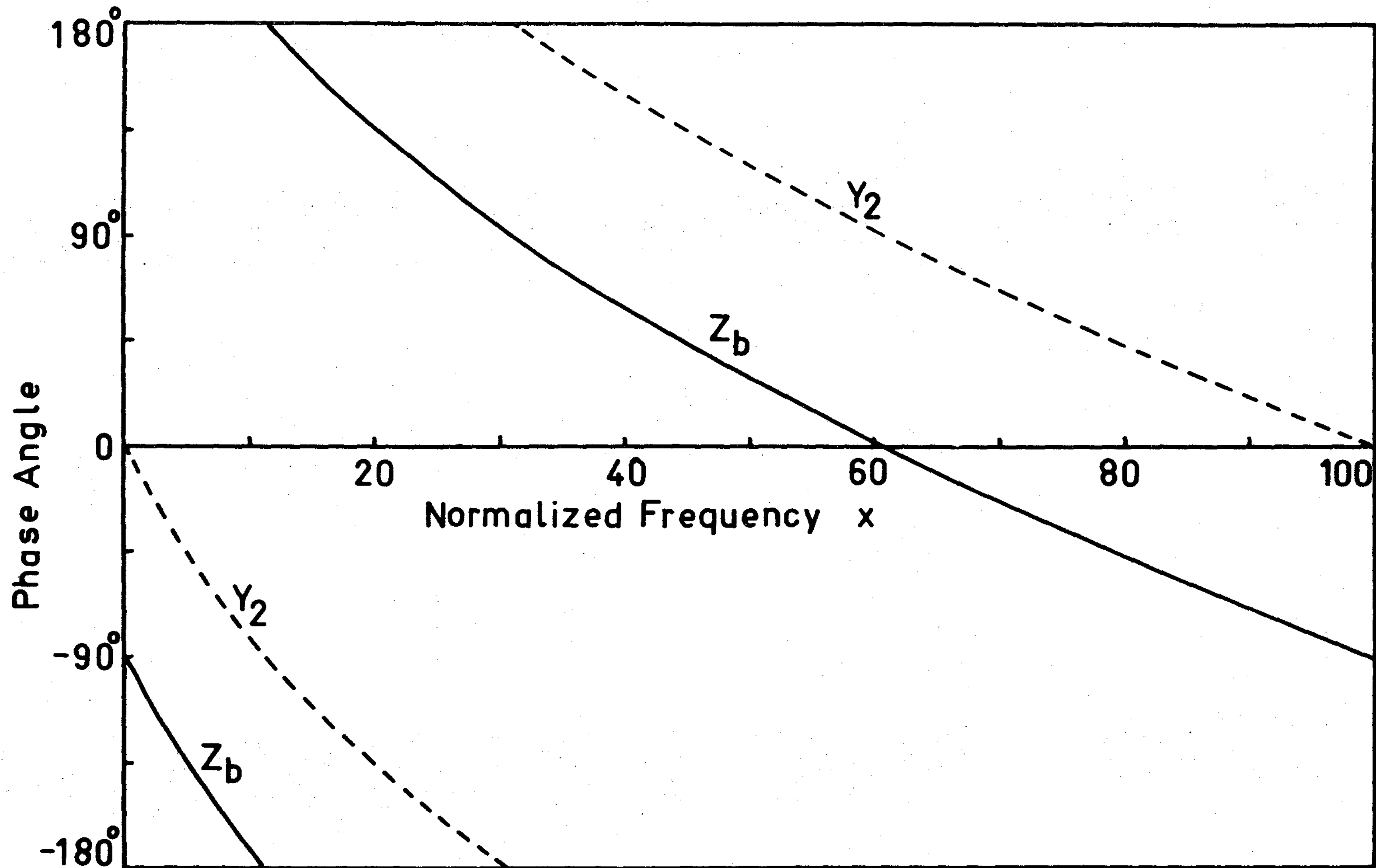

Figure 3.7 Phase Angle of Y_2 and Z_b as a Function of Normalized Frequency. (After J. Stein, Ref. 34)

with a positive inductor. The results are summarized[34] in Table 3.1:

Table 3.1

(After Ref. 34)

x (=ωRC)	Z_s	Y_p
0<x<11.19	R,L	-G,C
11.19	R	C
11.19<x<30.84	R,C	G,C
30.84	C	G
30.84<x<60.45	-R,C	G,L
60.45	-R	L
60.45<x<99.93	-R,L	-G,L
99.93	L	-G

For x>99.93, the whole pattern repeats itself.

There seems to be an endless number of combinations of (URC)-(lumped, passive elements) that will give a null on the jω-axis. We have chosen the lumped resistor in series with the T for the rest of the work that will follow. This configuration has been chosen because of the ease of realizing lumped resistors in thin-film form. Trimming of the resistors to very accurate values is also achieved quite readily as opposed to trimming of capacitors.

Consider this particular type of notch filter as depicted in Figure 3.8. The open circuit voltage transfer function of this filter may be determined by noticing that the two circuits are connected series-series. Therefore, the corresponding parameters may simply be

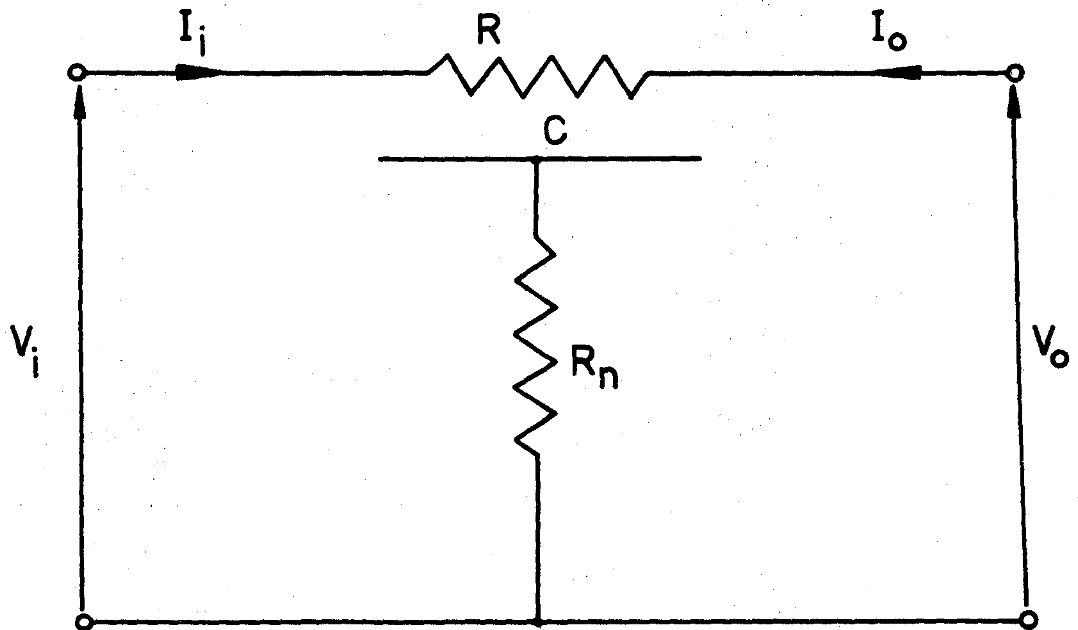

Figure 3.8 The URC-Notch Filter

added to obtain the z-parameters of the total circuit. It follows from equation (3.11) that

$$z_{11} = z_{22} = \frac{R}{\gamma} \cdot \coth\gamma + Z_n \tag{3.28}$$

$$Z_{12} = z_{21} = \frac{R}{\gamma} \cdot \mathrm{cosech}\gamma + Z_n \tag{3.29}$$

where $Z_n = R_n$. The open circuit voltage transfer function is then given by

$$T = \left.\frac{V_o}{V_i}\right|_{I_2=0} = \frac{z_{21}}{z_{11}} = \frac{\alpha + \gamma\cdot\sinh\gamma}{\alpha\cdot\cosh\gamma + \gamma\cdot\sinh\gamma} \tag{3.30}$$

where $\alpha = \frac{R}{R_n}$ = notch parameter, and

$$\gamma = \sqrt{j\omega RC} = \sqrt{jx} \quad . \tag{3.31}$$

The transfer function will have a zero of transmission if the numerator of T is equal to zero:

$$\alpha + \gamma\cdot\sinh\gamma = 0 \tag{3.32}$$

$$\alpha + \sqrt{jx} \cdot \sinh\sqrt{jx} = 0 \quad . \tag{3.33}$$

To get the approximate solution to this transcendental equation, let us assume $x \gg 1$. Then

$$\sinh\sqrt{jx} \doteq \frac{e^{\sqrt{jx}}}{2} = \frac{e^{(1+j)y}}{2} \tag{3.34}$$

where $y = \sqrt{\frac{x}{2}}$.

Substituting (3.34) into (3.33) and simplifying, one obtains:

$$2\alpha + (1+j)ye^{(1+j)y} = 0 \quad .$$

Equating the real and imaginary parts of this expression individually to zero, one obtains:

$$2\alpha + ye^{y} \cdot \cos y - ye^{y} \cdot \sin y = 0 \tag{3.35}$$

$$ye^{y} \cdot \cos y + ye^{y} \cdot \sin y = 0 \tag{3.36}$$

$$\therefore \quad \cos y = -\sin y \ . \tag{3.37}$$

Substituting (3.37) into (3.35), α is obtained as:

$$\alpha = ye^{y} \cdot \sin y \ . \tag{3.38}$$

Because of the periodicity of the trigonometric functions, (3.37) has an infinite set of solutions which is denoted by $\{y_n\}$.

$$\{y_n\} = (n\Pi - \frac{\Pi}{4}); \qquad n = 1,2,\ldots,\infty \tag{3.39}$$

and

$$\alpha_n = y_n \cdot e^{y_n} \cdot \sin y_n \ .$$

For n=1: $y_1 = \sqrt{\frac{x}{2}} = 2.356$

$$\therefore \quad x_1 = 2y_1^2 = 11.10$$

and

$$\alpha_1 = 17.58 \ .$$

Following the same procedure for the exact expression as given in equation (3.33), the following transcendental equation in x is obtained:

$$\tanh\sqrt{\frac{x}{2}} = -\tan\sqrt{\frac{x}{2}} \tag{3.40}$$

α is given by

$$\alpha = 2\sqrt{\frac{x}{2}} \cdot \sin\sqrt{\frac{x}{2}} \cdot \cosh\sqrt{\frac{x}{2}} \ . \tag{3.41}$$

(3.40) has an infinite set of solutions which is denoted by $\{x_n\}$. Only the values of x corresponding to n odd will be of importance, because α is negative for n even. We will only be interested in x_1, for α becomes too large, i.e., R_n too small, for n=3,5,7 etc. If one uses a resistive film with $R=250\Omega$, the first solution will require an R_n of approximately 14.056Ω. The third order solution will require an $R_n=7.24\times10^{-3}\Omega$. This, clearly, is impractical.

(3.40) may be solved by means of a computer and x_1 and α_1 turn out to be

$$x_1 = 11.1902$$
$$\alpha_1 = 17.786 \qquad (3.42)$$

Table 3.2

n	1	2	3	4	5
x_n	11.1902	60.451	149.278	277.583	445.366
α_n	17.786	-949.161	3.451×10^4	-1.0891×10^6	3.1924×10^7

The values obtained by the approximate method compare quite well with these.

The magnitude and phase of the voltage transfer function, equation (3.30), is plotted in Figure 3.9.

3.3.2 The Influence of Parasitic Inductance

The notch impedance in Figure 3.8 was taken to be purely resistive throughout the whole discussion of the notch filter. This

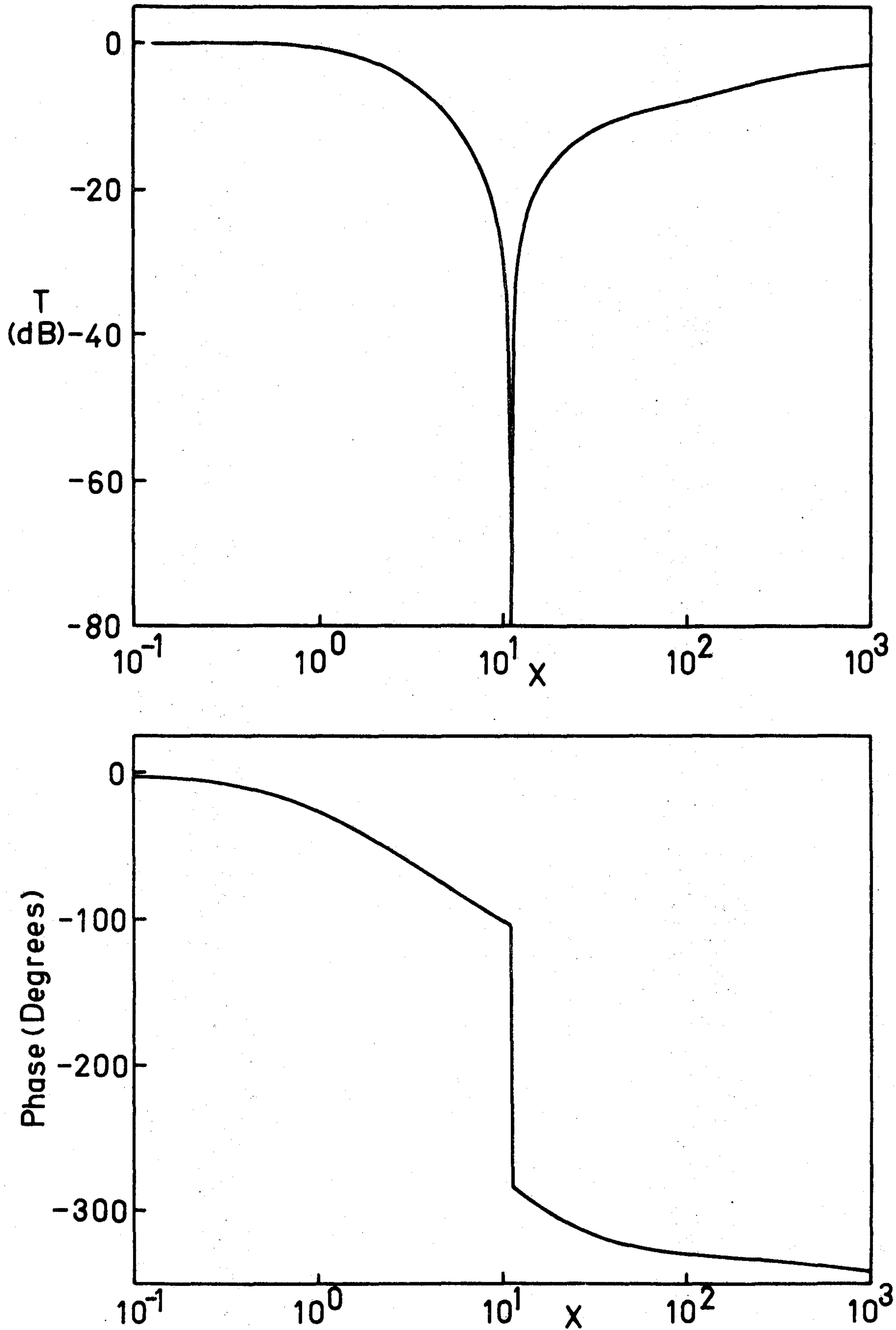

Figure 3.9 Theoretical Magnitude and Phase Response of the URC-Notch Filter

may not be the case in a practical situation because of the fact that even very short inter-connections may introduce some parasitic inductance. This may have quite an effect at high frequencies as will be indicated. It may be seen from Table 3.1 that a resistor-inductor combination will give an optimum notch, but the frequency where it occurs will be lower than that expected for a pure resistor alone. The value of the notch resistor R_n will also be different.

To be general, let us assume that the dielectric is lossy and that there is an inductance L_n in series with R_n.

It follows from equations (3.28) and (3.29) that

$$z_{11} = z_{22} = \frac{R}{\gamma} \cdot \coth\gamma + R_n + sL_n \tag{3.43}$$

and

$$z_{12} = z_{21} = \frac{R}{\gamma} \cdot \operatorname{cosech}\gamma + R_n + sL_n \tag{3.44}$$

where $s = \sigma + j\omega$. The open circuit voltage transfer function is given by

$$T = \left.\frac{V_o}{V_i}\right|_{I_2=0} = \frac{z_{21}}{z_{11}} = \frac{\frac{R}{\gamma} \cdot \operatorname{cosech}\gamma + R_n + j\omega L_n}{\frac{R}{\gamma} \cdot \coth\gamma + R_n + j\omega L_n} . \tag{3.45}$$

After some simplification:

$$T = \frac{\alpha + (1+jx\eta\alpha)\cdot\gamma\cdot\sinh\gamma}{\alpha\cdot\cosh\gamma + (1+jx\eta\alpha)\cdot\gamma\cdot\sinh\gamma} \tag{3.46}$$

where

$$\alpha = \frac{R}{R_n}$$

$$x = \omega RC$$

$$\eta = \frac{L_n}{R^2 C} = \frac{\omega_o L_n}{R} \tag{3.48}$$

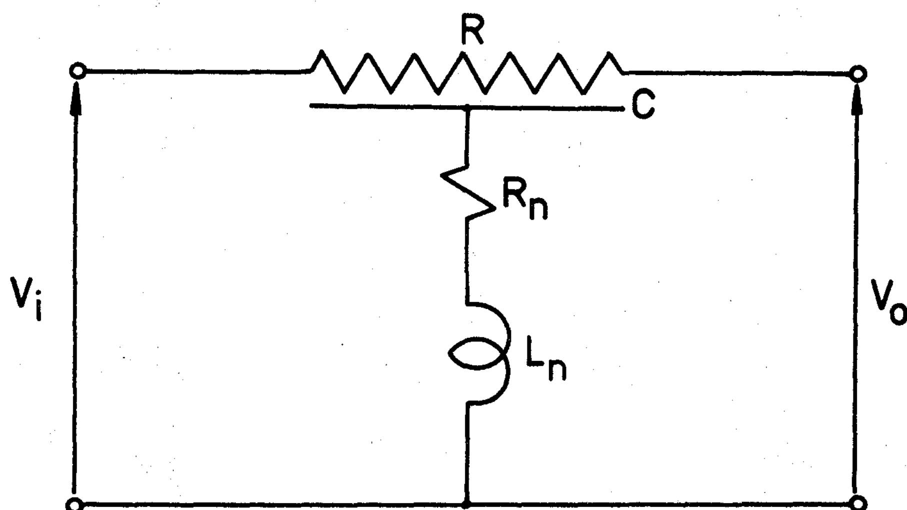

Figure 3.10 The URC-Notch Filter with Parasitic Notch Inductance

$$\gamma = \sqrt{\frac{jx}{1+jxB(x)}} \tag{3.22}$$

$$B(x) = \frac{1}{R \cdot G_s(x)} \; . \tag{3.23}$$

The value of x_n, i.e., the set of frequencies where the null will occur, may be obtained by setting the numerator of (3.46) equal to zero.

$$\alpha + (1+jx\eta\alpha) \cdot \gamma \cdot \sinh\gamma = 0 \quad . \tag{3.49}$$

To simplify the calculations, let us assume that

$$\gamma = \sqrt{\frac{jx}{1+jxB(x)}} \equiv P+jQ \quad . \tag{3.50}$$

Substituting (3.50) into (3.49), one gets:

$$\alpha + (1+jx\eta\alpha) \cdot (P+jQ) \cdot (\sinh P \cdot \cos Q + j\sin Q \cdot \cosh P) = 0 \; .$$

Setting the real and imaginary parts equal to zero:

$$\alpha + (P-x\eta\alpha Q) \cdot \sinh P \cdot \cos Q - (Q+x\eta\alpha P) \cdot \sin Q \cdot \cosh P = 0 \tag{3.51}$$

and

$$(P-x\eta\alpha Q) \cdot \sin Q \cdot \cosh P + (Q+x\eta\alpha P) \cdot \sinh P \cdot \cos Q = 0 \tag{3.52}$$

α follows directly from (3.52).

$$\alpha = \frac{P \cdot \tan Q + Q \cdot \tanh P}{x\eta(Q \cdot \tan Q - P \cdot \tanh P)} \quad . \tag{3.53}$$

Substituting (3.53) into (3.51), one obtains the transcendental equation needed to solve for x_n.

$$1 - x\eta \cosh P \cdot \cos Q \cdot \left\{ \frac{(Q \cdot \tan Q - P \cdot \tanh P)^2}{(P\tan Q + Q\tanh P)} + (P\tan Q + Q\tanh P) \right\} = 0 \; . \tag{3.54}$$

Both P and Q are functions of x and B(x). Because of the periodicity of the trigonometric functions, equation (3.54) has an infinite set of solutions. For practical reasons, as were described in paragraph 3.3, we will only be interested in the solution which occurs at the lowest frequency.

Computer calculated solutions that resulted from (3.54) and (3.53) are shown in Figures 3.11 and 3.12, which relate the dependence of α_1 and the normalized notch frequency x_1 on the inductance parameter η, for various values of the dielectric loss parameter B(x). Values of B(x) employed in each case are held to be constant in the vicinity of the notch frequency. It is to be noted that the effect of the inductance parameter η is to decrease both the notch frequency $x_1 = \frac{\omega_1}{\omega_o}$ and the related optimum value of α_1.

It is important to note at this point that although the series inductance may be quite small, say 1 nH, its effect may be quite pronounced in a device which was designed to operate at high frequencies. This comes about because of the fact that the inductance parameter η is not only a function of L_n alone, but is also directly proportional to the characteristic frequency ω_o of the URC-network. As such, careful attention should be paid to the inductance if these devices are being designed to operate at high frequencies.

The effect of the inductance is illustrated by the following example:

A filter was fabricated using a Nichrome - Y_2O_3 - Al structure. The parameters were as follows:

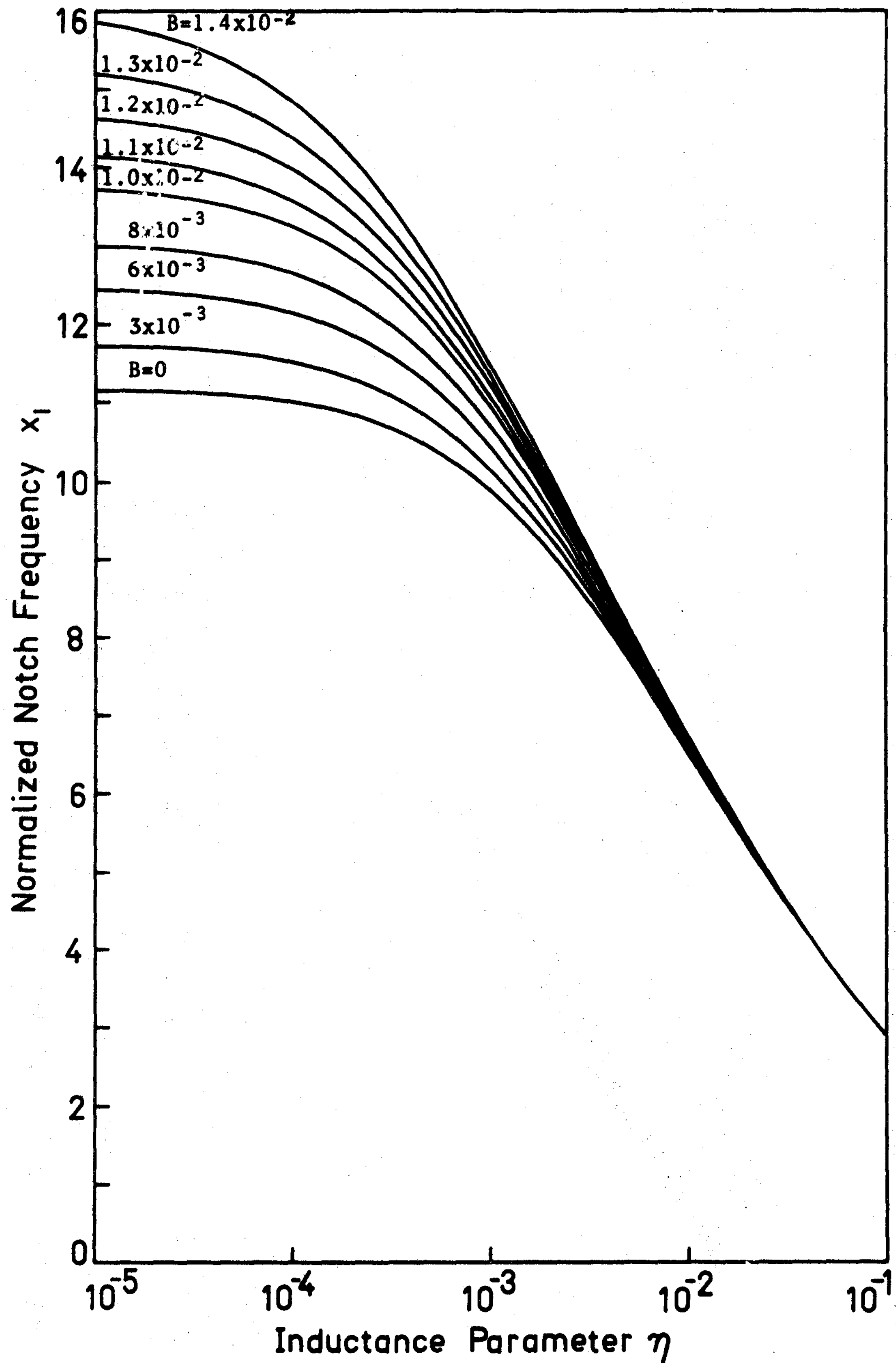

Figure 3.11 Effect of the Notch Inductance Parameter η on the Normalized Notch Frequency x_1 for Various Values of the Dissipation Parameter B.

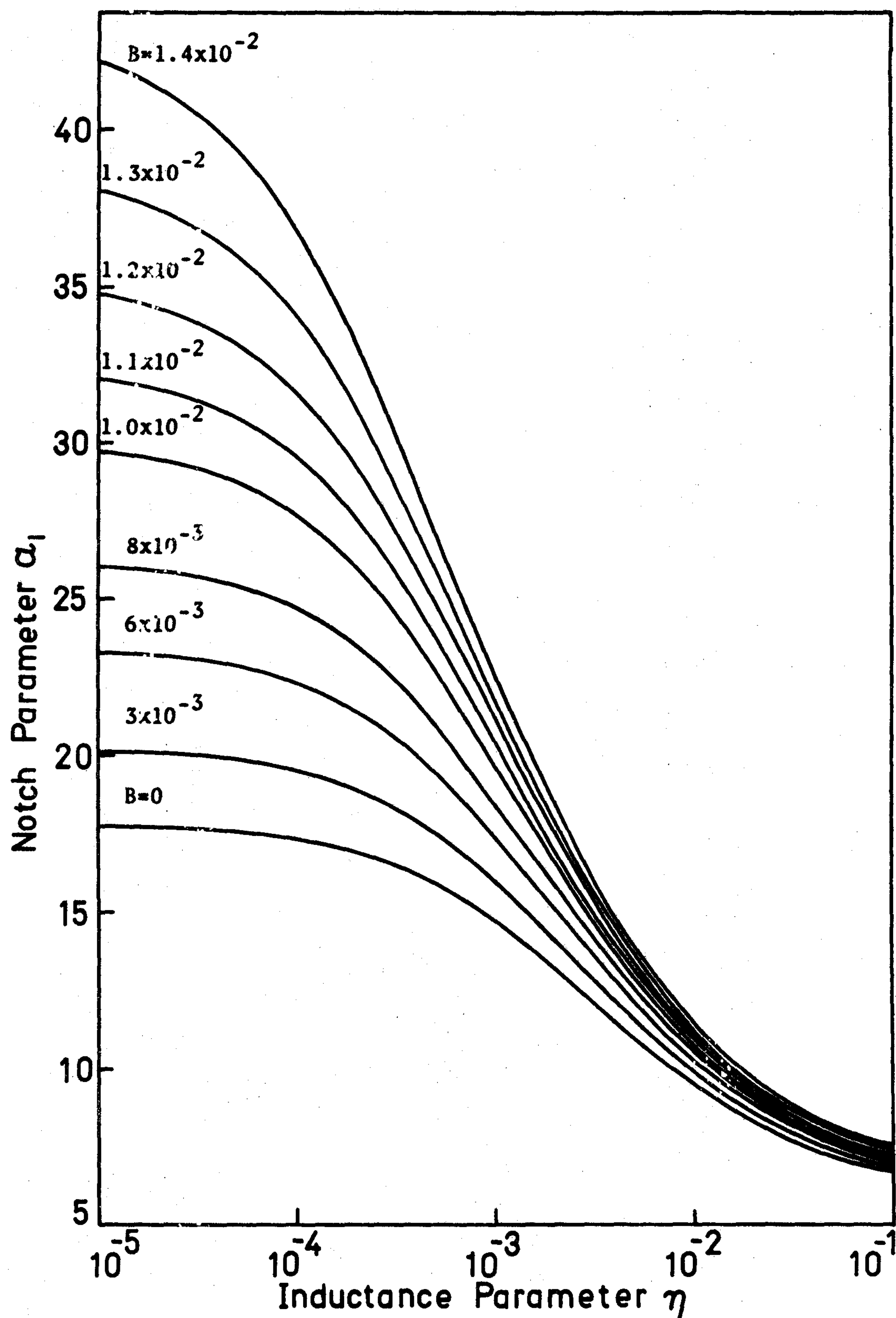

Figure 3.12 Effect of the Notch Inductance Parameter η on the Notch Parameter α for Various Values of the Dissipation Parameter B.

$$C = 2.331 \text{ nF}$$

$$R = 265.71\Omega$$

$$L_n = 0.9\mu H \ .$$

The inductance was put in intentionally to demonstrate the effect of the inductance

$$f_o = \frac{1}{2\Pi \ RC} = 2.57 \times 10^5 \text{ Hz}$$

$$\eta = \frac{\omega_o L_n}{R} = 5.5 \times 10^{-3}$$

If $\eta=0$: $R_n = \frac{R}{\alpha_1} = \frac{265.71}{17.786} = 14.94\Omega$

For $\eta = 5.5\text{x}10^{-3}$, $B=0$: $R_n = \frac{265.71}{10.76} = 24.7\Omega$.

Experimentally it was found that $R_n=24.5\Omega$ gave an optimum notch. This compares well with the 24.7Ω calculated theoretically. The difference may be due to contact resistance. The experimental curve and the theoretical curve corresponding to equation (3.46) with $\eta = 5.5\text{x}10^{-3}$ and B=0 are identical up to about 3MHz where dielectric loss probably starts to become important. It may also be noted that the theory predicts correctly the nearly 30% change in the notch frequency compared to the value that is predicted if η=B=0. The effect of the inductance is also to narrow the rejection band of the filter and to improve its symmetry with respect to the null frequency. Y_2O_3 was used as the dielectric because of its extremely low losses (see Chapter 6).

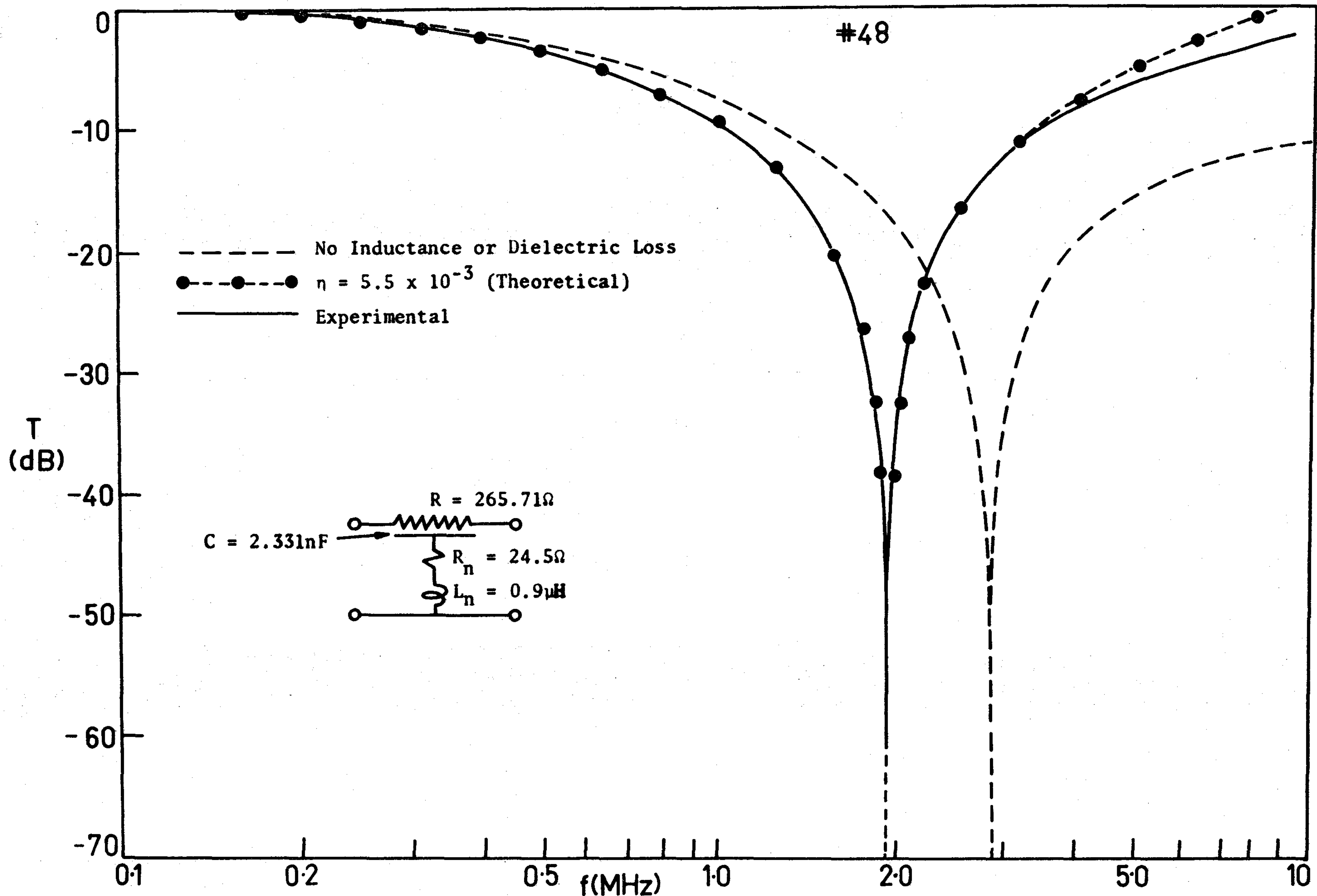

Figure 3.13 Predicted Transfer Function Response of an $A\ell$-Y_2O_3-Nichrome Notch Filter for $\eta=0$ (dashed line) and $\eta=5.5\times10^{-3}$ (dot-dash line) compared with Experimental Response (solid line).

3.4 The URC-Bandpass Filter

3.4.1 Introduction

The basic URC-network may be used in conjunction with amplifiers and lumped passive elements in order to get complex poles in the voltage transfer function[36-39]. A large variety of circuit configurations is possible and the choice of a particular one will be determined in practice by the sensitivity of the transfer function to changes in amplifier gain, circuit element values, etc. The circuit shown in Figure 3.14 was only chosen on the basis that the expression for the voltage transfer function is independent of the amplifier gain as long as it is very much greater than one, i.e., $|A| >> 1$.

3.4.2 Ideal URC High Q Bandpass Filter

As is shown in Figure 3.14, the bandpass amplifier consists of a notch filter in the feedback loop of a high gain wideband amplifier. If one assumes an ideal amplifier, i.e., negligible input admittance and output impedance, and a very large gain A, the voltage transfer function is determined solely by the properties of the URC network and R_1. Since the input impedance is very large,

$$I_{in} \doteq I_2 \ .$$

It follows then that

$$V_i \doteq I_2 R_1 \ .$$

Since $|A| >> 1$, the input of the wideband amplifier is a virtual ground. Therefore $I_2 = y_{21} V_o$ where y_{21} refers to the null network.

$$\therefore \qquad T = \frac{V_o}{V_1} = \frac{1}{y_{21} R_1} \ . \tag{3.55}$$

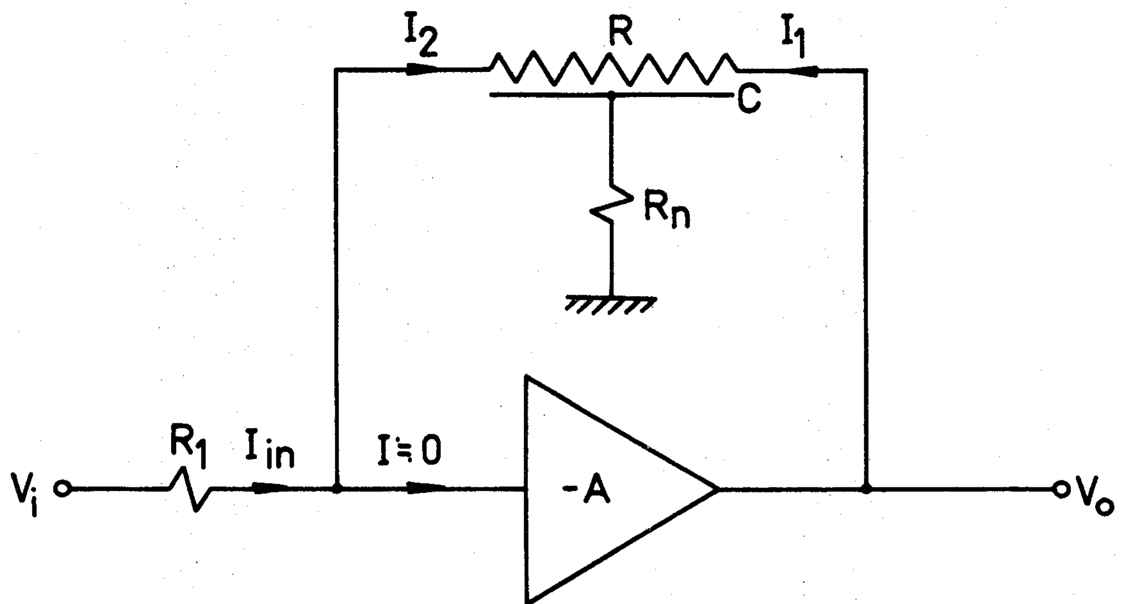

Figure 3.14 The URC-Bandpass Amplifier

The y-parameters of the URC-network can be obtained from the z-parameters as given by equations (3.28) and (3.29). They are presented again for convenience:

$$z_{11} = z_{22} = \frac{R}{\sqrt{sRC}} \cdot \coth\sqrt{sRC} + Z_n(s) \tag{3.56}$$

$$z_{12} = z_{21} = \frac{R}{\sqrt{sRC}} \cdot \operatorname{cosech}\sqrt{sRC} + Z_n(s) \tag{3.57}$$

where $s = \sigma + j\omega$ and $Z_n = R_n$ if no parasitic inductance is present.

From linear two-port theory:

$$y_{21} = \frac{-z_{21}}{\Delta_z} = \frac{-z_{21}}{z_{11}z_{22} - z_{12}z_{21}} = \frac{-z_{21}}{z_{11}^2 - z_{21}^2}$$

$$= \frac{\frac{R}{\sqrt{sRC}} \cdot \operatorname{cosech}\sqrt{sRC} + R_n}{-\frac{R^2}{sRC} + \frac{2R}{\sqrt{sRC}} \cdot R_n[\operatorname{cosech}\sqrt{sRC} - \coth\sqrt{sRC}]} \; . \tag{3.58}$$

Use was made of the fact that

$$\operatorname{cosech}^2 x - \coth^2 x = -1 \; .$$

Substituting (3.58) into (3.55) and simplifying, it follows that

$$T = \frac{2\gamma\{1-\cosh\gamma\} - \alpha\sinh\gamma}{\beta\gamma\cdot\{\alpha+\gamma\sinh\gamma\}} \tag{3.59}$$

where

$$\alpha = \frac{R}{R_n}$$

$$\beta = \frac{R_1}{R}$$

$$\gamma = \sqrt{sRC} \; .$$

The characteristic equation of T is given by

$$\alpha + \gamma \sinh\gamma = 0 \qquad (3.60)$$

$$\gamma = \sqrt{sRC} = \sqrt{(\sigma+j\omega)RC} = P+jQ \quad . \qquad (3.61)$$

Substituting (3.61) into (3.60) and setting the real and imaginary parts equal to zero, one obtains

$$\begin{aligned} &\alpha + P\sinh P\cdot\cos Q - Q\sin Q\cdot\cosh P = 0 \\ &P\cdot\sin Q\cdot\cosh P + Q\cdot\sinh P\cdot\cos Q = 0 \end{aligned} \qquad (3.62)$$

These two equations define the root locus of the characteristic equation. It is not possible to get an explicit analytic expression for the root locus, and it has to be solved by iteration. An alternative way of finding the conditions that the poles lie on the $j\omega$-axis, is to make $\sigma=0$ and to solve for α and x.

For this case (3.62) simplifies to

$$\begin{aligned} &\tanh\sqrt{\frac{x}{2}} = -\tan\sqrt{\frac{x}{2}} \\ &\alpha = 2\sqrt{\frac{x}{2}}\cdot\sin\sqrt{\frac{x}{2}}\cdot\cosh\sqrt{\frac{x}{2}} \end{aligned} \qquad (3.63)$$

These are exactly the same expressions as were obtained for the URC notch filter in equations (3.40) and (3.41). Therefore, conditions for oscillation are defined by $\alpha_1=17.786$ and $x_1 = 11.1902$.

In order to demonstrate the transfer function that may be obtained with an ideal amplifier and URC network, the expression for T was evaluated using the following practical parameter values:

$R_1 = 439\Omega$

$R = 265.71\Omega$

$R_n = 14.94\Omega$

$C = 2.331$ nF .

It follows then that $\beta = 1.652$ and

$$f_o = 2.57\text{x}10^5 \text{ Hz}$$

$$\alpha = 17.786 \ .$$

The transfer function was evaluated by computer and is depicted in Figure 3.15. The theoretical transfer function of the same filter arrangement, but with α=19.565 and α=25.0, is depicted on the same graph.

3.4.3 URC Bandpass Network with a Non-Ideal Wideband Amplifier and Distributed Network

In practice it is necessary to include the effects of the non-ideal properties of the wideband amplifier and the parasitics in the URC null network in order to compare the experimental and theoretical results.

Consider a wideband amplifier with input admittance Y_{in}, output impedance Z_o and gain $A\angle\phi$. Let there be dielectric loss in the URC network as well as a parasitic inductance L_n in series with the notch resistor R_n. From Figure 3.16 it follows that

$$V_o = A\angle\phi \cdot V_{in} - Z_{out} \cdot I_1 \tag{3.64}$$

$$V_s = (I_2 + V_{in} \cdot Y_{in}) \cdot Z_1 + V_{in} \quad . \tag{3.65}$$

For the URC null network $z_{11} = z_{22}$ and $z_{12} = z_{21}$. Therefore

$$V_o = I_1 z_{11} + I_2 z_{12} \tag{3.66}$$

$$V_{in} = I_1 z_{12} + I_2 z_{11} \quad . \tag{3.67}$$

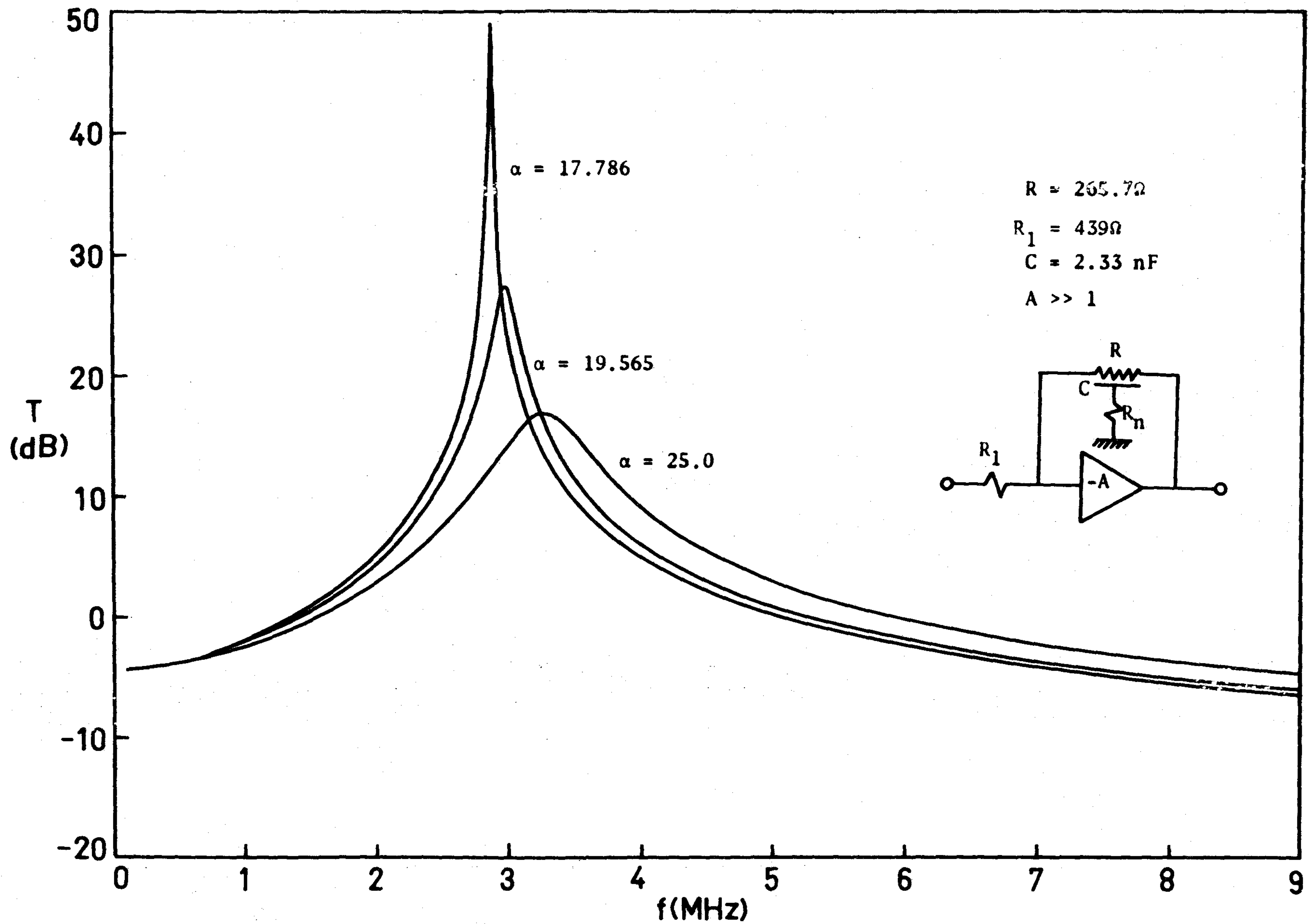

Figure 3.15 Ideal URC Bandpass Amplifier Response for three different values of the notch parameter α.

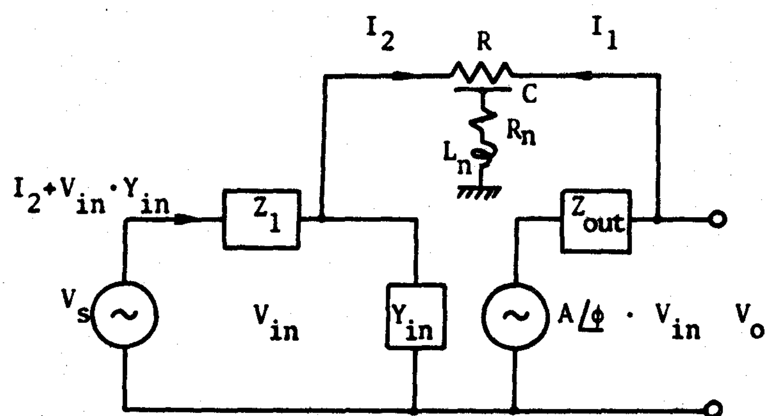

Figure 3.16 URC Bandpass Network with a Non-Ideal Wideband Amplifier and Distributed Network.

From (3.66) and (3.67)

$$V_o\, z_{12} = I_1 z_{11} z_{12} + I_2 z_{12}^2$$

$$V_{in}\, z_{11} = I_1 z_{11} z_{12} + I_2 z_{11}^2 \; .$$

Substract:

$$I_2 = \frac{V_{in}\, z_{11} - V_o\, z_{12}}{\Delta_z} \tag{3.68}$$

where

$$\Delta_z = z_{11}^2 = z_{12}^2 \; .$$

Substituting (3.68) into (3.66), and solving for I_1, one obtains

$$I_1 = \frac{V_o}{z_{11}} + \frac{(V_o \cdot z_{12} - V_{in} \cdot z_{11}) z_{12}}{\Delta_z \cdot z_{11}} \; . \tag{3.69}$$

Substituting (3.68) and (3.69) into (3.64) and (3.65):

$$V_o = A\angle\phi \cdot V_{in} - Z_{out} \left\{ \frac{V_o}{z_{11}} + \frac{(V_o z_{12} - V_{in} z_{11}) \cdot z_{12}}{\Delta_z \cdot z_{11}} \right\} \tag{3.70}$$

and

$$V_s = \left\{ \frac{V_{in}\, z_{11} - V_o\, z_{12}}{\Delta_z} + V_{in}\, Y_{in} \right\} \cdot Z_1 + V_{in} \tag{3.71}$$

From (3.64)

$$V_{in} = \frac{1 + \dfrac{Z_{out}}{z_{11}} + \dfrac{Z_{out}\, z_{12}^2}{\Delta_z \cdot z_{11}}}{A\angle\phi + \dfrac{Z_{out}\, z_{12}}{\Delta_z}} \cdot V_o \tag{3.72}$$

Substituting (3.72) into (3.71), one obtains the following expression for the voltage transfer function:

$$T = \frac{V_o}{V_s} = \frac{A\angle\phi + \dfrac{Z_{out}\cdot z_{12}}{\Delta_z}}{\left\{\dfrac{z_{11}Z_1}{\Delta_z} + Z_1\cdot Y_{in}+1\right\}\left\{1+\dfrac{Z_{out}}{z_{11}}+\dfrac{Z_{out}\cdot z_{12}^2}{\Delta_z\cdot z_{11}}\right\} - \dfrac{z_{12}Z_1}{\Delta_z}\left\{A\angle\phi + \dfrac{Z_{out}\cdot z_{12}}{\Delta_z}\right\}} \quad \ldots\ldots (3.73)$$

3.5 Conclusion

The ideal theory of the uniformly distributed RC-network has been given. The influence of parasitic effects such as dielectric losses and stray inductance was introduced and the theory developed to take it into account. This was applied to an $A\ell$-Y_2O_3-Nichrome notch filter and good agreement between experiment and theory was obtained.

CHAPTER 4

The Tunable URC-Filter

4.1 Introduction

A tunable filter would be an asset for many circuit applications. This is especially true for null networks and bandpass filters. The ideal situation is obtained when the centre frequency may be shifted by adjusting a single circuit parameter. Some means of achieving a tunable URC filter have been described in the literature, but they all suffer from the deficiency of either a non-optimum null (in the case of null-networks) or two parameters that need to be altered in order to achieve the minimum of change in the notch depth[40].

A tunable thin-film filter will now be described which, ideally, does not suffer from any of the drawbacks mentioned above. Consider the notch filter: It was shown in Table 3.2 that an optimum notch will occur when

$$\alpha_1(R,R_n) = \frac{R}{R_n} = 17.786 \quad . \tag{4.1}$$

The null will be at a frequency

$$\omega_1(R,C) = \frac{x_1}{RC} = \frac{11.1902}{RC} \quad . \tag{4.2}$$

Because α, the parameter determining whether the notch is optimum, is independent of C, while the notch frequency is inversely proportional to it, C seems to be the ideal parameter to vary. By changing C, one would expect a translation of the URC-notch filter characteristic along the frequency axis, but without a change in the

transfer function in any other respect.

The variable capacitance C may be realized in practice quite readily with thin-film technology. A thin-film semiconductor is evaporated between the insulator and highly conducting layer of the non-tunable URC-network. The resulting structure is shown schematically in Figure 4.1 together with the proposed circuit symbol for it. To be specific, let us suppose it is an n-type semiconductor. As described in detail in Chapter 2, the application of a positive bias between the resistive layer and the ohmic contact onto the semiconductor will maximize the capacitance. It will approach the capacitance of the insulator alone. If the resistive layer is made negative with respect to the conducting layer, the electrons near the semiconductor-insulator interface will be depleted and the capacitance will be reduced. If it is assumed that the frequency is so high that the inversion layer cannot respond, the capacitance will reach a minimum value C'_{min}.

The available tuning range is given by

$$\frac{f_{max}}{f_{min}} = \frac{C_i}{C'_{min}} = 1 + \frac{\varepsilon_i}{\varepsilon_s t_i}\sqrt{\frac{4\varepsilon_s kT\ \ell n(\frac{N_d}{n_i})}{q^2 N_d}} \tag{4.3}$$

as was derived in Chapter 2.

A wide tuning range is therefore possible if the following conditions are met:

(i) The relative dielectric permittivity of the insulator, ε_i, should be as high as possible.

(ii) The insulator thickness, t_i, should be small.

(iii) The doping density, N_d, should be low.

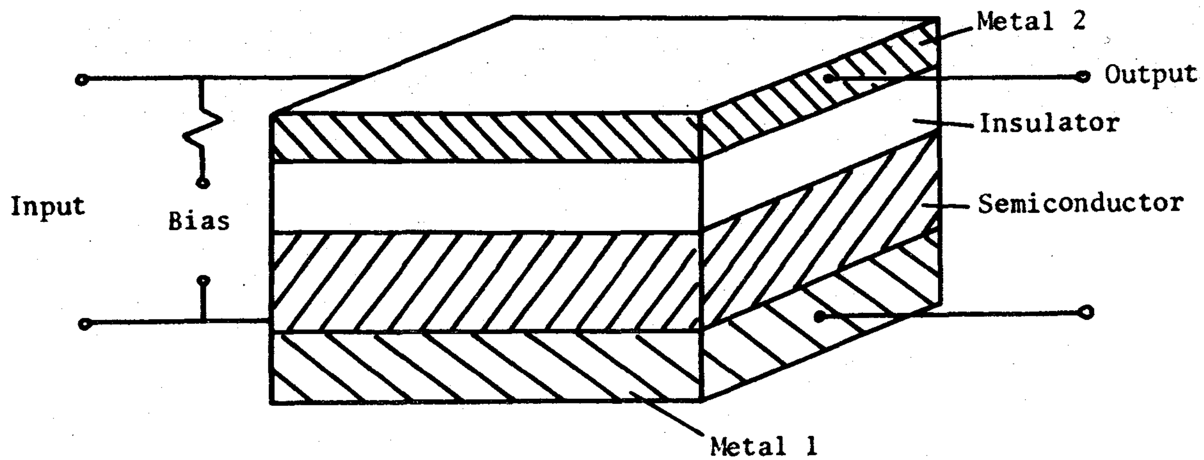

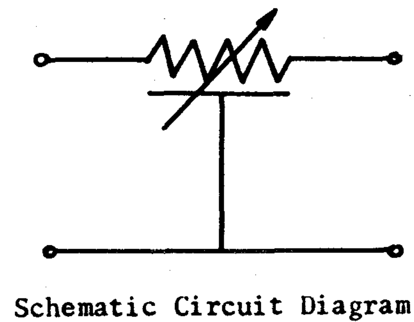

Figure 4.1 Pictorial Representation of Tunable URC Distributed Filter.
(Not to Scale)

In order to get typical figures for the magnitude of the tuning range, let us assume the following constants for the insulator and semiconductor materials (these figures are based on Y_2O_3 and CdS):

Insulator: $\varepsilon_i = 10$

$t_i = 3000$ Å

Semiconductor: $\varepsilon_s = 10$

$10^{15} < N_d < 10^{17}$ cm^{-3}

$n_i = 2.1 \times 10^{-2}$ cm^{-3}

$T = 300^{\circ}$K

For a structure consisting out of these materials, the ratio

$$1.5 < \frac{C_i}{C'_{min}} < 6 \quad .$$

For the same materials, with $t_i = 1000$ Å,

$$2.5 < \frac{C_i}{C'_{min}} < 16 \ .$$

The insulator thickness cannot be reduced indefinitely. Practical considerations such as leakage currents, dielectric breakdown and pin-holes, restrict the value of t_i to greater than say 1000 Å. For Y_2O_3, which was used in this investigation, a typical thickness is approximately 3000 Å.

The doping density of the semiconductor depends on the material and the processing techniques. A full discussion of CdS will be given in Chapter 7. For the processing parameters used in this Thesis, the lowest doping density obtained was of the order of 10^{16} cm^{-3}.

Taking all these factors into consideration it would seem possible to get a tuning range of about one octave with the materials employed.

4.2 Ideal Tuning Characteristics of the Tunable Notch Filter

The effects of dielectric loss (MIS-loss) and parasitic inductance may be neglected for the ideal URC-notch filter. The open-circuit voltage transfer function of such a device was derived in Chapter 3 as:

$$T = \frac{\alpha + \gamma \sinh\gamma}{\alpha\cosh\gamma + \gamma\sinh\gamma} \tag{4.4}$$

where $\alpha = \frac{R}{R_n}$ (4.5)

and $\gamma = \sqrt{j\omega RC(V)}$ (4.6)

Let us again assume the hypothetical MIS-structure which was considered in Section 2.2.1. The device parameters are:

$A = 0.38 \times 0.38\ cm^2$

$t_i = 3200\ \mathring{A}$

$\varepsilon_i = \varepsilon_s = 10$

$n_i = 2.1 \times 10^{-2}\ cm^{-3}$

$N_d = 2 \times 10^{16}\ cm^{-3}$

$T = 300^\circ K$.

These numbers are based on the material parameters of Y_2O_3 and CdS. The insulator thickness, area and doping density were chosen to yield convenient values for C_i and C'_{min}. The ideal high frequency CV-curve is shown in Figure 4.2. This curve is ideal in the sense that the effects of interface states, bulk states, ions in the insulator, metal-semiconductor work function difference, etc., have been neglected.

If this particular MIS-structure is incorporated into a URC-notch filter with a distributed resistor $R = 400\Omega$ and a notch resistor $R_n = 22.49\Omega$, the transfer characteristics as depicted in Figure 4.3 will

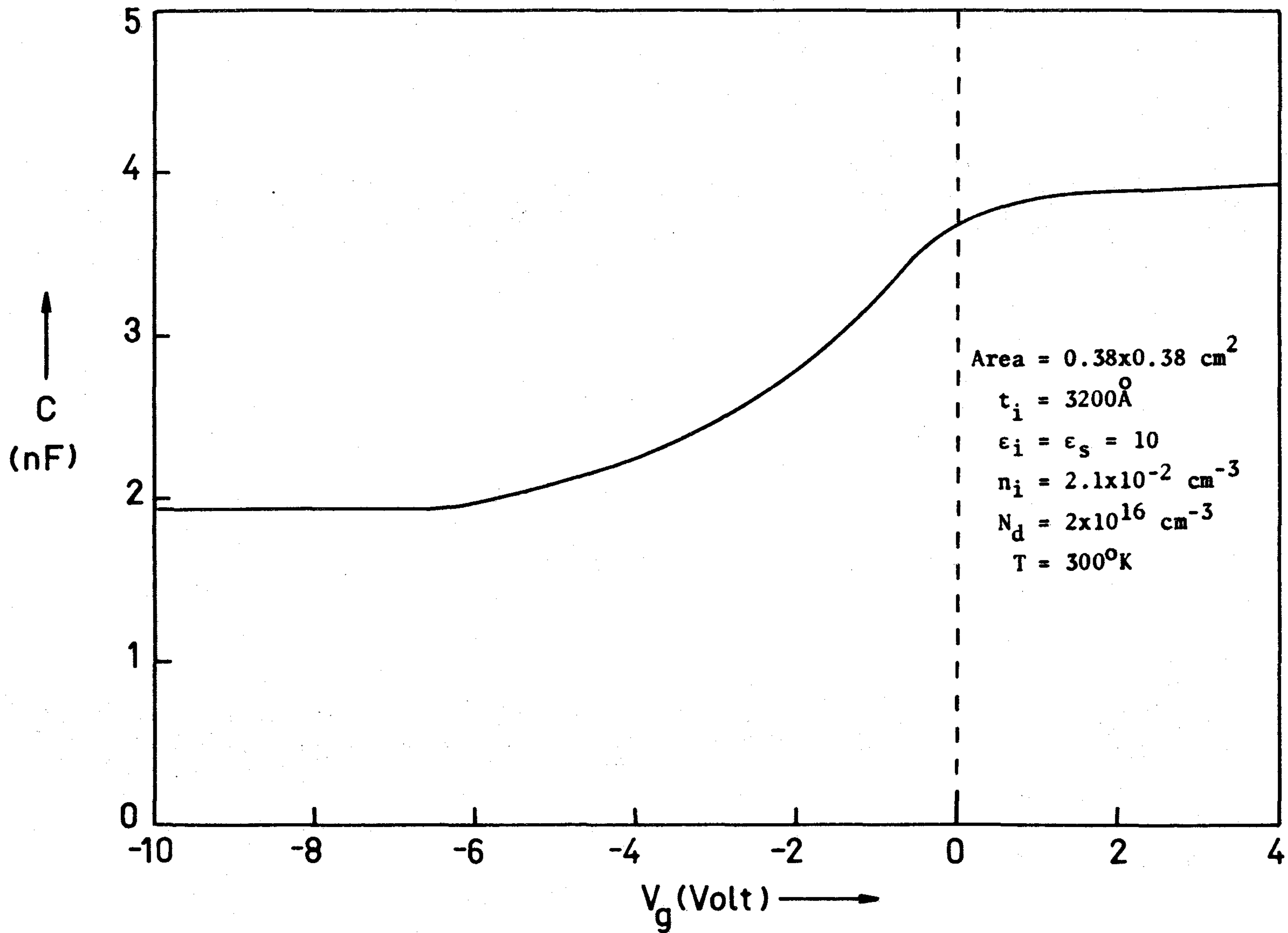

Figure 4.2 The Ideal High Frequency Capacitance-Voltage Curve.

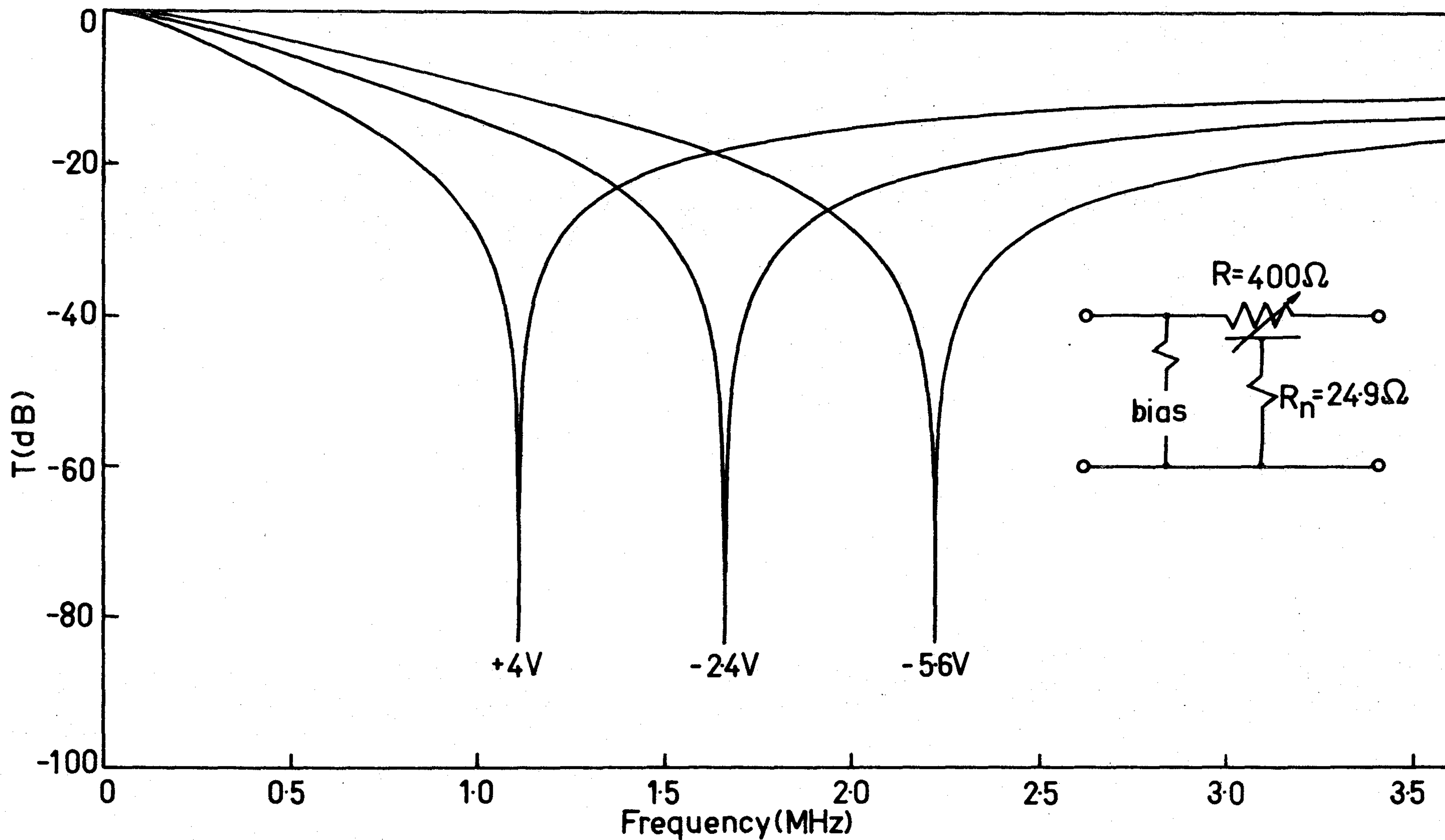

Figure 4.3 The Voltage Transfer Function of the Ideal URC-Notch Filter Calculated for Three Different Bias Voltages.

be obtained. These have been calculated for only three bias voltages, namely +4V, -2.4V and -5.6V. The horizontal displacement, without change in shape, is clear from this Figure.

4.3 Effects of MIS-Losses and Parasitic Inductance on the Tunable URC Notch Filter

One expects the shape of the voltage transfer function of the ideal URC tunable notch filter to be completely independent of the dc bias that is applied to it. This is so because of the fact that α_1, the notch parameter, is only dependent on R and R_n. It was pointed out in Chapter 3 that losses in the dielectric and semiconductor, and parasitic inductance in series with a notch resistor, may affect the optimum values of α_1 and x_1, where x_1 is the normalized frequency where the null occurs. The functional dependence of α_1 and x_1 on η and B is shown in Figures 3.11 and 3.12.

The inductance parameter η and the loss parameter B were defined as follows:

$$\eta = \frac{L_n}{R^2 C} \tag{4.7}$$

$$B = \frac{R_s}{R} \tag{4.8}$$

where R_s is an effective resistor in series with the capacitor to account for losses.

It may therefore be said that

$$\alpha_1 = \alpha_1(R,R_n,\eta,B) = \alpha_1(R,R_n,L_n,C,R_s) \tag{4.9}$$

and

$$x_1 = x_1(R,R_n,\eta,B) = x_1(R,R_n,L_n,C,R_s) \quad . \tag{4.10}$$

The fact that α_1 and x_1 are functions of η and B leads only to a change in the optimum value of α_1 for the non-tunable notch filter. In addition, the normalized frequency where the notch occurs will be shifted. The situation is a little bit more serious for the tunable notch filter. Since C is a function of voltage, and R_s is in general a function of both voltage and frequency, the actual value of η and B may be changed if the bias voltage is changed. This will lead to a "de-tuning" of the filter, i.e., the null will not be optimum for the whole tuning range.

The transfer function in the presence of MIS-losses and parasitic inductance is given by equation (3.46)

$$T = \frac{\alpha + (1+jx\eta\alpha)\cdot\gamma\cdot\sinh\gamma}{\alpha\cdot\cosh\gamma + (1+jx\eta\alpha)\cdot\gamma\cdot\sinh\gamma} \qquad (4.11)$$

where $$\gamma = \sqrt{\frac{jx}{1+jxB}} \qquad (4.12)$$

and $$x = \omega RC \; . \qquad (4.13)$$

In this expression x, C, B, γ and η are functions of voltage and/or frequency. The nature of the losses in an MIS-system was discussed in some detail in Chapter 2. A detailed knowledge of the interface states and bulk states, the nature of the ohmic contact on the semiconductor, and the losses in the insulator is required in order to evaluate B at all voltages and frequencies. This is extremely difficult, if not impossible, for a real, evaporated thin-film semiconductor-insulator system. Instead, we will merely assume a fixed value for B, i.e., independent of both voltage and frequency.

In order to illustrate the tuning behaviour of a non-ideal URC-notch filter, let us consider the same device which was considered in Section 4.2. We will take the loss parameter B to be constant at 10^{-2}, i.e., $R_s = 4\Omega$ for $R = 400\Omega$. Two sets of curves will be evaluated, namely for L_n = 32 nH and 320 nH, respectively. Both sets of curves will be evaluated for capacitance values between 2 nF and 4 nF, in steps of 0.2 nF. In both the calculations, R_n will be adjusted to give an optimum null at the highest frequency, i.e., when C = 2 nF. At this value of capacitance, the values of η corresponding to the two values of L_n is 10^{-4} and 10^{-3} respectively. Table 4.1 summarizes the values of α_1 and x_1 for the filter to be optimal at C = 2 nF.

Table 4.1

	α_1	x_1
$B = 10^{-2}$ $\eta = 10^{-4}$	27.742875	13.264853
$B = 10^{-2}$ $\eta = 10^{-3}$	19.797763	10.969014

The results of the calculations are shown in Figures 4.4 and 4.5. It may be seen that even an inductance as small as 32 nH will cause a detuning of more than 30 dB over the tuning range. A study of Figure 3.12 indicates that η should be kept less than 10^{-5} to minimize the effect of detuning due to inductance. A large value for R, the distributed resistance, reduces both η and B.

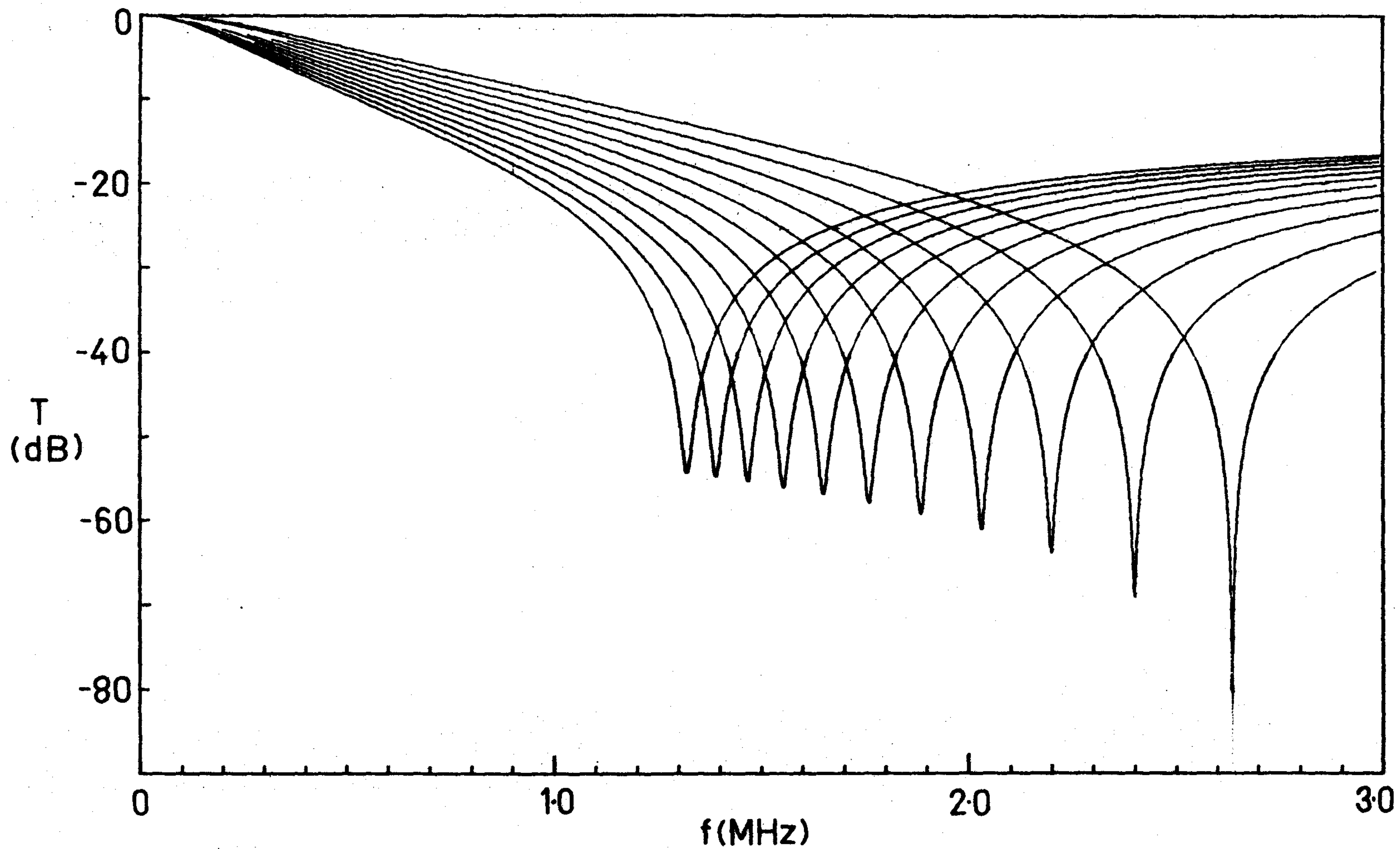

Figure 4.4 Calculated Tuning Characteristics of the Tunable URC-Notch Filter in the Presence of MIS-losses and Notch Inductance. $B(\omega)=B=10^{-2}$; L_n=32nH; R=400Ω; R_n=14.4181Ω. The Capacitance is Varied between 2nF and 4nF in steps of 0.2nF.

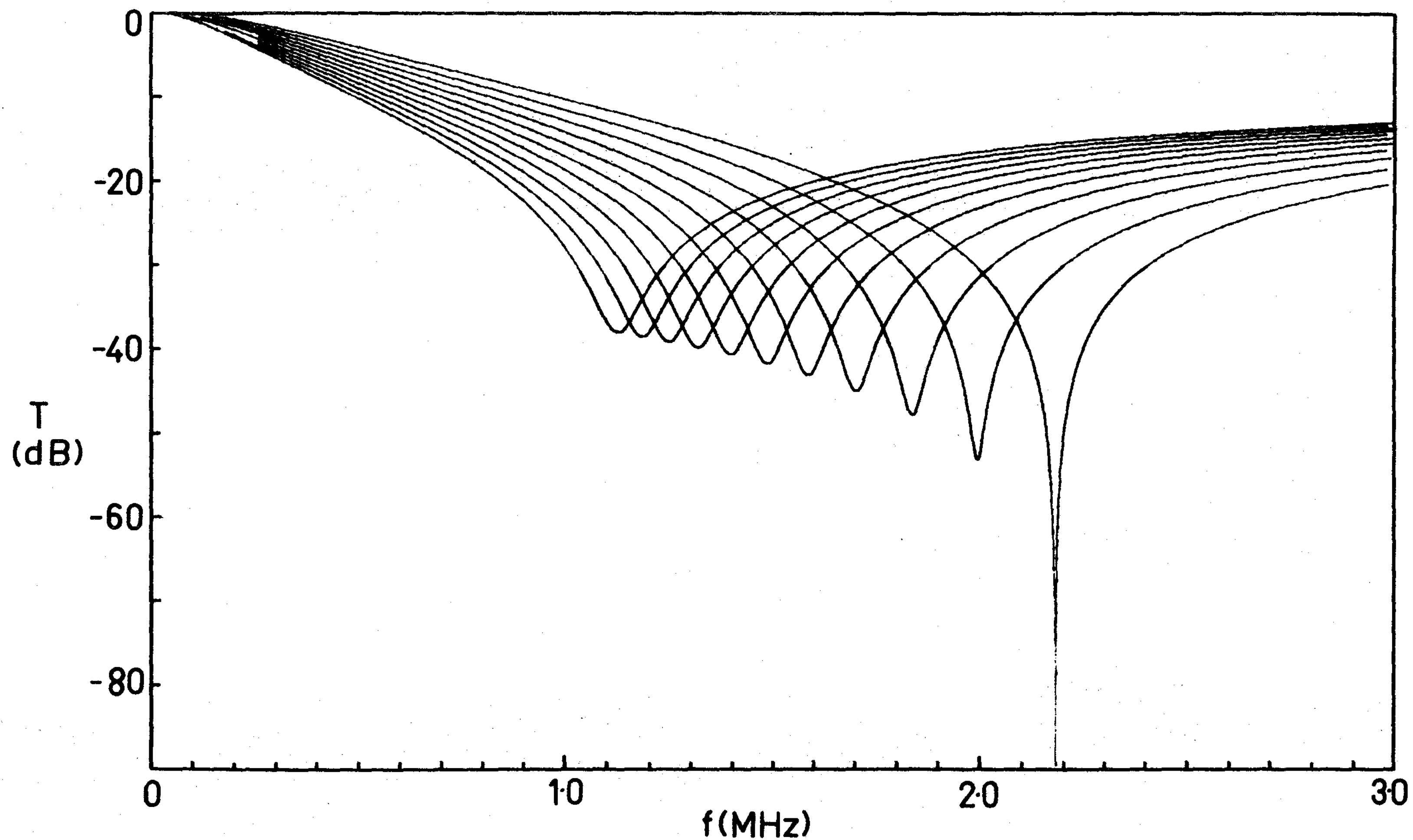

Figure 4.5 Calculated Tuning Characteristics of the Tunable URC-Notch Filter in the Presence of MIS-losses and Notch Inductance. $B(\omega)=B=10^{-2}$; $L_n=320nH$; $R=400\Omega$; $R_n=20.2043\Omega$. The Capacitance is Varied between 2nF and 4nF in steps of 0.2nF.

The parasitic inductance also causes a reduction in the available tuning range. This may best be illustrated by means of the previous example with L_n = 320 nH. The values of η at C = 2 nF and 4 nF are 10^{-3} and 5×10^{-4}, respectively. The corresponding optimum values for α_1 and x_1 are given in Table 4.2:

Table 4.2

	α_1	x_1
$B = 10^{-2}$, $\eta = 10^{-3}$	19.80	10.97
$B = 10^{-2}$, $\eta = 5\text{x}10^{-4}$	22.83	11.94

If the device is optimized at both C = 2 nF and C = 4 nF, the available tuning range is given by

$$\Delta f = f_u - f_\ell$$

where $$f_u = \frac{10.97}{2\pi \text{x} 400 \text{x} 2 \text{x} 10^{-9}} = 2.182 \text{ MHz}$$

and $$f_\ell = \frac{11.94}{2\pi \text{x} 400 \text{x} 4 \text{x} 10^{-9}} = 1.188 \text{ MHz} \quad .$$

The percentage change in frequency is defined as

$$\%\Delta f = \frac{f_u - f_\ell}{f_u}$$

$$\doteq 46\% \; .$$

Without parasitic inductance and MIS-losses this change will be:

$$\%\Delta f = \frac{\frac{1}{C_u} - \frac{1}{C_\ell}}{\frac{1}{C_u}}$$

$= 50\%$ for this example.

4.4 Conclusion

The distributed capacitance in the URC filter seems to be the ideal parameter to vary in order to change the cut-off frequency of the device. This capacitance may be varied independently of the distributed resistance by making use of a metal-insulator-semiconductor structure. The available tuning range is mainly dependent on the doping density of the semiconductor and the thickness of the insulator.

Parasitic effects such as MIS-losses and notch inductance seem to play an important role. The effect of inductance is especially serious at high frequencies. A notch filter with an upper null at 100 MHz, for instance, will have to have $L_n < 0.018$ nH for $\eta < 10^{-5}$. (It was assumed that $R = 100\Omega$ and $C = 178$ pF.) The effects of parasitic inductance become less serious for low frequency devices and can just about be neglected in the audio frequency range.

CHAPTER 5

Apparatus and Materials for the Fabrication of Evaporated Thin-Film Filters

5.1 Introduction

The samples necessary to study the properties of the dielectric, the semiconductor, and the URC-filters were made by vacuum evaporation techniques. These techniques, together with the properties of the materials used, will be described in this Chapter.

5.2 The Vacuum Coating Unit

The devices used in the investigations were made by the evaporation of different kinds of metals, insulators and semiconductors in a modified Edwards 19E2 vacuum system. The pressure during an evaporation was usually around 10^{-6} torr, except when gases like oxygen or nitrogen were bled into the system intentionally.

During an evaporation, liquid nitrogen was passed through a coil of copper tubing inserted into the throat of the diffusion pump. This assured that the back streaming vapors of the diffusion pump oil did not excessively contaminate the films.

The devices were made during one pump-down cycle of the vacuum system. This was possible because of the microcircuit jig assembly located inside the stainless steel bell jar. It consists of two rotating plates which are positioned, one above the other, by means of two conical position pins. The upper plate can carry a maximum of six substrates. The lower plate contains six metal masks which define

the eventual geometry of the evaporated material on the substrate. During a mask change the mask carriage moves down approximately 3/4", is turned through 1/6 revolution, and then may be moved up into close contact with the substrate. Only one substrate is exposed to the molecular vapor stream of material from the source. After the bottom plate has gone through one whole revolution, the next substrate is moved into position, and the process may start all over again. This last mentioned facility is optional, and in the second mode of operation, the movement of the bottom plate is not coupled to the top plate. In this instance the same mask may be used more than once during the preparation of the same device.

The substrates can be heated from the back by a spring-loaded heater-block which presses against the aluminum plate to which the substrate is attached. The temperature is monitored by a thermo-couple in the heater-block and a thermistor protruding through the mask.

The film thickness may be determined roughly by a quartz crystal oscillator and after the evaporation, more accurately by means of an optical interferometer.

The materials to be evaporated are carried in boats and crucibles (six altogether) on a rotatable turret head.

Resistance heating is used for the evaporation of the metals, the semiconductor, and an insulator like SiO. It was found unsuitable for the evaporation of Y_2O_3 and Si_3N_4. For evaporating these materials, an electron beam system was installed in the vacuum system. The fact that resistive heating as well as an electron gun is available, makes the system very versatile.

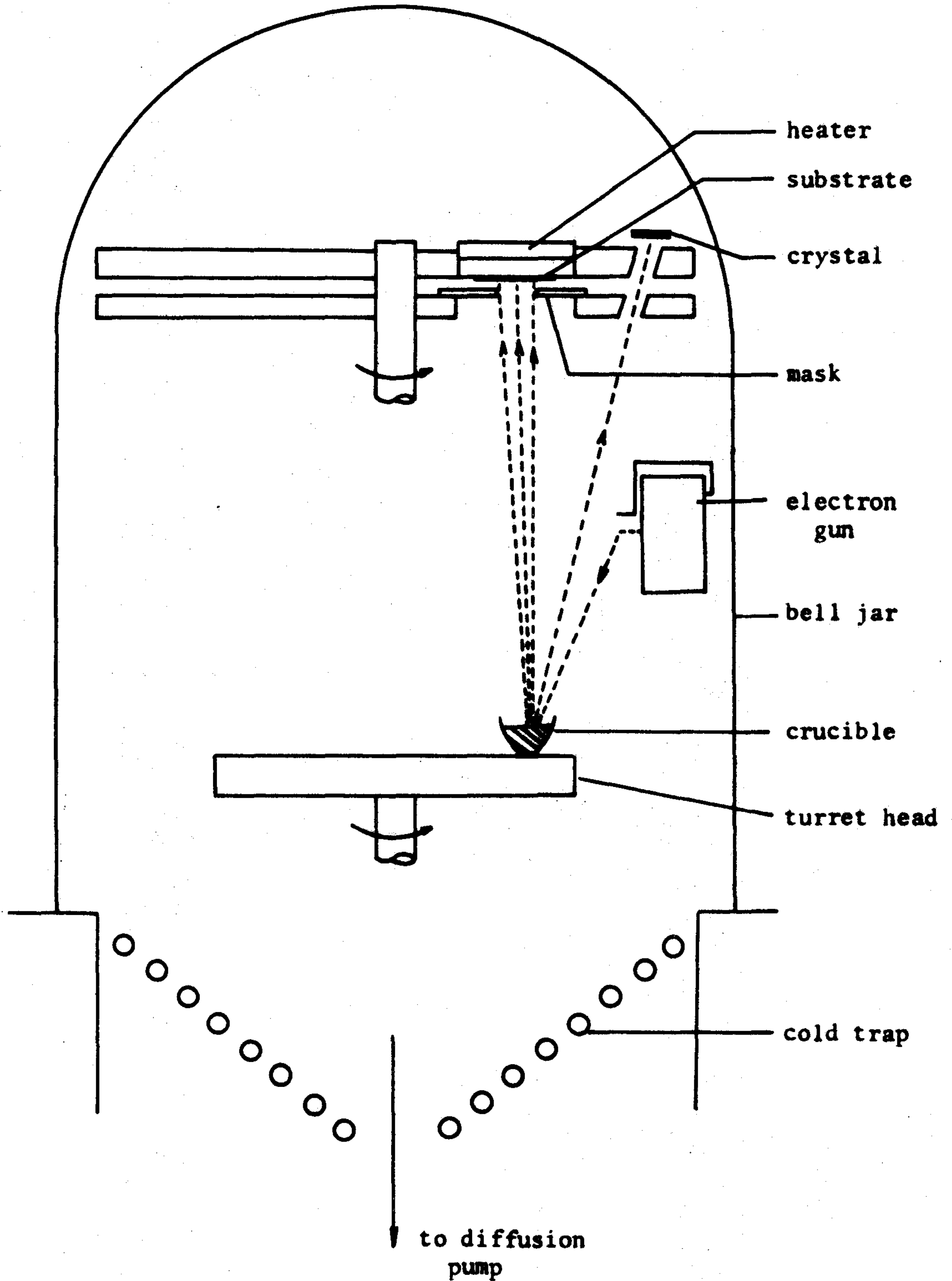

Figure 5.1 Schematic Diagram of the Vacuum System

The vacuum system is shown schematically in Figure 5.1.

5.3 The Thickness Monitor (Ref. 45, Chapter 3)

The film thickness was monitored during deposition by means of a quartz crystal located near the substrate. Material is deposited simultaneously onto the substrate and the crystal. Due to the change in mass of the crystal, its natural frequency of oscillation is decreased. As the crystal forms part of an oscillator unit, the changes in frequency may be measured by means of a frequency counter or a specially constructed circuit[44] which differentiates the frequency to get the rate of change of frequency, as well as the frequency change.

The change in frequency is directly proportional to the change in mass as long as $\Delta f \leq 200$ kHz for the particular crystal used.

If the crystal has a fixed position with respect to the substrate, and if their temperatures are held constant, a calibration curve which relates the thickness of deposited material on the substrate to the frequency change of the crystal may be obtained.

$$t = \frac{K \cdot \Delta f}{\rho}$$

where t = film thickness on substrate in Å

Δf = frequency change of crystal oscillator

ρ = density of deposited material gram/cc

K = constant which depends on the properties of the crystal, the relative positions of the evaporation source, the substrate and the crystal. It is also dependent on the crystal temperature T_x and substrate temperature T_s as well as the

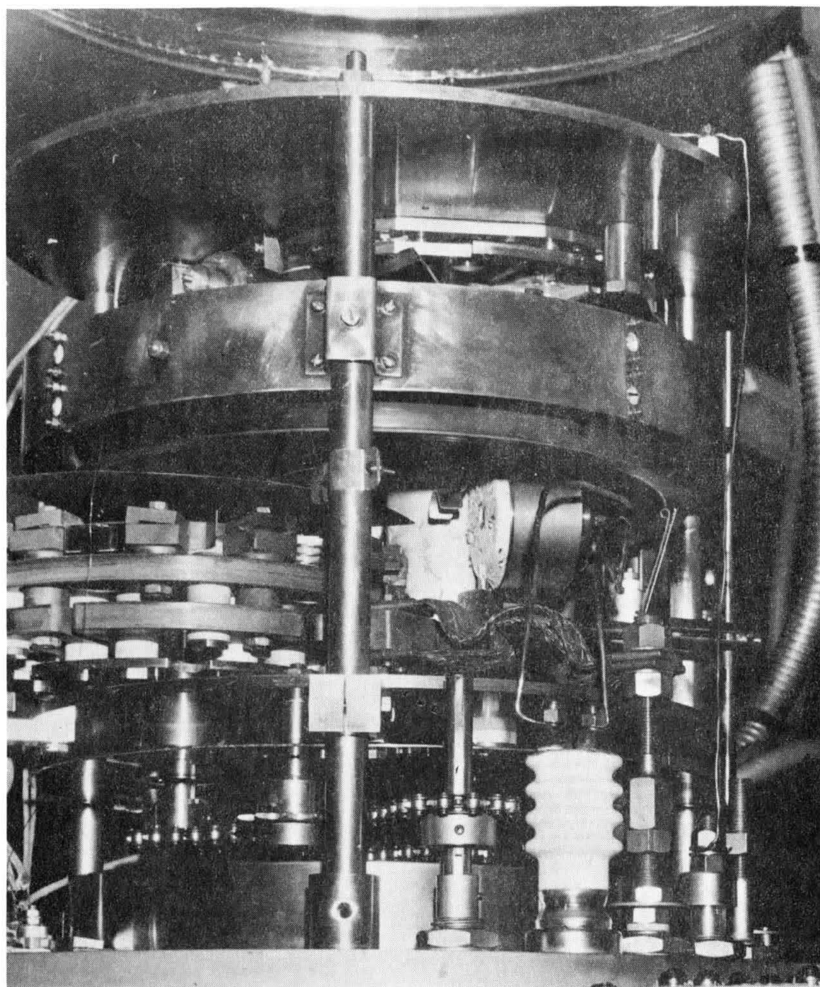

Figure 5.2 Photograph of the Interior of the Vacuum Evaporation System. The Electron Gun can be seen just Right of Centre.

type of material due to sticking coefficient variation.

The system was calibrated for a 6MHz AT-cut quartz crystal with both the substrate and the crystal at room temperature. The constant K was found to be 3.7 for an yttrium oxide film.

The sticking coefficient[45,p.149] of a vapor onto a substrate depends on the surface properties of the substrate, the temperature, the amount of material already condensed, etc. So, for instance[45], the sticking coefficient of gold onto a glass substrate will be reduced by approximately 50% if the substrate temperature is raised from 25°C to 360°C. Also, the sticking coefficient of Cd to a Cu substrate is increased from 0.26 to 0.6 if the film thickness changes from 4.9Å to 42.9Å respectively.

As the substrate temperature is normally changed to get the desirable properties of the evaporated film, the use of a single constant K for all materials and for all substrate temperatures is not justified. A system where the quartz crystal and the substrate are held at the same temperature[46] is probably better and may be calibrated easier for different substrate temperatures.

For this investigation, the reading given by the quartz crystal thickness monitor was only used as a rough estimate of the film thickness. Critical film thickness, like the insulator for instance, was always measured after the evaporation using a Sloan type M-100 angstrometer. It is estimated that the accuracy of these measurements is of the order of 5% to 10% for a 3000 Å film.

5.4 Measurement of the Substrate Temperature

The substrate temperature plays an important role in determining the properties of the evaporated films. The resistivity of cadmium sulfide, for instance, is a very strong function of the substrate temperature[47]. Silicon monoxide films evaporated onto room temperature substrates, will have such high stresses induced into them when exposed to air that they will rupture[48].

All these facts make it imperative that the substrate temperature should be controllable, and accurately measured.

In the Edwards 19E2 vacuum system the substrates may be heated by a spring-loaded metal block which presses against the 2" x 2" x 1/4" aluminum spacer onto which the substrate is attached. The brass heater block consists of a nichrome heater element whose power dissipation may be controlled by a variac. In the standard unit the temperature is measured by a thermocouple which is mounted into the heater block. This temperature may be raised to 300°C.

In order to measure the temperature on the front surface of the substrate, a specially mounted thermistor was attached with springsteel to the mask. It protruded approximately 1/8" through a hole in the mask. When the mask is moved up against the substrate, the thermistor presses firmly against it and makes good thermal contact. The set-up is shown schematically in Figure 5.3.

The thermistor was calibrated in a Delta Design Oven MK2300 in the range 36°C to 146°C. The upper temperature was limited by the indium which surrounded the thermistor. The resistance was measured by a

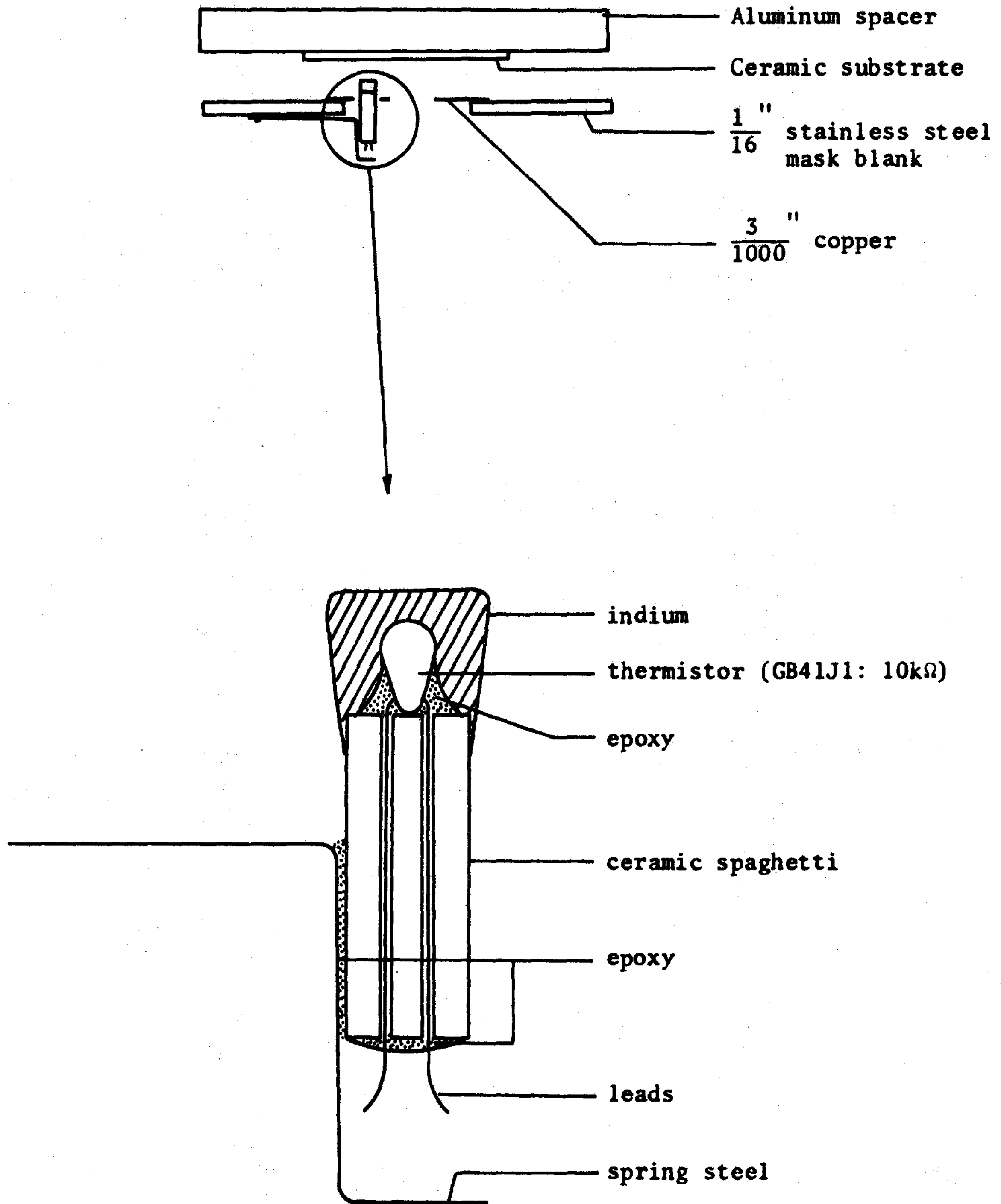

Figure 5.3 Details of Substrate Temperature Sensor.

Hewlett-Packard 3450A Digital Multifunction meter. The calibration curve is shown in Figure 5.4.

It may be seen that the functional relationship between the resistance and absolute temperature is of the form

$$R = ae^{\frac{b}{T(^oK)}} \quad . \qquad (5.1)$$

The points corresponding to $\ell n(R)$ versus $\frac{10^3}{T(^oK)}$ have been fitted by means of the least squares method to a straight line.

The constants a and b of equation (5.1) turned out to be

$a = 3.159278354 \times 10^{-2}$

$b = 3.798156063 \times 10^{3}$.

The correlation coefficient r = 0.9999094695.

It was estimated that the substrate temperature could be measured to ±5°C by this method.

The temperature of the front surface of the substrate and the temperature of the heater are compared in Figure 5.5 as a function of time. The variac was set at the maximum allowable level and it reached a maximum temperature of 300°C. It was within 10°C of this final temperature within 45 minutes. The front surface of the substrate, on the other hand, had a much longer time constant and after one hour there was still a 130°C difference between the substrate and heater temperatures. After one hour the front surface of the substrate reached 165°C and the rate of change of temperature was slow enough to assume the temperatures to be constant during the duration of an evaporation which lasted only a few minutes.

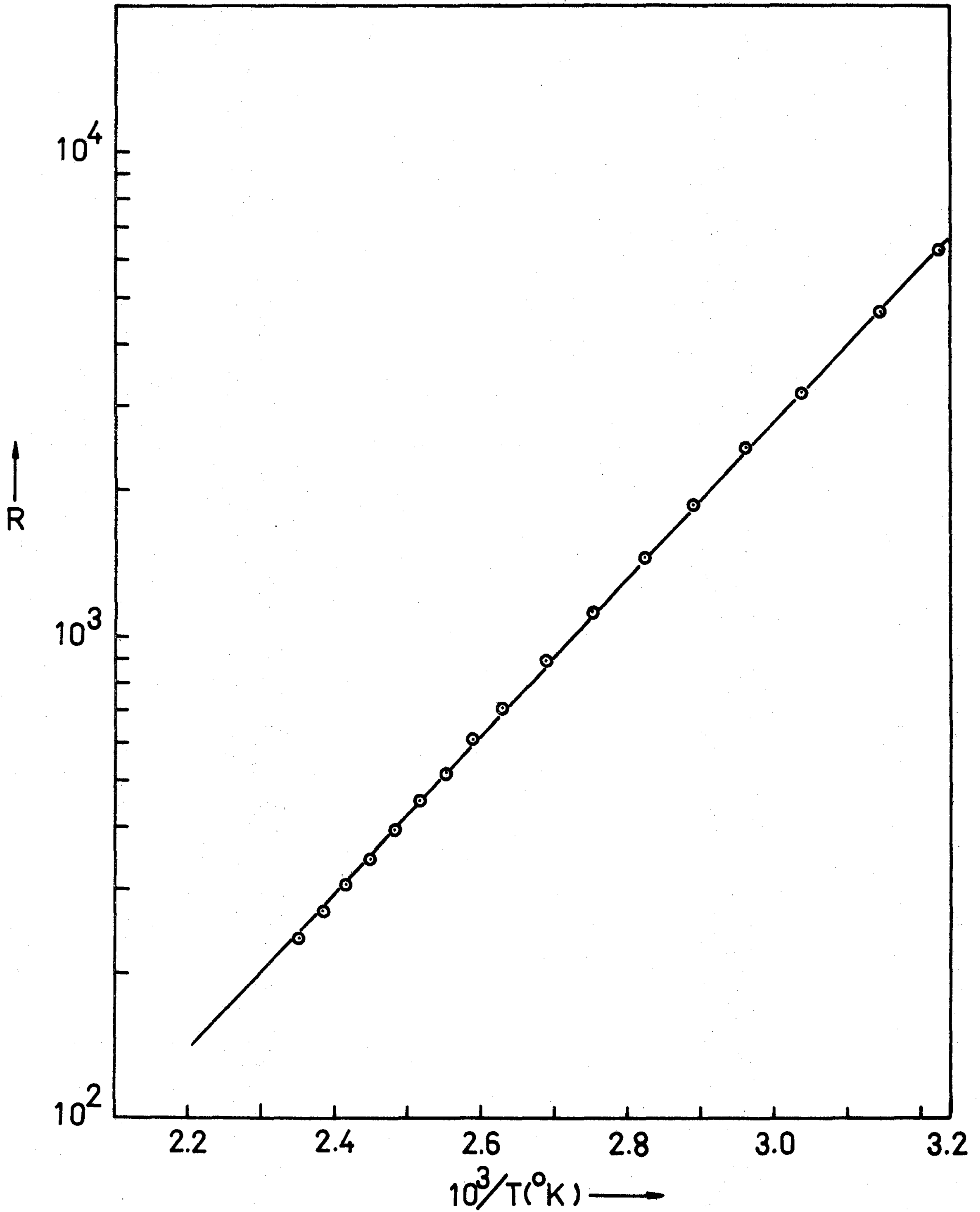

Figure 5.4 Calibration Curve for the GB41J1 Thermistor (10kΩ).

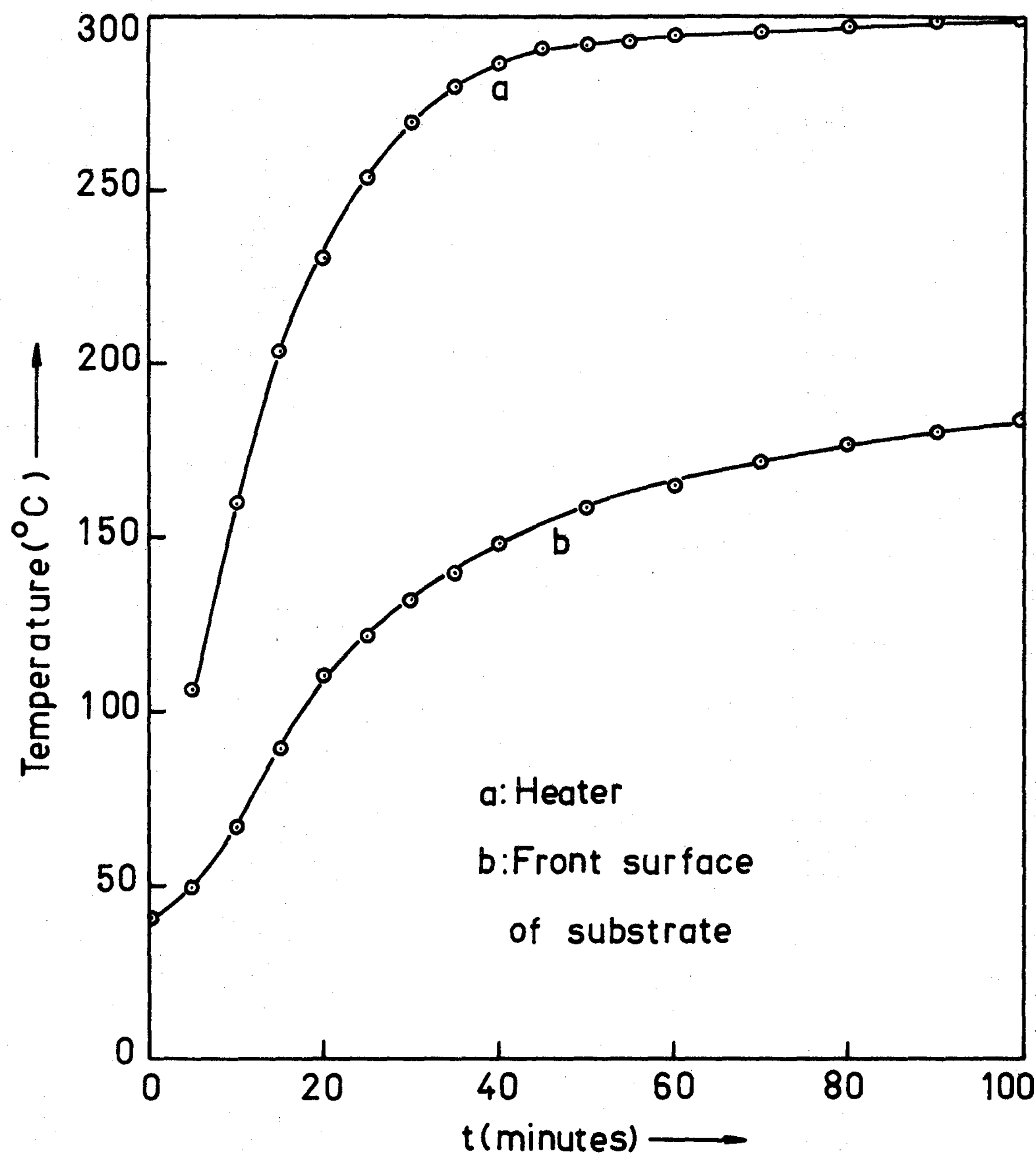

Figure 5.5 Comparison between the Temperature of the Front Surface of the Substrate as obtained by the Thermistor and the Temperature of the Heater.

5.5 The Electron Beam Evaporation System

An electron beam evaporation system was installed in the vacuum system in order to achieve the high temperatures necessary for the evaporation of Y_2O_3 and Si_3N_4. A Veeco Model VeB-6 electron beam gun system was chosen because of its small size, absence of magnetic focussing and because no water cooling is necessary. It is a self-accelerated, fixed focus Pierce-type gun with a maximum beam power of 6 kw at 300 mA. Three voltages, namely 11kV, 15kV and 20kV are available. As the beam diameter remains constant at 1/8" for about 2" from a point 2" from the face of the unit, allignment of the gun is not critical.

The six-position turret head carrying the materials allows one to evaporate any one of six materials with the gun.

In addition to the facilities described in the previous paragraphs, the gun was also equipped with a pulsing unit and a rate controller, details of which are described in Appendix B. The pulsing unit switches the high voltage on and off for various lengths of time while keeping the filament current constant. This is very useful for evaporating alloys and compounds with widely differing vapour pressures. The rate controller is an SCR-unit which adjusts the filament current in order to keep the evaporation rate constant.

5.6 Evaporation Sources and Materials

5.6.1 Cadmium Sulfide

Cadmium sulfide was evaporated from a boron nitride crucible heated externally by a molybdenum crucible heater. Best results may be obtained if the CdS, which comes in a powder form, is compressed and then

outgassed in vacuum for a period of up to 45 minutes. If the outgassing is not performed slowly, so much gas will be liberated that the material will be ejected from the crucible. Electron beam evaporation of CdS had been attempted, but it was found that big particles are ejected, presumably because of electrostatic charges.

The vapour pressures of cadmium and sulfur differ by nearly four orders of magnitude (refer to Chapter 7). This causes CdS to dissociate according to the reaction[20]:

$$CdS\ (solid) \rightarrow Cd\ (vapour) + \tfrac{1}{2}S_2\ (vapour)\ .$$

In addition, the sticking coefficients of Cd and S_2 onto the substrates differ significantly and are strong functions of the substrate temperature. All these factors control the eventual stoichiometry of the film condensing on the substrate.

The CdS used in this work was evaporated at a rate of approximately 10Å/second onto a substrate held at temperatures in the vicinity of 100°C.

5.6.2 Yttrium Oxide

The evaporation temperature of Y_2O_3 is approximately 2300°C as determined by an optical pyrometer. For this reason an electron beam system was used for its evaporation.

The Y_2O_3 powder (obtainable from Alfa Inorganics 99.9% purity) is compressed into pills of approximately 1/4" diameter. These pills are then placed in a boron nitride crucible which is heated externally by a tungsten basket to facilitate outgassing and simultaneously to prevent a thermal shock when the electron beam is turned on too quickly.

The ambient atmosphere during the evaporation is not critical. Films evaporated in a 10^{-4} torr oxygen ambient did not differ significantly from films evaporated in a 10^{-4} torr nitrogen atmosphere. This is quite contrary to what was observed for silicon monoxide. This point will be discussed in Chapter 6.

The Y_2O_3 films were deposited at a rate of 2 to 5Å/seconds onto a substrate held at room temperature. Every 1000Å the evaporation was interrupted for approximately two minutes. This gave the ambient gas a chance to interact with the film, but most importantly for the gun and surroundings to cool down.

5.6.3 Silicon Monoxide

Silicon monoxide lumps were evaporated in an oxygen atmosphere and the subsequently deposited film used as a dielectric in some of the devices made during the initial stages of this project. It was also used as a protective cover over some of the finished devices.

The properties of the evaporated SiO-films depend strongly on the evaporation conditions, i.e., evaporation rate, gas ambient, source temperature, substrate temperature, etc.

The material used was obtained from Ladd Research Industries. The lumps, approximately 1/16" to 1/8" diameter, were evaporated from a baffled molybdenum source to avoid spitting of discrete particles onto the film. This may cause pinholes.

Below follows a summary of the properties of evaporated SiO as a function of the evaporation parameters[41].

<u>Pressure < 10^{-5} torr oxygen</u>

Rate:

1-5Å/sec: Porous, low-density films are formed which oxidize quickly in air to colorless films which have the characteristics of SiO_2.

6-12Å/sec: These films have an amber colour and a density comparable to bulk SiO.

25-30Å/sec: The film density exceeds that of SiO, and it may be a solid solution of Si and SiO_2.

<u>Pressure: 10^{-4} torr oxygen</u>

Clear films result and they consist possibly of SiO_2 and higher phases like Si_2O_3.

The relative dielectric permittivity and dielectric loss are functions of the ratio of the molecular impingement rates of O_2 and SiO on the substrate[49]. They are independent of the absolute values of pressure or rate within the ranges 2×10^{-5} torr to 2×10^{-4} torr and 10Å/sec. to 110Å/sec. When this ratio, α, is less than 1 (excess SiO), the dielectric loss increases sharply. The dielectric loss is a decreasing function of α.

Therefore, films formed at high rates or low O_2 pressures (α<1) have high dielectric loss due to the free Si content. Films deposited at low rates and in high O_2 pressures (α>1) contain a greater percentage of the higher oxides like SiO_2 and Si_2O_3. The free Si content is lower and dielectric losses are therefore lower. The relative dielectric permittivity, however, is also lower ($3.5 \leq \varepsilon_i \leq 4.5$).

The source temperature T_b and the substrate temperature T_s also determine the concentration of the higher oxides in the film, as well as mechanical stresses. A low source temperature (<1250°C) and a low substrate temperature cause high tensile stress, but the films are stable in vacuum. The tensile stress changes slowly to compressive stress when exposed to moisture or oxygen. This causes a lifting or peeling-off of the films.

Typical evaporation conditions of SiO

T_b = 1300°C

T_s = 100°C

P = 10^{-4} torr O_2

Rate = 1-4Å/sec.

The material was evaporated from a baffled molybdenum boat. These films were baked in air at 300°C for approximately thirty minutes. This had the effect of relieving the mechanical stresses and reducing the dielectric loss. The dissipation factor varied between 0.01 and 0.4 in the audio frequency range, and the relative dielectric permittivity was approximately 3.9.

5.6.4 Silicon Nitride

Evaporated silicon nitride films may be used as protective covers for devices. The diffusion coefficient for impurities, e.g., sodium, is much lower than in the case of SiO_2 for instance[50].

Electronic grade silicon nitride powder (obtained from Alfa Inorganics) were compressed into 1/4" diameter pills and evaporated from

a boron nitride crucible. The crucible is heated externally by a tungsten basket for more than thirty minutes to outgas the crucible and the Si_3N_4 before the evaporation with the electron beam commences. The substrate has to be heated ($\doteq 100^{o}C$ in this work) to get mechanically stable films[51]. Baking afterwards in air also serves the same purpose.

5.6.5 Nichrome

Nichrome is a very widely used material for the fabrication of thin-film resistors. It consists of an 80% nickel - 20% chromium alloy.

It has a higher bulk resistivity than chromium and its temperature coefficient is closer to zero. Both the resistivity and the temperature coefficient of resistance depend on the film thickness and evaporation conditions[54].

The bulk resistivity of nichrome is approximately 107 μΩ-cm. Due to the large defect concentration, the polycrystalline nature and the effects of surface scattering, the resistivity of thin films is higher than the bulk value. Below 100Å thickness, the resistivity of nichrome increases rapidly as the thickness is reduced. In addition, probably due to tunneling between discrete islands, the temperature coefficient of resistivity becomes negative.

It has been shown[55] that

$$\sigma_F = \sigma_o(\nu)e^{-\frac{\Delta E_n}{kT}}$$

where

σ_o = function of the tunneling probability

ΔE_n is the energy separation between the nth and $(n+1)^{th}$ energy levels in an island. It is a function of the number of islands.

σ_F = conductivity of the discontinuous film.

Therefore

$\alpha = \frac{1}{\rho}\frac{\partial \rho}{\partial T} \leq 0$ = temperature coefficient of resistivity (see also chapter 6 in ref. 45).

The resistive films (100-200Å in thickness) used in this work were formed by the evaporation of nichrome wire from tungsten filaments. The evaporation temperature is between 1450 to 1600°C. If the substrate is not heated, the resistance of the films may change significantly after they have been removed from the vacuum system. In order to stabilize them, the finished devices were baked for periods of up to sixteen hours at 300°F. It was usually found that the resistance would go up by a few percent. This was possibly due to oxidation.

5.6.6 Aluminum

Aluminum films were used as contacts on the resistive films of the URC-filters. This ensures a uniform current flow through the structure. In addition, aluminum films were used to make ohmic contact to the CdS films. Aluminum is known to make ohmic contact to CdS if it is evaporated on top of the CdS[80]. If the aluminum is evaporated from a tungsten basket, contamination of the aluminum film may take place possibly due to the formation of a tungsten-aluminum compound[43]. For this reason, aluminum was evaporated only once from a tungsten basket after which the basket was replaced with a fresh one.

The aluminum was evaporated from a tungsten basket at a rate of approximately 10Å/sec. The substrate temperature was not an important parameter.

5.6.7 Gold

Gold also forms an ohmic contact if the CdS is evaporated on top of it.[80] It was used in some of the devices.

It may be evaporated quite readily from an open molybdenum boat, but it has a tendency to attack the boats after a few evaporations.

A purity of 99.999% of gold was obtained from Materials Research Corporation and evaporated at a rate of approximately 10Å/second. The substrate temperature is not very important.

5.7 Mask Construction[43]

A thin-film device consists usually out of a multilayer structure of different materials with different geometries. These geometries may either be defined during the deposition of the films by means of a series of metal masks, or after deposition by means of chemical etching, etc. The first mentioned approach was followed in this thesis because it allows one to make a complete device without breaking vacuum.

The six masks used for this purpose each consisted of a mask blank made from 1/16" stainless steel plus a small 1/2" x 1/2" copper plate, 0.003" thick, spotwelded onto the hole in the centre of the mask blank. This copper sheet formed the mask proper while the stainless steel provided the mechanical rigidity and the precision holes necessary for positional alignment between the different masks.

The desired pattern was drawn twenty times full scale on "Ulano" plastic on a coordinatograph, photographed, step-and-repeated if necessary, and reduced to the proper size. Two crosses on the master drawing served as references between the different masks. Holes were punched, corres-

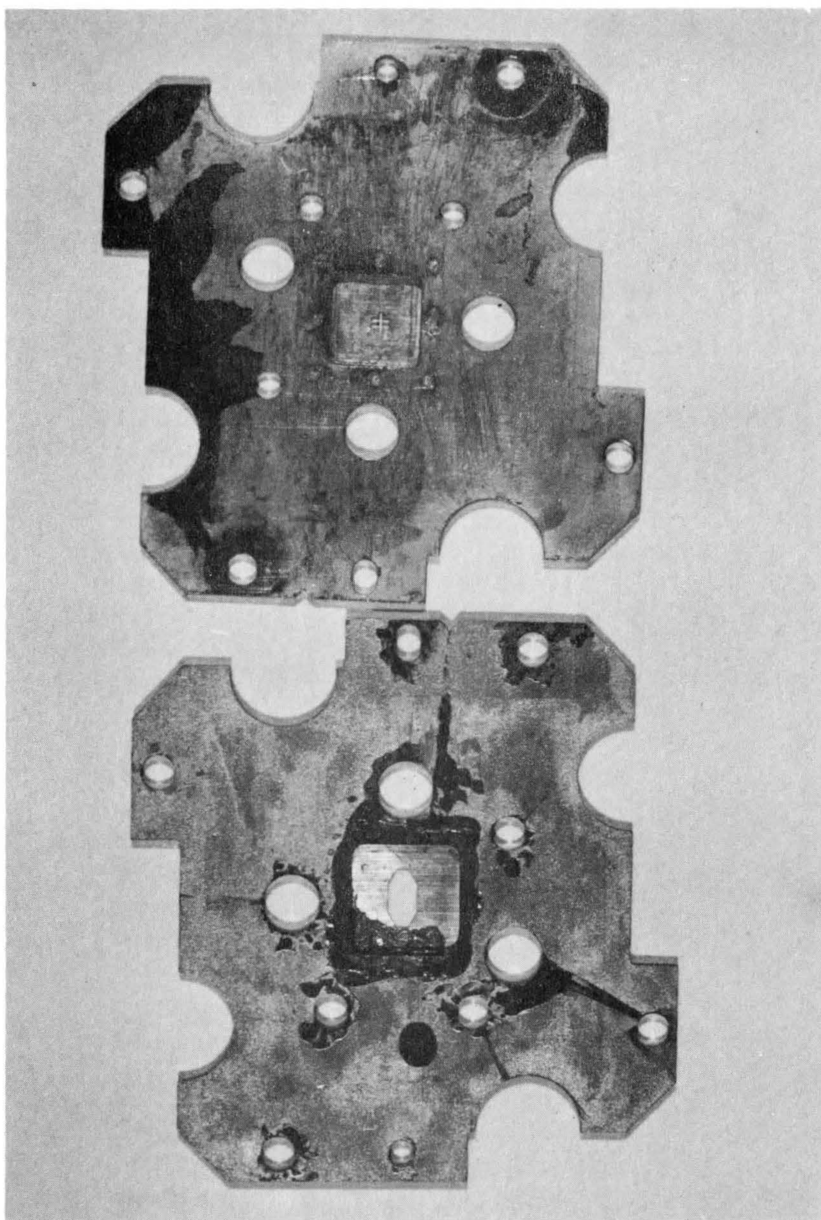

Figure 5.6 Photograph of Two of the Masks. The Upper One Defines the Semiconductor Geometry in the Hall-Effect Sample. The Lower Mask Determines the Shape of the Conducting Electrode of a URC-Filter.

ponding to these crosses, in a special punch.

The desired pattern was obtained on the mask blank by coating it with a thin layer of Kodak Thin Film Resist (KTFR). The negative was placed on top of the mask blank in a special jig and then exposed. After developing the photoresist, the copper may be etched electrochemically in an ammonium persulphate bath. Alternatively, the copper may first be nickel plated before the undesired parts are etched away. The last mentioned approach was only followed in the case of the delicate Hall-sample masks where the undercutting of the copper during the etch may be undesirable. Details about all the processes discussed above were given by Vallo, reference 43.

Figure 5.6 shows photographs of two of the masks.

CHAPTER 6

The Vacuum Evaporation of Yttrium Oxide

6.1 Introduction

Recent work[56] on yttrium oxide thin-films indicated that such films have generally excellent electrical properties. The high value for the relative dielectric permittivity, mechanical stability when out of vacuum, and low dielectric losses, make this material particularly well suited to their application in thin-film circuits. A concise account will be given in this Chapter on the methods of depositing Y_2O_3 thin-films and on its physical and electrical properties.

6.2 Techniques for Producing Thin Y_2O_3 Films

Various methods for depositing thin Y_2O_3 films have been described in the literature. These methods range from the anodic oxidation of thin yttrium metal films as described by Rairden[58] and Goldstein[59] to a spray technique using acetylacetonates developed by Frank and Groth[63]. Goldstein[60] and Goldstein and Wigginton[61] also prepared these films by reactive sputtering and r.f. sputtering respectively.

Campbell[56] and Tsutsumi[57] were the first to study the properties of electron beam evaporated Y_2O_3 thin-films. This was also the technique chosen in this thesis because of its convenience and compatibility with the preparation of other materials in the same vacuum system during the same pump-down cycle.

The properties of the films depend in general on the deposition techniques used. Table 6.1 summarizes the electrical properties of Y_2O_3 films as obtained by various workers.

TABLE 6.1

Electrical Properties of Yttrium Oxide Thin Films

(After C.K. Campbell, Ref. 56)

Fabrication Method	Dissipation factor tanδ (at 25°C and 1kHz)	Temperature Coefficient of Capacitance (p.p.m./°C)	Relative Dielectric Permittivity	Breakdown field strength ($V/cm \times 10^6$)	Electrical Resistivity (Ω-cm)
Electron Beam Evaporation (56)	0.00255±0.00002	+320 ± 50	13.5 ± 1.5	2.8 ± 0.3	$>2 \times 10^{14}$
R.F. Sputtered (61)	0.003	+200	11.0	2.4	-
Reactively Sputtered (66)	0.004	+240	15.1 ± 0.2	3.5	-
Anodized (66)	0.008	+375	17.1 ± 0.8	4.4	-
Bulk Y_2O_3 (67)	0.0013	-	11.10	-	-

All the above mentioned processes, except the electron beam technique, suffer either from the drawback of relatively high losses in the case of anodized films, or long processing time and the inability to produce the insulator and the other materials in the same pump-down cycle.

The electron beam technique produced films with the lowest losses so far. It may also be used in the same vacuum system that the other materials are deposited in, and films may be produced in a fairly short time with a minimum of preparation.

Campbell[56] described the electron beam evaporation of Y_2O_3 in detail. His technique was slightly modified for this work in that the boron nitride crucible was not cooled externally and, secondly, it was found that the ambient of 10^{-4} torr oxygen is not very important. The air bake after the evaporation seemed to be a much more important process.

6.3 Mechanisms of Evaporation

Ackermann, et al[62] did mass-spectrometric studies of Y_2O_3 vapour from a tungsten Knudsen cell. They found that the gaseous species was composed of YO, O and a small amount of free Y. A study of the evaporated material left in the cell after the evaporation revealed a very small deficiency of oxygen, so that the material left could be described as $Y_2O_{2.996}$. X-ray and electron diffraction studies by Tsutsumi[57] failed to reveal any of the sub-oxide YO in his evaporated thin films.

The above evidence probably indicates that Y_2O_3 in the solid phase evaporates predominantly by the following reaction:

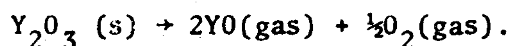

$$Y_2O_3\ (s) \rightarrow 2YO(gas) + \tfrac{1}{2}O_2(gas).$$

The sub-oxide YO is oxidized to the sesquioxide Y_2O_3 upon reaching the substrate. It was found in this work that the ambient

atmosphere in the bell-jar of the vacuum system did not play an important part in determining the dielectric losses of the resulting films. Filters were deposited using either 10^{-4} torr oxygen or 10^{-4} torr nitrogen. This presumably confirms the fact that the amount of free yttrium evaporated is small and secondly, that the free suboxide in the resulting film does not influence the dielectric properties significantly. This, however, has to be investigated more fully in order to make a definite statement.

The substrate temperature also seems to be unimportant in determining the dielectric properties of the films.

Even though Tsutsumi heated his substrates to $250^{o}C$, while Campbell's had not been, the dielectric properties of the resulting films were very much the same. These are given in Table 6.2.

The fact that the Y_2O_3 films do not contain free Y probably accounts for the low dielectric losses in evaporated films. This is quite the contrary to what may be observed for other insulators, e.g., evaporated SiO. As was pointed out in Chapter 5, the evaporation rate and ambient oxygen pressure determine to a great extent the amount of free Si in SiO films. Evaporated SiO-films made during the course of this research, had dissipation factors varying from 0.04 at 1kHz to 0.4 at 20kHz. Also, the occurence of Si, SiO, SiO_2 and Si_2O_3 in the same film is not uncommon.

Table 6.2 A Comparison Between Electron Beam Evaporated Y_2O_3 Films Using Different Evaporation Conditions

	Evaporation rate (Å/sec)	Substrate Temperature (°C)	Ambient	Thickness (Å)	Electrodes	Substrate	Relative Dielectric Permittivity (ε')	Dissipation Factor at Room Temperature (tanδ)	Temperature Coefficient of Capacitance (p.p.m./°C)	Breakdown Field Strength (V/cmx10^6)	Electrical Resistivity (Ω-cm)
Campbell[56]	2	not heated	10^{-4} torr Oxygen	2000 - 15,000	Al-Au	Glazed Alumina	13.5±1.5	0.00255	320	2.8	$>2\times10^{14}$
Tsutsumi[57]	2	250	5×10^{-6} torr	1200 - 5000	Al-Al	Borosilicate Glass	13.0	0.003	300	3.0	$\doteqdot 10^{15}$

6.4 Structural Properties of Electron Beam Evaporated Y_2O_3 Films

Electron diffraction patterns of thin (500 Å) Y_2O_3-films studied by Tsutsumi[57], indicated that the films are polycrystalline, with the crystallites body centred cubic. In addition, they also showed that the evaporated films didnot contain any suboxide. The importance of this point has been discussed in the previous paragraph.

6.5 Electrical Properties of Y_2O_3 Films Deposited for this Work

Y_2O_3 films with thickness between 3000Å and 4000Å have been evaporated using the electron beam technique. Both nitrogen and oxygen have been used as the ambient gas for different samples. No significant difference in the electrical properties of these two types were observed. The two types of electrodes which were used, namely Al-Y_2O_3-Al and Al-Y_2O_3-Au also did not seem to be of prime importance in determining the dielectric losses, leakage current and relative dielectric permittivity. Most of the following results will be for Al-Y_2O_3-Al capacitors with the Y_2O_3 evaporated in 10^{-4} torr N_2.

It was generally found that baking of the completed devices in air improved the dielectric losses. Figure 6.1 shows the dramatic reduction of the losses by one order of magnitude for an air bake of 2½ hours at 300°F. A further bake of an additional 1½ hours at 300°F and 14 hours at 400°F reduced the dissipation factor $\tan\delta$ another 25% to approximately 0.004.

It may be seen from figure 6.1 that the dissipation factor is relatively constant with frequency. This is to be expected for an

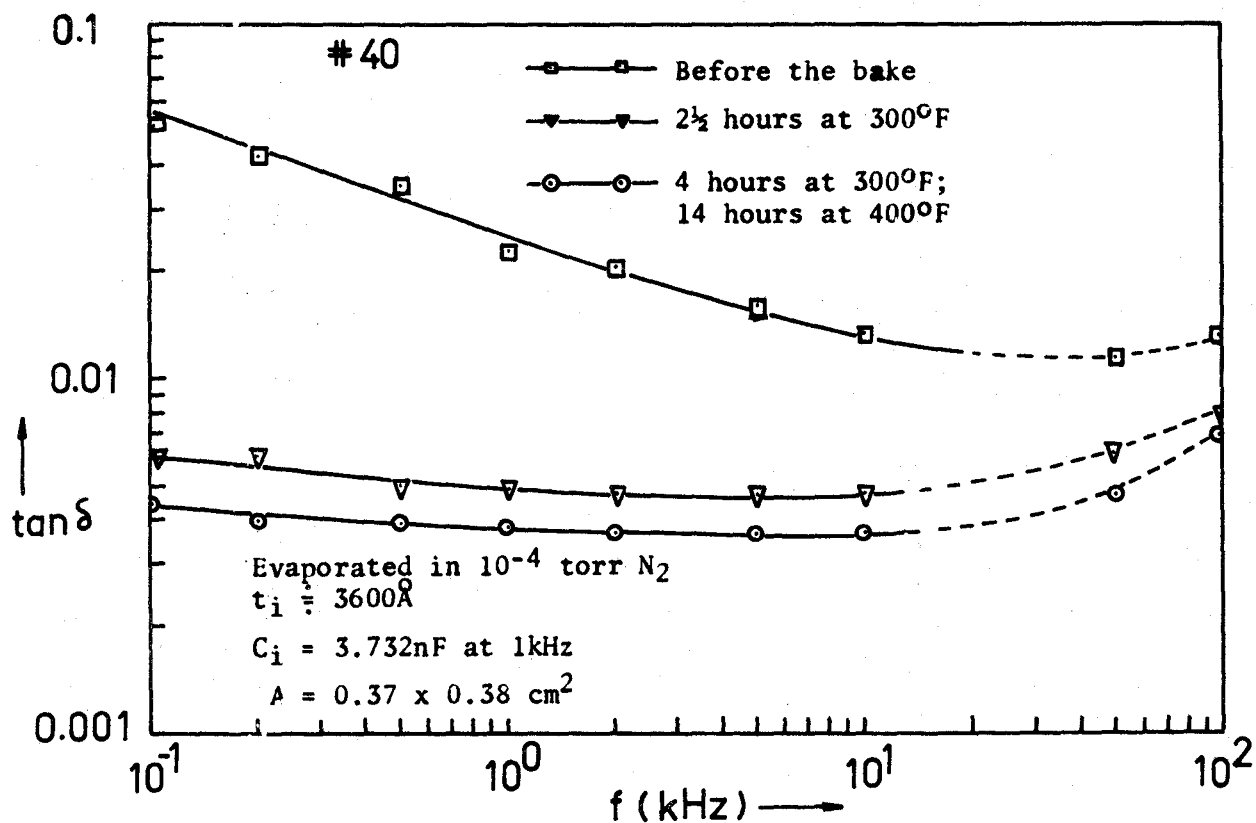

Figure 6.1 Dielectric Losses in an $A\ell$-Y_2O_3-$A\ell$ Capacitor as a Function of the Post-Evaporation Treatment.

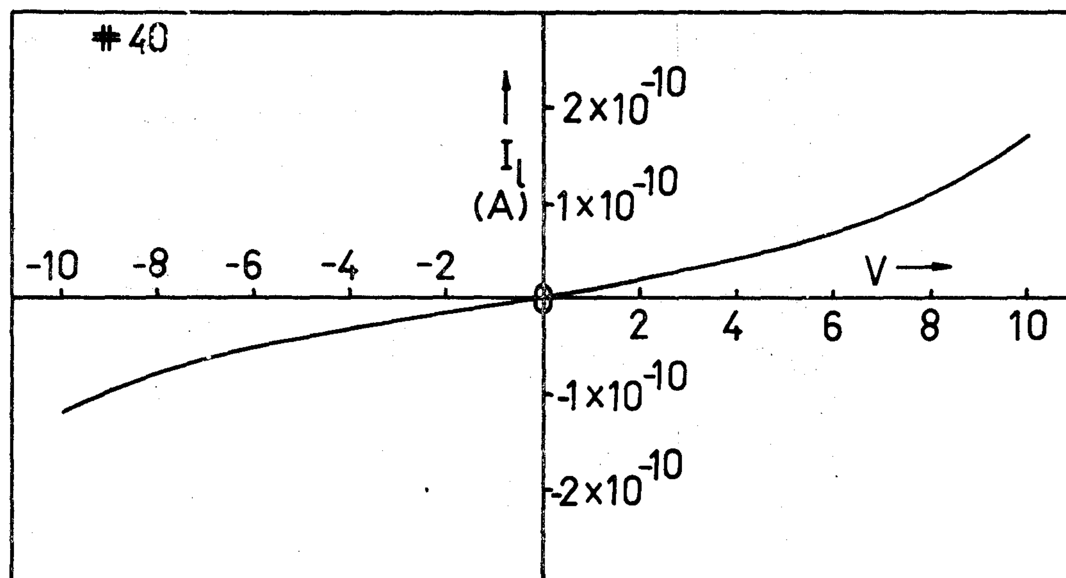

Figure 6.2 Leakage Current in Device #40 after the Bake in air.

evaporated film with a large number of defects and therefore a distribution of relaxation times. The section of the dissipation curve at high frequencies seems to increase with increasing frequency. This is possibly due to electrode and lead resistance which had not been compensated for. This may be quite important for the large capacitance values of nearly 4 nF which had been used in these measurements, as may be shown by the following calculation:

$$\tan\delta = \tan\delta' + \omega R_s C_s$$

where

$\tan\delta$ = measured dissipation factor

$\tan\delta'$ = dissipation factor of the dielectric

R_s = parasitic series resistance

C_s = capacitance of the structure.

If C_s = 4nF, f = 1MHz and R_s = 1Ω, then $\omega R_s C_s$ = 0.025 which may be considerably larger than the value of $\tan\delta'$.

Figure 6.2 shows the fairly low leakage currents obtained for Y_2O_3 films. In the linear portion of the curve, i.e., V<5V, the resistivity turns out to be approximately 4×10^{14}Ω-cm, which is of the same order of magnitude as the value obtained by Campbell[56]. This value goes down to about 2×10^{14}Ω-cm at 10V.

The value of relative dielectric permittivity for Y_2O_3 has been determined to be approximately 11.0. Figure 6.3 shows the interference fringes for a 4000Å Y_2O_3 film. The undeformed line spacing corresponds to 2945Å, which is the half wavelength of the sodium line. The average value of the thickness of that particular Y_2O_3 film turned out to be 4002Å ± 145Å. Using the parallel plate capacitance formula with

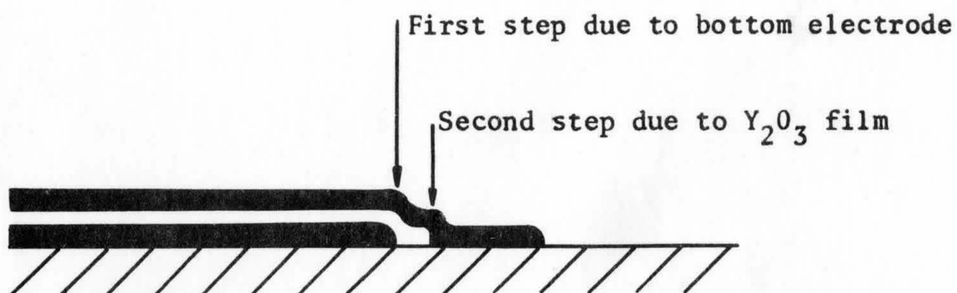

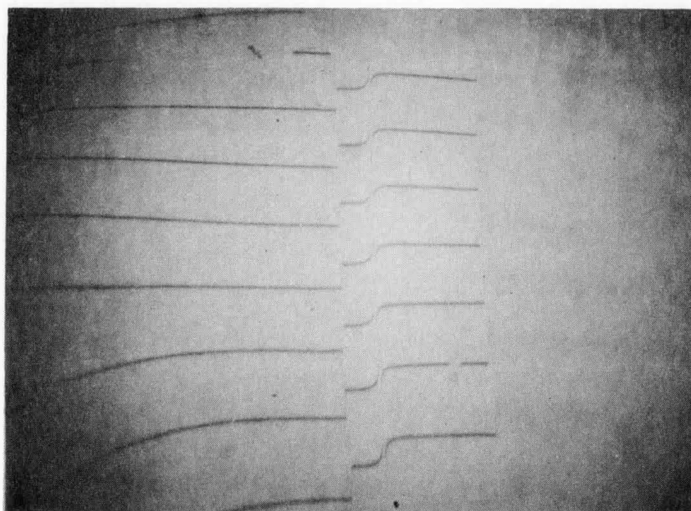

Figure 6.3 Interference Fringes for an Al-Y_2O_3-Al Sandwich. The Y_2O_3 Film is 4000Å Thick. The Undistorted Line Spacing Corresponds to 2945Å. (Half-Wavelength of the Sodium Line.)

$A = 0.38x0.37\ cm^2$, the relative dielectric permittivity turned out to be: $\varepsilon_i = 10.8 \pm 0.4$.

6.6 Conclusion

The properties of electron beam evaporated yttrium oxide thin-films make them particularly well suited for use in thin-film electronic circuits. Of these, the low dielectric losses, the high value of the relative dielectric permittivity and the low leakage currents are the most important for distributed circuits.

The overall qualities of the evaporated dielectric materials may be compared by using a Figure of Merit F.

$$F = \frac{10^{-9}}{\tan\delta} \varepsilon_i E_b$$

where ε_i = real part of the relative dielectric permittivity

E_b = breakdown field strength in V/cm

$\tan\delta$ = dissipation factor.

If we use Campbell's data for electron beam evaporated Y_2O_3 films, F turns out to be

$$F/Y_2O_3 = 14.8 \quad .$$

Evaporated films of SiO and SiO_2 have Figures of Merit of 0.4 and 4 respectively. (Chopra, Ref. 45, p. 472.)

CHAPTER 7

The Vacuum Evaporation and Properties of Cadmium Sulfide Thin-Films

7.1 Introduction

Cadmium sulfide is a material with very desirable properties for a large number of applications. It has found application in photoconductors[75], solar cells[83], electroluminescent panels[84], piezo-electric transducers[46], infrared detectors, thin-film diodes and field-effect transistors[80], lasers, etc. Despite this impressive list of applications, many properties of CdS, especially in its non-single crystal form, are not well understood at all. It is not the purpose of this section to give all the explanations, but rather to point out the problems, and above all, to emphasize the useful properties of this material.

It was one of the first semiconductors to be used for vacuum evaporated thin-film field-effect transistors[80]. Its high resistivity, ease of vacuum evaporation, and the wide control of the electrical properties of the evaporated films by simple means, made it a very attractive material for thin-film devices. We will review the methods of depositing CdS thin-films in the first part of this Chapter. In the last part the physical and electrical properties will be considered with emphasis on the difficulties in characterizing this material. A considerable section will deal with the Hall-field effect for its importance in studying the mobility and measuring the carrier concentrations.

7.2 Preparation of CdS Thin-Films

The techniques for depositing CdS thin-films may be divided into two distinct categories, namely vacuum- and non-vacuum techniques. We will only be interested in the vacuum deposition processes. The other techniques, e.g., the sintered-layer method, the chemical-spray process, etc., are described elsewhere[78].

Several alternatives exist for the vacuum evaporation of CdS. The most important ones of these processes are:

(i) Sputtering: (a) RF sputtering of CdS

(b) Reactive sputtering of Cd in H_2S atmosphere.

(ii) Evaporation by resistive heating:

(a) Single source

(b) Multiple source.

We will only be interested in the evaporation by resistive heating for its importance to this thesis.

(a) Single Source

The single source evaporation technique is probably the most widely used. Polycrystalline CdS powder or pieces are placed in a boron nitride crucible (this work) and heated externally until the temperature is sufficiently high (600 - 1000°C) to get a vapour pressure which is high enough to allow evaporation at a reasonable rate. (Alumina coated molybdenum sources have also been described in the literature[78].) The evaporant then condenses on a heated glass or ceramic substrate. CdS molecules dissociate upon vaporization according to the reaction[81]:

$$CdS \text{ (solid)} \rightleftharpoons Cd \text{ (vapour)} + \tfrac{1}{2}S_2 \text{ (vapour)} .$$

In an ideal thermodynamic steady state the evaporation rates of cadmium and sulfur are the same. In practice, this is not the case due to the large difference in vapour pressure of cadmium and sulfur[76] (nearly four orders of magnitude). (See Figure 7.1.) The upper layers of CdS are depleted of sulfur and the diffusion from the bulk is too slow to allow stoichiometric evaporation.

The molecular beam composed of Cd and sulfur in some ratio, strikes the substrate which is located in its path. Depending on the substrate temperature, the atoms and molecules will diffuse on the surface of the substrate until they reach a nucleation site. Those that do not reach a nucleation site in time will be re-evaporated from the substrate.

The rate of condensation of either element from the vapour is determined by the temperature of the substrate. De Klerk[46] found that if sulfur is evaporated on its own, it will not stick to the substrate if the substrate temperature $T_s > 50^oC$. Cadmium, on the other hand, sticks preferentially if $T_s > 200^oC$. If both species are present, a film will be formed[46] in this range of 50 to 200^oC. In this range the deposition rate is determined by the lower of the two vapour pressures, i.e., Cd in this instance.

The widely differing vapour pressures[76] of cadmium and sulfur, and their temperature sensitive sticking coefficients[82], result in a non-stoichiometric film on the substrate. The doping density is determined principally by this non-stoichiometry. It is well known that sulfur vacancies (excess of Cd) act as donors[103] with an activation energy[47] of approximately 0.03 eV.

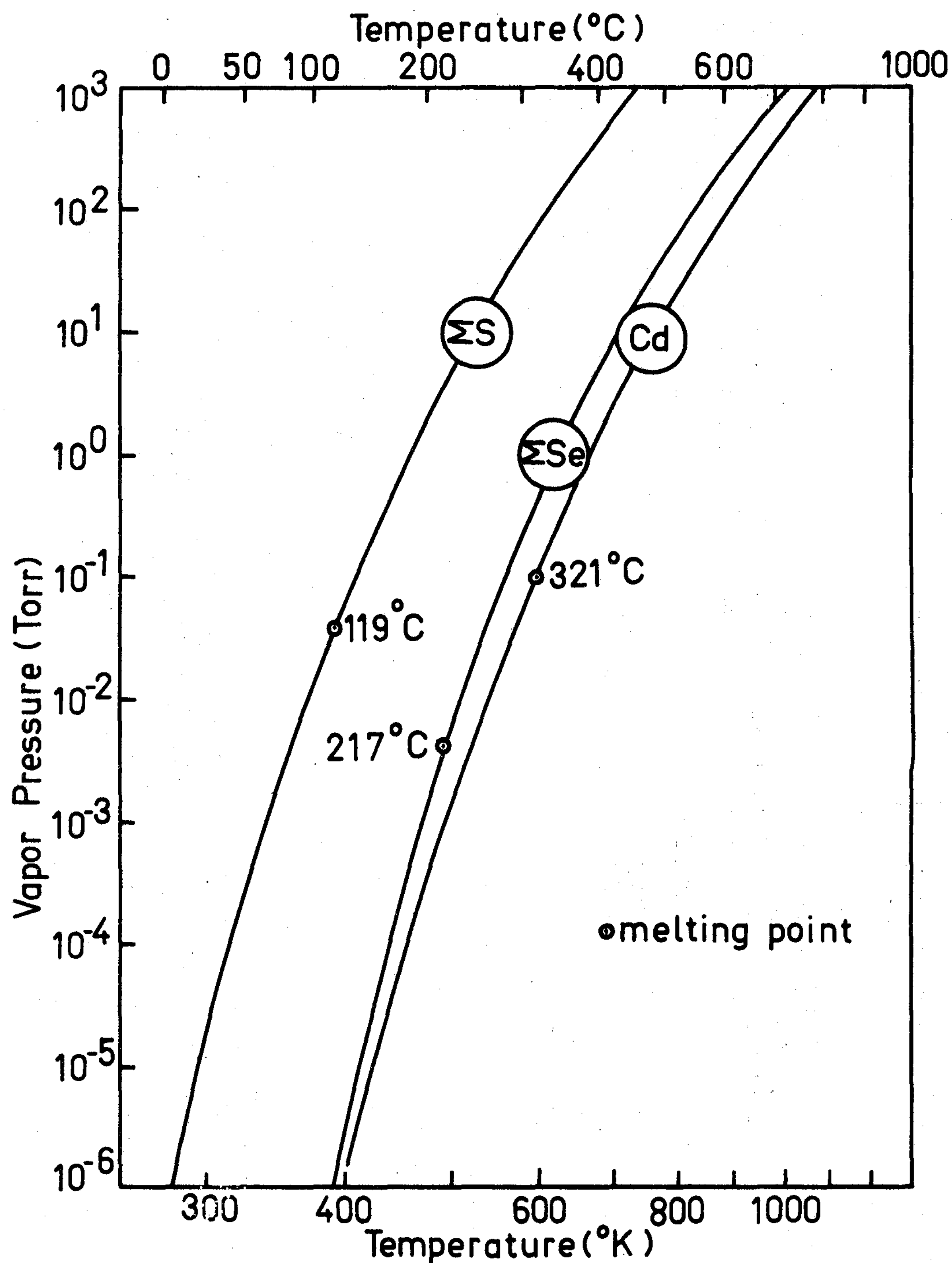

Figure 7.1 Equilibrium partial vapor pressures of sulfur, cadmium and selenium as a function of temperature. (After Honig, Ref. 76.)

Dresner and Shallcross[77] found that the resistivity is a strong function of the substrate temperature. Films evaporated onto a substrate held at room temperature have an excess of Cd and consequently a low resistivity, as low as 0.1 Ω-cm. The resistivity keeps increasing with increasing substrate temperature until the sticking coefficients are so low that it takes an unreasonably long time for a film to be deposited. These investigators reported resistivities up to 10^6 Ω-cm for films evaporated onto substrates held at 340°C.

The initial step in the condensation process is the adsorption of Cd and $\frac{1}{2}S_2$ from the vapour phase on the substrate. Following an argument by Neugebauer[47], one may postulate that the ratio of Cd to S_2 in the resulting film will be a function of the adsorption energy of Cd and S_2 on the substrate. Thus, if the flux of Cd and $\frac{1}{2}S_2$ is the same, the ratio of Cd atoms to adsorbed $\frac{1}{2}S_2$ is proportional to:

$$\exp\left\{\frac{E_{ad}(Cd) - E_{ad}(S_2)}{kT}\right\}$$

where $E_{ad}(Cd)$ = adsorption energy for Cd,

and $E_{ad}(S_2)$ = adsorption energy for S_2.

If $E_{ad}(Cd) > E_{ad}(S_2)$, then the excess of cadmium atoms becomes smaller as the substrate temperature is increased.

There is also a dependence of the resistivity on the source temperature. It is reduced as the source temperature is increased. Neugebauer, et. al[47], made a study of the resistivity of fairly thick (10,000 Å) CdS films as a function of the substrate temperature. Their results are summarized in Figure 7.2.

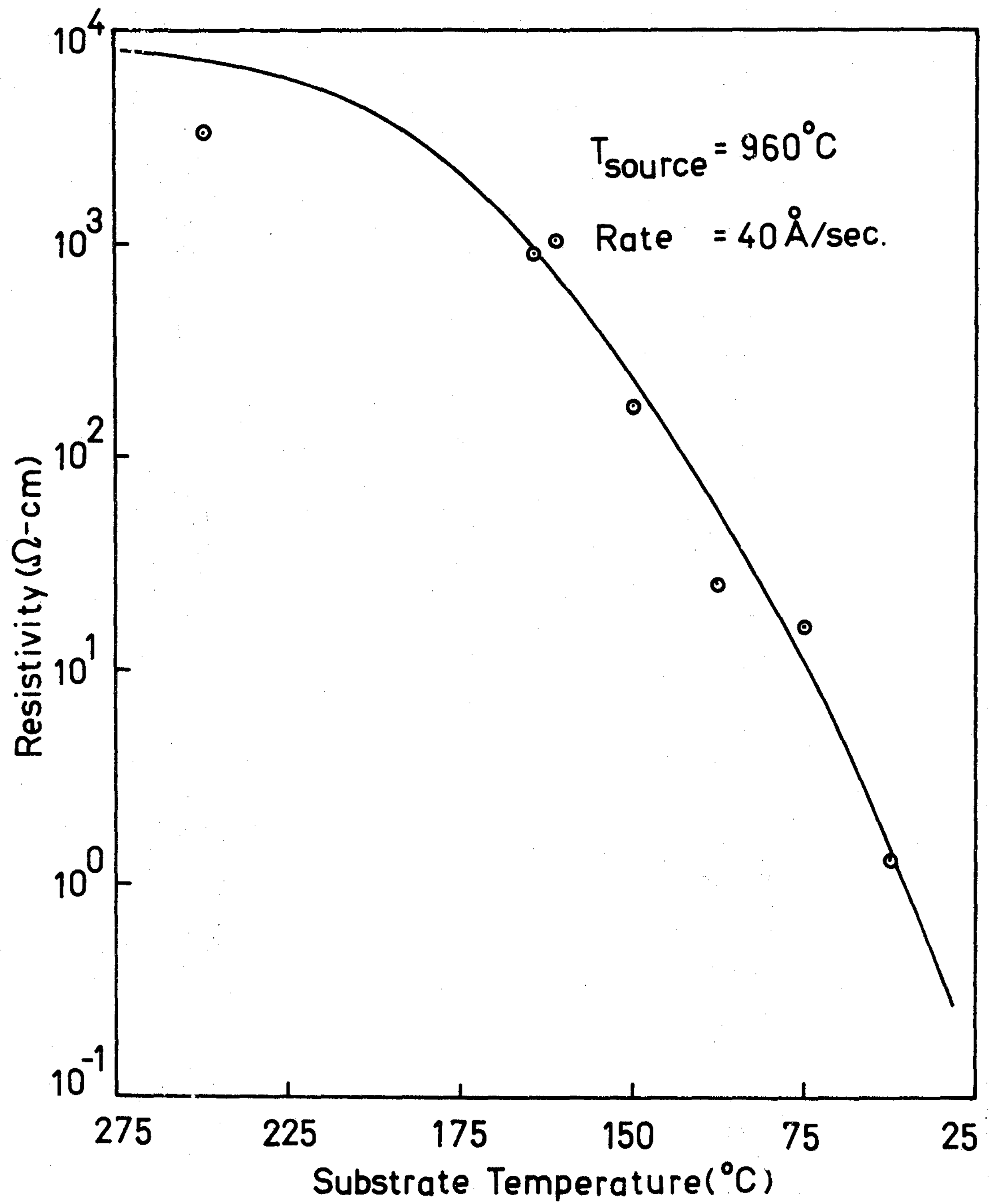

Figure 7.2 Resistivity of Evaporated CdS as a Function of the Substrate Temperature. (After Neugebauer, ref. 47)

Evaporated films are usually polycrystalline[77] due to the large number of randomly distributed nucleation sites on an amorphous substrate. The average size of the crystallites increases with increasing substrate temperature[77]. The average diameter of crystallites in the films evaporated for this work was of the same order as the thickness of the films. Although the films are polycrystalline, a preferred orientation of the hexagonal crystals (for $T_s > 150^oC$) was observed[46,68,69,78,79]. In nearly all the investigations it was found that the crystallites had their c-axes perpendicular to the substrate.

(b) Multiple Source Evaporation

Whereas useful semiconducting CdS may be prepared by the evaporation of CdS powder onto a heated substrate, the deposition of good piezo-electric films is rather more complex as De Klerk[46] pointed out.

These films have to have a high resistivity in addition to being well oriented, i.e., the wurtzite structure with the c-axis perpendicular to the substrate.

As previously indicated, the low resistivity is caused by a sulfur deficiency in the films. Pizzarello[85] increased the resistivity by coevaporating sulfur with the CdS. He used a source temperature of 95^oC for the sulfur crucible and between 600 and 700^oC for the CdS crucible. When evaporating onto substrates held at between 200 and 300^oC, he succeeded in increasing the resistivity of the films to 10^7 Ω-cm. Although these films were semi-insulating, their crystallographic orientation prevented the generation of pure compressional or

pure shear modes. This leads to the development by De Klerk[46] of a new method for producing highly insulating (up to 10^{12} Ω-cm resistivity) well-oriented CdS thin-films. Two separate sources of Cd and S are used and the temperature of each is controlled separately. Instead of having a molecular beam inpinging on the heated substrate, a baffle is placed between the sources and the substrate. The substrate temperature is the most important parameter[82] in the evaporation technique.

7.3 Post-Evaporation Treatments

Efforts to restore the bulk electrical and optoelectronic properties of CdS into evaporated thin-films of this material, gave impetus to a study of the recrystallization and post-evaporation treatments of the films. The differences between the properties of the evaporated thin-film and the bulk single crystal material are believed to be mainly due to the structure and the composition of the thin-film. Various techniques have been described in the literature for obtaining the desired properties in the films. A brief summary of the most important ones will be given below.

(a) Gilles and Van Cakenberghe Recrystallization Process[86]

Metals from Group I (e.g., Ag or Cu) which act as donors in CdS, were found to induce crystal growth at elevated temperatures. Gilles and Van Cakenberghe evaporated approximately 100Å of Ag onto an evaporated film of CdS and heated the sandwich between 500 and 600°C. They discovered that a marked recrystallization took place. It was also found that halogens such as Cℓ will help the diffusion of the Group I metals into the CdS.

Dresner and Shallcross[69] who used the Ag-recrystallization process also discovered that the density of deep traps is reduced by more than an order of magnitude, while the resistivity and mobility are increased.

(b) Embedding Technique

Gans[87] described a method whereby the activators (in the case of photoconducting films) may be introduced by heating the film while it is packed in a bed of CdS powder which contains the necessary activator, e.g., Cu. As has been pointed out in the previous section, the diffusion of the activator may be enhanced by introducing a halogen into the system. The halogen simultaneously enhances the photoconducting properties by acting as a sensitizer[75]. The embedding technique also enhances crystal growth.

Böer, et. al[70], applied this process in order to produce good photoconducting CdS thin-films. They evaporated 1μ thick CdS films onto glass slides held at 180°C. These films were packed in a bed of CdS and Cu powder in a tube furnace. By heating it between 600°C and 650°C for about 30 minutes in the presence of N_2, O_2 and HCℓ, a marked recrystallization took place. The oxygen was introduced to enhance the crystal growth. The crystallites increased in average diameter from less than 1000Å to more than 10μ.

Böer, et. al[70], also discovered that the electrical properties of the recrystallized layers can be varied over a wide range by changing the processing parameters. The partial pressure of O_2 and HCℓ, the

treatment temperature and the % Cu were found to be the most important parameters. These films had a low trap density, high sensitivity for modulated light, low noise spectrum and a high photoconductive gain.

Dresner and Shallcross[69] used this method of diffusing acceptor impurities into evaporated CdS thin-films. They performed the baking in an argon or air atmosphere between 250 and 500°C from 1 to 90 hours. The CdS powder was luminescent grade doped with copper or silver as acceptors, and with Ga or Cℓ as donors. They also found that oxygen accelerated the recrystallization process.

(c) Organometallic Techniques

Heating of evaporated II-VI films in an inert organic liquid, e.g., silicone fluid, containing traces of organometallic compounds, e.g., copper diethyldithiocarbamates, lead to recrystallization and activation of the films. Vecht[79] observed large crystallites which were photo-conductive.

Nearly all the techniques described above necessitate the removal of the substrate from the vacuum system after the evaporation of the CdS has occured. This may be undesirable, for it may lead to unnecessary contamination. This is especially true in the case of the organometallic techniques. For that reason, all the devices made for the purpose of this thesis were first completed before air bakes were performed on them.

7.4 Physical and Electrical Properties of Evaporated CdS Films

The evaporation conditions and post-evaporative treatments have drastic effects on the physical and electrical properties of CdS thin-films. Evaporated films usually have low mobilities[100], high trap densities[69] and they are polycrystalline[69].

In films with no post-evaporative treatment, the size of the crystallites, their orientation, the doping density of the film and the mobility of the electrons, depend on the conditions during the evaporation. The substrate temperature and surface features, the deposition rate, the source temperature, the ambient gases present in the vacuum system, all are important in determining the properties of the film.

The density of nuclei, for example, depends on the substrate temperature. Experiments by Dresner and Shallcross indicated that the size of the crystallites increases as the substrate temperature is increased.

The crystallographic phases present, for instance, also depend on the substrate temperature. De Klerk[46] found that between 180°C and 200°C the hexagonal wurtzite structure was present, while at lower temperatures both the cubic and hexagonal phases were present. Shallcross[78] differs from De Klerk in that he observed the hexagonal phase only above 300°C.

Evaporated CdS films have a preferred orientation[46,69], namely the c-axis is perpendicular to the substrate.

The electrical properties are primarily determined by the structure, the deviations from stoichiometry and impurities present.

Evaporated CdS is invariably[71,72,78] n-type, and the doping density is determined to a great extent by the stoichiometry. The absence of p-type CdS is probably due to the fact that the hole mobility is low, the effective mass high, and the acceptor states deep lying[78]. Group VII and III elements, e.g. Cℓ, Aℓ, Ga and In act as donors, while Group I elements, e.g., Cu, Ag, Au, K and Na act as acceptors[71]. Increasing the acceptor concentration will lead to higher and higher resistivities until the material becomes insulating. It is also believed that sulfur vacancies, or an excess of Cd, act as donors.

Chemisorbed oxygen also influences the electrical properties significantly. It acts as a deep lying donor[78].

Films deposited during the course of this work were polycrystalline with the average crystallite size of the same order as the thickness of the film, i.e., a few thousand angstrom. The electron Hall mobility was of the order of 1 $cm^2 - V^{-1} sec^{-1}$ and the doping density between 10^{16} and 3×10^{17} cm^{-3}. There is a lot of problems attached to the determination of the Hall mobility and the free electron concentration as will be described in the next section.

Evaporated CdS films are characterized by large trap densities[69, 74], in the order of 10^{19} - 10^{21} cm^{-3}, compared to 10^{14} - 10^{16} cm^{-3} for single crystal CdS. The trap densities may be determined by the method of Thermally Stimulated Currents as described by Bube[88] or the "Wechsellichtmethode" of Niekish[89,90]. Dresner and Shallcross[69] used the TSC method on evaporated CdS films to determine the effect of various treatments on the trap densities. Their results are summarized

Table 7.1

Source	Process	Crystallite size (μ)	Electron Mobility cm^2-$V^{-1}sec^{-1}$		Total Trap Density (cm^{-3})	Energy Range (eV)	Electron Life-time	Trapping Levels (From C.B.)
			Light	Dark				
Dresner and Shallcross[69]	Evaporated on 170°C substrate; no other treatment.	0.1-0.3	2-10	1-5	10^{19} — 10^{21}	0.1 — 0.33eV	-	Broad Distribution
	170°C substrate; baked in CdS:Cu for 90 hours at 250°C.	0.2-0.5	35-100	35-100			-	
	170°C substrate; baked in CdS:Cu for 1.5 hours at 400°C.	1-2	35-100	3-25			-	
	170°C substrate: baked in CdS:Cu for 4.5 hours at 400°C.	7-10	160-340	15-30			-	
	170°C substrate: re-crystallized by Gilles & Van Caken-berghe Process (Ag) at 520°C.	0.1-0.5cm	70-230	-	$6x10^{19}$ 10^{17}-10^{18}	< 0.2 0.4-0.6	-	
Böer, Feitknecht and Kannenberg[70]	Recrystallized at 630°C in N_2, HCℓ, O_2 and Cu atmosphere.				$3x10^{11}cm^{-3}eV^{-1}$ $4x10^{17}cm^{-3}$	0.3-0.4 0.65	30μsec	2.36, 2.25, 2.13, 2.00, 1.76, 0.65, 0.35

in Table 7.1. They could not measure traps lying deeper than about 0.3 eV from the conduction band in most samples, because the dark current becomes larger than the thermally stimulated current at high temperatures. Nevertheless, it is evident that there exists a broad distribution of traps in the bandgap of evaporated CdS. Niekisch[89,90], on the other hand, did experiments with sinusoidally modulated light on single crystal CdS. He found a set of discrete trapping levels at 0.12, 0.22, 0.31, 0.4 -- 0.45, 0.55 -- 0.65, 0.7 -- 0.8 eV with densities between 10^{13} and 10^{16} cm^{-3} - eV^{-1} and capture cross-sections between 1.5 x 10^{-15} and 4 x 10^{-14} cm^2.

In summary it may be said that evaporated films of CdS contain large densities of traps distributed throughout the whole of the bandgap. These may influence the device behaviour directly as in the case of opto-electronic devices, or more subtly as in the case of tunable distributed filters.

Wide discrepancies exist in the published data on the physical constants of single crystal CdS. A comparison of a few is shown in Table 7.2. For calculations in this thesis, the following values were assumed. (300^0K)

$\varepsilon_s = 10$

$m_e = 0.17$

$m_h = 0.6$

$E_g = 2.42$ eV

$E_d = 0.03$ eV .

<u>Table 7.2</u>

Some of the Physical Constants of Single Crystal CdS

($T = 300^{o}K$)

Source	Static Dielectric Permittivity	Effective Mass		Donor Ionization Energy E_d(eV)	Bandgap (eV)	Mobility	
		m_e	m_h			μ_n cm^2-$V^{-1}sec^{-1}$	μ_p cm^2-$V^{-1}sec^{-1}$
Sze[4], p.21	10	0.17	0.6	-	2.42	300	50
Hannay[71]	6.5-17.7 (average= 11.6)	0.25 (p.292) 0.2-0.4 (p.587)		0.01-0.02 (p.586)	2.5 (p.52)		
Abrikosov, et al[72].		0.1-0.3	0.4-0.5		2.4		
Piper & Halsted (Prague Conference (1960) p. 1046)[73]	9.2	0.16		0.032 ± 0.002			

7.5 Hall Mobility and Free Carrier Density Determination in Evaporated Thin-Films of CdS

Evaporated CdS thin-films are generally difficult to characterize. Great care must be exercised in interpreting Hall-effect data which may be used to obtain free carrier densities and Hall mobility. These difficulties arise from the following sources, to mention just a few:

(a) The evaporated films are generally not uniform, i.e., the doping density may vary from the first deposited layers through the film to the last atomic layers. This is possibly caused by the fact that the evaporation source becomes rich in the less-volatile component (Cd) as the evaporation proceeds, and secondly, the sticking coefficients of the component vapours are changing as the evaporation proceeds.

(b) Adsorbed and chemisorbed atoms and molecules on the surface, surface states, etc., cause either an accumulation or depletion layer at the surface. If the thickness of the film is not much greater than a Debye length, this will cause a significant error in the determined carrier density.

(c) The determined mobility may be in error due to the distributed nature of the space charge layer. This point will be discussed further on in greater detail.

7.5.1 Proposed Experiment for Determining Doping Densities and Transport Properties of Thin Semiconductor Films

An essentially new experiment will consequently be described for determining the doping density and Hall mobility in thin uniformly doped semiconductor films. A knowledge of the transport properties of carriers in thin semiconductor films is of great importance to thin-film devices, such as field-effect transistors for example. This method is a modification of an experiment performed by Waxman, et al[100].

The structure differs from Waxman's[100] in that it is symmetric. In other words, it consists of a semiconductor film sandwiched between two insulating and two metal films. It is therefore an MISIM-structure. The structure is shown schematically in Figures 7.3 and 7.4. The two metal plates are connected electrically and are used as field-plates, to change the semiconductor surface potential on both surfaces of the film. This particular configuration has been chosen because the potential distribution inside the semiconductor is symmetric with respect to the mid-plane and may be solved quite readily. The potential distribution is shown schematically in Figure 7.5.

A small voltage is applied between the contacts A_1 and A_2 and a magnetic field perpendicular to the surface of the film. The Hall voltage $V_{H_1H_2}$ or $V_{H_3H_4}$ is then measured as a function of the surface potential. The conductance of the semiconductor film may simultaneously be determined by measuring the voltage $V_{H_3H_1}$ or $V_{H_4H_2}$, and the current $I_{A_1A_2}$.

If the thickness of the semiconductor film is of the same order as the Debye length, the potential V_o in the centre of the film will, in

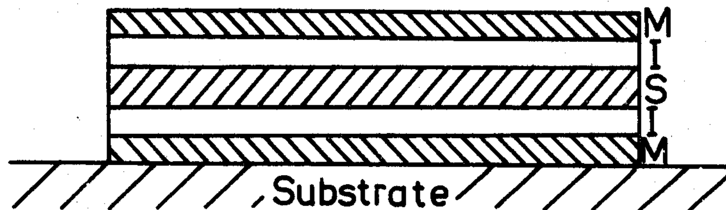

Figure 7.3 Cross-Sectional View of MISIM Structure

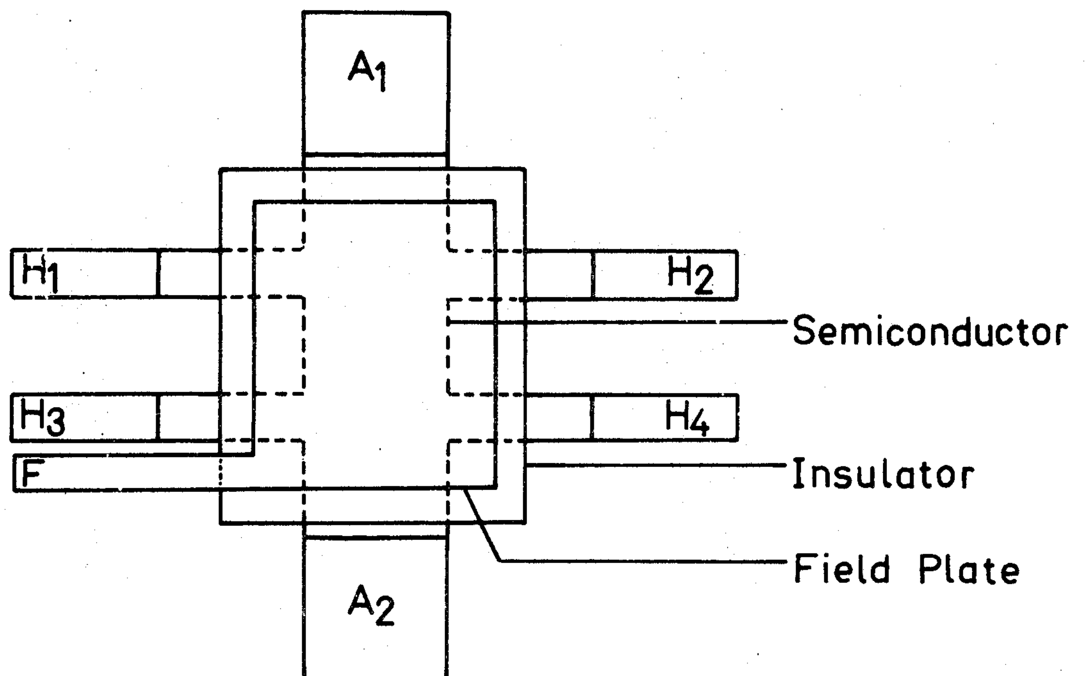

Figure 7.4 Top-view of Hall-Field Effect Configuration
F ≡ field plate.
A_1, A_2 ≡ contacts to establish a current in the semiconductor.
H_1, H_2, H_3, H_4 ≡ Contacts for measuring Hall voltage and determining conductivity.

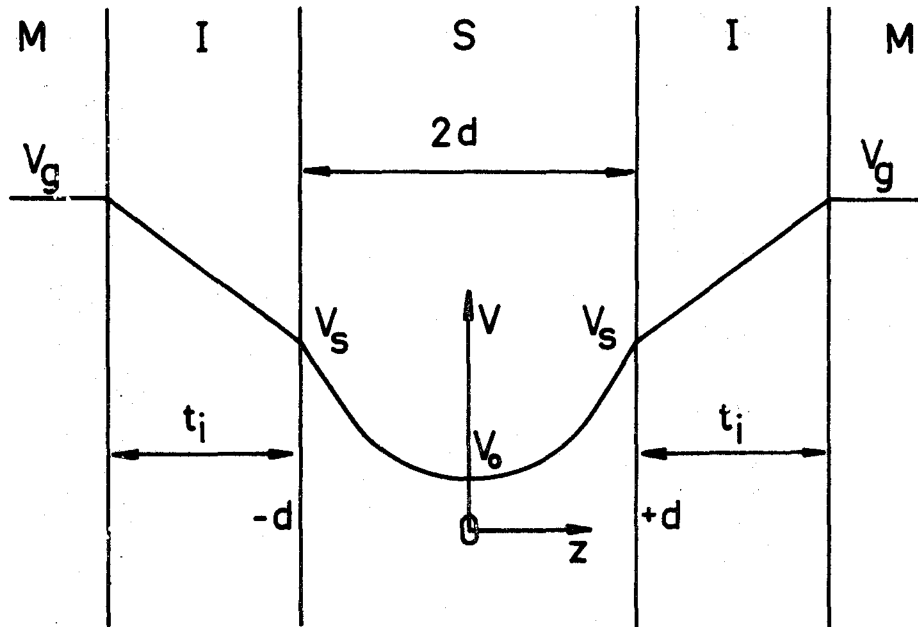

Figure 7.5 Potential Distribution in the Ideal MISIM-Structure

general, not be equal to zero[93].

The potential distribution may be obtained by solving Poisson's equation under the appropriate boundary conditions.

If we neglect all surface and bulk states, and assume that $p, N_a << n, N_d$, Poisson's equation becomes:

$$\frac{d^2V}{dz^2} = \frac{-\rho}{\varepsilon_s} = \frac{-q(N_d-n)}{\varepsilon_s} \quad . \tag{7.1}$$

Say $$n = N_d \cdot e^{\frac{qV}{kT}} \tag{7.2}$$

$$\therefore \quad \frac{d^2\phi}{dz^2} = \frac{1}{L_D^2}(e^{\phi}-1)$$

where $\phi = \frac{qV}{kT}$

and

$$L_D = \sqrt{\frac{\varepsilon_s kT}{q^2 N_d}} = \text{Debye length} \quad . \tag{7.3}$$

But $$\frac{d^2\phi}{dz^2} = \frac{1}{2}\frac{d}{d\phi}\left(\frac{d\phi}{dz}\right)^2 \; .$$

Therefore: $$\frac{d}{d\phi}\left(\frac{d\phi}{d\lambda}\right)^2 = e^{\phi}-1$$

where $$\lambda = \frac{\sqrt{2}z}{L_D} \quad . \tag{7.4}$$

At $\lambda=0$, $$\frac{d\phi}{d\lambda} = 0 \text{ and } \phi = \phi_o \tag{7.5}$$

$$\therefore \quad \frac{d\phi}{d\lambda} = \pm\sqrt{e^{\phi} - \phi + \phi_o - e^{\phi_o}}$$

$$= \pm F(\phi,\phi_o) \tag{7.6}$$

where the + sign holds for $\lambda > 0$.

Equation (7.6) may be integrated:

$$\text{For } \lambda>0: \quad \int_0^{\lambda_d} d\lambda = \lambda_d = \int_{\phi_o}^{\phi_s} \frac{d\phi}{\sqrt{e^{\phi}-\phi-e^{\phi_o}+\phi_o}} \quad . \tag{7.7}$$

This integral cannot be evaluated analytically, except under certain simplifying assumptions. We will treat two different cases:

(i) $\phi_s, \phi_o, \phi \ll 1$

$$\therefore \quad e^{\phi}-\phi-e^{\phi_o}+\phi_o \doteq 1+\phi+\frac{\phi^2}{2}-\phi-(1+\phi_o+\frac{\phi_o^2}{2})+\phi_o$$

$$\doteq \frac{\phi^2-\phi_o^2}{2}$$

$$\therefore \quad \lambda_d \doteq \int_{\phi_o}^{\phi_s} \frac{\sqrt{2}\, d\phi}{\sqrt{\phi^2-\phi_o^2}} \quad . \tag{7.8}$$

From the CRC Abridged Mathematical Tables:

$$\int \frac{dx}{\sqrt{x^2-a^2}} = \ln(x+\sqrt{x^2+a^2}) \quad .$$

Therefore, equation (7.8) becomes:

$$\lambda_d \doteq \sqrt{2}\, \ln\left(\frac{\phi_s}{\phi_o} + \sqrt{\left(\frac{\phi_s}{\phi_o}\right)^2 - 1}\right) \quad . \tag{7.9}$$

It may be seen from this expression that ϕ_o is proportional to ϕ_s, i.e., ϕ_o versus ϕ_s will be a straight line for a constant λ_d.

For thick films with $\phi_s \ll 1$, but $\phi_s \gg \phi_o$, (7.9) may be simplified further.

$$\phi_o \doteq 2e^{\frac{-\lambda_d}{2}} \cdot \phi_s \quad . \tag{7.10}$$

(ii) $\phi_s, \phi_o, \phi >> 1$

These conditions will hold when $\lambda_d<<1$ and $\phi_s>>1$. Under these circumstances $e^{\phi}>>\phi$, $e^{\phi_o}>\phi_o$:

$$\therefore \qquad \lambda_d \doteq \int_{\phi_o}^{\phi_s} \frac{d\phi}{\sqrt{e^{\phi}-e^{\phi_o}}} \quad . \tag{7.11}$$

Say $e^{\phi}=\eta$ and $e^{\phi}d\phi=d\eta$. Equation (7.11) then becomes:

$$\lambda_d = \int_{\eta_o}^{\eta_s} \frac{d\eta}{\eta\sqrt{\eta-\eta_o}} \tag{7.12}$$

where $\eta_o = e^{\phi_o}$.

From the Tables of Integrals:

$$\int \frac{dx}{x\sqrt{a+bx}} = \frac{2}{\sqrt{-a}} \tan^{-1}\sqrt{\frac{a+bx}{-a}} \qquad \text{for } a < 0$$

$$\therefore \qquad \lambda_d \doteq \frac{2}{\sqrt{e^{\phi_o}}} \cdot \tan^{-1}\sqrt{\frac{e^{\phi_s}-e^{\phi_o}}{e^{\phi_o}}} \quad \text{for } \phi_s>>1,\ \lambda_d<<1 \quad . \tag{7.13}$$

Solving for ϕ_s

$$\phi_s \doteq \ln\left\{\frac{e^{\phi_o}}{\cos^2\left(\frac{\lambda_d}{2}\sqrt{e^{\phi_o}}\right)}\right\} \quad . \tag{7.14}$$

There is a pole at $\frac{\lambda_d}{2}\sqrt{e^{\phi_o}} = \frac{\Pi}{2}$

i.e., at $\phi_o=\phi_{os}=2\ln\left(\frac{\Pi}{\lambda_d}\right)$ (7.15)

This means that ϕ_o will saturate at a value ϕ_{os} for large ϕ_s.

(iii) Numerical Solution

Equation (7.7) cannot be solved analytically, but a numerical solution is possible.

$$\lambda_d = \int_{\phi_o}^{\phi_s} \frac{d\phi}{\sqrt{e^{\phi}-\phi-e^{\phi_o}+\phi_o}} \quad . \qquad (7.7)$$

The integrand has a branch point at $\phi=\phi_o$, but it is integrable. In order to do the integration let us separate (7.7) into two integrals

$$\lambda_d = \int_{\phi_o}^{\phi_o(1+\Delta)} \frac{d\phi}{F(\phi,\phi_o)} + \int_{\phi_o(1+\Delta)}^{\phi_s} \frac{d\phi}{F(\phi,\phi_o)} \qquad (7.16)$$

$$= I_1 + I_2$$

where $\Delta<<1$ and $F(\phi,\phi_o) = \sqrt{e^{\phi}-\phi-e^{\phi_o}+\phi_o}$.

Consider I_1:

$$I_1 = \int_{\phi_o}^{\phi_o(1+\Delta)} \frac{d\phi}{F(\phi,\phi_o)} \quad .$$

Near $\lambda=0$, i.e., $\phi=\phi_o$, ϕ can be expanded in a Taylor series:

$$\phi = \phi_o+\lambda\left(\frac{d\phi}{d\lambda}\right)\Bigg|_{\phi=\phi_o} + \frac{\lambda^2}{2}\left(\frac{d^2\phi}{d\lambda^2}\right)\Bigg|_{\phi=\phi_o} + \ldots$$

$$= \phi_o + \frac{1}{2}\lambda^2\phi_o'' \qquad \left(\frac{d\phi}{d\lambda} = 0 \text{ at } \phi=\phi_o \text{ because of symmetry.}\right)$$

$$\therefore \qquad \frac{d\phi}{d\lambda} = \lambda\phi_o'' \quad .$$

But $$\lambda = \sqrt{\frac{2(\phi-\phi_o)}{\phi_o''}} \quad .$$

From Poisson's Equation: $\phi'' = \frac{1}{2}(e^{\phi}-1)$

$$\therefore \qquad \phi_o'' = \frac{1}{2}(e^{\phi_o}-1)$$

$$\therefore \qquad I_1 = \int_{\phi_o}^{\phi_o(1+\Delta)} \frac{d\phi}{\sqrt{(e^{\phi_o}-1)(\phi-\phi_o)}}$$

$$= 2\sqrt{\frac{\Delta\phi_o}{e^{\phi_o}-1}} \qquad (7.17)$$

$$\therefore \qquad \lambda_d = 2\sqrt{\frac{\Delta\phi_o}{e^{\phi_o}-1}} + \int_{\phi_o(1+\Delta)}^{\phi_s} \frac{d\phi}{\sqrt{e^{\phi}-\phi-e^{\phi_o}+\phi_o}} \qquad (7.18)$$

where $\Delta \ll 1$.

The second part of equation (7.18) can be integrated numerically. This has been done and ϕ_o as a function of ϕ_s with λ_d as parameter is shown in Figure 7.6. For comparison, the second approximation for thin films with high surface potentials (equation (7.14)) is also shown.

7.5.2 Calculation of the Relationship Between the Measured Mobility and the Mobility of Electrons in the Film

It has been shown theoretically by Schrieffer[99] that the mobility of carriers in space charge layers in the vicinity of the

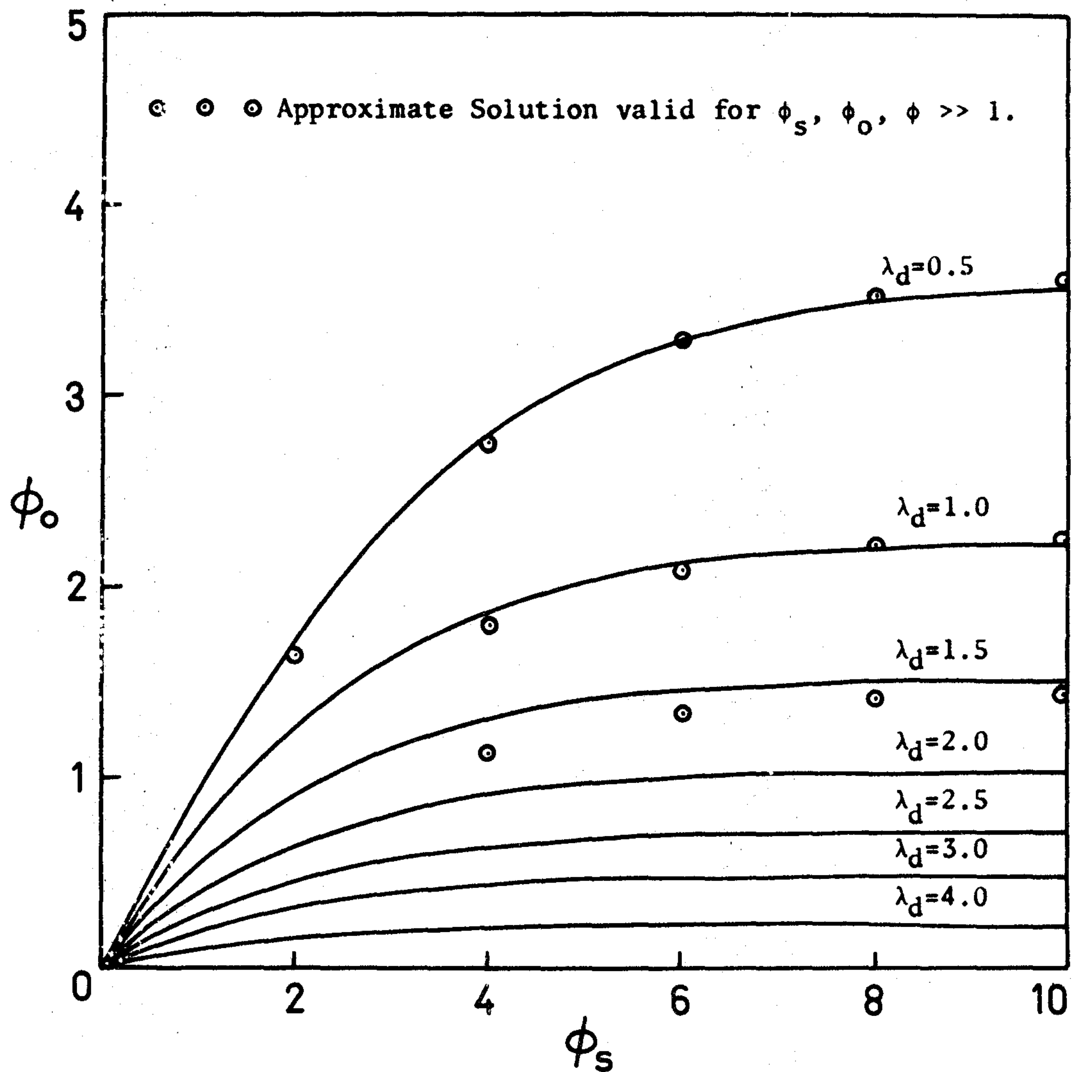

Figure 7.6 Mid-plane Potential ϕ_o as a Function of Normalized Surface Potential in a Symmetrical MISIM-Structure.

surface of a semiconductor is reduced due to diffuse surface scattering. The effects of ionized impurity scattering, intercrystalline barriers in the case of polycrystalline films[100], and surface phonons may also become important, in determining the mobility. It may therefore be said that $\mu=\mu(z,\phi_s,\phi)$ and $n=n(z,\phi_s,\phi)$, where n is the electron concentration in the space charge layer. (We are only considering accumulation layers in an n-type semiconductor film.) The current density in the x-direction between A_1 and A_2 is therefore a function of three variables:

$$j_x(z,\phi_s,\phi) = q\mu_n(z,\phi_s,\phi) \cdot n(z,\phi_s,\phi) \quad . \tag{7.19}$$

We are making the assumptions that the mobility is a localized function of the potential, and secondly that the voltage across A_2-A_1 is very small compared to V_g.

Suppose a magnetic field B_z is applied in the z-direction as shown in Figure 7.7. A Hall voltage V_h will be generated across H_1-H_2. Due to the fact that the current density and the conductance is a function of z, the total Hall voltage has to be calculated by integrating all the individual voltages generated across a section W·dz as shown in Figure 7.7.

The differential Hall voltage $v_h(z)$ appears in series with a resistance r(z), where r(z) is given by

$$r(z) = \frac{W}{q\mu \cdot n(z) \cdot \ell \cdot dz} \tag{7.20}$$

$$g(z) = \frac{1}{r(z)} = \frac{q\mu \cdot n(z) \cdot \ell \cdot dz}{W} \tag{7.21}$$

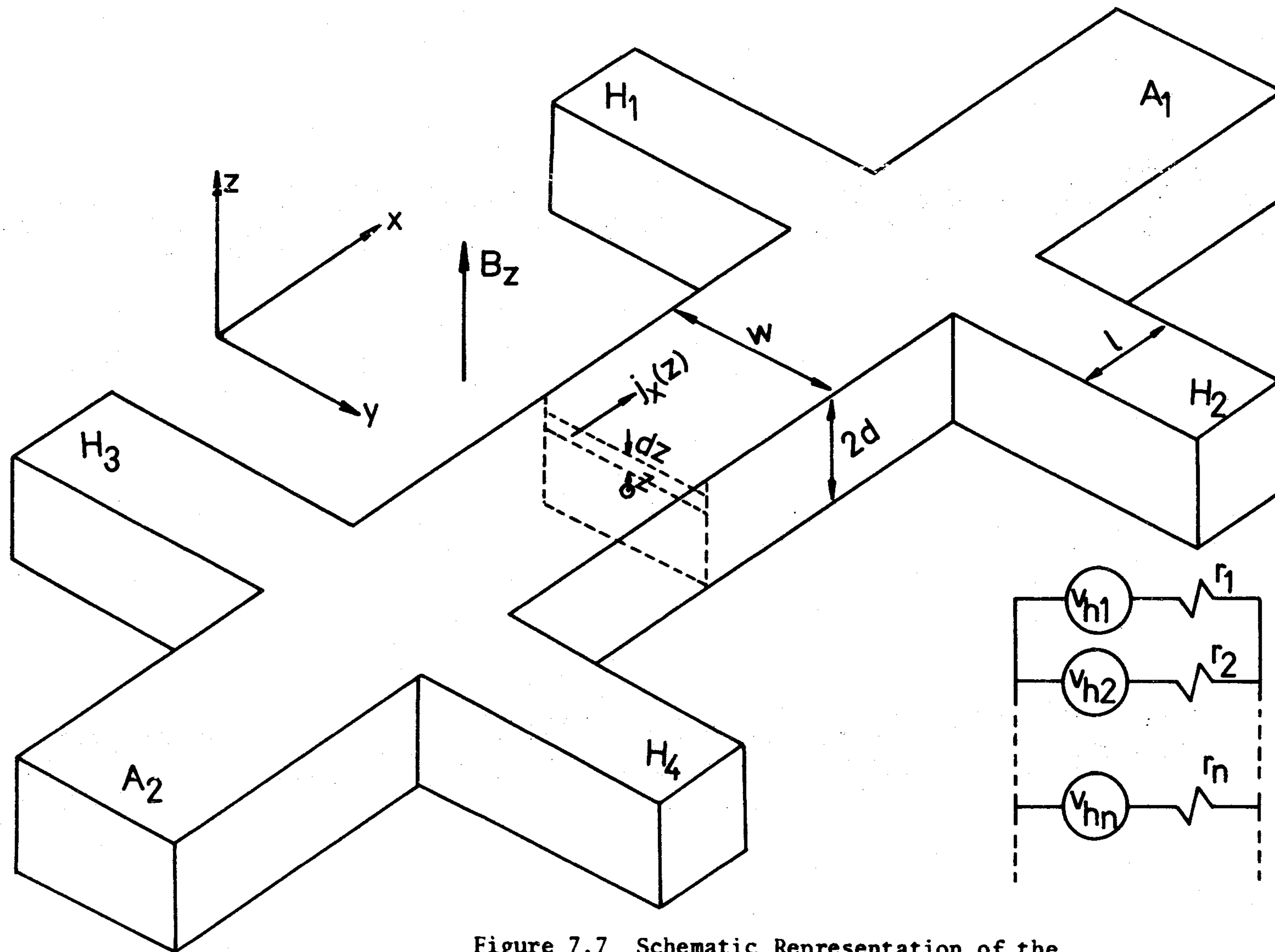

Figure 7.7 Schematic Representation of the Semiconductor in the Hall-Field Effect Sample.

where μ = drift mobility for electrons.

The differential Hall voltage is given by

$$v_h(z) = \mathcal{E}_y(z)w = \frac{j_x(z)\cdot rB_z w}{qn(z)} \quad . \tag{7.22}$$

But $\quad j_x(z) = q\mu\, n\mathcal{E}_x$

$$\therefore\ v_h(z) = r\mu\, B_z w\mathcal{E}_x$$

where r = scattering parameter (assumed to be 1).

If we convert the voltage sources to current sources, we may sum (integrate) them. The same procedure may be followed for the conductances.

$$I_h = \ell rqB_z\mathcal{E}_x \int_{-d}^{d} n\mu^2\, dz$$

and (7.23)

$$G = \frac{q\ell}{w}\int_{-d}^{d} n\mu\, dz$$

$$V_h = \frac{I_h}{G} = wrB_z\mathcal{E}_x \frac{\int_{-d}^{d} n\mu^2\, dz}{\int_{-d}^{d} n\mu\, dz} \quad . \tag{7.24}$$

But $V_h = \mathcal{E}_y w = \mathcal{E}_x r\mu\, B_z w = \mu_h'\, B_z\mathcal{E}_x w$

$$\therefore \quad \mu_h' = r\,\frac{\int_{o}^{d} n\mu^2\, dz}{\int_{o}^{d} n\mu\, dz} = r\,\frac{\langle n\mu^2\rangle}{\langle n\mu\rangle} \tag{7.25}$$

where $\quad \langle n\mu^2\rangle = \int_{o}^{d} n\mu^2\, dz$

and $$\langle n\mu\rangle = \int_o^d n\mu \, dz \quad .$$

The integrals appearing in (7.25) may be made with respect to ϕ by substituting the expression for $\frac{d\phi}{d\lambda}$ as obtained in equation (7.6) into (7.25).

Assume r=1:

$$\mu_h' = \frac{\int_{\phi_o}^{\phi_s} \mu^2 \frac{e^{\phi} \cdot d\phi}{\sqrt{e^{\phi}-\phi-(e^{\phi_o}-\phi_o)}}}{\int_{\phi_o}^{\phi_s} \mu \frac{e^{\phi} \cdot d\phi}{\sqrt{e^{\phi}-\phi-(e^{\phi_o}-\phi_o)}}} \tag{7.26}$$

We have made the assumption that μ, the parameter that we want to determine, is a function of the potential alone. This may not be the case in practice, especially for surface scattering. We are, however, not considering the region where surface scattering is of importance.

If we use the same procedure as that leading to equation (7.17), the integrals in (7.26) may be written in such a way as to remove the singularity at $\phi=\phi_o$.

$$\mu_h' = \frac{2\sqrt{\frac{\Delta\phi_o}{e^{\phi_o}-1}} \; e^{\phi_o}\mu^2(\phi_o) + \int_{\phi_o(1+\Delta)}^{\phi_s} \mu^2 \frac{e^{\phi} \cdot d\phi}{\sqrt{e^{\phi}-\phi-e^{\phi_o}+\phi_o}}}{2\sqrt{\frac{\Delta\phi_o}{e^{\phi_o}-1}} \cdot e^{\phi_o}\mu(\phi_o) + \int_{\phi_o(1+\Delta)}^{\phi_s} \mu \frac{e^{\phi} \cdot d\phi}{\sqrt{e^{\phi}-\phi-e^{\phi_o}+\phi_o}}} \quad . \tag{7.27}$$

By assuming a functional relationship for $\mu(\phi)$, μ_h' may be calculated quite readily using the expression for μ_h' in (7.27). This has been done for various examples and the results indicate that $\mu_h'(\phi_s)$ differs indeed by a significant amount from the assumed $\mu(\phi)$. Waxman, et. al[100], measured the electron Hall mobility in thin CdS films as a function of the field-plate voltage (asymmetric structure). They observed the mobility to increase quite rapidly for increasing field-plate voltages, until finally it saturated and then decreased. They explained the initial sharp increase in mobility by assuming a model consisting of semiconductor crystallites surrounded by highly insulating barriers. An increase of surface potential modulates the barrier heights and leads to an effective higher mobility. Using Bethe's[102] expression for the transmission of electrons through potential barriers, they derived an expression for the mobility of the form:

$$\mu = c \cdot \frac{a+\phi_s}{b+\phi_s} \quad . \tag{7.28}$$

μ_h' has been calculated for different values of λ_d using equations (7.27) and (7.28). These calculations showed that thicker films have a larger discrepancy between μ and μ_h'. This follows from the following argument: The thicker the film, the greater the difference between ϕ_s and ϕ_o as may be seen from Figure 7.6. The mobility of the carriers in the centre is therefore much lower than that of the carriers near the surface.

7.5.3 Calculation of μ when μ_h' is known

Equation (7.27) has been derived to indicate how the effective Hall mobility (the mobility that is measured by means of the Hall effect) may be calculated if the functional dependence between the carrier mobility and the potential in the semiconductor film is known. Ordinarily one would prefer to go the other way, i.e., measure μ_h' and calculate μ.

$$\mu_h' = \frac{\langle n\mu^2 \rangle}{\langle n\mu \rangle} \quad .$$

Experimentally one may obtain $\mu_h'(\phi_s)$ and $\langle n\mu \rangle$ which is proportional to the conductance. (We assume that ϕ_s may be obtained from V_g.)

$$\therefore \qquad \mu_h' \langle n\mu \rangle = \langle n\mu^2 \rangle \quad . \tag{7.29}$$

From (7.27):

$$\mu_h' \langle n\mu \rangle = \nu = \chi(\phi_o) + \int_{\phi_o(1+\Delta)}^{\phi_s} \frac{\mu^2(\phi) e^{\phi}\, d\phi}{\sqrt{e^{\phi}-\phi-e^{\phi_o}+\phi_o}} \tag{7.30}$$

where
$$\chi(\phi_o) = 2\sqrt{\frac{\Delta\phi_o}{e^{\phi_o}-1}} \cdot e^{\phi_o}\, \mu^2(\phi_o) \quad . \tag{7.31}$$

Differentiate (7.30) with respect to ϕ_s:

$$\frac{d\nu}{d\phi_s} = \frac{d\chi(\phi_o)}{d\phi_o} \cdot \frac{d\phi_o}{d\phi_s} + \frac{d\Gamma}{d\phi_s} \tag{7.32}$$

where
$$\Gamma = \int_{\phi_o(1+\Delta)}^{\phi_s} \frac{\mu^2(\phi) e^{\phi}\, d\phi}{\sqrt{e^{\phi}-\phi-e^{\phi_o}+\phi_o}} \quad . \tag{7.33}$$

The second term on the right hand side of (7.32) may be evaluated as follows:

If $$\Lambda(\phi_s) = \int_{\phi_o(\phi_s)}^{\phi_s} f(\phi,\phi_o)d\phi$$

Then $$\frac{d\Lambda}{d\phi_s} = f(\phi_o,\phi)\Big|_{\phi=\phi_s} - \frac{d\phi_o}{d\phi_s}\cdot f(\phi,\phi_o)\Big|_{\phi=\phi_o} + \frac{d\phi_o}{d\phi_s}\int_{\phi_o}^{\phi_s}\frac{\partial f}{\partial\phi_o}d\phi \ . \quad (7.34)$$

From (7.34), (7.33), (7.32) and (7.31):

$$\mu^2(\phi_s) = \frac{\dfrac{d\nu(\phi_s)}{d\phi_s} - \dfrac{d\chi(\phi_o)}{d\phi_o}\dfrac{d\phi_o}{d\phi_s} + \dfrac{d\phi_o}{d\phi_s}\left\{\dfrac{\mu^2(\phi_o)e^{\phi_o}}{\sqrt{\phi_o\Delta(e^{\phi_o}-1)}} - \displaystyle\int_{\phi_o(1+\Delta)}^{\phi_s}\dfrac{\mu^2(\phi)e^{\phi}(e^{\phi_o}-1)}{2(e^{\phi}-\phi-e^{\phi_o}+\phi_o)^{\frac{3}{2}}}d\phi\right\}}{\dfrac{e^{\phi_s}}{\sqrt{e^{\phi_s}-\phi_s-e^{\phi_o}+\phi_o}}} \quad \text{.... (7.35)}$$

$\frac{d\phi_o}{d\phi_s}$ may be determined from Figure 7.6.

Equation (7.35) may be solved by iteration. $\mu_h'(\phi)$ is used as the first guess for $\mu(\phi)$. The $\mu(\phi_s)$ that is obtained is then used as the second guess, etc.

In an actual experiment, only V_g is known and ϕ_s must be obtained by other means. The quasi-static CV-technique[106] as described in Chapter 8 may be used.

7.5.4 Modulation of Ionized Impurity Scattering by the Field-Effect

Recent experimental work by St. J. Murphy, et al.[97] indicated a similar fast increase in mobility when the field-plate voltage is

increased. Since they used single crystal Si material, intercrystalline barrier effects cannot serve as an explanation for their results. It would therefore seem probable that another effect is also important.

The initial fast increase in mobility may be explained by a model which assumes ionized impurity scattering as the major scattering mechanism. This may also be of importance for polycrystalline CdS films.

When electrons are accumulated near the surface, the impurity atoms are screened, with a corresponding reduction in the scattering probability. This will cause an increase in the effective mobility.

The electric field of an ionized impurity in a solid is not given by the coulomb potential, but the effect of the conduction electrons has to be taken into account too. It turns out that the potential of the ion is given by the so-called Thomas-Fermi screening formula[94], namely

$$\theta(r) = \frac{Zq^2}{4\pi r \varepsilon} e^{-\zeta r} \tag{7.36}$$

where Zq is the effective charge of the ionized impurity ($Z \equiv$ difference in valency of the impurity ion and the ion for which it is substituted).

$\frac{1}{\zeta}$ = screening length

ε = dielectric permittivity for the semiconductor.

$$\zeta^2 = \frac{q^2}{\varepsilon kT} n(2 - \frac{n}{N_d}) \doteq \frac{q^2}{\varepsilon kT} n \tag{7.37}$$

if all the donors are ionized.

n = number of free electrons

N_d = donor density

q = electronic charge .

If we assume that the electrons are effectively free, the transition probability may be calculated by using Fermi's Golden Rule[104].

$$P_i^f = \frac{2\pi}{\hbar} |\langle i|H'|f\rangle|^2 D_f(E_i) = \frac{2\pi}{\hbar} |V_{fi}|^2 D_f(E_i) \tag{7.38}$$

where H' is the perturbing Hamiltonian

P_i^f = transition probability from $|i\rangle$ to $|f\rangle$

$|V_{fi}|^2 = |\langle i|H'|f\rangle|^2 = |\text{matrix element}|^2$

and $D_f(E)$ = density of final states.

$$V_{fi} = \int \psi_{\underline{k}}^* \theta(r) \psi_{k'} \, d\underline{r} = \frac{Zq^2}{\varepsilon\{|\underline{k}-\underline{k}'|^2 + \zeta^2\}} \tag{7.39}$$

$\underline{k}$ is the momentum of the electron in the initial state, while $\underline{k}'$ is the momentum of the scattered electron.

It follows then that the differential scattering cross-section per unit solid angle is given by[94]

$$S(\theta) = \left(\frac{2mZq^2}{4\pi\varepsilon\hbar^2}\right)^2 \left\{\frac{1}{|\underline{k}-\underline{k}'|^2 + \zeta^2}\right\}^2 . \tag{7.40}$$

$S(\theta)$ represents the contribution from scattering through the angle θ between $\underline{k}$ and $\underline{k}'$. (The scattering is assumed to be elastic so that $|\underline{k}| = |\underline{k}'|$.)

In order to calculate the total effective cross-section, the differential cross-section has to be weighted by a factor which is proportional to the relative change in the component of the electron momentum along the initial direction of motion.

$$S = 2\pi \int_0^{\pi} (1-\cos\theta)\ S(\theta)\ \sin\theta\ d\theta \quad . \tag{7.41}$$

After some algebraic simplification, this integral may be evaluated.

$$S = \frac{\pi}{2|k|^4} \left(\frac{2mZq^2}{4\pi\varepsilon\hbar^2}\right)^2 F(E) \tag{7.42}$$

where $$F(E) = \ln(1 + \frac{4|k|^2}{\zeta^2}) - \frac{1}{1 + \frac{\zeta^2}{4|k|^2}} \tag{7.43}$$

and $$|k|^2 = \frac{2m_e^* E}{\hbar^2} \quad . \tag{7.44}$$

Now that the total effective cross-section is known, the mean free time may be calculated:

$$\frac{1}{\tau(E)} = N_i S v$$

where N_i = number of uniformly distributed ionized impurities, each of effective charge Zq

and $v = \sqrt{\frac{2E}{m_e^*}}$ for parabolic bands.

$$\therefore \quad \frac{1}{\tau(E)} = \frac{\pi}{\sqrt{2}} \frac{Z^2 q^4 N_i}{(4\pi\varepsilon)^2 E^{\frac{3}{2}} m_e^{*\frac{1}{2}}} F(E) \tag{7.45}$$

where $$F(E) = \ln\left(1 + \frac{8m_e^* E}{\hbar^2 \zeta^2}\right) - \frac{1}{1 + \frac{\hbar^2\zeta^2}{8m_e^* E}} \quad . \tag{7.46}$$

The electrical conductivity may be calculated under certain simplifying assumptions[94] from the linearized Boltzmann equation. Under the conditions of spherical energy surfaces, etc., it turns out to be:

$$\sigma = \frac{2q^2 n}{3m_e^* kT} \langle E\tau(E) \rangle \tag{7.47}$$

where < > indicates an average over the electron distribution. The last-mentioned averaging is rather complicated for the expression in (7.47). Following Brooks[95], the integral may be evaluated by replacing F(E) with its value where the rest of the integrand is a maximum, i.e., E=3kT. This doesn't influence the results very much, because F(E) is a slowly varying function.

σ turns out to be:

$$\sigma = \frac{2^{\frac{7}{2}}}{\Pi^{\frac{3}{2}} m_e^{*\frac{1}{2}}} \frac{(4\pi\varepsilon)^2 (kT)^{\frac{3}{2}} \cdot n}{Z^2 q^2 N_i F(3kT)} \quad . \tag{7.48}$$

But $\quad \sigma = q\mu_i n$

$$\therefore \qquad \mu_i = \frac{2^{\frac{7}{2}}}{\Pi^{\frac{3}{2}}} \cdot \frac{(4\pi\varepsilon)^2}{Z^2 q^3 m_e^{*\frac{1}{2}}} \frac{(kT)^{\frac{3}{2}}}{N_i} \cdot \frac{1}{F(3kT)} \quad . \tag{7.49}$$

This expression is due to Brooks and Herring[95].

It may be seen from (7.49) that the mobility due to ionized impurity scattering is a function of the number of free carriers. This dependence is incorporated in the term F(3kT) which is a function of the Thomas-Fermi screening length. It may be illustrated effectively by considering the inverse of the mobility as given by (7.49).

$$\frac{1}{\mu_i} = K \cdot F(3kT) = K\left\{\ell n\left(1 + \frac{24m_e^* kT}{\hbar^2 \zeta^2}\right) - \frac{1}{1 + \frac{\hbar^2 \zeta^2}{24m_e^* kT}}\right\} . \tag{7.50}$$

But $\zeta^2 \doteq \frac{q^2}{\epsilon kT} n$ (7.51)

and $n = N_d e^{\phi}$ (7.52)

$$\therefore \quad F(3kT) = \ell n\left\{1 + \frac{2.1955 \times 10^{20} \ T^2}{N_d e^{\phi}}\right\} - \left\{\frac{1}{1 + \frac{N_d e^{\phi}}{2.1955 \times 10^{20} \ T^2}}\right\} \tag{7.53}$$

if we use CdS with $\epsilon = 10\epsilon_o$ and $m_e^* = 0.17m$.

For $N_d < 10^{18}$ cm^{-3} and $T > 200^oK$, (7.53) may be simplified to the following:

$$F(3kT) \doteq 45.838 + 2\ell nT - \ell nN_d - \phi$$

$$= C(T,N_d) - \phi$$

$$\frac{1}{\mu_i} = 1.9833 \times 10^{-18} \ Z^2 N_i T^{-\frac{3}{2}} \{C(T,N_d) - \phi\} \quad . \tag{7.54}$$

This result has been derived for CdS.

It may be possible to obtain $N_i Z^2$ from (7.54). By measuring μ_h' and the conductance by means of the Hall-field effect experiment, $\mu(\phi_s)$ may be calculated by using equation (7.35). If ionized impurity scattering is indeed the dominant scattering mechanism, a plot of $\frac{1}{\mu}$ versus ϕ_s will be a straight line. The slope of this curve will be proportional to $N_i Z^2$ and the value of $\frac{1}{\mu}$ at $\phi_s = 0$ is proportional to N_d.

7.6 Conclusion

An attempt was made in this Chapter to give a review of the deposition techniques and properties of thin-film CdS. It was emphasized that the physical properties of CdS thin-films are not well known. The section on the Hall-field effect discussed a possible experiment which may be performed to determine the doping density and mobility of electrons in thin semiconductor films. The screening of the ionized impurities by the electrons in the accumulation layer was given as a possible explanation of the results obtained by other workers.

CHAPTER 8

Measuring Equipment

8.1 Introduction

The equipment that was used for determining the properties of the MIS-samples and the characteristics of the filters will be described briefly in this chapter.

8.2 Apparatus for the Measurement of the CV, IV and the Quasi-static CV-characteristics of MIS Devices

Nearly all the experiments on the MIS-samples and filters can be performed on the devices while they are in a protective vacuum chamber. The chamber consists of a 3½ inch diameter copper cylinder which is 4½ inches high. Three ports, 120° apart, allow one to probe the devices inside with probes consisting of indium tipped needles secured into nylon rods. The nylon rods may be manipulated in three directions by means of three Kulicke and Soffa micropositioners. Vacuum-tightness and relative movement between the micropositioners and the chamber are made possible by three brass bellows. The chamber rests on a ½ inch thick aluminum table. Vacuum-tightness between the table and the chamber is ensured by means of an "O"-ring. The same purpose is served by the "O"-ring between the top of the chamber and the perspex disc on top. The chamber may be evacuated by means of a rotary vacuum pump underneath.

Electrical connections are made by means of a 7-pin vacuum feedthrough. Different shielded cables may be plugged into the feedthrough

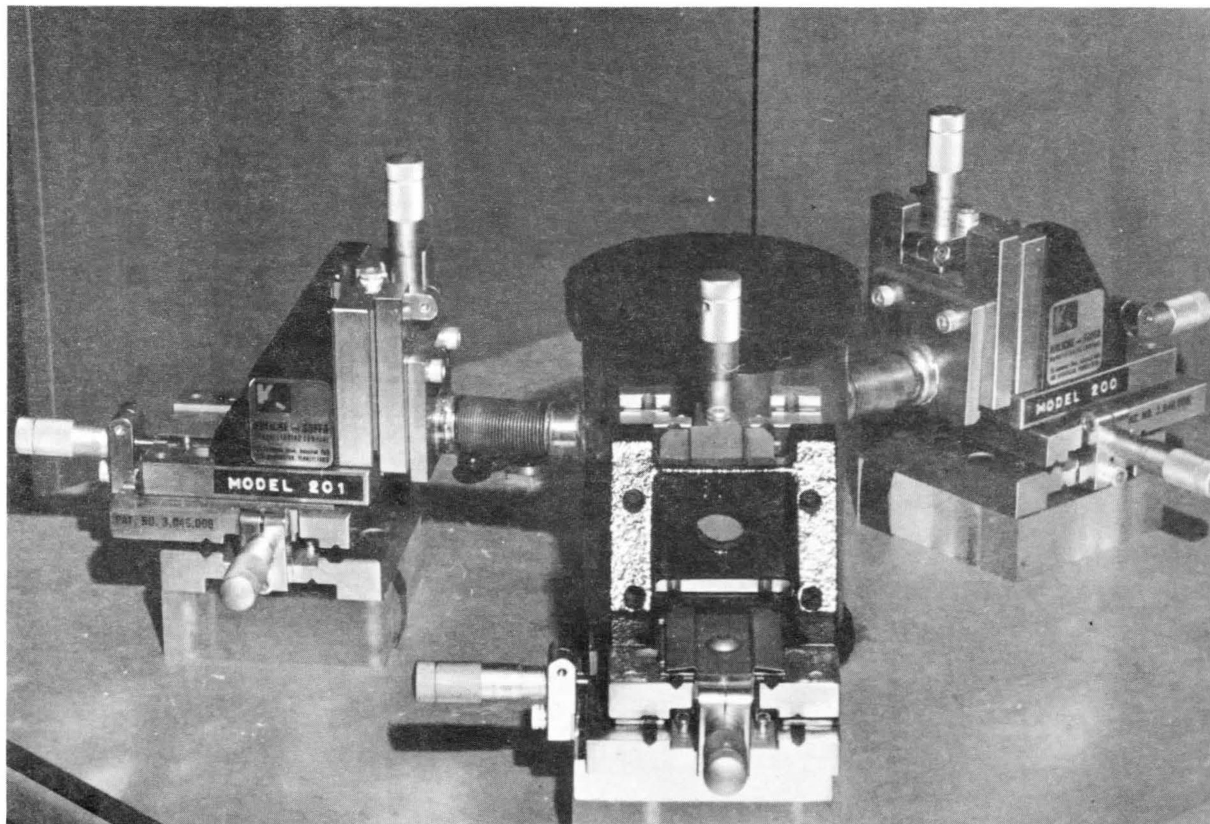

Figure 8.1 Photograph of the Micropositioners and the Vacuum Chamber Assembly.

to facilitate the various measurements. A photograph of the vacuum chamber assembly is shown in Figure 8.1.

In order to speed up the measurements, a measuring system was designed by which the devices could be freed from pinholes, the low-frequency CV and GV curves could be obtained, and IV and quasi-static CV-curves could be determined by simply setting a switch in different positions. The block diagram of the equipment used is shown in Figure 8.2. The switching network contains all the switches needed for connecting the appropriate instruments to the device. Detail of the switching network is given in Figure 8.3. Switch S4 determines the kind of measurement that is performed. S1 can either be set in the "calibrate" position or in + or -. When in "calibrate" the device is being replaced by an adjustable parallel RC-network. + or - changes the polarity of the device. The different modes of operation are described below:

(i) Small Signal Capacitance and Conductance Measurements

The small-signal capacitance and conductance of the MIS-devices may be determined by the method of phase-sensitive detection. This allows a continuous measurement with changing bias on the device. The circuit used has been described before by Shewchun and Waxman[105]. The reference signal of the Princeton Applied Research Model JB-4 lock-in amplifier is applied to the MIS-device which is connected in series with a small resistor. The voltage across the resistor is proportional to the current through the device. If this resistor is very much smaller than the impedance of the MIS-capacitor, and if the reference signal has a constant amplitude, the current is directly proportional

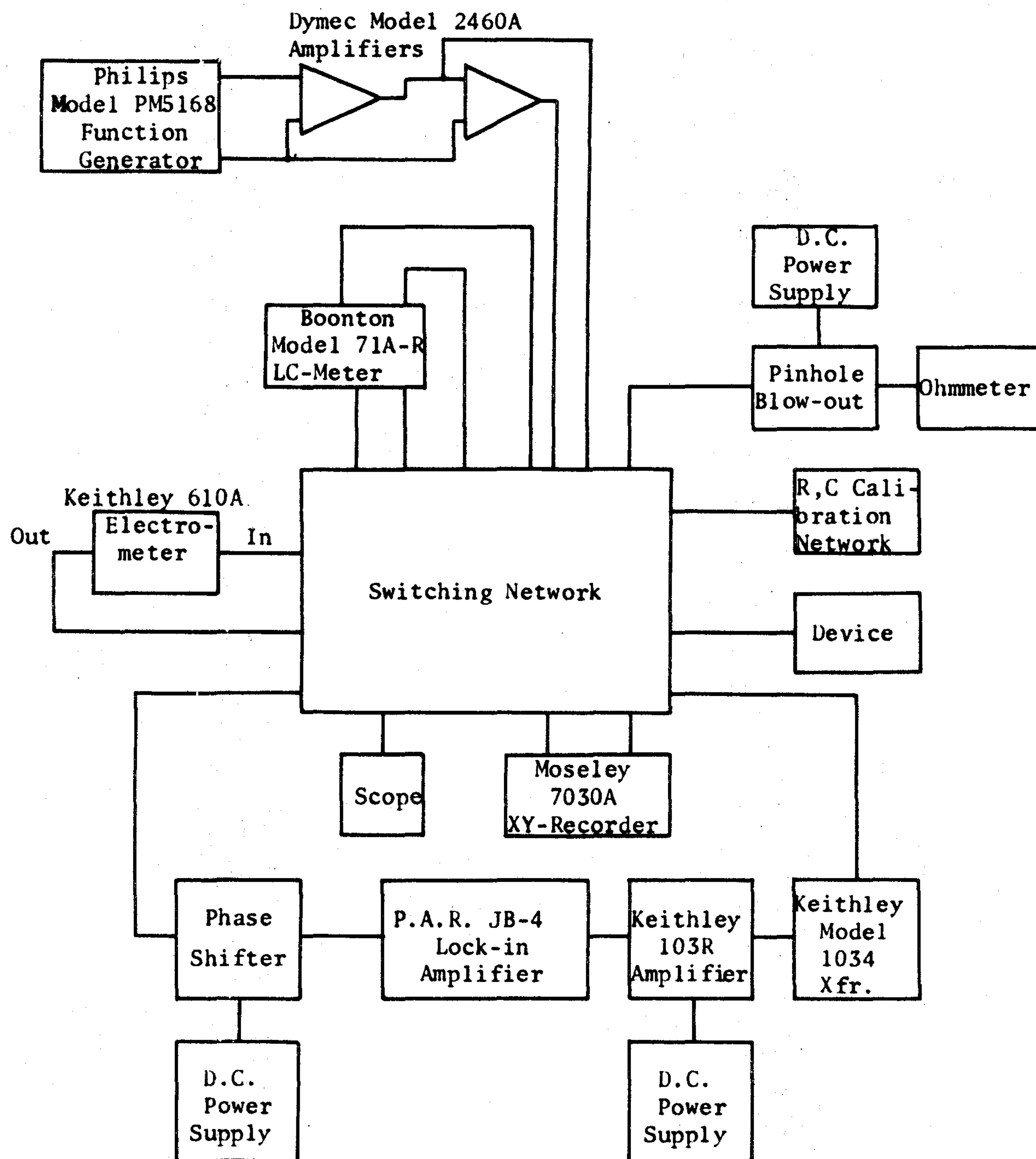

Figure 8.2 Block Diagram of the Experimental Set-up for Capacitance-Voltage and Current-Voltage Determinations. The Pinhole-Removal Circuit is also shown.

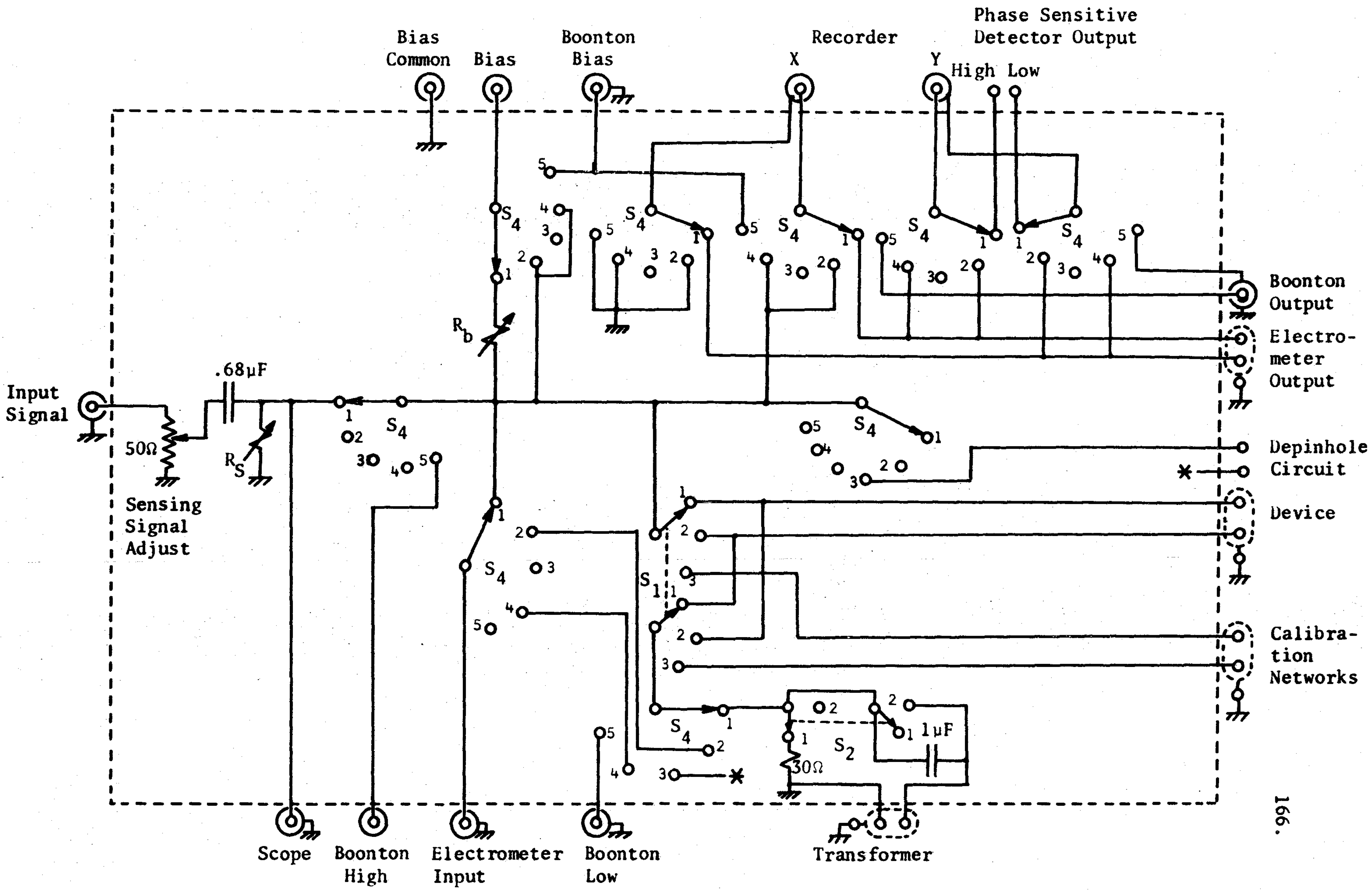

Figure 8.3 Switching Network

S1	
1	+
2	-
3	Calibrate

S2	
1	High
2	Low

S4	
1	Small Signal C and G
2	I-V Characteristic
3	Pinhole Blow-Out
4	Quasi-Static C-V
5	1 MHz Boonton LC-Meter

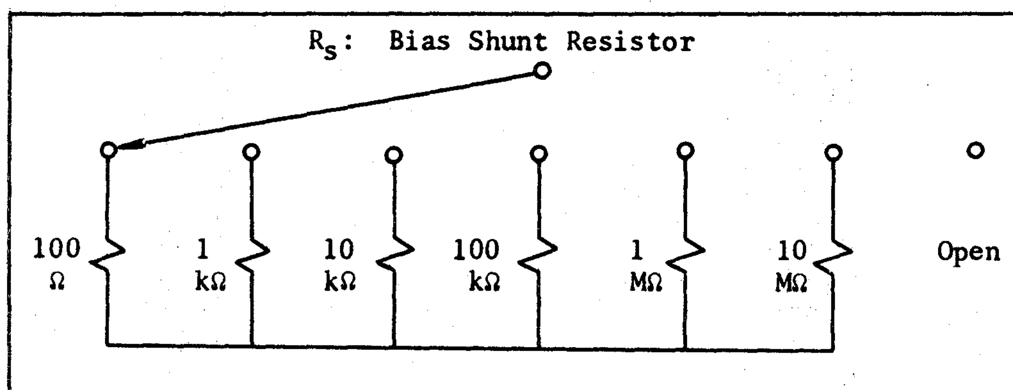

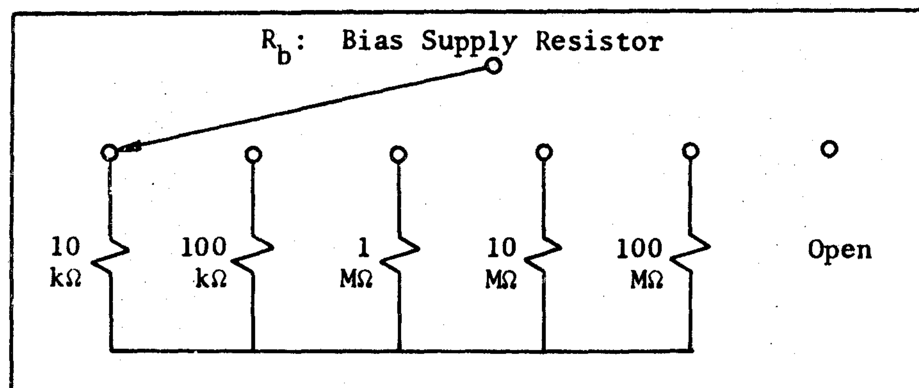

Figure 8.4 Switch Positions and Bias Resistors in Switching Network.

to the admittance of the device. The current-signal is amplified by a low-noise amplifier and then applied to the input of the lock-in amplifier. A phase shift network allows one to either determine the in-phase or quadrature component of the current-signal. (The reference signal of the lock-in amplifier is taken as reference.) These two components are proportional to the conductance and capacitance of the device under test, respectively. The output of the lock-in amplifier is a dc voltage which may be filtered to get rid of noise. The block diagram of the system used for the measurement of the small-signal capacitance and conductance is given in Figure 8.5. Details on the phase-shift network are given elsewhere[105].

(ii) Current-Voltage Characteristics

The second position of switch S4 allows one to determine the IV-characteristics of devices. This allows one to measure the leakage current of the MIS-devices as a function of bias. The Keithley 610A electrometer in the normal mode serves as the ammeter. The current-voltage curves may be displayed on an XY-recorder.

(iii) Pinhole Blow-out

Frequently thin-film devices contain so-called pinholes, i.e., small regions where heavy leakage currents flow between the electrodes of the capacitors. These pinholes may in many instances be removed quite readily by discharging a capacitor across it. The third position of S4 connects the device to such a pinhole blow-out circuit. It consists of a 0.5μF capacitor which may be charged to a voltage determined by the power supply to which it is connected. A switch connects either the capacitor or an ohmmeter across the MIS device.

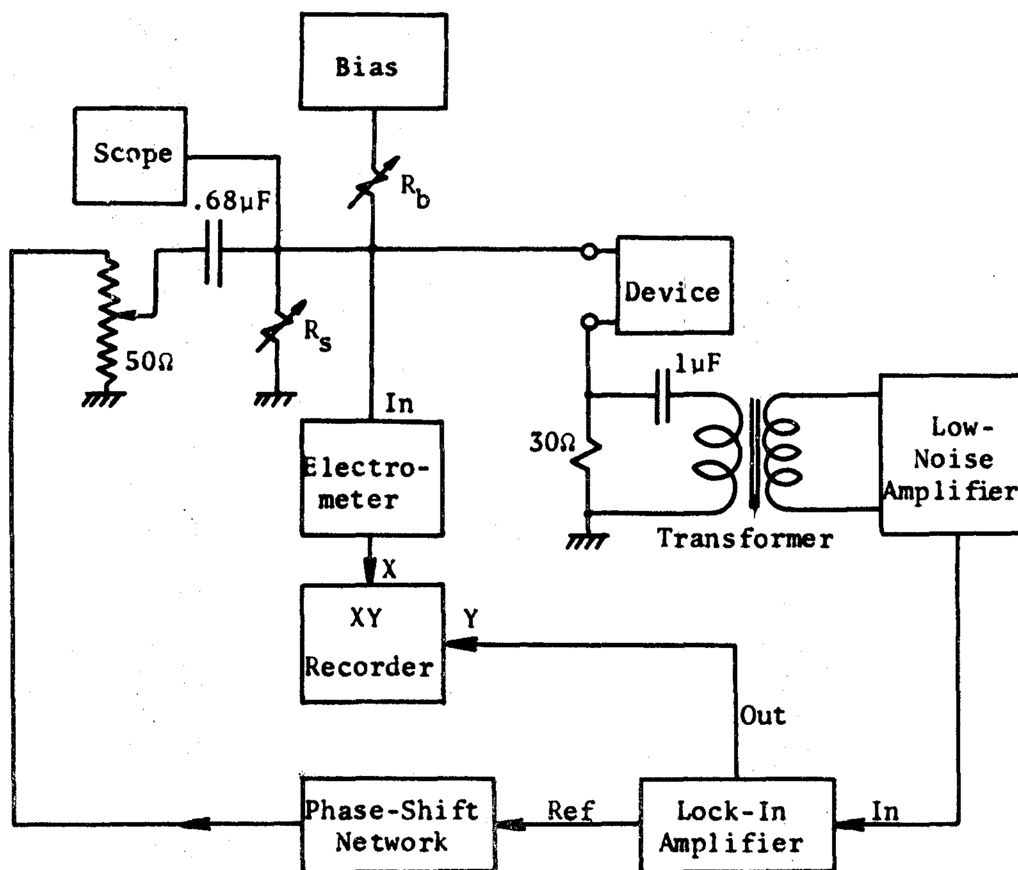

Figure 8.5 Block Diagram of CV and GV Measurement System

If the capacitor is connected to the MIS-device, it is not connected to the power-supply. This allows only a fixed amount of charge, Q=CV, to be discharged through the device.

(iv) Quasi-Static Capacitance-Voltage Measurements

The capacitance-voltage characteristics may be obtained under conditions of thermal-equilibrium by the so-called quasi-static technique[106]. The capacitance is determined from the displacement current when a linear voltage ramp is applied to it. If the leakage current is negligible, the capacitance is directly proportional to the charging current.

The method may be illustrated by considering Figure 8.6.

The total current flowing into the leaky capacitor may be separated into two components, namely the displacement current $i_d(t)$ and the leakage current $i_\ell(t)$

$$i(t) = i_d(t) + i_\ell(t)$$

$$= C(v) \cdot \frac{dv}{dt} + v \cdot G_\ell(v) \quad . \qquad (8.1)$$

If the input voltage is a linear ramp,

$v = \pm\alpha t$ where α is a constant.

$$\therefore \quad i = \pm\alpha C(V) + VG_\ell(V) \quad . \qquad (8.2)$$

If one uses a saw-tooth voltage with a peak value V_m and repetition frequency f, then

$$\alpha = 4fV_m$$

$$\therefore \quad i = \pm 4fV_m C(V) + i_\ell(V) \quad . \qquad (8.3)$$

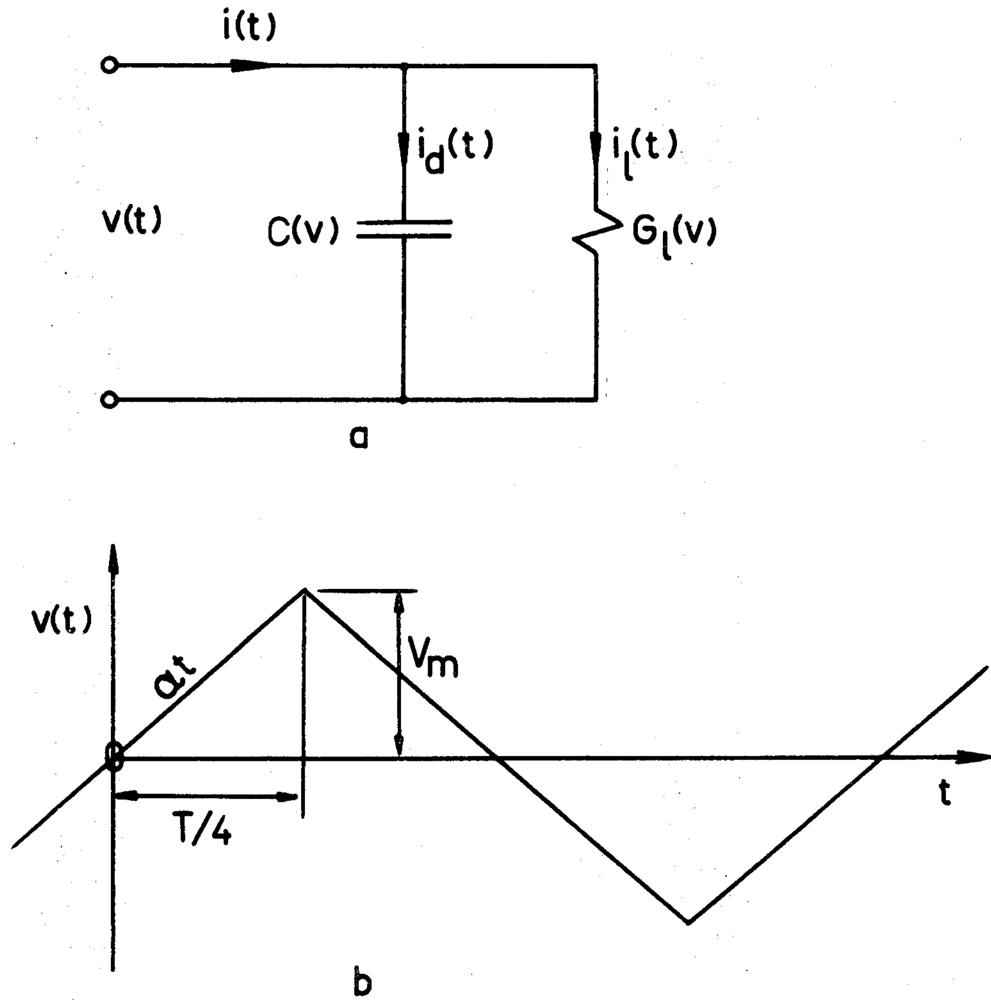

Figure 8.6 (a) Simplified Equivalent Circuit of a Leaky MIS-Device

(b) Voltage Waveform

This equation places lower limits on the sweep rate and capacitance for a given maximum leakage current.

If $i_\ell = 10^{-9}$A at 10V, and C = 2nF, f may have a minimum value of 1.8 Hz in order to have $i_\ell \leq 0.01\ i_d$. This may put a serious restriction on using this method on leaky devices.

The leakage current component may be eliminated by using the following argument: The displacement current will change sign when the slope of the sweep becomes negative.

$$i\big|_{\alpha>0} = i_d + i_\ell$$

$$i\big|_{\alpha<0} = -i_d + i_\ell$$

$$\therefore \quad C(V) = \frac{i\big|_{\alpha>0} - i\big|_{\alpha<0}}{8fV_m} \tag{8.4}$$

and

$$i_\ell(V) = \tfrac{1}{2}\left\{ i\big|_{\alpha>0} + i\big|_{\alpha<0} \right\} \tag{8.5}$$

As has been pointed out by Kuhn[106] and Berglund[107], quasi-static CV-curves may be used to determine the density of surface states as well as the surface potential of the semiconductor for a given field-plate voltage. This last-mentioned facility may be used for the Hall-field effect experiments as described in Chapter 7.

The surface state density is given by[106]

$$N_{ss}(\psi_s) = \frac{C_{ss}(\psi_s)}{q} = \frac{1}{q}\left(\frac{C(V_g)}{1 - \frac{C(V_g)}{C_i}} - C_{sc}(\psi_s) \right) \tag{8.6}$$

where ψ_s = surface potential

V_g = field-plate voltage

$C_{ss}(\psi_s)$ = surface state capacitance

$C(V_g)$ = measured capacitance

C_i = insulator capacitance

$C_{sc}(\psi_s)$ = space-charge capacitance.

The surface potential may be obtained to within an additive constant from

$$\psi_s(V_g) = \int \left\{1 - \frac{C(V_g)}{C_i}\right\} dV_g + \Delta \tag{8.7}$$

where Δ is a constant. Δ may be determined by comparing the experimental curves with ideal CV-curves.

(v) High-Frequency CV-Curves

The fifth position of S4 connects a 1 MHz Boonton Model 71A-R Capacitance-Inductance meter to the device. This may therefore be used to determine CV-curves at "high"-frequencies. A photograph of the measuring system is shown in Figure 8.7.

8.3 Transfer-Function and Impedance Measurement of URC-Filters

Point-by-point measurements of the filter characteristics may become extremely tedious, especially in the case of null-networks where many points have to be taken in the vicinity of the null. In addition, it is quite time-consuming to find the correct value of the notch resistor which will provide an optimum null.

All these problems may be solved by using a sweeping signal generator and an oscilloscope for the display. The real system that was used for this work consisted of a Hewlett-Packard Model 675A sweeping signal generator, a model 676A phase/amplitude detector and

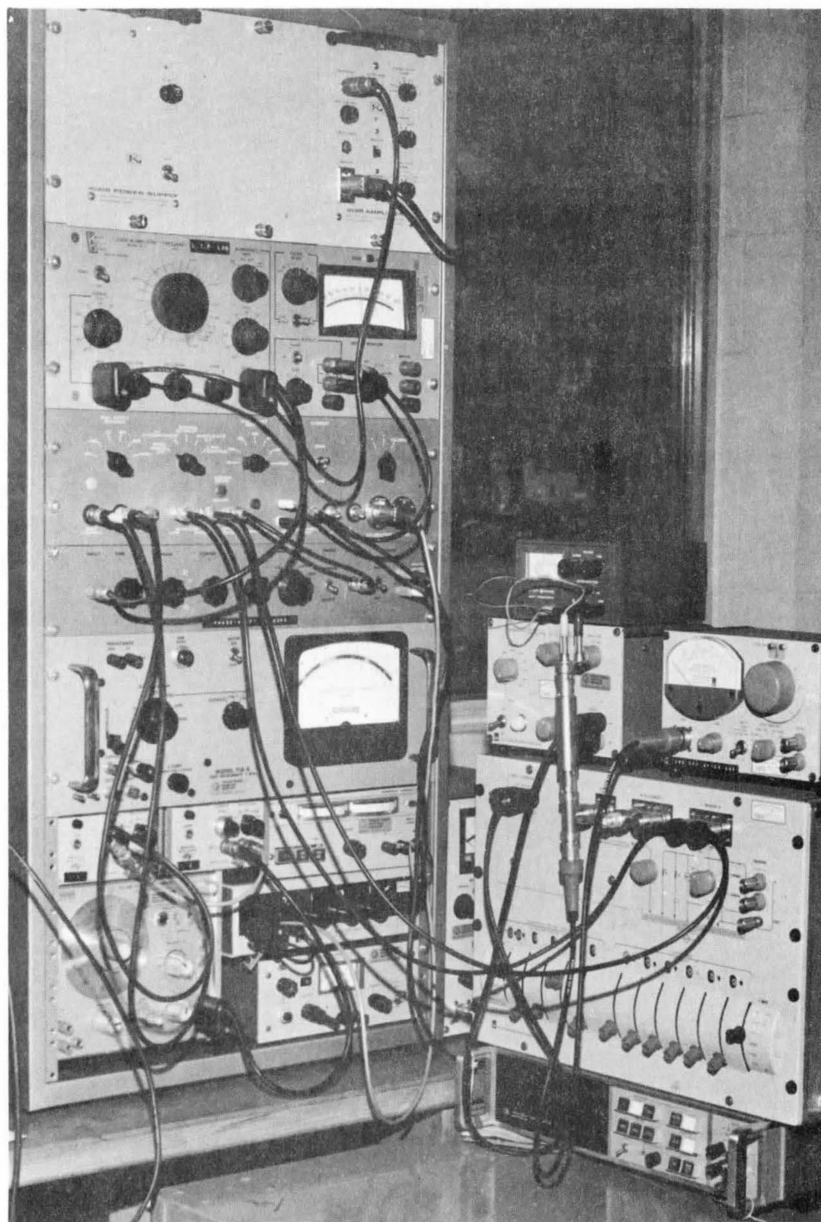

Figure 8.7 Photograph of the Apparatus for the Measurement of the CV, IV and the Quasi-Static CV-Characteristics of MIS-Devices.

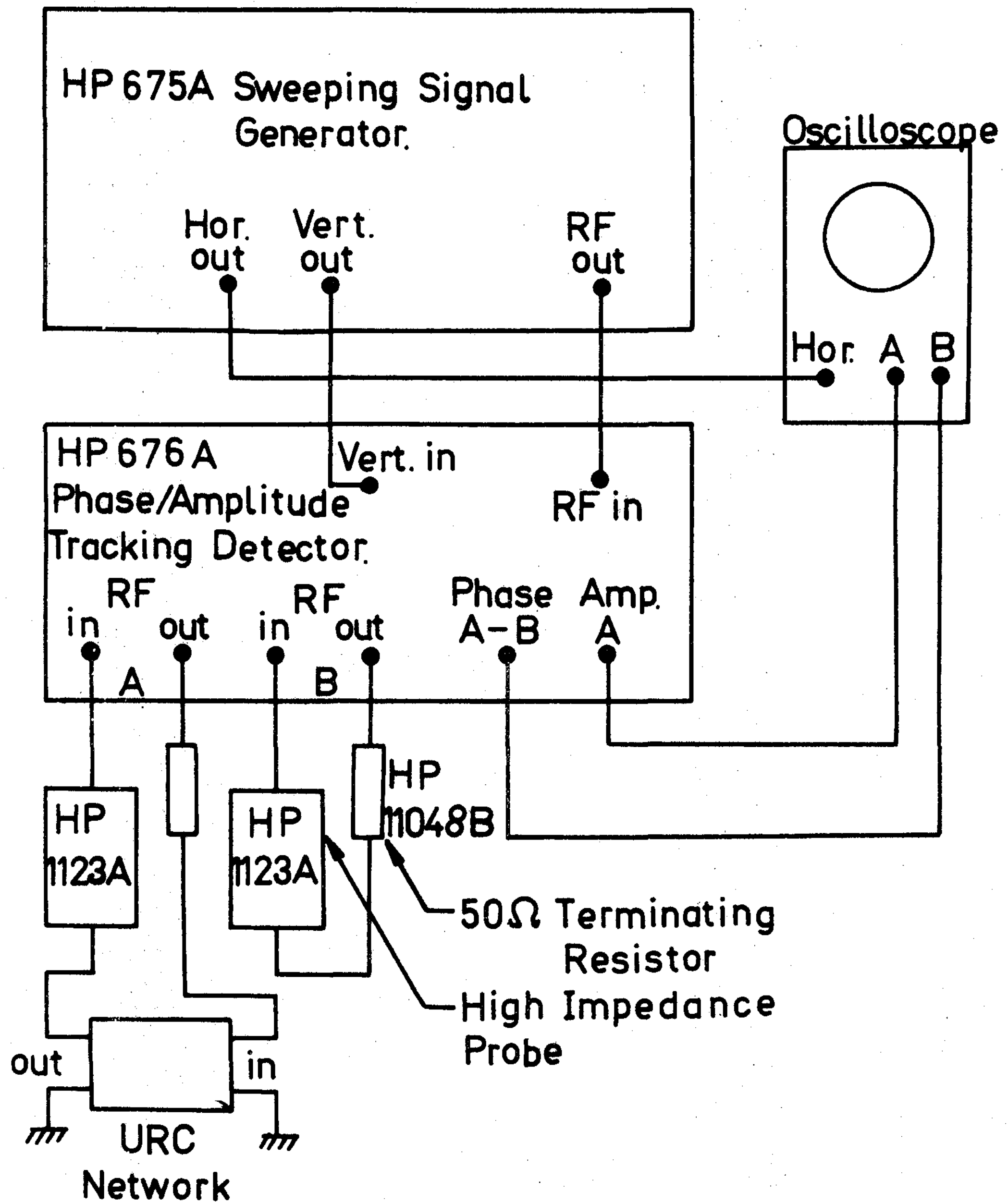

Figure 8.8 Open-Circuit Voltage Transfer Function Measurement

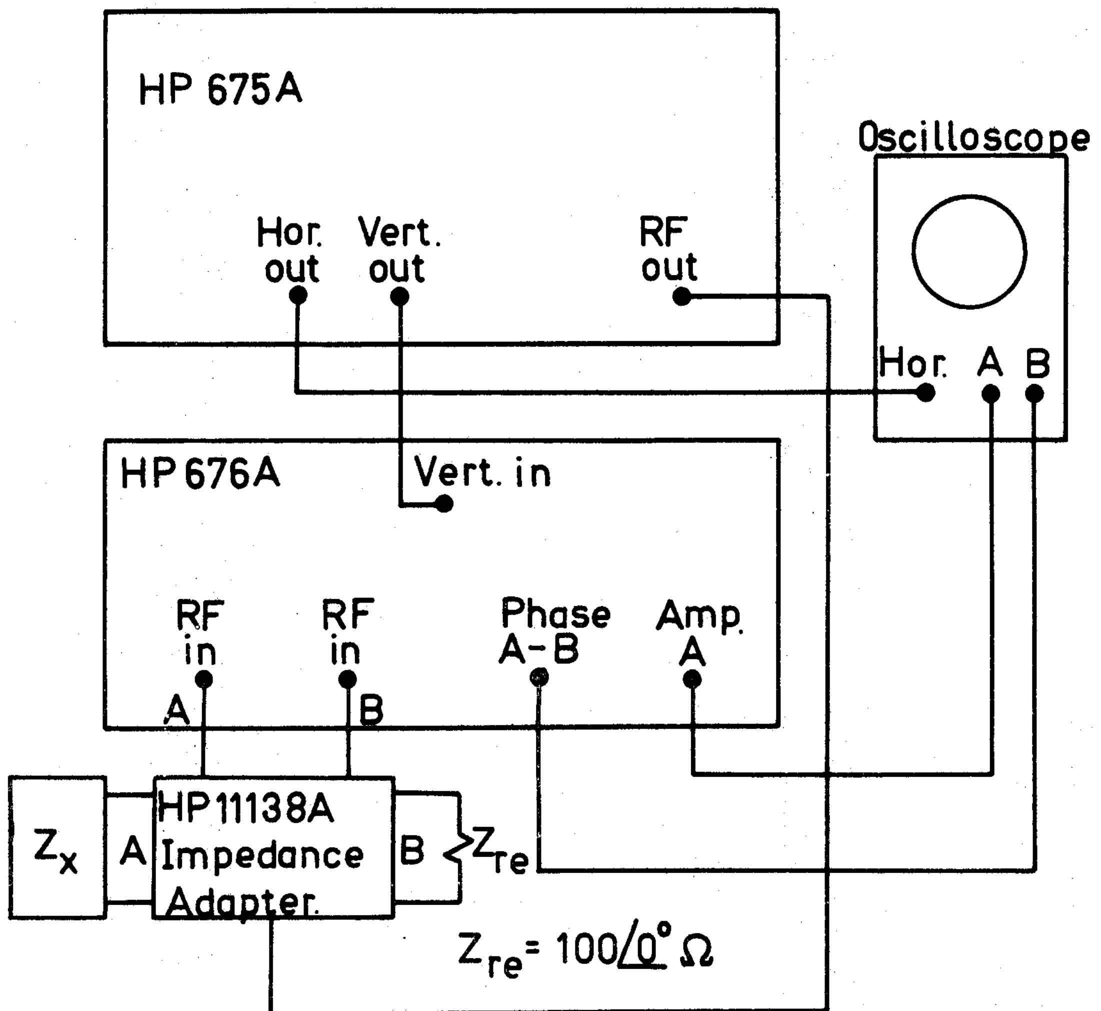

Figure 8.9 Magnitude and Phase Measurement of a Two-Terminal Impedance

two model 1123A high impedance probes. The probes allow one to determine the open circuit voltage transfer function with negligible loading effects. In addition to the above mentioned instruments, the experimental set-up also included a Hewlett-Packard Model 7562A Log. converter and the model 11138A impedance adapter. These two instruments allow one to display the frequency in a logarithmic fashion and to determine the input impedance of the devices, respectively. The block diagrams for transfer function and impedance measurements are shown in Figure 8.8 and 8.9. A photograph of the network analyzer is shown in Figure 8.10.

The transfer function curves of the devices can be displayed on an oscilloscope by using a sweep time of 0.1 to 0.01 seconds for the sweeping signal generator. Alternatively, the 100 seconds sweep time may be employed in conjunction with an XY-recorder. Photographs of oscilloscope traces are shown in the next Chapter.

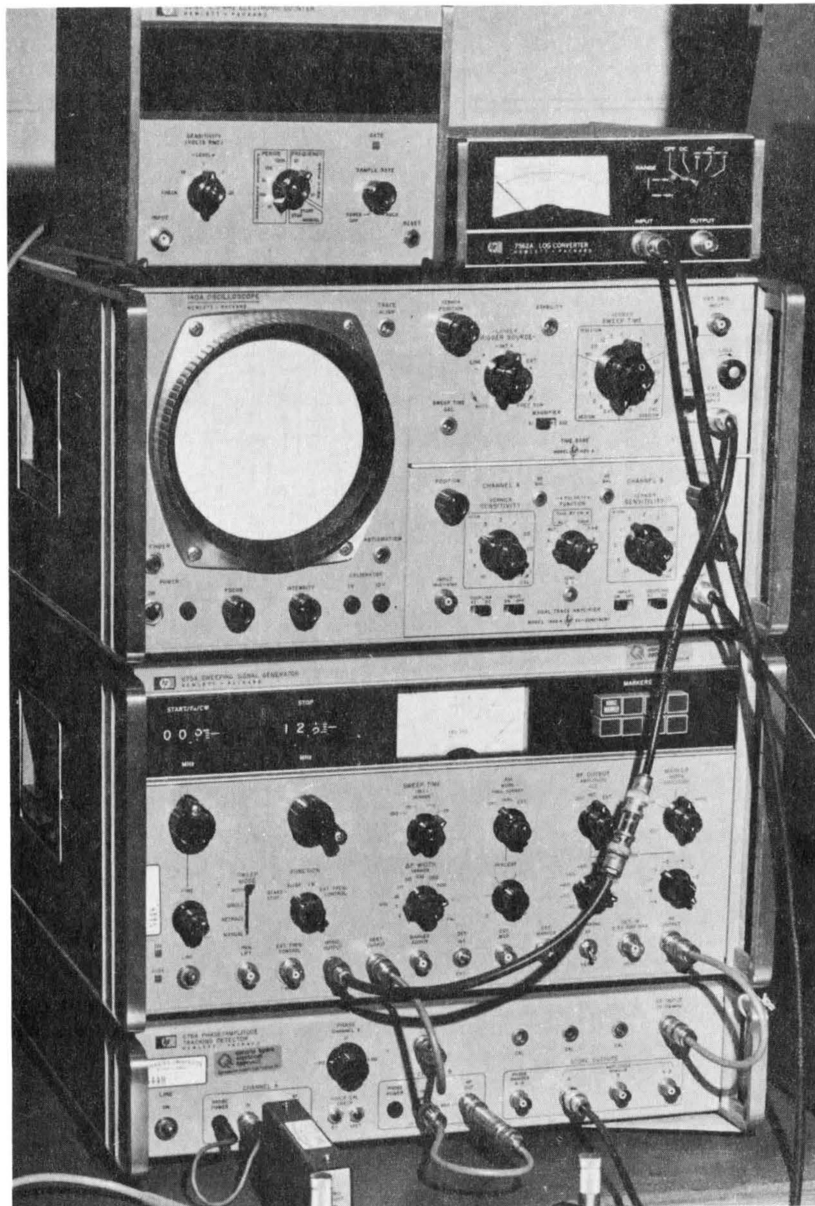

Figure 8.10 Photograph of the Network Analyzer.

CHAPTER 9

Experimental Analysis

9.1 Introduction

Thin-film tunable URC-filters were made using vacuum evaporation techniques. Since these techniques have been described fully in Chapters 5, 6 and 7, more emphasis will be placed on the electrical properties of the tunable notch and bandpass filters. In order to explain the experimental observations, the influence of parasitic effects is taken into account.

The devices consist of a multilayer structure of materials on an insulating substrate. The material properties allow one at least two configurations:

(i) Substrate - resistive layer - insulator-semiconductor - highly conducting layer.

(ii) Substrate - highly conducting layer - semiconductor-insulator - resistive layer.

Two low resistivity contacts to insure uniform current flow should also be provided for on the resistive layer.

The material constituting the "highly conducting layer" must not only have a low sheet resistivity, but must also form a good ohmic contact to the semiconductor for the proper operation of the tunable filters. Evaporated cadmium sulfide, which was used as the semiconductor film, has the peculiar property that aluminum evaporated on top of it, or gold underneath it, forms a good ohmic contact.

Two possible configurations corresponding to (i) and (ii) above, may therefore be:

Substrate - Nichrome - Y_2O_3 - CdS - Aℓ

or Substrate - Au - CdS - Y_2O_3 - Nichrome.

The first alternative was chosen for most devices made during this investigation. This configuration has the advantage that the resistive film is protected from the environment by the other films. A cross-sectional view of such a device is shown schematically in Figure 9.1.

The "active area" is approximately 0.37 x 0.38 cm^2. This particular area was chosen, for it corresponds to filters operating at very convenient frequencies with regard to the network analyser (HP676A) that was used in obtaining the transfer functions. This should by no means be taken to be the smallest size possible.

Typical thicknesses for the films employed were as follows:

Resistive film	: 200Å
Aluminum contacts on the resistive film	: 2000Å
Y_2O_3 film	: 2000-5000Å
CdS film	: 2000-10,000Å
Aluminum ohmic contact	: 2000Å

A photograph of a tunable URC-filter on a ceramic substrate is shown in Figure 9.2.

9.2 Post-Evaporation Treatment

High leakage currents and "dielectric losses" (this includes interface state losses, etc.) necessitated post-evaporation treatment

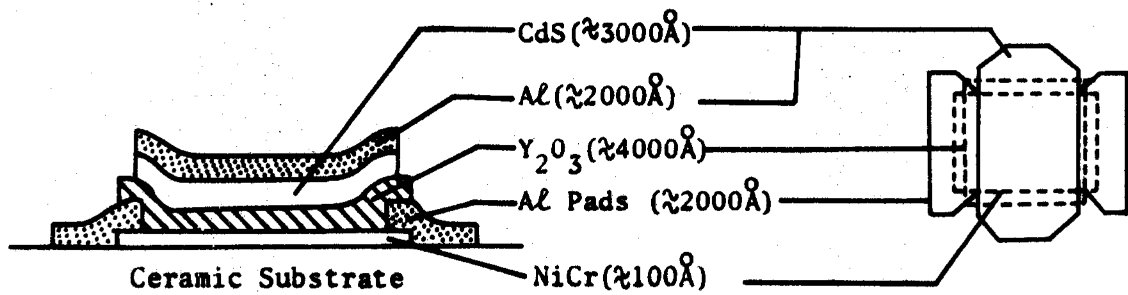

Figure 9.1 Cross-sectional View of a Tunable URC-Filter. (Not to scale.)

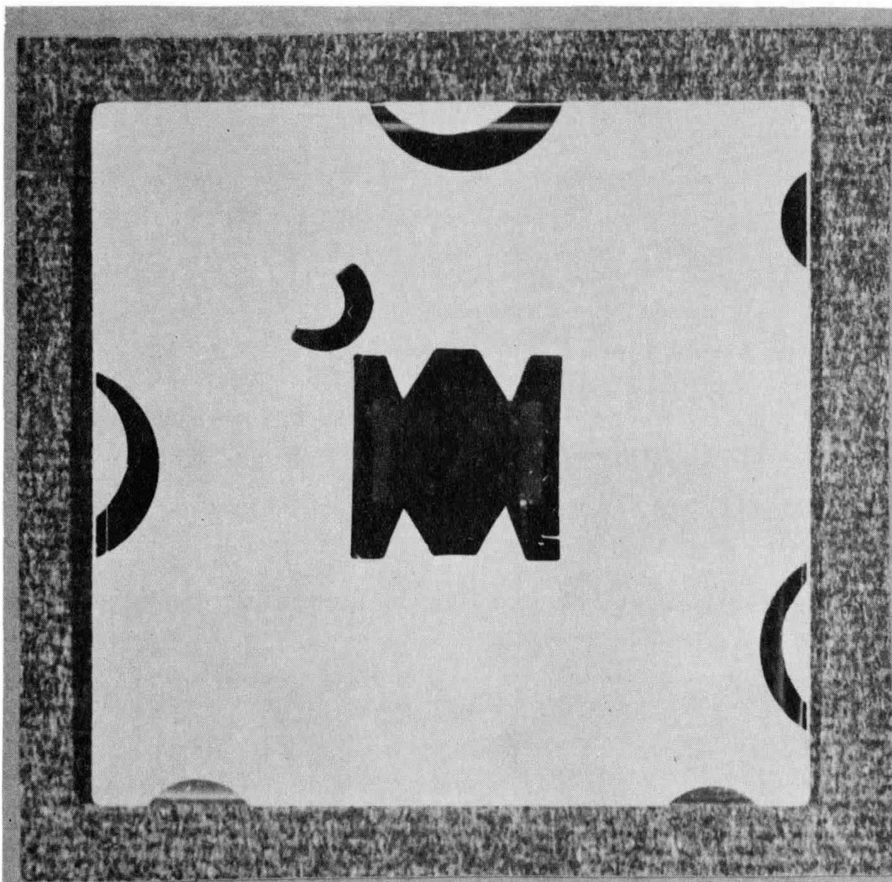

Figure 9.2 Photograph of a Tunable URC-Filter on a 1" x 1" Ceramic Substrate

of the completed devices. This treatment consisted of bakes in air for various lengths of time. Devices with a large number of pinholes could be made usable by discharging a capacitor through the insulator and semiconductor layers. Re-baking such a device after the pinhole removal usually yielded a workable device. This meant that the yield was very high, and practically all the evaporations produced good filters. Figure 9.3 illustrates the effects of the treatment on a Nichrome-$Y_2O_3(N_2)$-CdS-$A\ell$ device. This particular one was nearly useless when it was taken from the vacuum system. A total bake time of 15 hours at 300°F and two pinhole blow-outs at 15V and 20V reduced the leakage current to approximately 6 x 10^{-9}A at 5V.

The baking also had the effect of increasing the resistance of the nichrome layer, probably due to oxidation. This was, however, never more than a few percent. The resistance of the sample described above increased from 154.1Ω to 157.3Ω.

Although no effort was made to optimize the reproducibility of the devices, it was found that the insulator capacitance could be made to within 10 or 20% of the desired value. The resistive layer could be evaporated within 2% from evaporation to evaporation. The reproducibility could possibly be improved by better in-process monitoring. Contacts could be provided through the mask to monitor the resistance of the resistive layer as it is being deposited. Optical interference techniques plus a carefully calibrated quartz crystal thickness monitor may be used for the dielectric film.

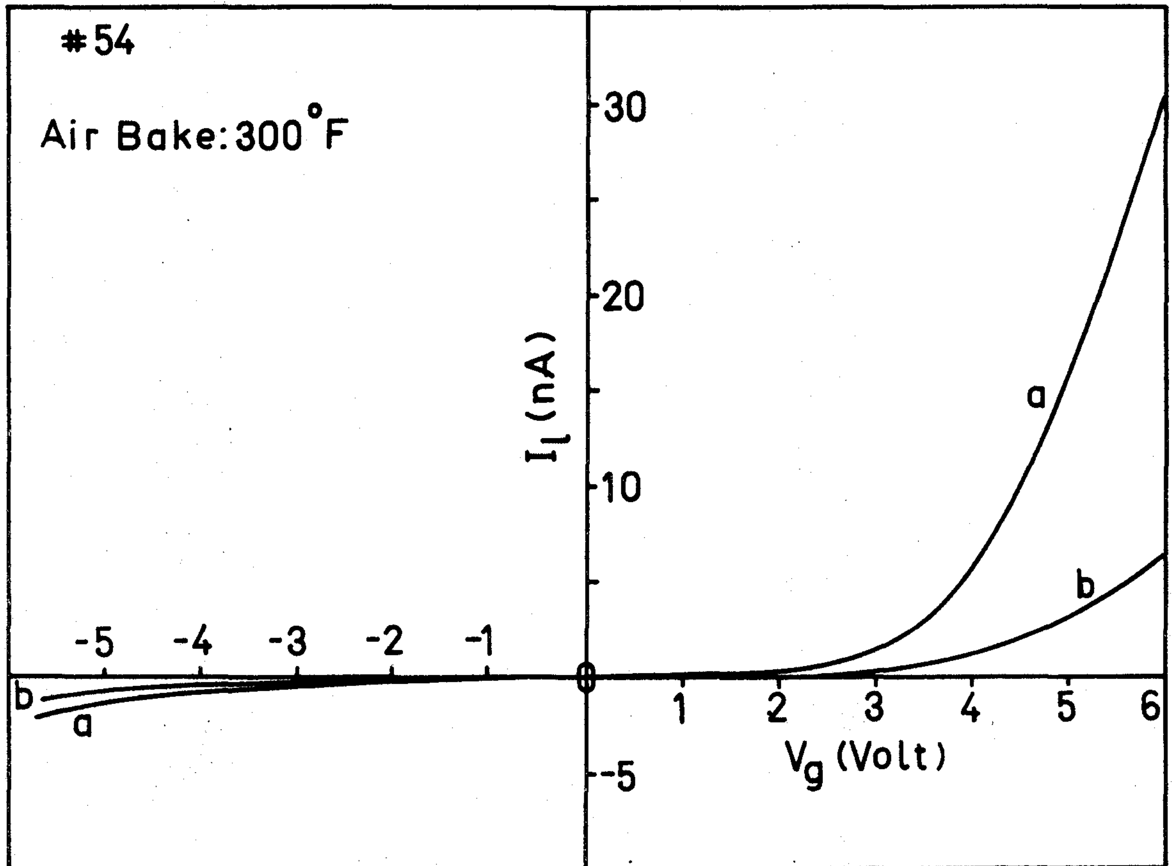

Figure 9.3 Leakage current as a function of bias voltage in a $N_iCr-Y_2O_3(N_2)$-CdS-Aℓ Thin-film Tunable Filter.

(a) 4 hour bake at 300°F followed by a pinhole blow-out at 15V, followed by another 4 hour bake at 300°F.

(b) Same as (a) except for another pinhole blow-out at 20V and an additional bake of 7 hours at 300°F.

9.3 MIS-Capacitance and -Conductance Measurements

Small-signal capacitance measurements were performed on actual Nichrome-Y_2O_3-CdS-$A\ell$ filters in order to determine the expected tuning range. The small-signal conductance was also measured as a function of both bias-voltage and frequency.

It must be noted that the effect of the distributed resistance due to the nichrome-layer has to be taken into account if the measurements are done on an actual filter. This is especially true for the conductance (or equivalent series resistance) as a function of frequency. The input impedance of the "ideal" URC-filter is given by equation (3.11):

$$Z_{in} = z_{11} = Z_o \coth\gamma = R_{11} + jX_{11}$$

$$= \frac{R}{\sqrt{j\omega RC}} \cdot \coth\sqrt{j\omega RC} \qquad (9.1)$$

The real part, R_{11}, is plotted in Figure 9.4. The parameters used, were those pertaining to sample #56, namely

$$R = 151.24\Omega$$

and $$C\Big|_{V=0} = 2.2405 \text{ nF} \quad .$$

It may be seen that R_{11} has a constant value of $\frac{1}{3}R$ for a large part of the frequency region under consideration. It is constant from at least $10^{-4}f_o$ to f_o, where $f_o = \frac{1}{2\pi RC} = 4.7 \times 10^5$Hz. This can be shown analytically by expanding (9.1) in terms of exponentials. If we expand the exponentials in Taylor series and retain terms up to third degree, it turns out that

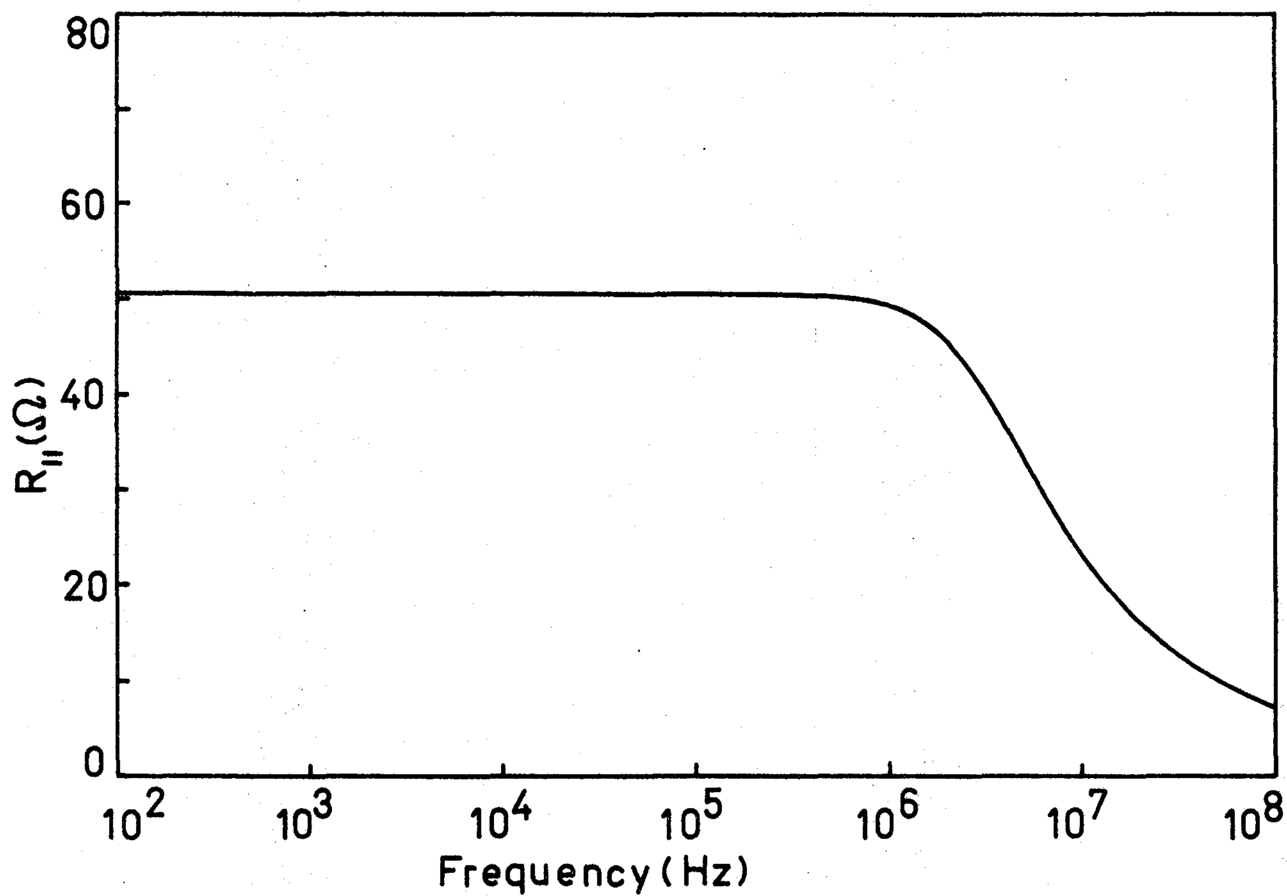

Figure 9.4 Calculated Real Part of the Input Impedance of an Ideal URC Filter as a Function of Frequency. ($R = 151.24\Omega$, $C = 2.2405$ nF).

$$R_{11} = \mathrm{Re}\{Z_{in}\} \doteq \frac{3R}{\frac{x^2}{4} + 9} \quad .$$

If x<1: $R_{11} \doteq \frac{R}{3}$. (9.2)

The real part of the impedance was measured as a function of frequency on a GR1615-A capacitance bridge. Some typical results are shown in Figure 9.5. The dashed curve corresponds to $\mathrm{Re}\{Z_{in}\}$ of the "ideal" filter. The two curves identified by the circles and triangles are the measured real parts of the input impedance for V_g=0V and V_g=+3V, respectively. The equivalent loss resistor R_s which was defined in Chapter 3, is equal to the difference between the dashed line and the other two curves. This difference for V=0 is indicated on the same figure with squares.

It may be seen that the loss resistor decreases with increasing frequency. The low frequency values are probably determined by interface states and bulk states in the semiconductor.

The results of a capacitance and conductance measurement as a function of the field-plate voltage V_g are shown in Figure 9.6. These particular curves have not been corrected for the distributed resistive layer. A few important points may be noted:

(i) There is a hysteresis effect in both the capacitance and conductance. The shift, which amounts to 5.6V, is probably caused by ion drift in the insulator. If we take the "insulator capacitance" to be 2.67 nF, this shift corresponds to a charge density

$$N_i = \frac{C_i \Delta V}{qA} = 6.65 \times 10^{11}\ \mathrm{cm}^{-2} \quad .$$

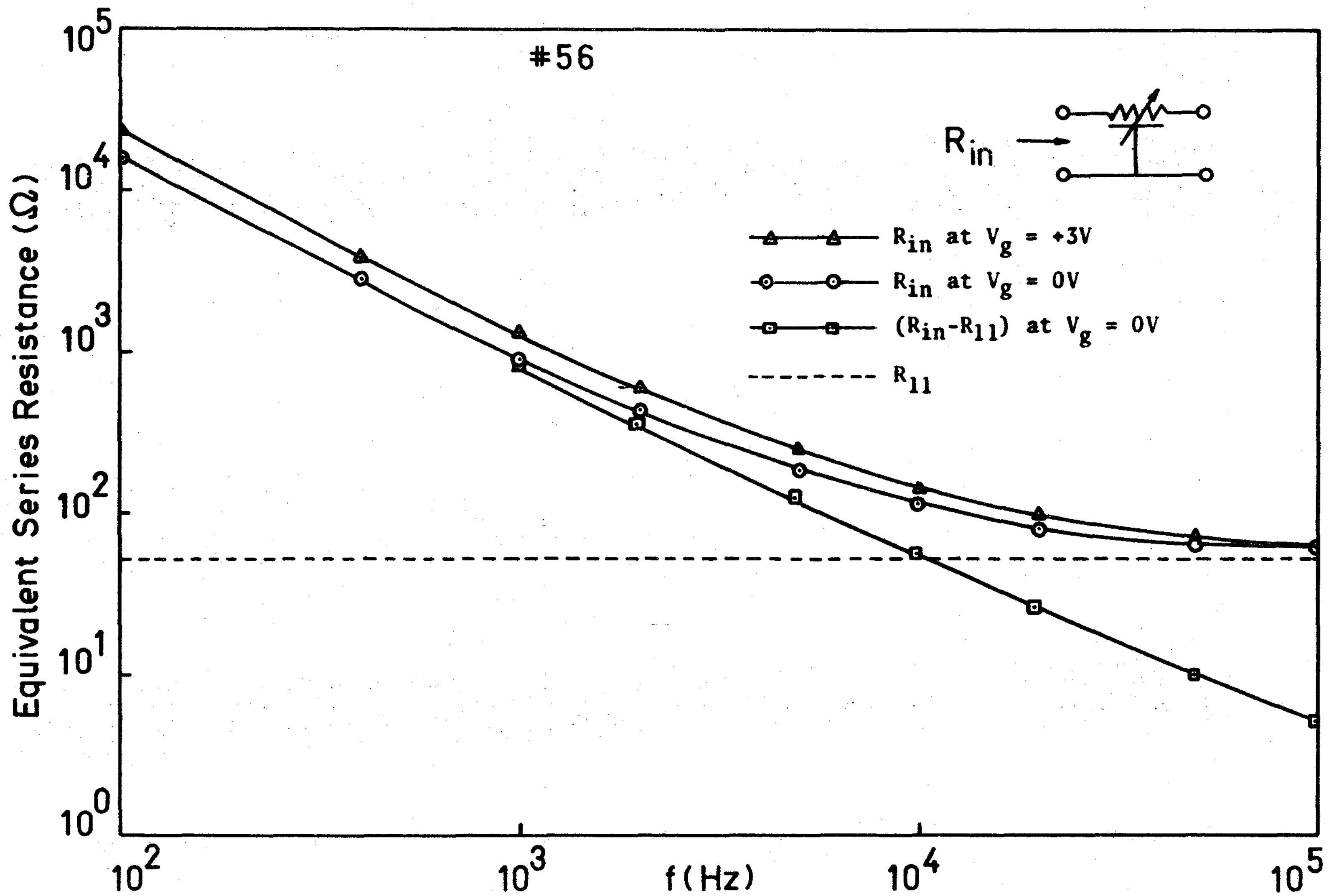

Figure 9.5 The Measured Real Part of the Input Impedance of a Nichrome-Y_2O_3-CdS-Aℓ Device as a Function of Frequency.

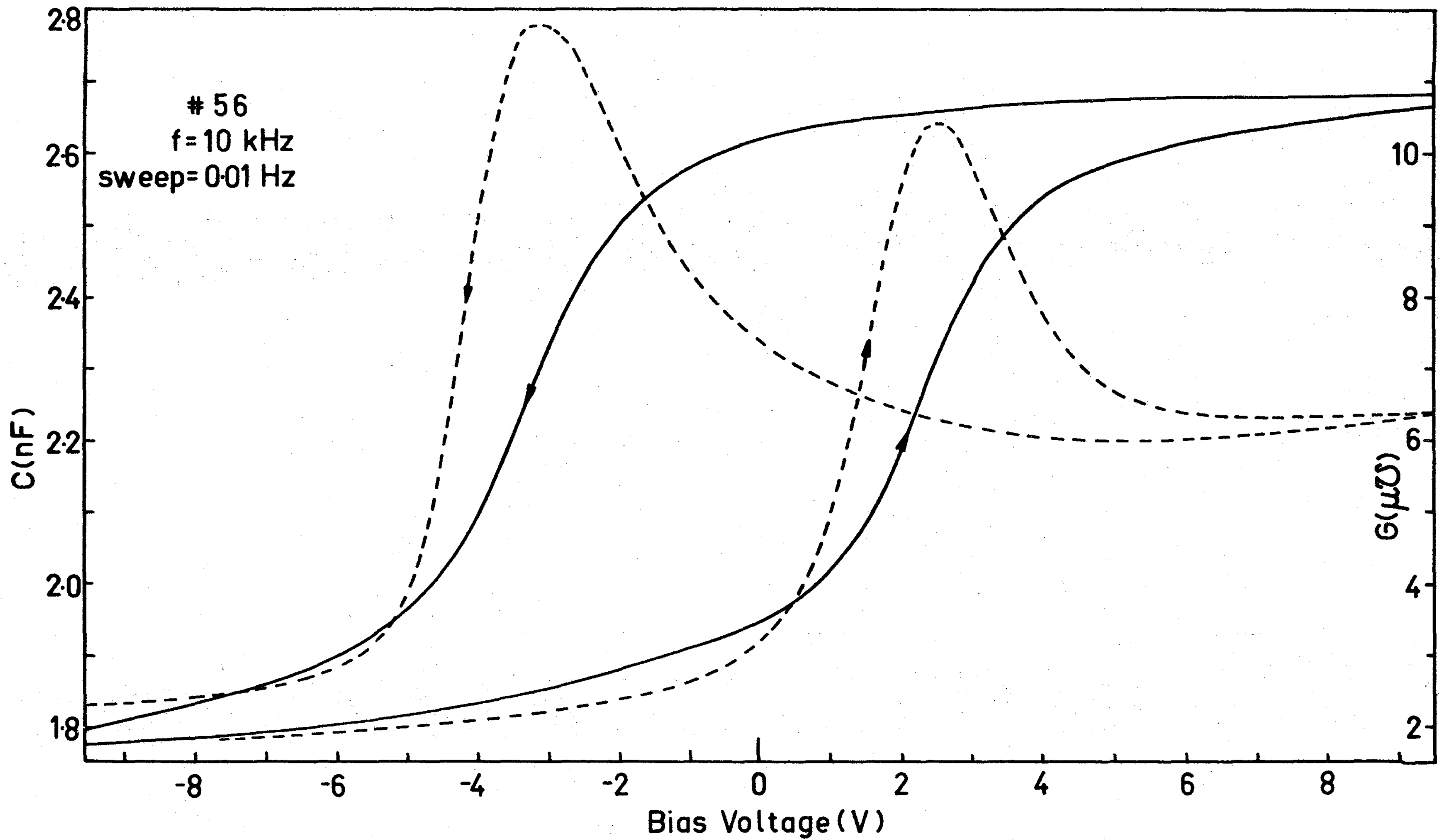

Figure 9.6 The Measured Capacitance (solid line) and Conductance (dashed line) of a Nichrome-Y_2O_3-CdS-Aℓ Device. (not corrected for R_{11})

(ii) The small-signal conductance curve has a maximum value when the interface potential is such that the semiconductor is in the depletion mode. This peak lies at the same value of capacitance for both the sections of the CV-curve. This indicates that the conductance peak is a unique function of the interface potential.

(iii) The fact that the conductance which is obtained when the bias is swept from a positive to a negative value has a higher peak, may be explained by the ion drift. If the field-plate potential is positive, the ions drift towards the semiconductor-insulator interface. It is possible that they may actually increase the number of interface states which in turn lead to a larger conductance.

(iv) The insulator thickness and doping density can be calculated from the CV-curve of Figure 9.6. If we use a relative dielectric permittivity of 10.4 for the Y_2O_3 and 10 for the CdS, the thickness turns out to be:

$t_i = 4847$ Å .

The doping density follows from the ratio of maximum to minimum capacitance. (Please refer to Section 2.2.1.)

$$\frac{C_i}{C'_{min}} = 1.5085 .$$

This corresponds to a doping density

$N_d = 4.28 \times 10^{16}$ cm^{-3} .

9.3.1 Calculation of the Doping Density

The doping density of evaporated semiconductor films may be determined by various means. These may involve either a Hall-effect experiment or CV-measurements. The problems associated with the Hall-effect technique lie mainly in the fact that space charge layers exist in the vicinity of the surfaces of the film. These may be caused by interface states, ions, adsorbed gases, etc. If the films are fairly thin, these space charge layers may occupy a considerable portion of the thickness of the film. If these are depletion layers, the doping density obtained from the Hall coefficient will be too low. Hall measurements done during the course of this work verified this statement.

The effective number of donors may as well be calculated from the capacitance-voltage measurements on an MIS-sample. Even though evaporated CdS-films have a non-uniform donor concentration, the CV-measurements yield probably the most reliable results. N_d can either be determined from the ratio of insulator capacitance to the high frequency minimum of capacitance, or by means of a curve-fitting procedure. The first mentioned method is less amenable to the effects of ion drift and interface states, as will be illustrated subsequently.

The CV-curves for Sample #51 are illustrated in Figure 9.7. The device was biased at -10V for approximately 20 minutes and the small-signal CV-curve was then measured with a bias sweep speed of 40 mV/second. The same procedure was repeated, but this time with a sweep speed of 800 mV/second. The test frequency in both cases was 10kHz. The two curves are denoted by "a" and "b" in Figure 9.7.

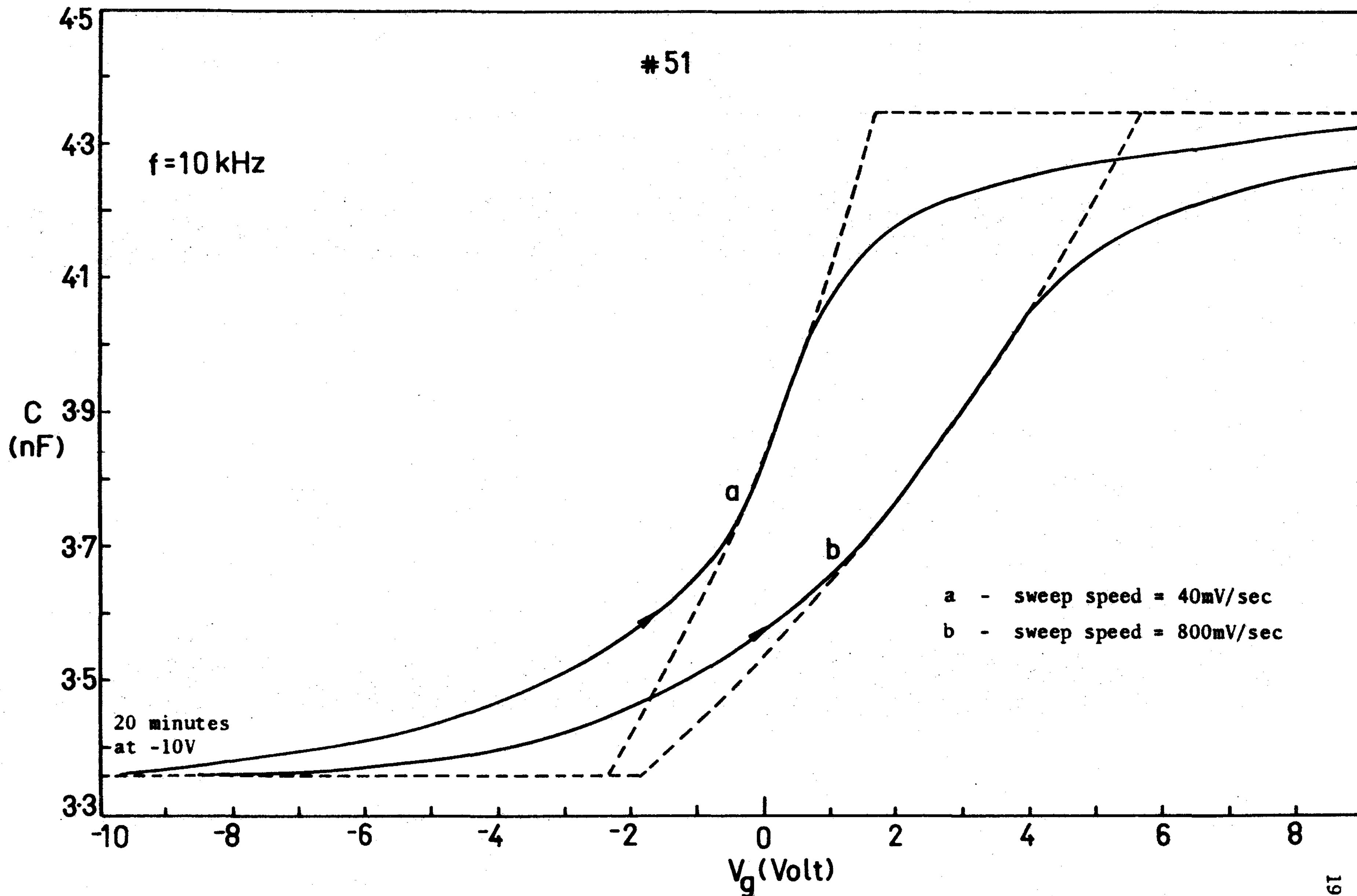

Figure 9.7 Determination of Doping Density by means of the Depletion Approximation. The Curves a and b were obtained at different Bias Sweep Speeds.

The relative dielectric permittivity of the insulator film is calculated by means of the parallel plate capacitance formula. Using an insulator thickness t_i=3000Å (measured by means of a Sloan Type M100 angstrometer), ε_i=10.49. This agrees quite well with the value 10.8 ± 0.4 as was determined in Chapter 6 for Y_2O_3. The ratio

$$\frac{C_i}{C'_{min}} = \frac{4.35}{3.36} = 1.295 \qquad \text{from Figure 9.7.}$$

If we use equation (2.21) to calculate the doping density of the semiconductor (employing ε_s=10 and n_i=2.1 x 10^{-2} cm^{-3}) a value

$$N_d = 3.55 \times 10^{17} \ cm^{-3}$$

is obtained.

The curve fitting procedure using the depletion approximation as was given by equation (2.18) yields N_d = 8 x 10^{16} cm^{-3} for curve "a" and 1.5 x 10^{17} cm^{-3} for curve "b". The large discrepancy between the value obtained from curve "a" and the value obtained from the C_i/C'_{min} -method, is possibly due to ion drift which occured during the time the CV-measurement was performed. This is more or less substantiated by the fact that the CV-curve obtained with a faster sweep speed yields a better value for N_d.

The doping density of these evaporated CdS films is determined to a great extent by the substrate temperature as was illustrated in Figure 7.2. Due to the limitation of the substrate heating system, the resistivity could not be made higher than approximately 10 to 50Ω-cm.

9.3.2 Instabilities in the Y_2O_3-CdS-System

A time-dependent drift was observed in the Nichrome-Y_2O_3-CdS-Aℓ samples at room temperature. The drift manifests itself as a continuous change in capacitance for a constant bias voltage. Since this type of behaviour is of prime importance in thin-film electronic devices, some of its aspects will be discussed.

The instability was observed by measuring the small-signal capacitance as a function of time after applying various bias voltages to the device. To be more specific, consider the curves depicted in Figure 9.8. The MIS-capacitor was biased into accumulation for various lengths of time. The bias was then switched to a negative value (from +11.5V to -11.5V) and the capacitance recorded as a function of time. It will be noted that the drift is dependent on the time the device has been in accumulation.

The asymmetric nature of the instability is shown in Figure 9.9. It was always found that the drift time constant from inversion (or depletion) to accumulation is much shorter than for the opposite bias voltage.

The time-dependent capacitance may be due to one or more of the following:

(i) Mobile positive ions in the insulator

(ii) Mobile negative ions in the insulator

(iii) Trapping of holes or electrons by states in the insulator. These states may be distributed throughout the whole insulator and carriers communicate with the traps by a tunneling mechanism.

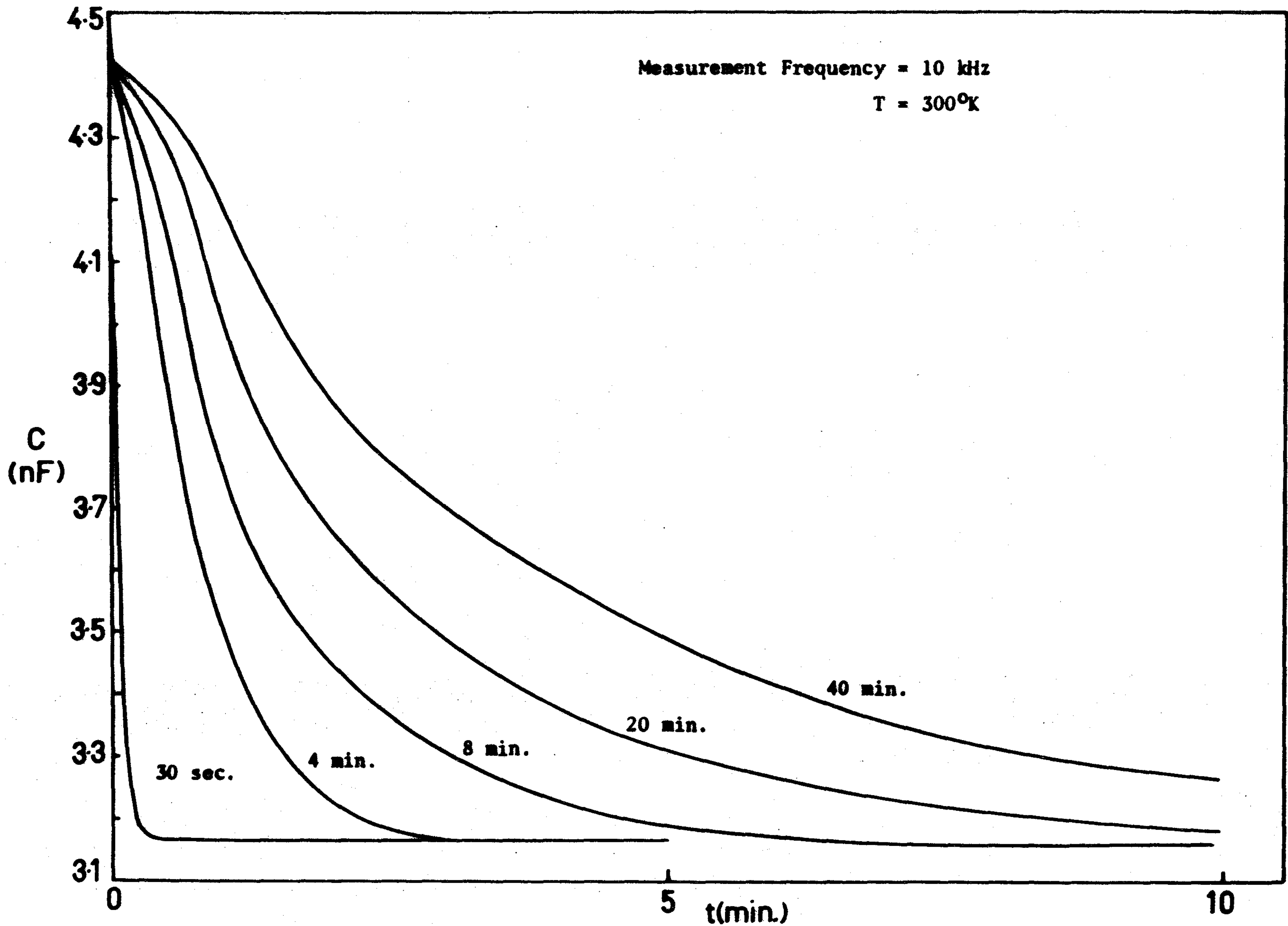

Figure 9.8 DC Drift in Sample #51. The device was kept in accumulation (+11.5V) for various lengths of time and then switched to -11.5V on the gate.

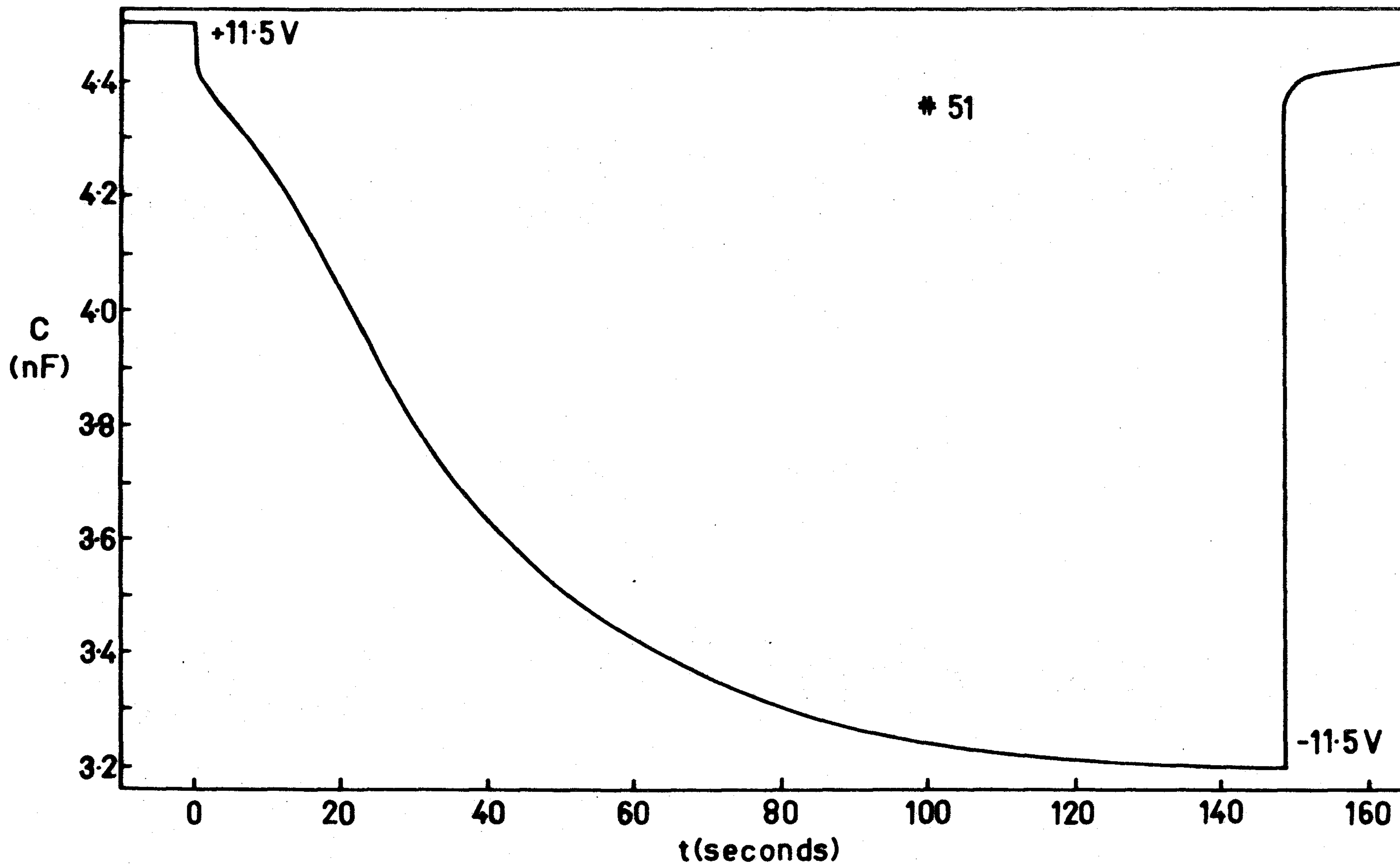

Figure 9.9 MIS-Capacitance as a Function of Time Illustrating the Asymmetric Drift Rates in a Nichrome-Y_2O_3-CdS-Al Structure.

This work was not able to distinguish between the different types of drift processes. For the sake of argument, we will assume that it is caused by positive ions. The asymmetrical drift rate may be explained by invoking an argument used by Swystun and Tickle[12] for evaporated CdSe-SiO_2-Aℓ units. Their model assumes that the ions are located predominantly in traps at the insulator-semiconductor and insulator-metal interfaces. The activation energy for the release of ions from these traps are not necessarily the same for both interfaces. The nature of the asymmetry in the Nichrome-Y_2O_3-CdS-Aℓ system indicated that the activation energy is higher at the Y_2O_3-CdS interface compared to the Y_2O_3-Nichrome interface. This is in contrast to the findings quoted above for CdSe-SiO_2-Aℓ. The longest time constant for their system was observed for ions emitted from the metal-insulator interface as opposed to the insulator-semiconductor junction.

The density of ions follows from the shift of the CV-curve after the drift has occured.

$$N_i = \frac{C_i \Delta V}{qA} \quad .$$

The experimental values varied between 6×10^{11} cm^{-2} and 2×10^{12} cm^{-2} for the units studied in this work.

9.4 The Tunable URC-Filter

9.4.1 The URC Notch Filter

The tunability of the thin-film distributed networks can best be observed by using them in the notch filter arrangement. The tuning behaviour of this particular type of filter is also quite sensitive to

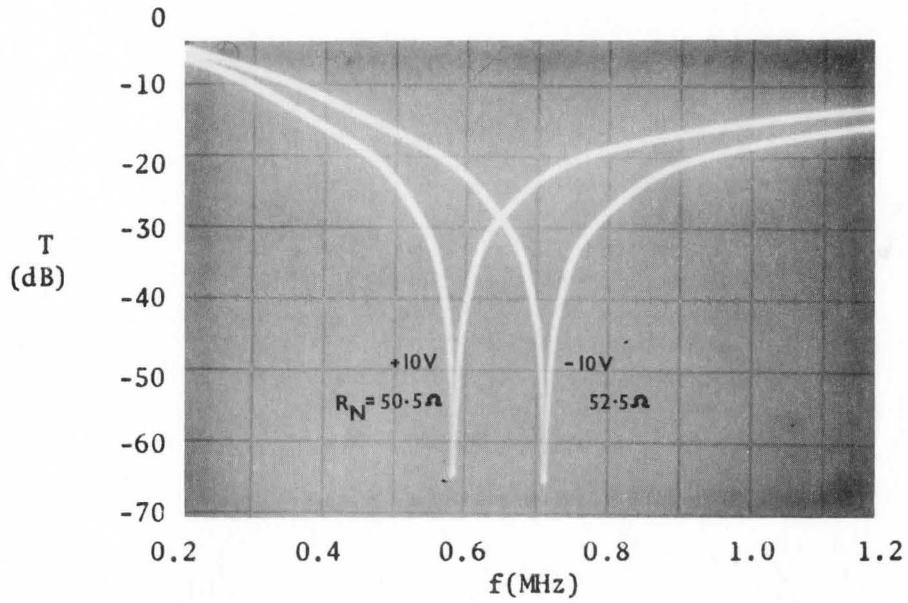

Figure 9.10 Tuning Range of #51 URC Tunable Notch Filter. (22% Change in Notch Frequency)

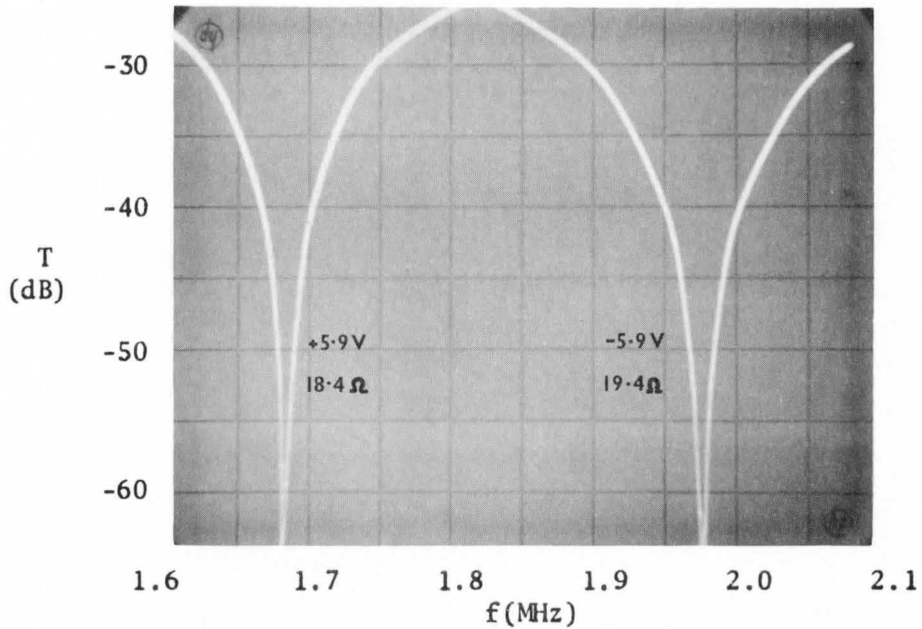

Figure 9.11 Tuning Range of #54 URC Tunable Notch Filter. (18% Change in Notch Frequency)

the parasitic effects such as MIS-losses and notch inductance. This fact allows one to make an evaluation of these parasitics.

It was indicated in Chapters 2 and 4 that the available tuning range is dependent on the thickness of the insulator and the doping density of the semiconductor. The thickness of the insulator is more or less fixed to a value greater than 3000Å due to leakage currents and the desired frequency range of operation. This leaves the semiconductor impurity concentration as the main factor governing the tuning range. This concentration, in turn, is dependent on the substrate temperature during the time of evaporation of the semiconductor film. The maximum tuning range achieved in this work was approximately 30%.

The characteristics of two typical tunable URC-filters are depicted in Figures 9.10 and 9.11. The relative frequency change in both cases was of the order of 20%. It may be noted that the notch resistor had to be changed by approximately 5% in each instance in order to get an optimum null at both extreme frequencies. This will be discussed in the next section.

The actual experimental circuit used for the tunable filters is shown in Figure 9.12. This includes blocking capacitors and a biasing resistor.

9.4.2 The Influence of Parasitic Losses and Stray Inductance

(a) Detuning

It was pointed out in Chapter 4 that inductance in series with the notch resistor and losses introduced by the MIS-system can lead to

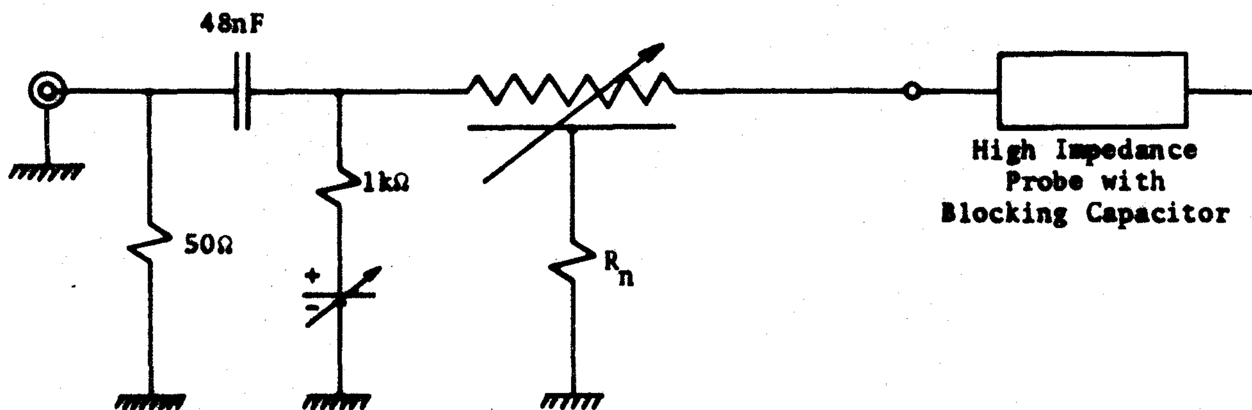

Figure 9.12 Experimental Arrangement for Determining the Voltage Transfer Function of the Tunable URC Notch Filter.

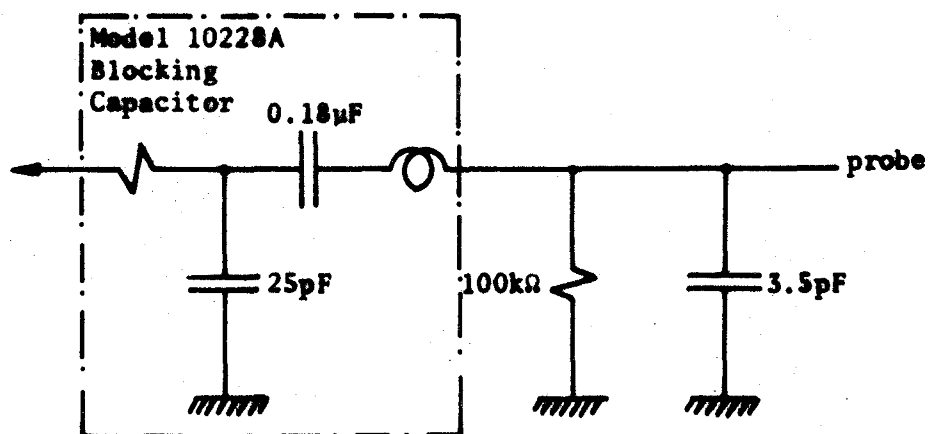

Figure 9.13 Schematic Diagram of the HP Model 1123 High Impedance Probe with the Model 10228A Blocking Capacitor.

detuning. This means that the notch will not stay optimum for the whole frequency range. This effect can quite clearly be seen in Figures 9.14 and 9.15.

The set of curves displayed in Figure 9.15 is particularly interesting, for it illustrates the complicated tuning behaviour that may be obtained in some instances. This type of behaviour will be observed if the losses in the MIS-system are frequency dependent. This occurs in devices operating at the lower frequencies where the interface-state losses are important compared to losses introduced by the ohmic contact. It is probably only fortuitous that the loss parameter B and inductance parameter η satisfy the optimum condition at more than one frequency (bias voltage). The detuning of device #54 is more typical of what was observed for the filters. It may be compared with the theoretical curves as displayed in Figures 4.4 and 4.5.

The introduction of parasitic inductance was inevitable during the experimental measurements. The leads and micropositioner probes introduced more than 100 nH in series with the notch resistor. A notch resistor deposited on the same substrate as the device will naturally have a much lower inductance associated with it.

(b) Tuning Range Compression

The CV-curve of device #56 is shown in Figure 9.6. The ratio of maximum to minimum capacitance is nearly 1.51. This is in contrast to the tuning ratio of the same device of only 1.11 (from Figure 9.17). This is a good example of the reduction in the ratio of maximum to minimum frequency that is caused by the parasitic effects. The

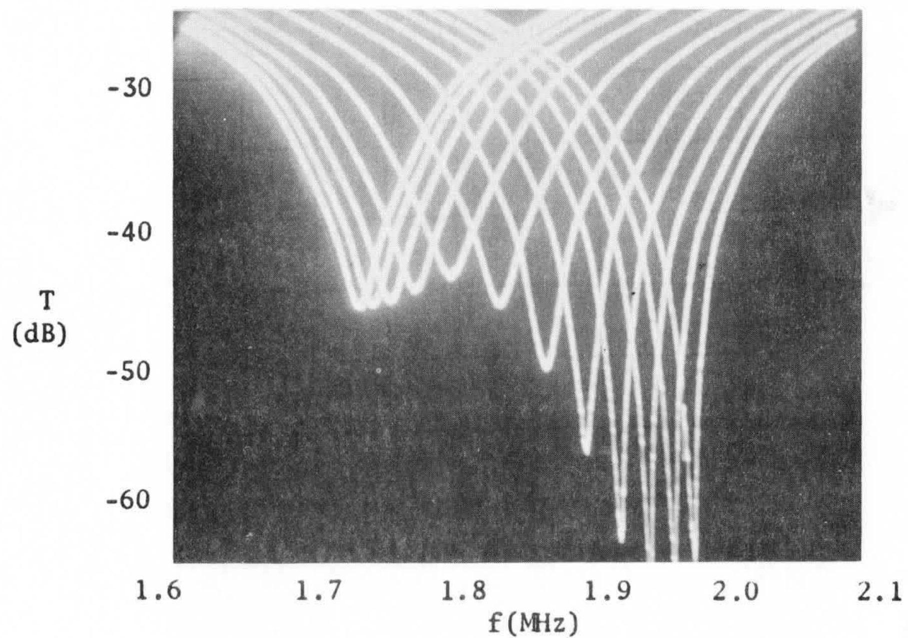

Figure 9.14 Tuning Characteristics of #54 URC Tunable Notch Filter (R_n=18.3Ω). $-5.8V<V_g<+5.7V$

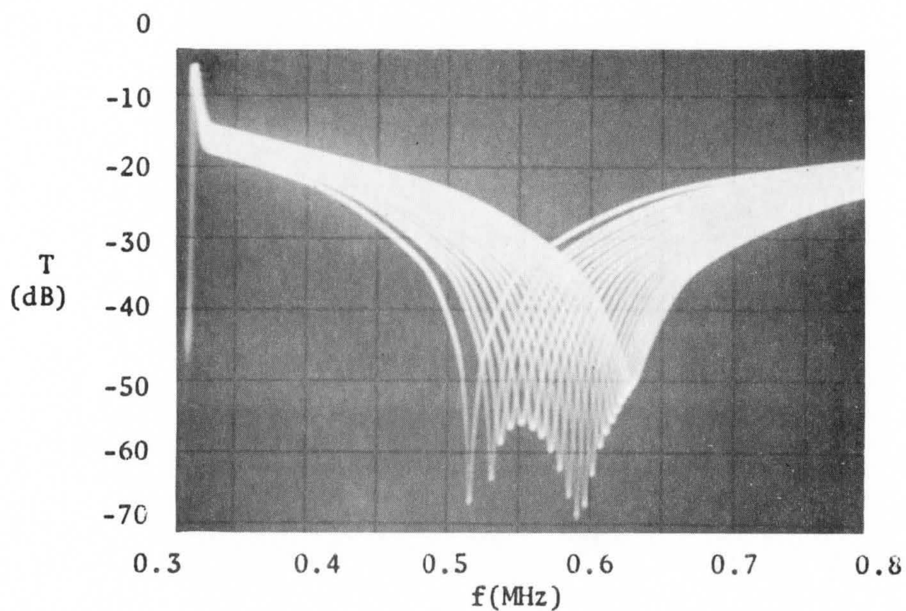

Figure 9.15 Tuning Characteristics of #51 URC Tunable Notch Filter. R_n=50.5Ω Note the Two Optimum Nulls. $-5V<V_g<+5V$

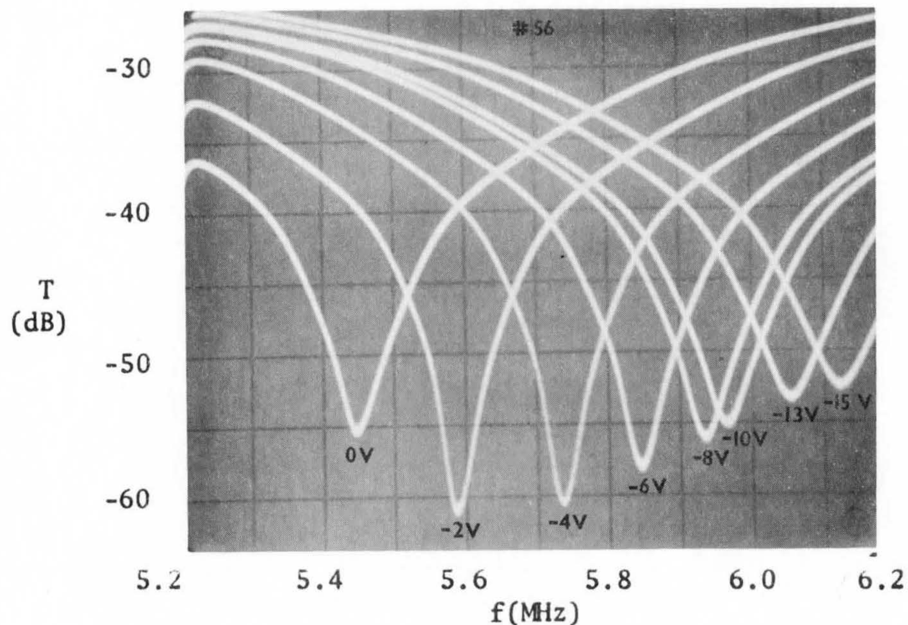

Figure 9.16 URC Tunable Notch Filter (#56).
The Detuning is less than 10dB.
(R_n = 9.13 Ω)

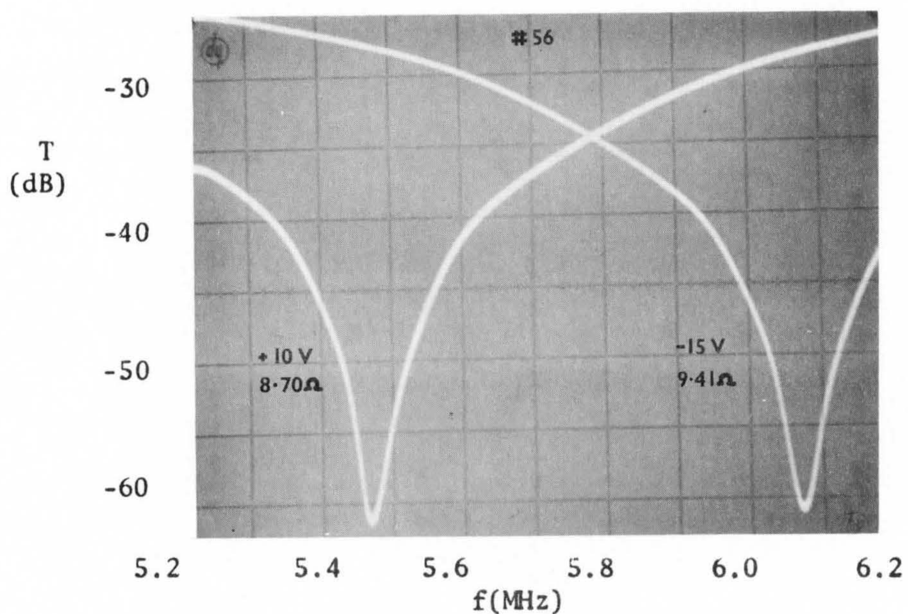

Figure 9.17 Example of Tuning Range Compression.
Although the Capacitance change is
51%, the Frequency Tuning is only 11%.

inductance is mainly responsible for this effect. Instead of having a normalized notch frequency x_1=11.1902 which is independent of bias, this particular filter had x_1=10.21 at the upper frequency (bias voltage = -15V) and x_1=13.88 at the lower frequency (bias voltage = +10V). This increase of x_1 towards the lower frequencies is due to the fact that η is reduced as C is increased. From Figure 3.11 it can be seen that lower values of η lead to higher values for x_1.

This effect will become especially important for devices operating at high frequencies. Even a very small inductance may cause a significant compression of the tuning range.

9.4.3 The Experimental URC Bandpass Filter

In order to demonstrate the URC bandpass filter in practice, and to study the effects of a non-ideal wideband amplifier, the URC null network was used in the feedback loop of an HP450A amplifier in cascade with a 180° phase shifter. The phase shifter was required because the phase shift is zero for the HP450A at midband frequencies. The phase shifter was so designed that the dc level at the output could be changed between +3.5V and -3.5V. This could be used to bias a tunable URC network in order to obtain a tunable bandpass amplifier. Details of the circuits are given in Figures 9.18 and 9.19.

A meaningful comparison between experiment and theory is only possible if the properties of the amplifier assembly are taken into account. Neglecting all parasitics, and assuming a wideband amplifier with a gain much greater than one, the transfer function given by equation 3.59 is applicable. In practice the effects of the finite

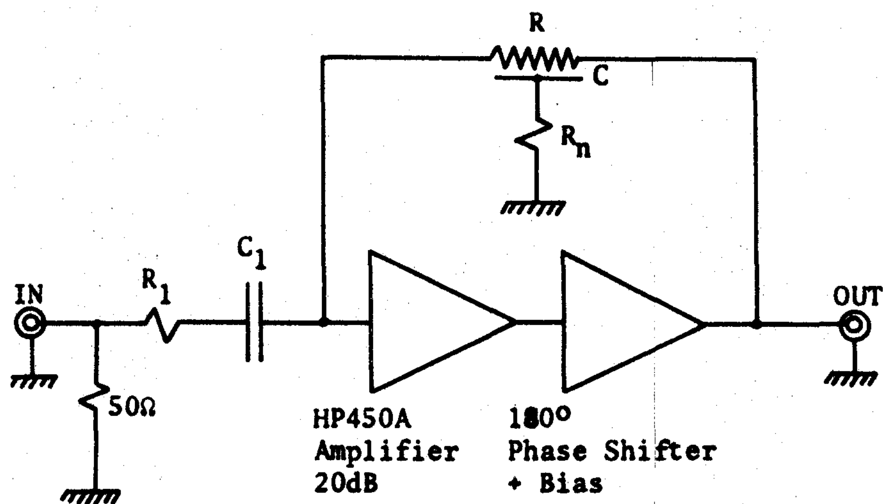

Figure 9.18 URC Bandpass Amplifier

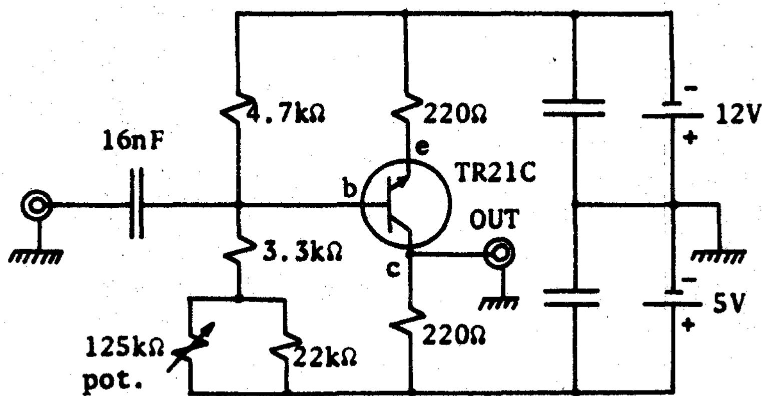

Figure 9.19 Phase Shifter and Bias for URC-Network.

input and output impedance of the amplifier, the phase shift and gain as a function of frequency and the parasitic effects in the null network have to be taken into consideration. The transfer function given by equation (3.73) then describes the behaviour of the network. It should be clear from this expression that the network behaviour will in general be quite different from what is to be expected from the "ideal" circuit.

A thin-film non-tunable Nichrome-Y_2O_3-ℓ filter (#48) was constructed for the purpose of illustrating the appropriateness of equation (3.73). Since the dielectric loss in the Y_2O_3 is very low, its effect could be neglected. The gain and phase of the wideband amplifier assembly were measured as a function of frequency by means of the HP675A and HP676A network analyser. The output impedance of the amplifier is very nearly equal to the 220Ω resistor in the phase shift network. The input admittance is given in the specification sheets of the H450A amplifier as 10^{-6}℧ in parallel with 15pF. The resistor R_1 and capacitor C_1 in Figure 9.18 are equal to 389Ω and 1.535 nF, respectively. The parameters of the URC-network are as follows (#48):

$R = 265.7\Omega$

$C = 2.331$ nF .

A comparison between the experimental (solid line) and theoretical results (dashed line) is made in Figure 9.20. L_n and R_n were the only adjustable parameters in the calculations. This good agreement between experiment and theory was obtained with $L_n = 1\mu H$ and $R_n = 166\Omega$. The value of R_n differs significantly from

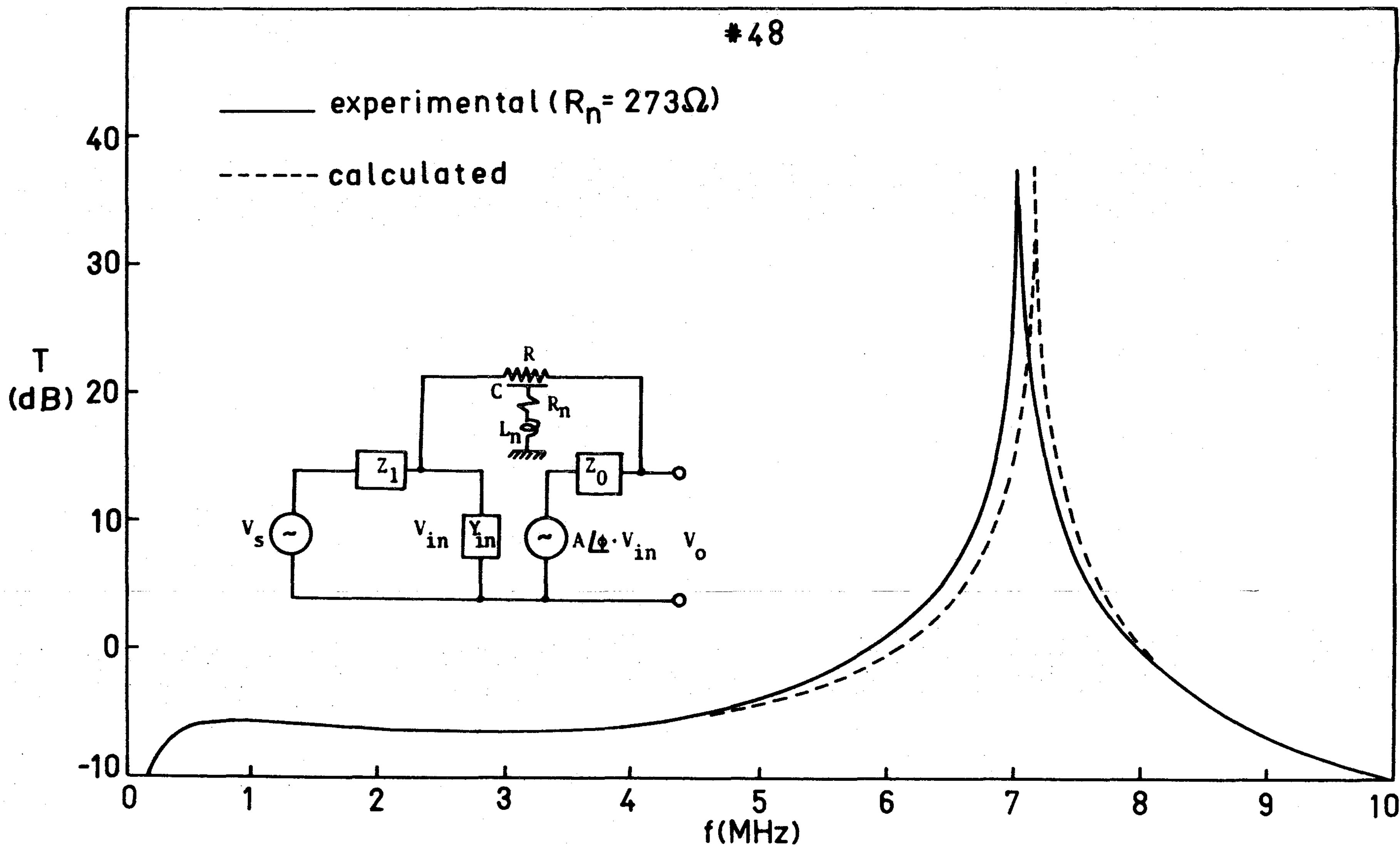

Figure 9.20 Comparison between the Experimental (solid line) and Calculated (dashed line) Response of the URC Bandpass Amplifier.

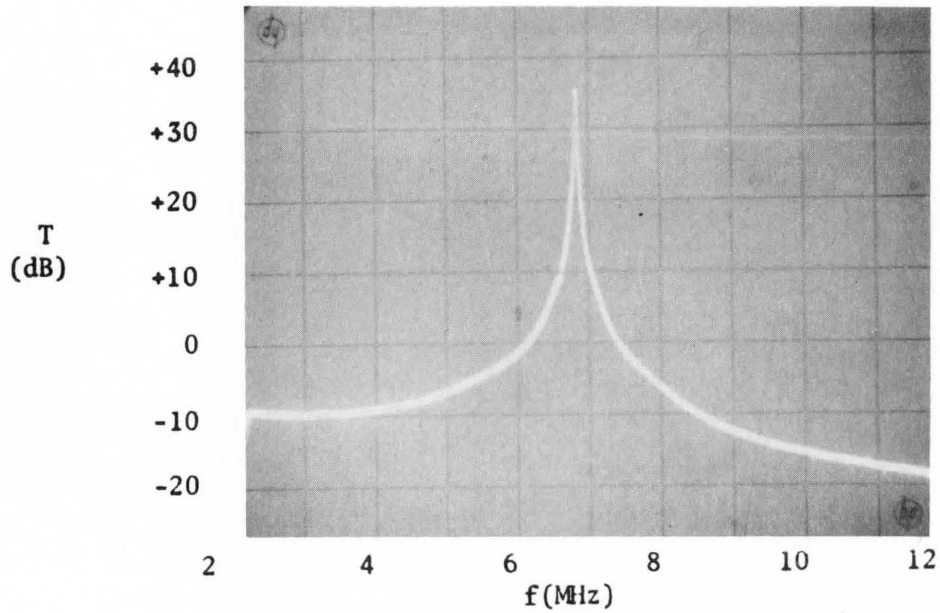

Figure 9.21 High-Q Tuned Amplifier (#48)
R_n = 208.4Ω

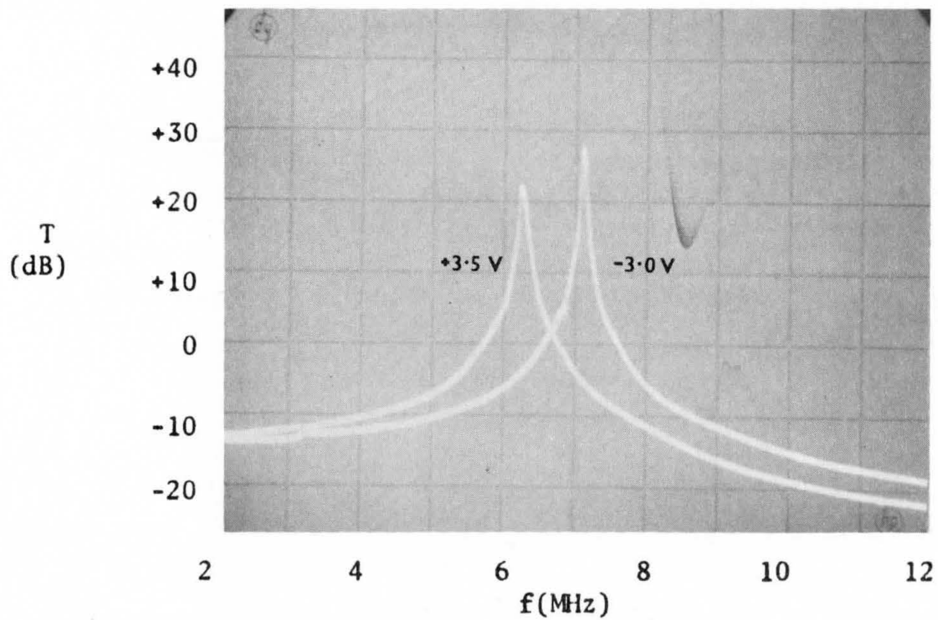

Figure 9.22 High-Q Tuned Amplifier with Tunable Centre Frequency (#54) R_n=166Ω

the experimental value of 273Ω. It is felt, however, that a different value of L_n will yield a better agreement.

The Q of the bandpass amplifier, defined as the ratio of the centre frequency to the 3dB bandwidth, was measured to be 742.

The centre frequency, which occurs at about 6.9 MHz, should be compared with the centre frequency of 2.88 MHz predicted by the "ideal" theory.

A tunable bandpass filter was also constructed using device #54. A frequency shift of nearly 17% was obtained using a bias voltage of -3.5V and +3.0V. The centre frequency could be moved from 7 MHz to 6 MHz. The experimental results are shown in Figure 9.22. No adjustment in R_n was made for the two curves.

9.5 Conclusion

We discussed the results pertaining to thin-film, evaporated, tunable URC-filters. After taking these devices from the vacuum system, a series of air bakes had to be performed to reduce the leakage currents and ac losses.

Useful measurements regarding MIS-losses and -capacitance could be made on the filters if the effect of the distributed resistance R was taken into consideration. Some suggestions were also made regarding the instability which was observed.

Actual tunable notch filters and bandpass filters performed satisfactorily. The deviations from expected behaviour could be accounted for by introducing the effects of losses and parasitic inductance.

CHAPTER 10

Conclusions and Recommendations

This research yielded a thin-film tunable filter that could be made entirely by vacuum evaporation. The experimental notch filters constructed, operated in the frequency range 500 kHz to 6 MHz. The maximum tuning range achieved in this work was of the order of 30%.

The tunable bandpass filter constructed, had a quality factor Q of more than 700 and a tuning range of 17%. Close agreement between experiment and theory was obtained by taking the real nature of the wideband amplifier into consideration.

The detuning effect observed experimentally for notch filters was attributed to losses in the metal-insulator-semiconductor system and the effect of a parasitic inductor in series with the notch resistor. These same parasitic effects were also employed to explain the reduction in the available tuning range.

The correspondence between the material properties and device characteristics was traced throughout the investigation. This revealed that the insulator thickness, relative dielectric permittivity of the insulator and the doping density of the semiconductor control the available frequency shift. The need for a high resistivity semiconducting material was stressed.

Y_2O_3 was used for the first time in conjunction with CdS in a filter arrangement. MIS-measurements indicated that mobile ions are

present in a concentration between 6×10^{11} and 2×10^{12} cm^{-2}. These ions caused an instability in the device characteristics. This may be serious in some applications, but for a filter in which the bias is switched rapidly and continually between $+V_g$ and $-V_g$, this drift may not be important. It was shown that the small-signal ac losses in the Y_2O_3 can be neglected in comparison with the losses introduced by insulator-semiconductor interface states, bulk states in the semiconductor, and the ohmic contact to the semiconductor film. The interface and bulk state losses are especially important at frequencies below a few hundred kHz. Above these frequencies the ohmic contact starts to become important.

A literature search revealed that many of the properties of evaporated CdS thin-films are not well understood. With this in mind, a new experiment was proposed which could yield information on the doping density and transport properties of electrons in these films. If this MISIM Hall-Field Effect experiment could be combined with capacitance-voltage, conductance-voltage and thermally stimulated current measurements, a reasonable understanding of CdS thin-films may evolve. Parenthetically, the modulation of ionized impurity scattering by the screening of electrons in the accumulation layer was given as a possible alternative explanation for experimental results observed by some other workers[100].

Further research should be conducted to improve the tunable filter by stabilizing the insulator and reducing parasitic effects. The parasitic inductance may be reduced quite readily by depositing a

thin-film notch resistor directly on the same substrate as the URC-network. Another alternative may be the utilization of a field-effect transistor in the linear mode as the notch resistor. By this means the notch inductance could virtually be eliminated. Recent work carried out by Waxman and Mark[22] on plasma anodized aluminum, demonstrated that thin-film field-effect devices can be made with low interface-state densities. Research on Y_2O_3 with its larger relative dielectric permittivity may be important in this respect.

A better CdS evaporation system utilizing the ideas put forth by De Klerk[46] will enable one to increase the resistivity. This will lead to an expansion of the tuning range.

Other semiconductor-insulator systems should be investigated with a reduction of the interface state density and ion drift in mind. All the semiconductors found suitable for thin-film transistors could be tried. Another material which is in many respects similar to CdS, namely CdSe, may yield good results. Oxides of the other rare earths will also have to be used as the insulator. Multilayer dielectrics, for instance Y_2O_3 and Si_3N_4, may reduce the problems associated with ion drift.

This work has strictly been applying thin-film semiconductors and evaporated insulators. There is no reason why single crystal silicon in conjunction with the steam grown native oxide could not be used.

Virtually no work has been done on the transient response of the tunable filter. In the experiments performed in this investigation

the notch filter could be tuned at a frequency of at least 10 Hz, i.e., the bias voltage could be changed at this rate with the notch following. The limiting frequency could not be established due to the fact that the sweeping signal generator had a maximum sweep rate of 100 Hz. A few suggestions may be made, however, on the expected transient behaviour:

(i) It is well known[5,108] that a transient in the capacitance of the MIS-device occurs if the bias is changed rapidly into the inversion regime of operation. This arises because of the fact that the inversion charge does not build up instantaneously. It has to wait for the generation of minority carriers. It can take up to several seconds for this transient to die down. Clearly, it will be undesirable to operate the tunable filter into the inversion regime if a rapid and repeatable switching is required.

(ii) The capacitance in the accumulation and depletion regimes may also be a function of the bias sweep speed due to interface states. A thorough study has to be made of the physical properties of these states before their effects could be evaluated. Without any surface states, the response time in these regimes is proportional to the dielectric relaxation time. This may be of the order of a few nanoseconds.

The application of the tunable URC-filter was restricted to the notch filter and bandpass amplifier. A potentially fruitful area of application lies in other more sophisticated circuits. The basic

unit may be used in conjunction with active and passive elements to form a voltage-controlled oscillator. A narrow band filter with automatic tracking capabilities is another possibility.

In summary, it may be said that useful thin-film tunable filters have been constructed and tested. Much more work is necessary in evaluating both the material properties and circuit applications. It is hoped that this work will serve as a stimulus for further investigation.

APPENDIX A

The resistors $R_{n,ss}$ and $R_{p,ss}$ which account for the flow of charge from the conduction band and valence band to the surface states have been calculated by Lehovec and Slobodskoy[29]. We follow here however, the treatment by Nicollian and Goetzberger[18].

Suppose there is a single level of surface states with energy E_t and density N_s cm^{-2}. In the accumulation and depletion regimes of operation, there is a very small density of minority carriers (holes for n-type material) at the surface. For this case, the interface states interact mainly with the majority carrier band at the surface.

If the states obey Shockley-Read statistics, the net current flow flowing into these states may be expressed as follows:

$$i_{ss}(t) = qN_s c_n\{1-f(t)\}n_s(t) - qN_s e_n f(t)$$

where $\quad N_s c_n\{1-f(t)\}n_s(t) = R_n(t)$ = recombination rate

and $\quad N_s e_n f(t) = G_n(t)$ = generation rate

and $\quad c_n$ = electron capture probability

e_n = electron emission constant

$f(t) = \bar{f}+\tilde{f}$ = time dependent Fermi function at the surface

$n_s(t) = \bar{n}_s+\tilde{n}_s$ = electron density at the surface

$$i_{ss}(t) = qN_s c_n\{1-\bar{f}-\tilde{f}\}\{\bar{n}_s+\tilde{n}_s\} - qN_s e_n\{\bar{f}+\tilde{f}\}$$

$$= qN_s c_n(1-\bar{f})\bar{n}_s - qN_s e_n \bar{f} + qN_s c_n\{(1-\bar{f})\tilde{n}_s - \bar{n}_s \tilde{f}\} - qN_s e_n \tilde{f}$$

$$= I_{ss} + \tilde{i}_{ss} \quad .$$

Using the principle of detailed balance, e_n may be solved in terms of c_n and eliminated from the equations.

$$I_{ss} = 0$$

$$\therefore \quad e_n = \frac{1-\bar{f}}{\bar{f}} \bar{n}_s c_n$$

$$\therefore \quad i_{ss}(t) = qN_s c_n\{(1-\bar{f})\tilde{n}_s - \bar{n}_s \frac{\tilde{f}}{\bar{f}}\} \qquad \text{(A1)}$$

But $i_{ss}(t) = qN_s \cdot \frac{d\tilde{f}}{dt}$.

If

$$\tilde{f} = f_m e^{j\omega t} \qquad \text{(A2)}$$

then

$$i_{ss}(t) = j\omega q N_s \tilde{f} \quad . \qquad \text{(A3)}$$

From (A1) and (A3)

$$f = \frac{\bar{f}(1-\bar{f})\tilde{n}_s}{\bar{n}_s\left(1+\frac{j\omega\bar{f}}{c_n\bar{n}_s}\right)} \quad . \qquad \text{(A4)}$$

Substituting (A4) into (A1)

$$i_{ss}(t) = \frac{j\omega q N_s \bar{f}(1-\bar{f})}{1 + \frac{j\omega\bar{f}}{c_n\bar{n}_s}} \cdot \frac{\tilde{n}_s}{\bar{n}_s}$$

But $$\frac{\tilde{n}_s}{\bar{n}_s} = \frac{e^{\beta(\bar{\psi}_s+\tilde{\psi}_s)} - e^{\beta\bar{\psi}_s}}{e^{\beta\bar{\psi}_s}} \doteq \beta\tilde{\psi}_s \qquad \text{where } \beta = \frac{kT}{q}$$

$$\therefore \qquad i_{ss}(t) = Y_{ss} \cdot \tilde{\psi}_s$$

where

$$Y_{ss} = j\omega \frac{q^2}{kT} \cdot \frac{N_s\bar{f}(1-\bar{f})}{1 + \dfrac{j\omega\bar{f}}{c_n\bar{n}_s}} \quad . \tag{A5}$$

This is the admittance of a series RC network with capacitance.

$$C_{ss} = \frac{q^2 N_s \bar{f}(1-\bar{f})}{kT}$$

and time constant

$$\tau_{n,ss} = \frac{\bar{f}}{c_n\bar{n}_s} \quad .$$

Similarly

$$R_{p,ss} = \frac{kT}{q^2} \frac{1}{c_p\bar{p}_s N_s \bar{f}}$$

where c_p = hole capture probability

$\bar{p}_s$ = dc hole concentration at the interface

$\bar{f}$ = Fermi function for the interface states.

$$\frac{R_{n,ss}}{R_{p,ss}} = \frac{c_p\bar{p}_s\bar{f}}{c_n\bar{n}_s(1-\bar{f})}$$

$$= \frac{c_p}{c_n} \frac{N_v \cdot e^{\frac{E_v - E_F}{kT}}}{N_c \cdot e^{\frac{E_F - E_c}{kT}} \cdot e^{\frac{E_t - E_F}{kT}}}$$

$$= \frac{c_p}{c_n} \cdot \frac{N_v}{N_c} \cdot e^{\frac{-(E_t - E_v + E_F - E_c)}{kT}} \quad .$$

APPENDIX B

B.1 Electron Beam Pulsing Unit

The basic Veeco VeB-6 Electron Beam Gun System was modified to allow operation in a pulsing mode. The high-voltage is applied in pulses to the gun while the filament current is kept constant. The evaporant may be lifted off in thin layers, giving a technique similar in some respects to the flash-evaporation process.

The circuit which was designed for this purpose consists of an astable and a monostable multivibrator. Adjustment of the pulse frequency and width is achieved by means of two variable resistors. Detail of the circuit is given in Figure B1.

B.2 The Electron Beam Rate Controller

An evaporation rate controller was designed for the electron beam system. The block diagram is shown in Figure B2. It utilizes the rate monitor which was built by Groth[44]. The "rate signal" is compared with a reference signal by means of the differential amplifier. The output of the differential amplifier controls a full-wave phase-controlled SCR circuit which, in turn, determines the filament current of the electron gun.

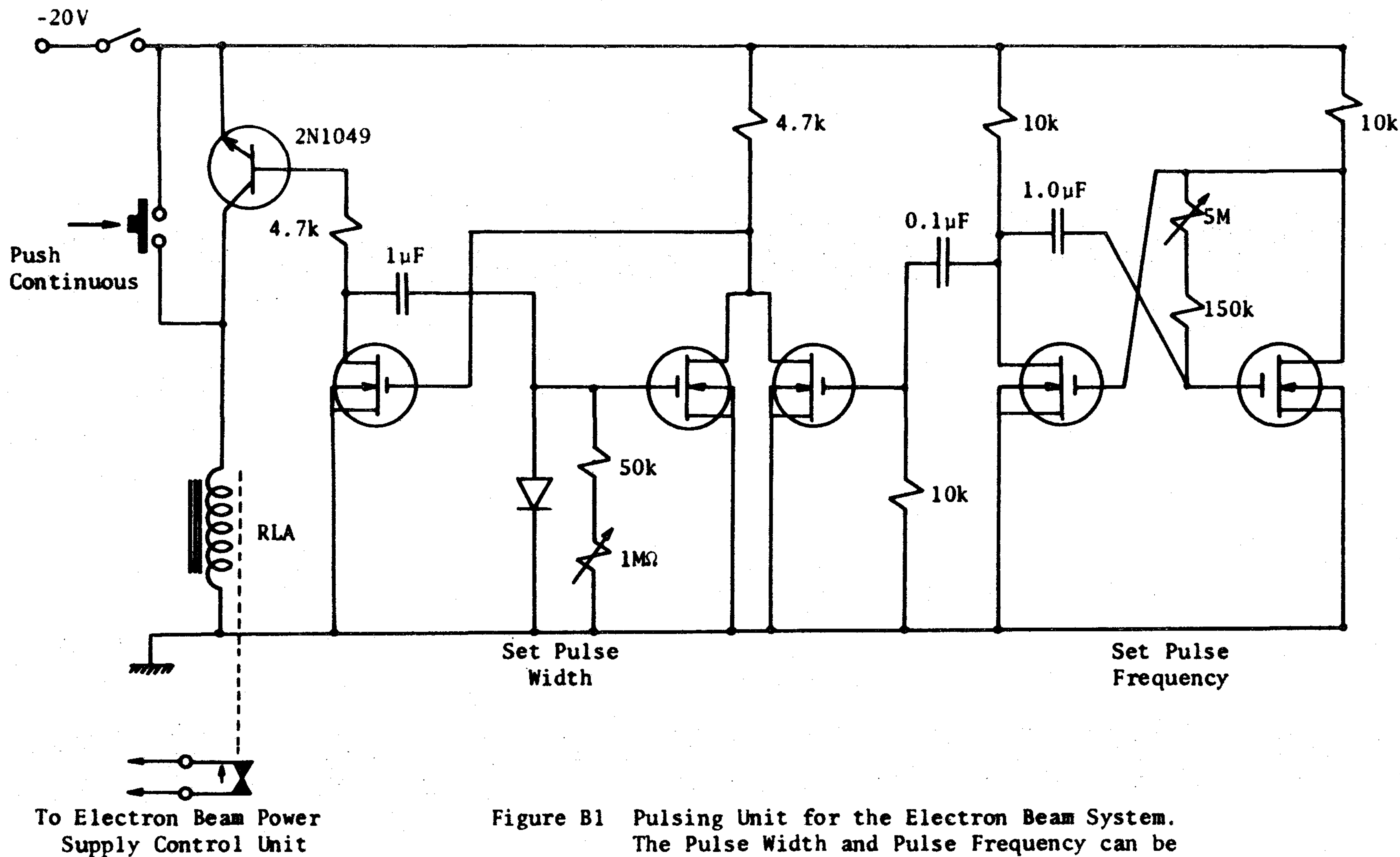

Figure B1 Pulsing Unit for the Electron Beam System. The Pulse Width and Pulse Frequency can be Set Independently.

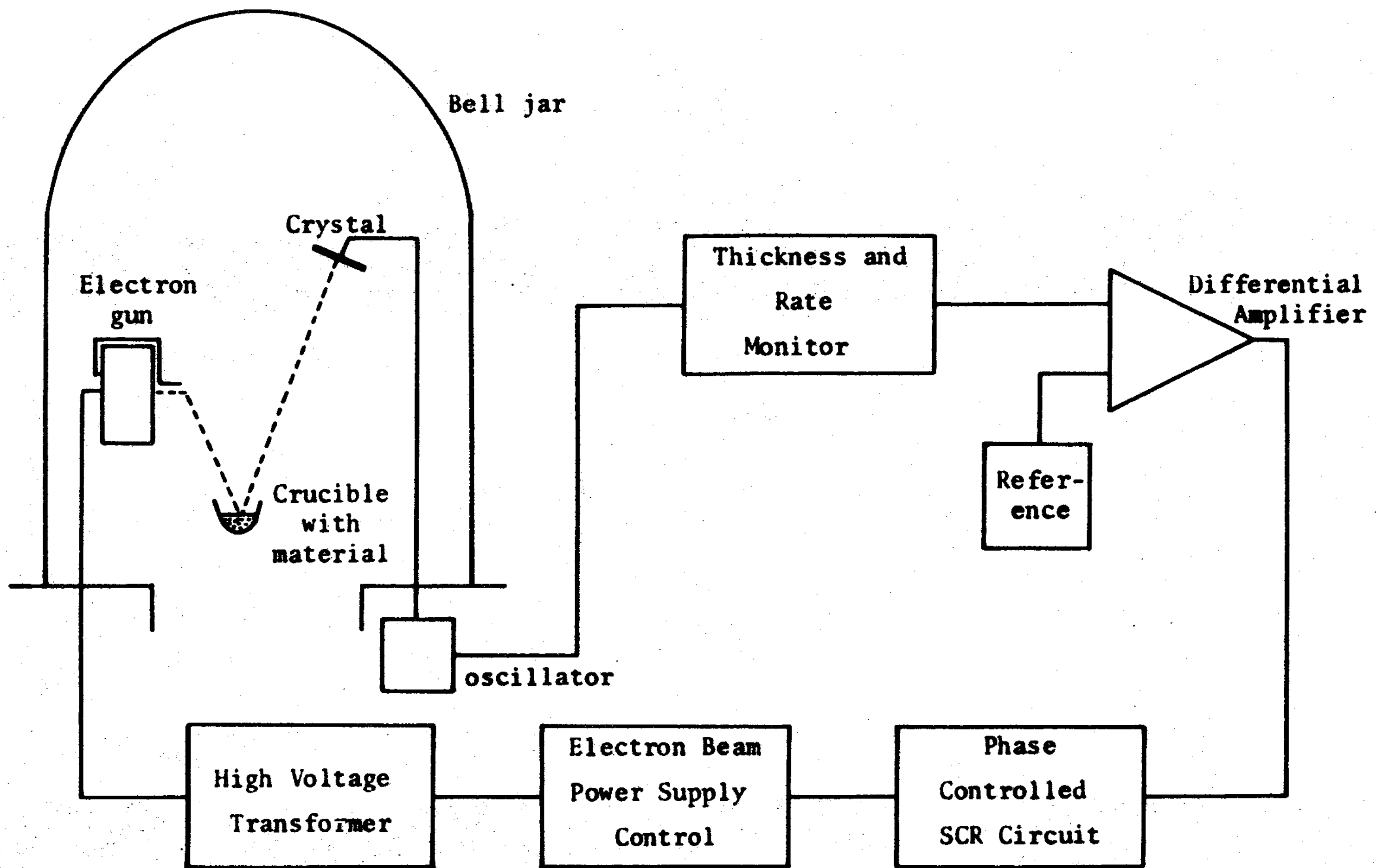

Figure B2 Block Diagram of the Electron Beam Rate Controller.

REFERENCES

1. Zainiger, K.H., F.P. Heiman, "The C-V Technique as an Analytical Tool, Part I and II", Solid State Technology, May 1970, pp. 49-56, June 1970, pp. 46-55.

2. Lamb, D.R., "Some Electrical Properties of the Silicon-Silicon Dioxide System", Thin Solid Films, 5, pp. 247-276, (1970).

3. Gray, P.V., "The Silicon-Silicon Dioxide System", Proc. IEEE, 57, pp. 1543-1551, (1969).

4. Sze, S.M., "Physics of Semiconductor Devices", Wiley-Interscience, New York, (1969), pp. 425-479.

5. Muller, J., B. Schiek, "Transient Responses of a Pulsed MIS-Capacitor", Solid-State Electronics, 13, pp. 1319-1332, (1970).

6. Marquardt, J., B. Schiek, "An Even C-V Characteristic Parametric Amplifier Using MIS Varactors", Proc. IEEE, 57, 2076, (1969).

7. Grove, A.S., B.E. Deal, E.H. Snow, C.T. Sah, "Investigation of Thermally Oxidised Silicon Surfaces Using Metal-Oxide Semi-conductor Structures", Solid-State Electronics, 8, pp. 145-163, (1965).

8. Deal, B.E., M. Sklar, A.S. Grove, E.H. Snow, "Characteristics of the Surface-State Charge (Q_{ss}) of Thermally Oxidized Silicon", J. Electrochemical Soc., 114, pp. 266-274, (1967).

9. Snow, E.H., A.S. Grove, B.E. Deal, C.T. Sah, "Ion Transport Phenomena in Insulating Films", Journal of Applied Physics, 36, pp. 1664-1673, (1965).

10. Hofstein, S.R., "Proton and Sodium Transport in SiO_2 Films", IEEE Trans. on Electron Devices, ED-14, pp. 749-759, (1967).

11. Hofstein, S.R., "Stabilization of MOS Devices", Solid-State Electronics, 10, pp. 657-670, (1967).

12. Swystun, E.J., A.C. Tickle, "Instability in Vacuum Deposited Silicon Oxide", IEEE Trans. on Electron Devices, ED-14, pp. 760-764, (1967).

13. Koelmans, H., H.C. de Graaff, "Drift Phenomena in CdSe Thin Film FET's", Solid-State Electronics, 10, pp. 997-1005, (1967).

14. Heiman, F.P., "Surface States and Related Effects Associated with a Metal-Oxide-Semiconductor Structure", RCA Technical Report, Princeton, New Jersey, (1964).

15. Tamm, I.E., Physik Z. Sowjetunion, 1, p. 733, (1932).

16. Shockley, W., Phys. Rev., 56, p. 317, (1939).

17. Allen, F.G., G.W. Gobeli, "Work Function, Photoelectric Threshold and Surface States of Atomically Clean Silicon", Phys. Rev., 127, p. 150, (1962).

18. Nicollian, E.H., A. Goetzberger, "The Si-SiO_2 Interface - Electrical Properties as Determined by the Metal-Insulator-Silicon Conductance Technique", The Bell System Technical Journal, Vol. XLVI, pp. 1055-1133, (1967).

19. Gray, P.V., D.M. Brown, "Density of SiO_2-Si Interface States", Appl. Phys. Letters, 8, pp. 31-33, (1966).

20. O'Hanlon, J.F., "Field-Effect Investigations in Thin Cadmium Sulfide Films", Ph.D. Thesis, Simon Fraser University, 1967.

21. Neugebauer, C.A., "Temperature Dependence of the Field-Effect Conductance in Thin Polycrystalline CdS Films", Journal of Applied Physics, 39, pp. 3177-3186, (1968).

22. Waxman, A., G. Mark, "Improved Stability in Al_2O_3-CdSe Thin-Film Transistors", Solid-State Electronics, 12, pp. 751-764, (1969).

23. Many, A., Y. Goldstein, N.B. Grover, "Semiconductor Surfaces", North-Holland Publishing Company, Amsterdam, 1965.

24. Garrett, C.G.B., "High-Frequency Relaxation Processes in the Field-Effect Experiment", Phys. Rev., 107, p. 478, (1957).

25. Berz, F., "Field Effect at High Frequency", J. Electron Control, 6, pp. 97-112, (1959).

26. Berz, F., "Variation with Frequency of the Transverse Impedance of Semiconductor Surface Layers", J. Phys. Chem. Solids, 23, p. 1795, (1962).

27. Yunovich, A.E., "Dependence of Field Effect in Semiconductors on Frequency", Sov. Phys., Tech. Phys., 3, p. 646, (1958).

28. Yunovich, A.E., Sov. Phys., Solid State, 1, p. 998, (1960).

29. Lehovec, K., A. Slobodskoy, "Impedance of Semiconductor-Insulator-Metal Capacitors", Solid-State Electronics, 1, pp. 59-79, (1964).

30. Hofstein, S.R., G. Warfield, "Physical Limitations on the Frequency Response of a Semiconductor Surface Inversion Layer", Solid-State Electronics, 8, pp. 321-341, (1965).

31. Sah, C.T., "Theory of the Metal Oxide Semiconductor Capacitor", Solid State Electronics Laboratory Technical Report No. 1, (1964), Electrical Engineering Research Laboratories, University of Illinois, Urbana, Illinois.

32. Lehovec, K., "Frequency Dependence of the Impedance of Distributed Surface States in MOS Structures", Appl. Phys. Letters, 8, p. 48, (1966).

33. Carson, J.A., C.K. Campbell, P.L. Swart, F.J. Vallo, "Effects of Dielectric Losses on the Performance of Evaporated Thin-Film Distributed RC Notch Filters", (To be published in IEEE Journal of Solid State Circuits, June 1971).

34. Stein, J., "A New Look at Distributed RC Notch Filters", Proc. IEEE, 58, p. 596, 1970.

35. Kaufman, W.M., "Theory of a Monolithic Null Device and Some Novel Circuits", Proc. I.R.E., 48, pp. 1540-1545, (1960).

36. Johnson, S.P., L.P. Huelsman, "A High-Q Distributed-Lumped-Active Network Configuration with Zero Real-Part Sensitivity", Proc. IEEE, 58, p. 491, (1970).

37. Shaffer, C.V., W.J. Kerwin, "Multiloop Distributed RC Active Networks for Low Parameter Sensitivity with Low Amplifier Gain", Proc. 2nd Asilomar Conf., pp. 197-201, Nov. 1968.

38. Howe, D.I., "Explicit Design Equations for an Active Distributed RC Network", Proc. IEEE, 57, pp. 1656-1658, (1969).

39. Ghausi, M.S., J.J. Kelly, "Introduction to Distributed Parameter Networks", Holt, Rinehart and Winston, New York, (1968).

40. Golembeski, J.J., "Distributed RC Network Tuning", IEEE Journal of Solid-State Circuits, SC-4, p. 425, (1969).

41. Schwartz, N., R.W. Berry, "Physics of Thin Films", Vol. 2, G. Hass and R.E. Thun, Editors, Academic Press, New York (1964), p. 363.

42. Morgan, C.H., "A Study of Evaporated Thin-Film Devices", M.Eng. Thesis, McMaster University, September 1967.

43. Vallo, F.J., "Performance Enhancement of Evaporated Thin Film Field Effect Transistors", M.Eng. Thesis, McMaster University, August 1969.

44. Groth, L., "Film Thickness Monitor for the Controlled Evaporation of Vacuum Deposited Films", M.Eng. Thesis, McMaster University, May 1968.

45. Chopra, K.L., "Thin Film Phenomena", McGraw-Hill, New York, 1969.

46. de Klerk, J., "Fabrication of Vapor-Deposited Thin Film Piezoelectric Transducers for the study of Phonon Behaviour in Dielectric Materials at Microwave Frequencies", Physical Acoustics, Vol. 4A, pp. 195-223, Academic Press, Inc., New York, 1966.

47. Neugebauer, C.A., D.C. Miller, J.W. Hall, "Polycrystalline CdS Thin Film Field Effect Transistors: Fabrication, Stability and Temperature Dependence", Thin Solid Films, 2, pp. 51-78 (1968).

48. Priest, J., H.L. Caswell, Y. Budo, Vacuum 12, p. 301, (1962).

49. Anastasio, T., "Dielectric Properties of Films Formed by Vacuum Evaporation of Silicon Monoxide", J. Appl. Phys., 38, p. 2606, (1967).

50. Dalton, J.V., "Sodium Drift and Diffusion in Silicon Nitride Films", J. Electrochem. Soc., 113, pp. 1650 (1966).

51. Elliott, E., R.D. Tomlinson, M.J. Hampshire, J.H. Calderwood, "Some Properties of Electron Beam Evaporated Si_3N_4 Films", Thin Solid Films, 3, R47-R48, (1969).

52. Himes, W., B.F. Stout, R.E. Thun, Trans. 9th Natl. Vacuum Symp., p. 144, The MacMillan Co., N.Y., 1962.

53. Pratt, I.H., Proc. Natl. Electron Conf., 20, p. 215, (1964).

54. Schwartz, N., R.W. Berry, in Hass G., R.E. Thun, (Editors), "Physics of Thin Films", 2, pp. 378-389, (1964).

55. Marton, J.P., "Electrical and Optical Properties of Metal Films", Special Series of Lectures Held in the Institute for Materials Research, McMaster University, January 1970.

56. Campbell, C.K., "Some Dielectric Properties of Electron-Beam Evaporated Yttrium Oxide Thin Films", Thin Solid Films, 6, pp. 197-202, (1970).

57. Tsutsumi, T., "Dielectric Properties of Y_2O_3 Thin Films Prepared by Vacuum Evaporation", Japanese Journal of Applied Physics, 9, pp. 735-739, (1970).

58. Rairden, J.R., "The Anodic Oxidation of Yttrium Thin Films", J. Electrochem. Soc., 114, p. 75, (1967).

59. Goldstein, R.M., "Thin Film Yttrium Oxide Capacitors Formed by Electrochemical Anodization Techniques", Proc. Electronic Components Conference, Washington, D.C., p. 141, May 1968.

60. Goldstein, R.M., F.W. Leonard, "Thin Film Dielectric Capacitors Formed by Reactive Sputtering", Proc. Electronic Components Conference, Washington, D.C., May 1967, p. 312.

61. Goldstein, R.M., S.C. Wigginton, "R.F. Sputtered Yttria Capacitors", Thin Solid Films, 3, R41, (1969).

62. Ackermann, R.J., E.G. Rauh, R.J. Thorn, "Thermodynamic Properties of Gaseous Yttrium Monoxide. Correlation of Bonding in Group III Transition-Metal Monoxides", J. Chem. Phys., 40, p. 883, (1964).

63. Frank, B., R. Groth, "Herstellung und Eigenschaften von Schichten aus Y_2O_3 und Oxiden der Seltenen Erden auf Glas", Thin Solid Films, 3, pp. 41-50, (1969).

64. Chopra, K.L., "Thin Film Phenomena", McGraw-Hill, New York, (1969), pp. 465-528.

65. Hass, G., R.E. Thun, "Physics of Thin Films", Vol. 2, Academic Press, New York, (1964), pp. 398-409.

66. Goldstein, R.M., "Thin-Film Yttrium Oxide Capacitors", Electrochemical Technology, 6, pp. 186-189, (1968).

67. Laboratory for Insulation Research, MIT, "Research on High-Temperature Dielectric Materials", Summary Tech. Rept. No. 1, Nov. 1965.

68. O'Hanlon, J.F., "Field-Effect Investigations in Thin Cadmium Sulfide Films", Ph.D. Thesis, Simon Fraser University, 1967, pp. 53-63.

69. Dresner, J., F.V. Shallcross, "Crystallinity and Electronic Properties of Evaporated CdS Films", Journal of Applied Physics, 34, pp. 2390-2395, (1963).

70. Böer, K.W., J.W. Feitknecht, D.G. Kannenberg, "Properties of Recrystallized Evaporated CdS Layers", Phys. Stat. Sol., 16, pp. 697-709, (1966).

71. Hannay, N.B. (Editor), "Semiconductors", Reinhold, New York, (1959).

72. Abrikosov, N. Kh., V.F. Bankina, L.V. Poretskaya, L.E. Shelimova, E.V. Skudnova, "Semiconducting II-VI, IV-VI and V-VI Compounds", Plenum Press, New York, (1969).

73. International Conference on Semiconductor Physics, Prague, (1960).

74. Breckenridge, R.G. (Editor), "Photoconductivity Conference", John Wiley, New York, (1956).

75. Larach, S., "Photoelectronic Materials and Devices", Van Nostrand, Princeton, (1965).

76. Honig, R.E., "Vapor Pressure Data for the More Common Elements", RCA Review, 18, p. 201, (1957).

77. Dresner, J., F.V. Shallcross, "Rectification and Space-Charge-Limited Currents in CdS Films", Solid-State Electronics, 5, pp. 205-210, (1962).

78. Shallcross, F.V., "Methods of Deposition and Physical Properties of Polycrystalline II-VI Films", RCA Review, 28, pp. 569-584, (1967).

79. Vecht, A., "Methods of Activating and Recrystallizing Thin Films of II-IV Compounds", in "Physics of Thin Films", Vol. 3, Hass, G., R.E. Thun (Editors), Academic Press, (1966).

80. Weimer, P.K., "The Insulated-Gate Thin-Film Transistor", in "Physics of Thin Films, Vol. 2, Hass, G., R.E. Thun (Editors), Academic Press, (1964).

81. Somorjai, G.A., "Condensation and Evaporation of Solids", E. Rutner, P. Goldfinger, J.P. Hirth (Editors), Gordon and Breach Scientific Publishers, New York, (1964), p. 417.

82. de Klerk, J., Westinghouse Research and Development Laboratories, Pittsburgh. Private Communication.

83. Reynolds, D.C., G. Leies, L.L. Antes, R.E. Marburger, "Photovoltaic Effect in Cadmium Sulfide", Phys. Rev., 96, p. 533, (1964).

84. Henisch, H.K., "Electroluminescence", Pergamon Press, New York, (1962).

85. Pizzarello, F.A., "CdS Thin-Film Formation by the Method of Co-evaporation", J. Appl. Phys., 35, pp. 2730-2732, (1964).

86. Gilles, J.M., J. van Cakenberghe, Nature, 182, p. 862, (1958).

87. Gans, F., Bull. Sci. A.I.M., 11, p. 897, (1953).

88. Bube, R.H., "Photoconductivity of Solids", John Wiley and Sons, Inc., New York, (1960).

89. Niekisch, E.A., "Wechsellicht Methode zur Messung von Haftstellen-Einfangquerschnitten beim Cadmiumsulfied", Zeitschrift fur Physik, 161, pp. 38-45, (1961).

90. Niekisch, E.A., "Haftstellenspektren von CdS-Kristallen", International Conference on Semiconductor Physics, Prague, 1960, pp. 1064-1068.

91. Ham, F.S., D.C. Mattis, "Electrical Properties of Thin-Film Semiconductors", IBM Journal, 4, pp. 143-151, (1960).

92. Fang, F., S. Triebwasser, "Carrier Surface Scattering in Silicon Inversion Layers", IBM Journal, pp. 410-415, (Sept. 1964).

93. Sébenne, C., et M. Balkanski, "La Region de Charge D'Espace a l'Equilibre dans les Semi-Conducteurs à Faible Densité de Porteurs Libres", Surface Science, 1, pp. 42-53, (1964).

94. Ziman, J.M., "Electrons and Phonons", Oxford at the Clarendon Press, (1967).

95. Brooks, H., "Advances in Electronics", Vol. 1, pp. 156-160, (1955).

96. Berz, F., "Ionized Impurity Scattering in Silicon Surface Channels", Solid-State Electronics, 13, pp. 903-906, (1970).

97. N. St. J. Murphy, F. Berz, I. Flinn, "Carrier Mobility in Silicon MOST's", Solid-State Electronics, 12, pp. 775-786, (1969).

98. van Heek, H.F., "Hall Mobility of Electrons in the Space-Charge Layer of Thin CdSe Transistors", Solid-State Electronics, 11, pp. 459-467, (1968).

99. Schrieffer, J.R., "Effective Carrier Mobility in Surface-Space Charge Layers", Phys. Rev. 97, pp. 641-646, (1955).

100. Waxman, A., V.E. Henrich, F.V. Shallcross, H. Borkan, P.K. Weimer, "Electron Mobility Studies in Surface Space-Charge Layers in Vapor-Deposited CdS Films", J. Appl. Phys., 36, pp. 168-175, (1965).

101. Conwell, E., V.F. Weisskopf, "Theory of Impurity Scattering in Semiconductors", Phys. Rev., 77, pp. 388-390, (1950).

102. Torrey, H.C., C.A. Whitmer, "Crystal Rectifiers", McGraw-Hill, New York, (1948).

103. Piper, W.W., R.E. Halsted, "Intrinsic Electrical Properties of n-Type CdS", International Conference on Semiconductor Physics, Prague, 1960, p. 1046.

104. Powell, J.L., B. Crasemann, "Quantum Mechanics", Addison-Wesley, Reading, Massachusetts, (1961).

105. Shewchun, J., A. Waxman, "Automatic Plotting of Conductance and Capacitance of Metal-Insulator-Semiconductor Diodes or any Two Terminal Complex Admittance", The Review of Scientific Instruments, 37, pp. 1195-1201, (1966).

106. Kuhn, M., "A Quasi-Static Technique for MOS C-V and Surface State Measurements", Solid-State Electronics, 13, pp. 873-885, (1970).

107. Berglund, C.N., "Surface States at Steam-Grown Silicon-Silicon Dioxide Interfaces", IEEE Trans. E.D., ED-13, pp. 701-705, (1966).

108. Heiman, F.P., "On the Determination of Minority Carrier Lifetime from the Transient Response of an MOS Capacitor", IEEE Trans. E.D., ED-14, p. 781, (1967).